Basin-Scale Leakage Risks from Geologic Carbon Sequestration: Impact on Carbon Capture and Storage Energy Market Competitiveness

---

Final Scientific/Technical Report
Report number DOE/FE0000749-41

Reporting Period Start Date: October 1, 2009
Reporting Period End Date: March 31, 2013

Catherine A. Peters [*,a], Jeffrey P. Fitts [a], Elizabeth J. Wilson [b], Melisa F. Pollak [b], Jeffrey M. Bielicki [b], Vatsal Bhatt [c]

[a] Department of Civil and Environmental Engineering, Princeton University, Princeton, NJ, United States
[b] Center for Science, Technology, and Public Policy, Hubert H. Humphrey School of Public Affairs, University of Minnesota, Minneapolis, MN, United States
[c] Brookhaven National Lab, Upton, NY, United States

*Corresponding author: cap@princeton.edu, 1-609-258-5645

Report Date: February 8, 2014

DOE Award: DE-FE0000749

Submitted by:
Department of Civil and Environmental Engineering
Princeton University, Princeton, NJ, United States

DISCLAIMER

Abstract

This three-year project, performed by Princeton University in partnership with the University of Minnesota and Brookhaven National Laboratory, examined geologic carbon sequestration in regard to CO_2 leakage and potential subsurface liabilities. The research resulted in basin-scale analyses of CO_2 and brine leakage in light of uncertainties in the characteristics of leakage processes, and generated frameworks to monetize the risks of leakage interference with competing subsurface resources. The geographic focus was the Michigan sedimentary basin, for which a 3D topographical model was constructed to represent the hydrostratigraphy. Specifically for Ottawa County, a statistical analysis of the hydraulic properties of underlying sedimentary formations was conducted. For plausible scenarios of injection into the Mt. Simon sandstone, leakage rates were estimated and fluxes into shallow drinking-water aquifers were found to be less than natural analogs of CO_2 fluxes. We developed the Leakage Impact Valuation (LIV) model in which we identified stakeholders and estimated costs associated with leakage events. It was found that costs could be incurred even in the absence of legal action or other subsurface interference because there are substantial costs of finding and fixing the leak and from injection interruption. We developed a model framework called RISCS, which can be used to predict monetized risk of interference with subsurface resources by combining basin-scale leakage predictions with the LIV method. The project has also developed a cost calculator called the Economic and Policy Drivers Module (EPDM), which comprehensively calculates the costs of carbon sequestration and leakage, and can be used to examine major drivers for subsurface leakage liabilities in relation to specific injection scenarios and leakage events. Finally, we examined the competiveness of CCS in the energy market. This analysis, though qualitative, shows that financial incentives, such as a carbon tax, are needed for coal combustion with CCS to gain market share. In another part of the project we studied the role of geochemical reactions in affecting the probability of CO_2 leakage. A basin-scale simulation tool was modified to account for changes in leakage rates due to permeability alterations, based on simplified mathematical rules for the important geochemical reactions between acidified brines and caprock minerals. In studies of reactive flows in fractured caprocks, we examined the potential for permeability increases, and the extent to which existing reactive transport models would or would not be able to predict it. Using caprock specimens from the Eau Claire and Amherstburg, we found that substantial increases in permeability are possible for caprocks that have significant carbonate content, but minimal alteration is expected otherwise. We also found that while the permeability increase may be substantial, it is much less than what would be predicted from hydrodynamic models based on mechanical aperture alone because the roughness that is generated tends to inhibit flow.

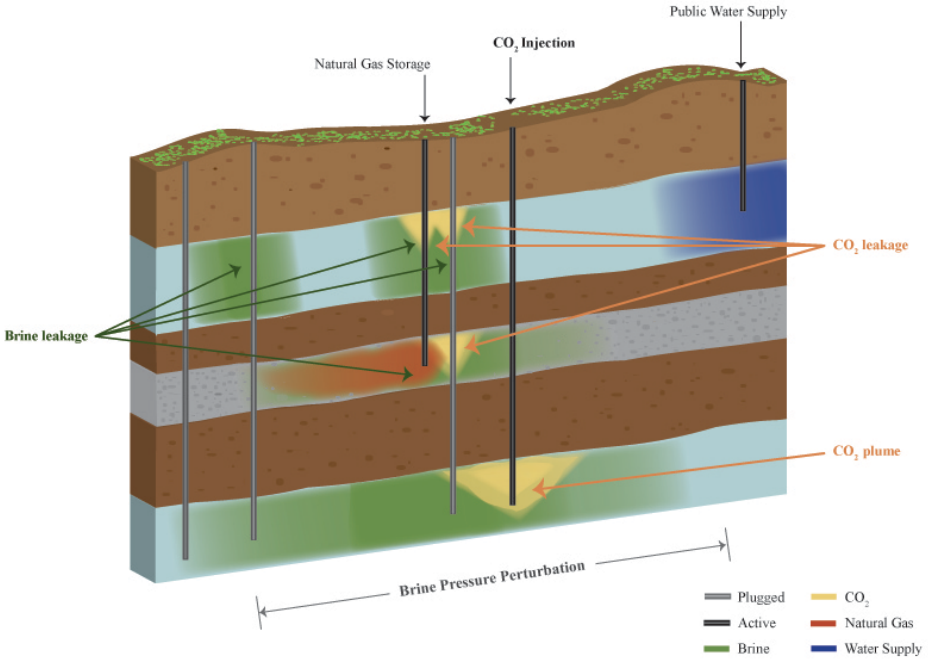

Table of Contents

Executive Summary

Widespread adoption of carbon capture and geologic sequestration (CCS) will occur only if CCS is economically competitive, politically feasible and if it comes close to meeting the US Department of Energy (DOE) performance goals of 99% CO_2 storage permanence and a 10% electricity cost premium. Costs and liabilities derive from the possibility of imperfect performance of a CCS project, in which some of the CO_2 stored in deep geologic formations leaks out. This leakage could translate into potential damages to and interferences with other subsurface resources such potable water. This project brought together a multidisciplinary team of experts to examine CO_2 leakage mechanisms and its financial consequences.

The geographic focus of the project was the state of Michigan, which is underlain by the Michigan sedimentary basin. We synthesized several data sources of the basin's hydrostratigraphy and applied kriging methods in Arc-GIS to construct a 3D topographical model of the basin. This model was used for the basin-scale leakage modeling analysis in which a probabilistic approach was used to handle uncertainty of the permeabilities of the formations and the leakage pathways. For the specific location of Ottawa County, MI, a 3D topographical model was constructed for the underlying sedimentary formations, with the goal of characterizing variability and uncertainty in the hydraulic properties. A statistical analysis was conducted to characterize the thicknesses, porosities and permeabilities of the formations, and the results were characterized using lognormal and generalized extreme value (GEV) distributions.

A major thrust of the project was to identify outcomes that may result from leakage, including interferences with subsurface resources, and to estimate the resulting financial consequences. This included developing methods to monetize leakage risk and stakeholder impacts at the basin-scale. In the Leakage Impact Valuation (LIV) model, we identified costs to a variety of stakeholders, including operators of other subsurface activities, such as oil and gas recovery and groundwater withdrawal. In a case study of leakage potential for CO_2 injection in the Michigan sedimentary basin, we found that costs could be incurred even in the absence of legal action or if the leakage does not affect other subsurface resources or reach the surface. The majority of leakage costs arise from activities to "Find and Fix a Leak" and from "Injection Interruption". Estimated costs range from $2.2MM for an event with only leakage from the injection formation to $154.7MM for leakage that reaches the surface. We also developed the RISCS (Risk Interference of Subsurface CO_2 Storage) model to integrate simulated predictions of basin-scale leakage with estimates of monetized leakage risk. We demonstrated RISCS in a case study for injection scenarios in the Mt. Simon sandstone in the Michigan sedimentary basin. We showed that CO_2 leakage can reach a shallow aquifer containing groundwater, but the rate is less than natural analogs of CO_2 fluxes to the land surface. We also showed that leakage may provide beneficial passive pressure relief and favorably reduce the Area of Review, and that violating the United States DOE's goal of at most 1% leakage would probably require an enormous number of leakage pathways, conditions that are unlikely in well-sited storage reservoirs.

Another major thrust of the project focused on the development of tools to predict leakage with low computational effort even in the case of complex geochemical processes that may alter leakage rates over time. Geochemical alterations of caprock flow paths may result from the acidity of CO_2-saturated brines and the resulting dissolution of caprock minerals. This may increase the permeability and transmissivity of the flow path and promote CO_2 and brine leakage. This work included (i) experimental observations of leakage pathway evolution due to geochemical reactions, (ii) fluid dynamics modeling to predict and understand reaction-induced permeability evolution of flow paths, and (iii) incorporation of permeability-evolution processes in basin-scale models to predict the effect of geochemical reactions on CO_2 and brine leakage

processes. The major finding is that fracture permeability can increase substantially if the rock contains calcite because of its potential to dissolve extensively and quickly, but caprocks that have minimal calcite are not likely to be affected by acid exposure. This observation demonstrates the vulnerability of carbonate caprocks which, if fractured, may jeopardize sealing integrity when hydrodynamic conditions promote flow of CO_2-acidified brine. We developed simplified geochemical models that can be used in a basin-scale leakage prediction model in a computationally tractable way. We showed that it is conceivable that permeability could triple over the course of 50 years if the conditions are favorable to drive calcite dissolution. Even with plausible simplifying assumptions, the chemistry is sufficiently complex that the simulation results reveal a non-monotonic relationship between permeability change and calcite content. For example, fractures in rocks with larger amounts of calcite may show smaller permeability change as buffering retards the advance of the dissolution front. The extent of the permeability change is dependent on a complex interplay of the initial fracture geometry, mineral spatial heterogeneity and variation, and fluid composition and flow rate. In the lab, we have identified processes that are currently not accounted for in any reactive transport model. For example, in rocks with calcite-dolomite mixtures, roughness and microporosity develop on fracture surfaces, making it difficult to apply conventional fracture flow models such as the Local Cubic Law. Also, because vertical transport is frequently orthogonal to sedimentary bedding layers, contiguous transverse features that do not dissolve may constrict flow even when there is extensive calcite dissolution. Another example is the case of mineral dissolution causing reduced fracture permeability, where mobilized clay particles clog the flow path. Reaction-induced permeability evolution in caprock flow paths presents new challenges for computationally tractable reactive transport models of permeability evolution.

The final thrust of the project was an examination of leakage in the context of the energy market competitiveness of carbon capture and sequestration (CCS). We developed an "Economic and Policy Drivers Module" (EPDM), which comprehensively calculates the cost of carbon sequestration along with the potential costs incurred by leakage for a particular geologic setting and injection scenario. The EPDM can be used to give order-of-magnitude cost estimates and determine the major drivers for leakage liabilities. We used the EPDM as input to MARKAL, an established DOE tool that predicts competition among energy production technologies in the energy systems market. For Michigan basin cases, we examined the competitiveness of selected CCS approaches under alternative financial strategies, government carbon tax policies, and leakage scenarios. This analysis should be considered preliminary, as the simulation results must first be validated by comparison with other energy system models. Keeping in mind the embedded uncertainty, our market penetration analysis shows that financial incentives, such as a carbon tax, are needed for coal combustion with CCS to gain market share. The effects of leakage on market penetration could not be fully examined because of limitations in MARKAL in accounting for complex economic risks outside the normal energy market.

This was a productive project resulting in 32 conference presentations, 6 of which were international. The work so far has generated 15 publications, 3 of which are still in preparation, in high impact journals including *Environmental Science & Technology*, *Energy and Fuels*, *Water Resources Research*, and *International Journal of Greenhouse Gas Control*. The project and the research products are compiled and archived online at http://www.subsurfacerisk.umn.edu/.

Chapter 1. Caprock Fracture Dissolution and CO_2 Leakage

This chapter has been published as:

J.P. Fitts and C.A. Peters, (2013) "Caprock Fracture Dissolution and CO_2 Leakage", In: Geochemistry of Geologic CO_2 Sequestration (Eds: DJ DePaolo, DR Cole, A Navrotsky, IC Bourg), *Reviews in Mineralogy & Geochemistry* Vol. 77: 461 – 482.

1.1 Introduction

Caprocks are impermeable sedimentary formations that overlie prospective geologic CO_2 storage reservoirs. As such, caprocks will be relied upon to trap CO_2 and prevent vertical fluid migration and leakage. Natural and industrial analogues provide evidence of long-term performance of caprocks in holding buoyant fluids. However, the large volumes of CO_2 that must be injected and stored to meaningfully reduce anthropogenic greenhouse gas emissions will exert unprecedented geomechanical and geochemical burdens on caprock formations due to elevated formation pressures and brine acidification.

Caprocks have inherent vulnerabilities in that wellbores, faults and fractures that transect caprock formations may provide conduits for CO_2 and/or brine to leak out of the intended storage formation. As a result, a critical criterion for CO_2 storage reservoir siting assessments will be to predict and reliably quantify the risk of leakage through caprock formations. We use 'flow paths' as a catchall term for any fluid conduit through caprocks including pore networks, fractures and faults along with any combination

of the three elements. It is useful to assess leakage rates through flow paths in terms of their individual transmissivity, T [m^4], which is the product of the permeability and the cross-sectional area of the flow path. Darcy's law can be used to relate these intrinsic flow path characteristics and the hydraulic potential (pressure) gradient to determine a volumetric flow rate, Q, or a leakage rate for the individual flow path:

$$Q = -\frac{T}{\mu}\frac{\Delta P}{\Delta z} = -\frac{Ak}{\mu}\frac{\Delta P}{\Delta z} \quad (1)$$

where P is the hydraulic potential [Pa], z is the depth [m], μ is the fluid viscosity [Pa s] and A [m^2] is the cross-sectional area of the flow path perpendicular to flow, and A equals the product of average fracture aperture and fracture length normal to the flow direction. Predicting leakage potential, however, is extremely complex because assessments must consider not only leakage through existing flow paths, but also the potential for the geomechanical and geochemical burdens to increase caprock transmissivity by creating new flow paths, increasing their cross-sectional area and/or increasing their permeability for decades and centuries to come.

This chapter reviews experimental observations and model developments that have advanced our ability to predict how the geochemical burdens of CO2 storage might alter leakage rates through caprocks. Our review is motivated by the question: Under what conditions and to what extent might mineral dissolution increase leakage rates through caprocks? This question anchors the focus of this paper on practical assessment tools, highlighting simplifying assumptions and the tradeoffs between assessment complexity and uncertainty. Thus far, assessments indicate that leakage risks will be manageably low at properly sited geologic CO2 storage reservoirs. Economic and commercial viability of GCS, concerns over environmental protection, as well as social dimensions of public acceptance will likely demand reductions in uncertainty about caprock performance that can only be addressed by improving the parameterization and computational efficiency of predictive models.

This chapter does not consider the geochemistry of well cements, and therefore, the reader should refer to Carey (2013) for a detailed review of the geochemistry of leakage through wellbores. While this chapter does not cover geomechanical processes that play a role in leakage risk, we acknowledge that geomechanical and geochemical processes are often coupled (Sonnenthal et al. 2004). Furthermore, the relevance of geochemical alteration of flow paths is predicated on the existence of flow paths, as might result from independent geomechanical forces (Heath et al. 2012; Manga et al. 2012; Shukla et al. 2010) such as induced seismicity (Zoback and Zinke 2001). We also acknowledge that it is unlikely that geochemical processes alone will create new caprock breaches through impermeable rock (Gaus et al. 2005; Gherardi et al. 2007).

In this chapter, we first survey efforts to define caprock performance standards, reviewing bounding analyses used to assess leakage risk through caprocks in terms of global emissions targets, geologic carbon sequestration (GCS) regulations, siting assessments, and barriers to market penetration and public acceptance of GCS. The review then summarizes the mineralogical reactivity criteria for the event of geochemical reaction induced changes to permeability in caprock flow paths, as well as what is known about the relevant flow paths through caprocks, and processes of brine acidification. We make the case for the development of simplified geochemical reactive transport models to predict permeability evolution, and we demonstrate this with an illustrative example of reactive flow through a 100 m one-

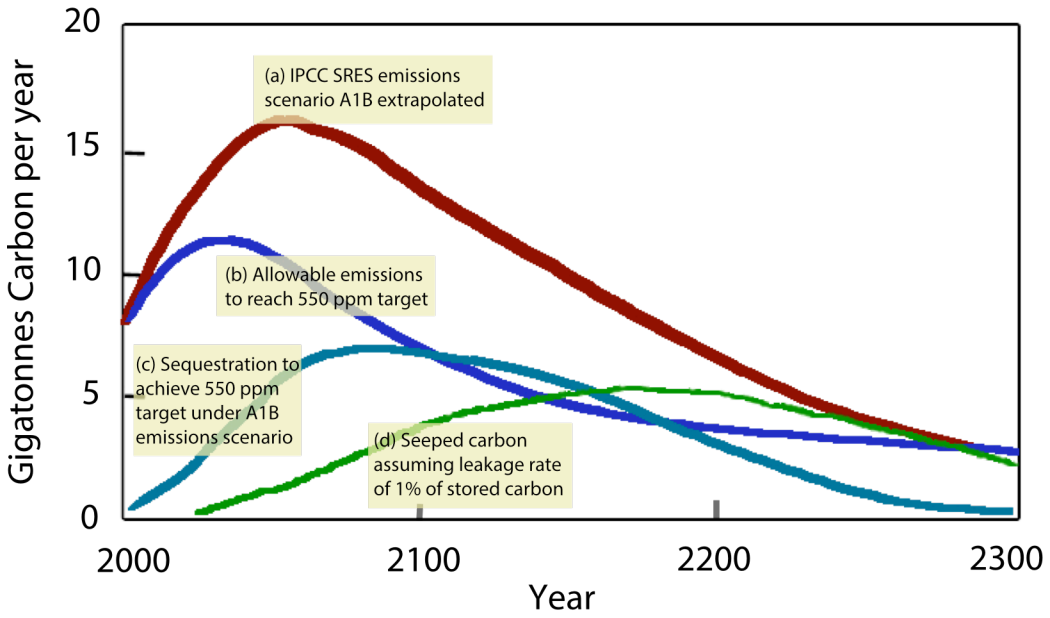

Figure 1. (a) Carbon emissions for the IPCC SRES A1B emissions scenario that assumes rapid global economic growth. (b) Allowable carbon emissions to achieve climate stabilization for CO_2 at 550 ppm. (c) The difference between curves (a) and (b) gives the reduction in CO_2 emissions needed, which here is assumed to be accomplished entirely by geologic sequestration. (d) Seepage of CO_2 assuming a leakage rate of 1% of the amount of CO_2 currently sequestered. [Adapted from: Hipple and Benson 2005].

dimensional flow path in a calcite-containing caprock. The final section brings together the experiments and simulations that reveal complex processes that are currently not part of existing reactive transport models. Such processes will require further research both to fully understand as well as to determine appropriate means of upscaling for application in practical models of caprock performance.

1.2 Big Picture Perspective of Caprock Performance

Structural or stratigraphic trapping by caprock formations is projected to be the most important mechanism keeping injected CO2 out of the atmosphere for 100's to 1000's of years. However, it has been recognized that given the necessity for storage over such long periods of time at many large storage sites distributed globally throughout sedimentary basins, leakage at some sites should be expected (Bachu 2008; Benson and Cole 2009). The longevity of CO2 storage is essential to providing the intended atmospheric greenhouse gas reductions, and while capillary, solubility and mineral trapping are projected to gradually reduce the relative importance of stratigraphic trapping, caprocks will remain the primary seal throughout the lifecycle of a CO2 geologic storage reservoir (Xu et al. 2004; Emberley et al. 2004). Therefore, we begin with the question: How good does a caprock need to be? The answer requires that we define acceptable leakage rates: acceptable in terms of reducing and maintaining reductions in atmospheric CO2 levels, acceptable in terms of human health and environmental impact, and acceptable economically and with respect to near- and long-term liability. The acceptable level of uncertainty in projections of caprock performance will also need to be defined and will depend both on the spatial scale over which the leakage rate estimates are applied [i.e., global vs. sedimentary basin vs. specific injection/storage site(s)] and the timeframe over which they are projected.

Hepple and Benson (2005) indirectly estimated caprock performance standards by considering the amount of CO2 that must remain underground in order to achieve different scenarios for global greenhouse gas emissions reductions and climate stabilization targets. Their modeling results showed how the range of acceptable rates of CO2 'seepage' to the atmosphere (0.01–0.1%/yr) depends on the global quantity of CO2 emissions reductions stored in geologic reservoirs, from 1000's of Gt to 10-100's of Gt for the relatively high allowable leakage. The authors also evaluated the sensitivity of their global performance standard to emission scenarios and sequestration requirements to achieve climate stabilization goals. This type of analysis is instructive in that it demonstrates the large uncertainties associated with the underlying parameters, and how acceptable leakage rates will need to be revised downward if CO2 emissions continue unabated. Global performance standards define an upper boundary for acceptable leakage to the atmosphere, and as a result, the greatest tolerance of uncertainty. The performance goal of 99% storage permanence was set by the U.S. Department of Energy (DOE) for its demonstration CO2 injection projects and storage projects being implemented in the Regional Carbon Sequestration Partnerships. Figure 1, based on the analysis by Hepple and Benson (2005), shows the amount of CO2 that would need to be offset, such as through geologic sequestration, to achieve climate stabilization of 550 ppm of CO2 under a rapid economic growth emissions scenario. Their analysis also showed that the 1% performance target may not be effective because by the year 2150 the leakage rate exceeds the allowable emissions. Siting assessments, however, will likely be held to more strict caprock performance standards as stakeholders demand assurances that leakage risk to economic, human health, environmental and societal interests will be low and manageable (Bielicki et al. 2013). Therefore, refined analyses of flow paths in the subsurface will be needed as required to predict both low probability high impact events and geospatial migration in a heavily utilized subsurface.

All currently proposed GCS regulatory frameworks are based on some formulation of what the United States Environmental Protection Agency (USEPA) refers to as an 'Area of Review' (AoR). The USEPA currently defines the AoR as the region surrounding the geologic sequestration project where underground sources of drinking water may be endangered by the injection activity. The AoR is delineated using computational modeling that accounts for the physical and chemical properties of all phases of the injected carbon dioxide stream and displaced fluids, and is based on available site characterization, monitoring, and operational data (USEPA, 2012). The purpose of the AoR is to determine the presence of flow paths through which significant amounts of injected CO_2 or displaced native brine could migrate out of the targeted storage formation. While the USEPA draft regulations consider the potential leakage risk of CO_2 and displaced native brine to freshwater aquifers, any comprehensive regulations will need to regulate a number of important dimensions of leakage including interference with other subsurface resources and releases of CO_2 back into the atmosphere. For example, hydraulic fracturing of shale formations for methane production has been highlighted as a subsurface activity that should be assessed for its potential impact on the seal quality of deep saline aquifer CO_2 storage formations (Elliot and Celia, 2012). Therefore, site-specific caprock assessments would ideally consider the permeability and areal extent of all potential flow paths within the AoR. Nogues et al. (2012a) bounded leakage for a prospective injection site in the Alberta basin by only considering leakage through wellbores (Figure 2). This approach could be adapted to include leakage through fractures and faults by characterizing/assigning the occurrence, areal extent and permeabilities. This study also demonstrates the application of probability distributions and Monte Carlo simulations to bound leakage rates through individual flow paths. The knowledge gaps in relation to fracture and fault occurrence and

characteristics are still too large to yield adequate uncertainties and satisfy statistical criteria of Monte Carlo analyses.

The most stringent caprock performance standards, however, will likely be required to overcome economic and commercial barriers to GCS implementation as well as to facilitate regulatory compliance and public acceptance. The potential risks of CO_2 leakage have already stirred local opposition to GCS implementation (*e.g.*, see refs in Little et al. 2010). Much work has been dedicated to evaluating the cost of GCS (see citations of Rubin et al. 2007), while a more limited number of studies have considered the additional costs of leakage risk. Pollak et al. (2013) developed the Leakage Impact Valuation (LIV) method, a systematic and thorough scenario-based approach to identify these costs, their drivers, and who incurs the costs across four potential leakage outcomes: 1) leakage only; 2) leakage that interferes with a subsurface activity; 3) leakage that affects groundwater; and 4) leakage that reaches the surface. The LIV method is flexible and can be used to investigate a wide range of leakage scenarios for subsurface activities and resources. The financial consequences of leakage estimated by the LIV method will vary across case studies due to differences in geologic, institutional, and regulatory settings. Bielicki et al. (2013) developed a methodology to monetize leakage risk throughout a basin, based on simulations of fluid flow, subsurface data, and estimates of costs triggered by leakage. Figure 3 shows the geospatial specificity of this method, where the semi-analytical code ELSA (Nordbotten et al. 2005a) was used to simulate leakage rates through existing wellbores into overlying permeable formations for the case of injection into the Mt. Simon formation in the Michigan basin. The results show how leakage infiltration

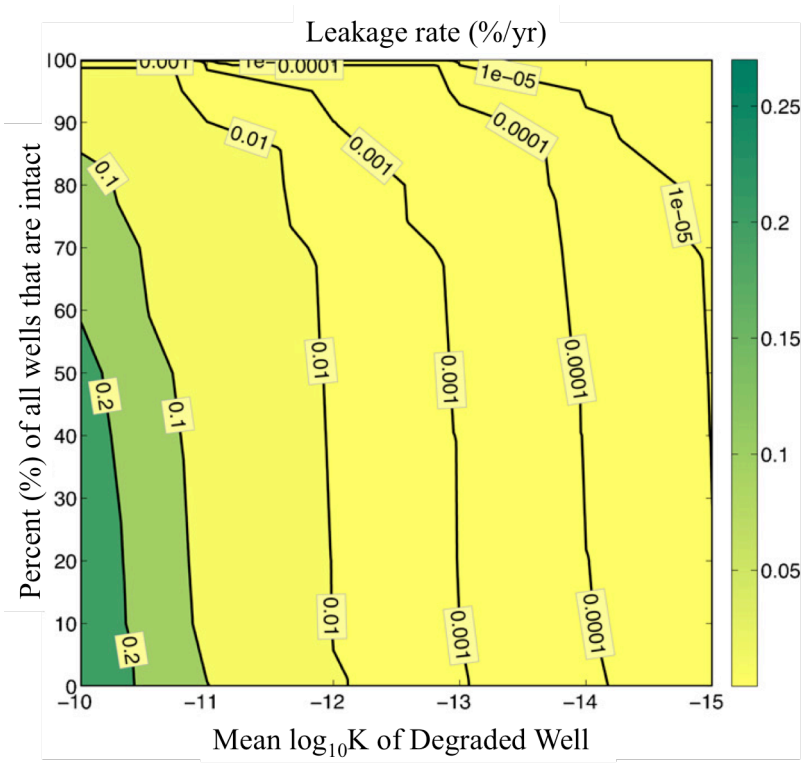

Figure 2. Contour map of leakage rate (%/yr) as a function of the wellbore permeability (log10K) and the percent of wells penetrating the injection formation that provide leakage conduits to the uppermost two aquifers in the stratigraphic column [Used by permission of Elsevier Ltd, from Nogues et al. (2012a), *International Journal of Greenhouse Gas Control*, Vol. 7, Fig. 4, p. 39.].

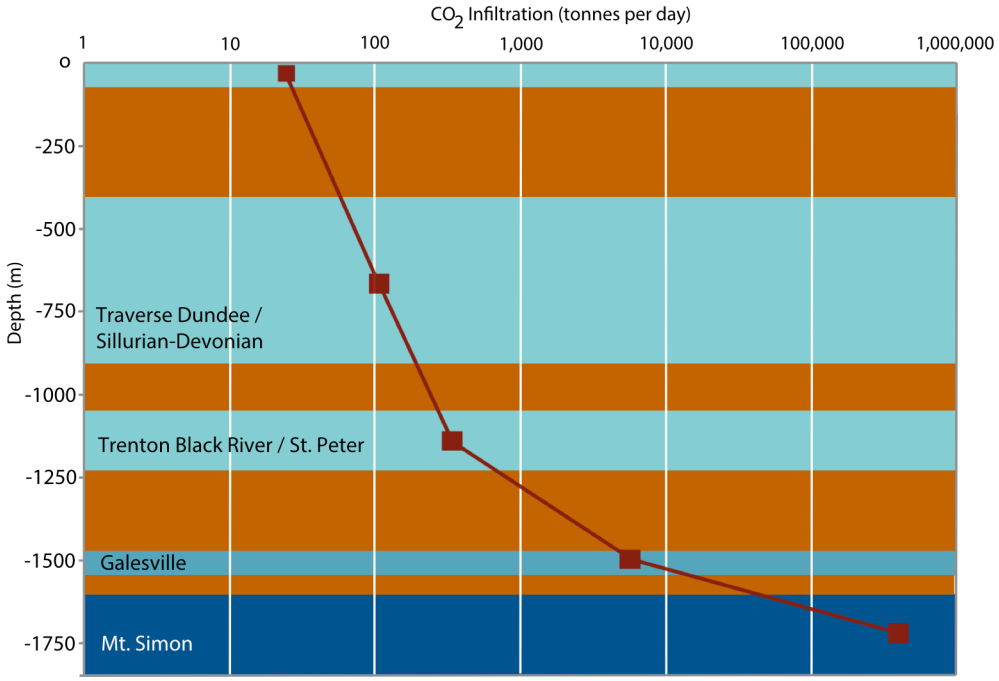

Figure 3. Leakage of CO_2 from the Mt. Simon formation in the Michigan basin and subsequent infiltration through the overlying geologic sequence after 30 years of continuous CO_2 injection and unabated leakage. [Modified with permission of JM Bielicki, see Bielicki et al., 2013].

into a formation varies with depth according to the physical extent and permeability of each sedimentary unit, pressure buildup in the injection formation (Cihan et al., 2013), and the flow path characteristics and proximity to the CO_2 source. While the amounts of infiltration to drinking water aquifers and the atmosphere are extremely small over 30 years of injection, the leakage rates of CO_2 and displaced native brine into deeper units are significant enough to impact other subsurface activities including wastewater injection and oil/gas extraction (Bielicki et al. 2013). Furthermore, this study shows how leakage risk is site-specific, and how assessments that account for geospatial variation of caprock performance can be applied to prioritize CO_2 storage site selection based on the location and hydrodynamic properties of flow paths and their proximity to other subsurface activities.

In summary, the goals for caprock performance should guide the appropriate level of detail required to predict leakage rates and their evolution with time. Furthermore, this paradigm can be used to identify risk factors (susceptibilities) and guidelines to limit model complexity.

1.3 Baseline Assessments of Caprock Dissolution Potential

Caprocks are sedimentary formations with relatively low permeability deriving from the low porosity of the rock as well as the unconnected structure of the pore network. Caprocks generally fall into three categories: (i) argillaceous rocks which are highly compacted clays, shales or mudstones, (ii) consolidated clastic rocks that are compacted and highly cemented due to long-term diagenesis, and (iii) evaporites which are precipitated chlorides, sulfates and carbonates that usually contain some detrital materials such as chert, sand, clay or carbonate remnants of marine organisms. Figure 4 shows electron microscopy images of three caprock samples, all with low permeability but each with very different lithology and mineralogy. Even at this small spatial scale, mineral heterogeneity can produce complexity in flow path

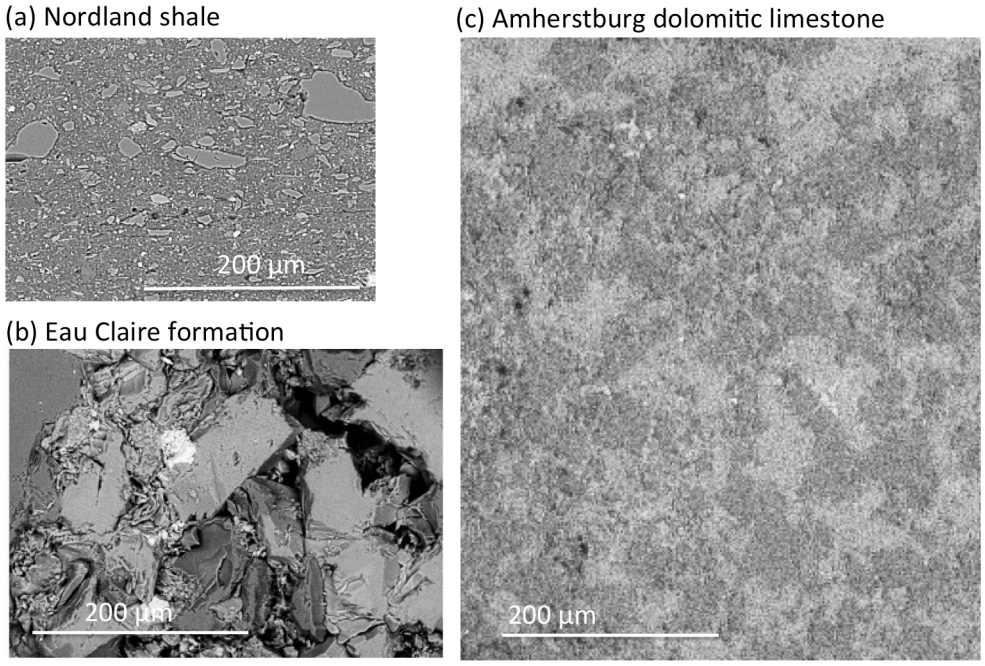

Figure 4. Backscattered electron micrographs of three different caprocks: (a) Nordland shale overlying the Utsira formation in the Sleipner Field, (b) Eau Claire formation overlying the Mt. Simon sandstone in the Illinois basin, (c) Amherstburg dolomitic limestone overlying the Bass Islands dolostone in the Michigan basin. Source for (a) is Harrington et al 2009 [Used by permission of the British Geological Survey, from Harrington et al. (2009), *Carbon dioxide sequestration in geological media—State of the science: AAPG Studies in Geology*, Vol. 59, Fig. 4, p. 521.].

permeability evolution.

The Nordland shale is an argillaceous rock overlying the Utsira sand, the target in the Sleipner Field for the CO_2 injection project in the North Sea. It is a shaley mudstone containing silt-grade grains of quartz, K-feldspar and calcite in a compacted but uncemented clay matrix of primarily mica and kaolinite (Harrington et al 2009). Specimens of this shale have porosity less than 1%, with permeability on the order of 10^{-19} m^2 (Harrington et al. 2009). This is negligible compared with the underlying Utsira formation which has a porosity between 30% and 40% and a permeability of 10^{-12} m^2 (Bickle et al 2007).

The Eau Claire formation is a highly compacted and consolidated clastic rock overlying the Mt. Simon sandstone in both the Michigan and Illinois sedimentary basins. In the Illinois basin, the Mt. Simon is the target for CO_2 injection for FutureGen 2.0. The Eau Claire formation has been characterized by several lithofacies, which have in common a detrital clastic mix of quartz and K-feldspar in cement matrices of clays such as illite or carbonates such as dolomite (Liu et al. 2012; Neufelder et al. 2012). Organics have also been found (Deng et al. 2013). Calcite is found nearly everywhere in the Eau Claire formation, with percentages as high as 41% particularly in the muddy siltstone and shale lithofacies (Neufelder et al. 2012). The study reported porosities ranging from less than 5% to more than 20%, and permeabilities mostly in the range of 10^{-22} m^2 to 10^{-16} m^2.

The Amherstburg is a dolomitic limestone evaporite that is considered as the primary seal for the Bass Islands dolostone, which was the target for the 2008-2009 CO_2 injection demonstration project in

Michigan (Gupta et al. 2011; Ellis et al. 2011). The Amherstburg is roughly equal parts calcite and dolomite with numerous well-formed fossil remnants. It has negligible porosity and permeability.

These three caprock formations are all considered to be excellent seals that would prevent upward migration of buoyant fluids. At the Sleipner field, time-lapse seismic observations have provided evidence that the Nordland shale is performing as an effective seal (Bickle et al. 2007). At the Bass Islands injection site, an array of monitoring approaches including wellhead measurements, downhole monitoring, crosswell seismic observation, and brine and cement sampling, indicated no evidence of CO_2 migration outside of the injection formation (Battelle 2011).

While reliable containment was achieved at the Michigan site, is being achieved at the Sleipner field, and is projected for the FutureGen 2.0 site, current leakage risk assessments do not account for possible geochemical evolution of caprock breaches. Caprock reliability assessments have historically been based on physical caprock integrity and hydrologic flow considerations. Implicit is an assumption that there is no risk of migration of acidified brines and reaction-induced erosion due to mineral dissolution. *Under what conditions might this be a concern, and how should computationally tractable models be developed for inclusion into practical basin-scale leakage models?*

To answer this question, we examine the mineralogical and geochemical conditions that present a risk for acid erosion of caprock flow paths. The minerals at risk are ones that are thermodynamically unstable at low pH as well as have negligible kinetic limitations for dissolution. There is only one mineral that fits this description: calcite. For formation brines that are near equilibrium with respect to calcite, if this system is perturbed by introduction of CO_2, the dissolved gas will lead to carbonic acid production. The resulting decrease in pH and increase in bicarbonate ion will lead to an increase in the thermodynamic driving force for calcite dissolution.

In addition to being quite soluble in acidic water, calcite's dissolution kinetics are extremely fast. According to kinetic data compiled by Palandri and Kharaka (2004), calcite's acid-driven dissolution rate constant is an order of magnitude larger than the next fastest reacting minerals, which are dolomite and anorthite, which have rate constants that are orders of magnitude faster than other minerals. Thus, while thermodynamics favors acid-driven dissolution for a host of minerals, calcite is the only one that is both highly soluble and will dissolve very fast. In reactive transport models that account for transport typical of deep subsurface conditions, it is often appropriate to model calcite dissolution as being locally instantaneous (*e.g.*, Nogues et al 2012b; 2013).

In addition to being highly soluble in acid and fast reacting, calcite is quite often abundant in sufficient quantity that its dissolution could substantially alter the volume of a flow path and alter its hydrodynamic properties. In the three caprock examples discussed above, calcite was present in all cases to various degrees. For other minerals that are fairly soluble and with fast dissolution kinetics, such as anorthite, even complete dissolution would not significantly change the permeability because these minerals are not present in sufficient quantities in typical sedimentary formations to cause a substantial porosity change.

The abundance of calcite is critical for permeability evolution of flow paths to be important, but the other necessary condition is a low concentration of calcium. A high calcium concentration in the brine would provide alkalinity that would effectively buffer the addition of acid, and may even favor calcite

precipitation rather than dissolution. Formation waters, site to site, are extremely variable in calcium content.

In summary, we argue that geochemical modeling efforts developed for the purpose of predicting reaction-induced permeability evolution focus on the system of equations that describe aqueous phase chemistry of pH, carbonate ions and calcium as well as water-rock interactions with calcite. This tremendously simplifies the range of complexity normally considered in geochemical reactive transport modeling.

1.4 Caprock Characteristics

To support geochemical modeling to predict reaction-induced permeability evolution, mineralogical, lithological and brine chemistry data are needed for potential injection formations and the overlying caprocks. Reviews of caprock characteristics specific to caprock seal performance assessments are limited. Griffith et al (2011) reviewed available information on the physical and chemical characteristics of geological seal strata within a number of geographically important basins considered for CO_2 sequestration in the US. They found limited published core analyses and downhole geophysical data describing the subsurface mineral and physical properties of the seals, and as a result, much of their tabulated data were derived from published studies of outcrops. An important finding for the basins examined was that fractures and faults penetrate seal strata, and calcite is among the common minerals found in caprocks. Michael et al. (2009) reviewed the seals of active injection sites and demonstration sites, and identified various seal lithofacies for sixteen injection operations as of 2009.

The basin scale reviews all point to the need for site-specific assessments with core data and geophysical measurements tailored on a site-by-site basis. The spatial scope of these site-specific reviews, which the US EPA calls Area of Review, is still being debated and researchers generally recommend that site characterization criteria be allowed to evolve as experience is gained. Birkholzer and Zhou (2009) modeled the areal extent of the pressure pulse and suggest that the area characterized in a permitting process may comprise a very large region within the basin. Understanding the reactive potential of caprock minerals, under relevant temperatures, pressures, and salinities, should be part of site-specific assessments. Sedimentological assessments of caprocks are even more rare in terms of assessing geochemical reactivity. Transverse sedimentary features, however, can be the predominant control on the permeability evolution of fractures (Deng, et al 2013).

1.5 Flow Paths through Caprocks

Wellbores have been the primary flow paths considered in leakage risk assessments of caprocks (Celia et al. 2011; Birkholzer et al. 2011). The geochemistry of wellbores and the potential for geochemically-driven permeability evolution is reviewed in chapter 16 (Carey, 2013). We face even greater uncertainties when assessing the occurrence, potential for creation and reactivation, and hydrodynamic properties of all other types of flow paths through caprocks. Aydin (2000) categorizes the two most common types of structural heterogeneities that facilitate hydrocarbon migration and flow as dilatant fractures (joints, veins, and dikes) and shear fractures/faults. These flow paths are typically characterized using geophysical methods, analog outcrop studies, conceptual models, and core logs. Both natural and induced fractures have been widely documented in consolidated sedimentary formations (Curtis 2002; Long and Ewing

2004), including geothermal (Wood et al. 2001) and CO_2 storage sites (Iding and Ringrose 2010; Griffith et al. 2011).

The hydrodynamic properties needed to evaluate the leakage rate through caprock flowpaths are most practically characterized according to transmissivity (T) and permeability (k) as shown in equation (1). Studies that assign hydrodynamic properties of these flowpaths are limited. Permeability of these structures may, on average, be a few orders of magnitude higher than those of the corresponding matrix rocks. Fractures are especially important flowpaths due to their prevalence (Bonnet et al. 2001), and potential impacts on flow and reactive transport (Singurindy and Berkowitz 2005).

Creation and reactivation of flow paths through caprocks is an especially important consideration given the large volumes of fluid that must be injected at each well. Induced seismicity (see citations of Chiaramonte et al. 2008) and formation overpressure (Birkholzer et al. 2011) produced by injecting large fluid volumes have been shown to create, activate and propagate fractures in consolidated sedimentary formations (Zoback and Zinke 2002). Geomechanical studies have demonstrated that during CO_2 injection caprocks are exposed to shear stresses (Chiaramonte et al. 2008), thermal stresses (Gor et al. 2013) and crystallization (Noiriel et al. 2010). Morris et al. (2011) simulated the effect of injection pressures from multi-million ton injection scenarios on fault reactivation. Although they were able to devise plausible injection scenarios where faults were reactivated and the seal was compromised, they report significant parameter sensitivity that suggests the need for further model development and detailed site-specific characterization.

In combination, the widespread occurrence of calcite and the network of flow paths point to a significant influence of calcite dissolution on flow path hydrodynamic properties. We must first consider the geochemical driving forces created by brine acidification.

1.6 Relevant Brine Acidification Processes

The acidification of native brine will be the primary geochemical burden on caprocks and the greatest geochemical challenge to long-term caprock performance. A typical pH range for CO_2-acidified brine is 3 to 4.5 depending on alkalinity, which represents a substantial perturbation to typical formation brines that range from pH 6 to 8. Three factors of brine acidification, however, are especially important to predict caprock dissolution and must be considered in order to quantify the spatial distribution of the proton driving force: 1) the relative distribution and migration of fluid phases within the pore-space (e.g., supercritical, liquid and gaseous CO_2, and brine), 2) the source of the acid, which is primarily carbonic acid, but may also include oxidized sulfur species and organic acids, and 3) mass transfer rates into the brine.

The distribution of acidity within the native brine depends on mass transfer rates and the proximity to the source of acidity, in this case the pure phase CO_2. During injection and as the plume extends, the chemistry of the fluid that will be accessible to a flow path will change. Nordbotten et al. (2005b) modeled the advance of the plume front. However, detailed models of spatial and temporal variation of pH in an injection formation are lacking. Ellis et al. (2010) modeled pH profiles for three simplified acid mass transfer scenarios ranging from rapid brine phase dispersion to slow diffusive mass transfer, and found that it may take several hundred years for a large portion of the brine in an injection formation to be

saturated with acid. However, such acid transport must be coupled with plume and brine transport models to provide reliable results.

When the CO_2 plume reaches the entry point for a caprock flow path, two-phase flow of brine and CO_2 is expected to occur. Nordbotten et al. (2005b) predicted upconing would prolong the time that mixed phase fluids would flow through the flow path. Phase changes and two-phase flow can have important implications for the quantity, continuity and duration of the source of acidity (*e.g.*, Oldenburg et al. 2012; Gor et al. 2013; Suekane et al., 2005). Multiphase flow impacts on leakage through a fracture were modeled by Lu et al. 2012. Accounting for phase changes and the relative abundance of different phases is predicted to become especially complex over long flow paths (Oldenburg et al. 2012). Andreani et al. (2008) alternated the flow of CO_2-saturated brine and CO_2 gas through a fractured limestone and suggested that the pure phase CO_2 created locally acidic waters that were trapped in the diffusion controlled regime of the fracture boundary.

Previous authors have evaluated the implications of co-injecting SO_2 with CO_2 as this would potentially bring both environmental and economic benefits. The potential for increased acidification is substantial given the strong acidic nature of sulfurous and sulfuric acid (Knauss et al. 2005; Xu et al. 2007). The additional acidification contributed by SO_2 depends, however on solubility and mass transfer kinetics, which vary with temperature and pressure, as determined by Crandell et al. (2010). The extent to which

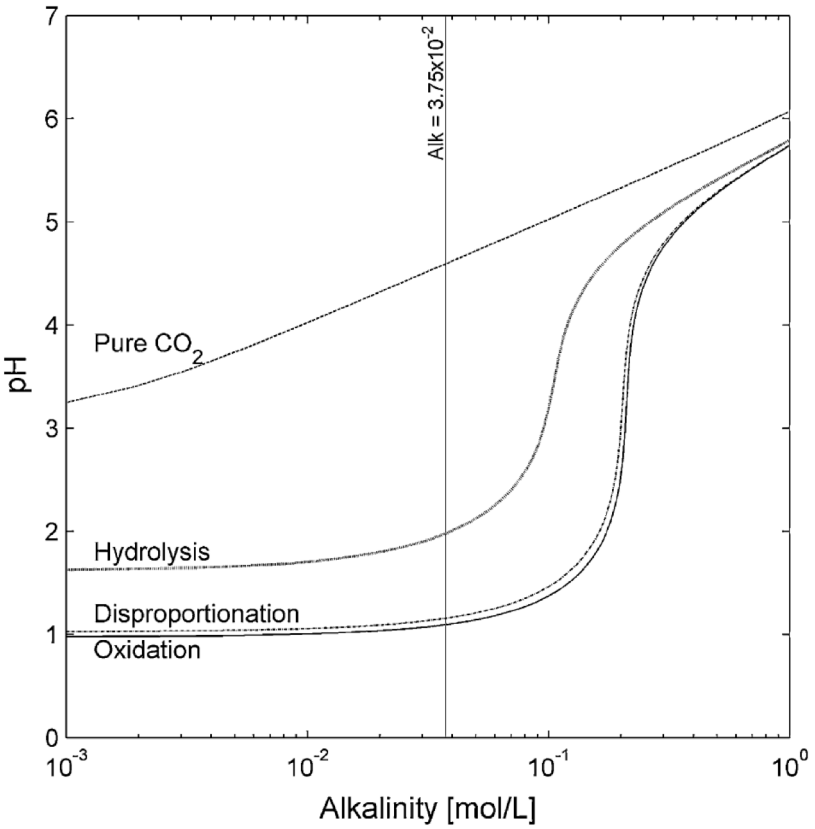

Figure 5. Brine acidification (pH) as a function of brine alkalinity for pure CO_2, CO_2 plus SO_2 with hydrolysis of SO_2, and CO_2 plus SO_2 with SO_2 disproportionation or oxidation [Used by permission of Elsevier Ltd, from Ellis et al. (2010), *Inter. J. Greenhouse Gas Control*, Vol. 4, Fig. 5, p. 575.].

SO_2 may be oxidized to sulfate is also an important factor (Ellis et al. 2010) as shown in Figure 5.

1.7 Predicting the Evolution of Caprock Flow Paths

Baseline assessments of caprock mineralogy, formation water composition, flow paths, and brine acidification help bound the conditions and geologic storage settings where flow path permeability evolution may occur. Reactive transport modeling, however, is the only practical method capable of exploring the vast parameter space that is beyond the reach of experimental observation. This is especially true for downhole conditions that are difficult to replicate in the laboratory, the complex combination of variables that determine permeability evolution, and the need to predict caprock leakage potential over long time periods.

Here we demonstrate the power of the simple modeling approach we advocate with a reactive transport model that accounts for pH, carbonate ions and calcium, and reactions with only calcite., We present a simulation of permeability evolution due to CO_2-acidified flow through a one-dimensional vertical flow path in a caprock. The system domain is a 100 m long by 0.2 m diameter cylindrical flow path containing a porous rock matrix with an initial porosity of 30% and initial permeability of 10^{-13} m^2. The porous rock matrix within the flow path contains calcite according to a specified initial volume fraction of calcite, over which a sensitivity analysis is conducted. For simplicity, this simulation assumes a fixed cylindrical boundary beyond which there is no flow and mineral erosion does not occur. Permeability evolution manifests due to calcite dissolution within the system boundary. In reality, it is expected that the walls of the flow path would erode and the system domain would increase especially near the bottom where the acidity is the greatest. However, this is beyond the scope of this simple illustrative modeling exercise.

The water entering the system from the bottom has a typical brine composition, with calcium concentration assumed to be 0.3 mol/L, total carbon concentration 0.8 mol/L, and pH 3.3. This is a substantial perturbation from the initial brine chemistry in the model system, which is assumed to have calcium concentration of 0.3 mol/L, total carbon concentration $1.5x10^{-3}$ mol/L, and pH 6.9. The pH 3.3 boundary condition is a worst-case scenario in that it corresponds to a case in which the inflowing brine is equilibrated with supercritical CO_2 with no buffering. If the storage reservoir were to have substantial soluble carbonate minerals, then the brine flowing from it into the leakage pathway would already be buffered to some extent and the pH would be higher. One way in which this simulation condition is not the worst case is that the flowing fluid is single-phase brine. If there were two-phase flow of both brine and CO_2, this would be a worst-case scenario as there is little chance for depleting the acidity through buffering along the leakage flow path. The flow of CO_2 as a separate phase serves as a persistent source of acidity.

In this reactive transport simulation, the model accounts for Darcy flow in one dimension, performs geochemical aqueous phase speciation, and treats calcite to be at local equilibrium with the fluid. The pressure gradient is fixed at 10.5 kPa/m. The permeability evolution is related to porosity change through the cubic law (discussed below), and the permeability for the entire domain is the harmonic average of the permeabilities of the nodes in the grid.

Even with a simplified geochemical model, with only one reactive mineral phase, the resulting behavior is complex because of the interplay between mineral dissolution and the buffering that results from the

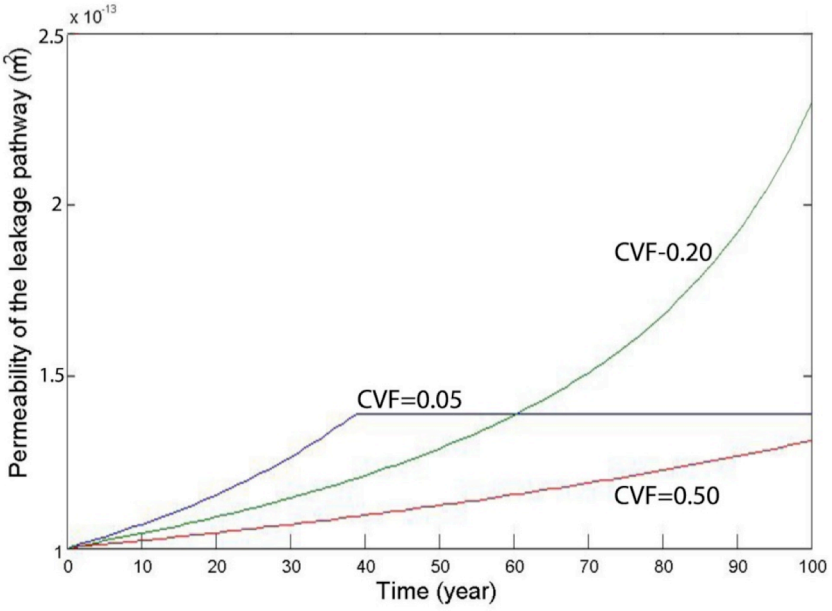

Figure 6. Simulated permeability evolution of a 100 m long flow path through a caprock as a function of time, for three different initial calcite volume fraction (CVF) values.

increased alkalinity. Figure 6 shows the simulation results for the permeability evolution over a one hundred year time frame, for initial calcite volume fraction (CVF) values ranging from 5% to 50%. These values might represent the range of conditions in the Eau Claire caprock, for example. For a given curve, the domain permeability evolves slowly early on, as calcite dissolves only near the inlet. As a result the increased concentration of calcium ions near the inlet neutralizes the acid and reduces its effect up the column. Over time, the calcite is depleted near the inlet and the reaction front advances up the column. The permeability remains constrained by the original permeability at the top until the reaction front breaks through. At this point, the permeability has reached a maximum.

For a small amount of calcite mineral (e.g. CVF = 0.05), the acid neutralization effect is smaller than for a larger CVF, and the reaction front advances more quickly. However, it is also the case that for a system with a small amount of calcite mineral, the net potential for volume change is smaller so the reaction reaches a limit earlier than for a larger CVF. This behavior leads to the counter-intuitive result that after 100 years the system with the biggest increase in permeability is the system with the intermediate calcite volume fraction. That is, the worst-case scenario is the system for which the reaction is not so buffered and is advancing at a significant rate, and for which the ultimate permeability change is substantial. If the CVF is too large, the acid neutralization is so substantial that the reaction front advances insignificantly.

Note that these results are purely illustrative and are not intended to be representative for at any particular site. The resulting tripling of the permeability shown in Figure 6 may actually be underestimated, as this model does not allow for a moveable system boundary. In reality, reactive flow in a caprock flow path will dissolve not only the rock matrix inside the flow domain, but will also erode the walls of the flow path thus increasing the transmissivity, not just the permeability.

The ultimate goal is to develop generalizable approaches to modeling flow path alterations with

appropriate and justifiable simplifying assumptions. Such models will be computationally tractable and can be plugged into field-scale and basin-scale models that estimate CO_2 containment reliability and leakage risk. However, recent experimental and modeling activities at Princeton and elsewhere have revealed additional levels of complexity that are not currently accounted for in any model. In the next section, we describe the complex permeability evolution processes that derive from heterogeneities and variations in mineral spatial patterns, flow path geometry, and fluid composition and flow rate.

1.8 Geochemically-Driven Evolution of Flow Paths

In this section we summarize experimental and simulation studies suggesting that when acidified brines dissolve calcite within caprock flow paths a complex set of factors and processes will determine not only the magnitude and rate of permeability evolution, but also whether the permeability will increase or decrease. Importantly, existing reactive transport models being used to predict flow path permeability evolution do not account for these factors and processes.

Three dimensional (3D) imaging with micro X-ray computed tomography (xCT) (Gouze et al. 2003; Werth et al. 2010; Karpyn et al. 2007; Wildenschild et al. 2013) provides non-invasive geometric measurement tools, and their application has enabled observations of acid-driven geometric evolution of fractures (Detwiler et al. 2003; Detwiler et al. 2008; Gouze et al. 2003; Nicholl et al. 1999; Noiriel et al. 2007). Ellis et al. (2011) flowed CO_2–acidified brine through an artificially fractured carbonate core from the Amherstburg formation of the Michigan sedimentary basin. The experimental conditions were selected to approach storage formation conditions including 14 MPa confining pressure, 10 MPa hydrostatic pressure and 27°C core temperature. X-ray CT analysis provided a means of quantifying the volumetric changes of the fracture caused by mineral dissolution, and a spatial map of the fracture volume, as shown in Figure 7. Along the 6.5 cm length of the core, the fracture void volume prior to flow of CO_2-acidified brine was ~0.6 mL, the median aperture was 270 μm, and the average cross-sectional area was 0.09 cm^2. After seven days of reaction, the fracture had a void volume of ~1.6 mL, the median aperture was 860 μm, and average cross-sectional area of 0.24 cm^2. This represents an increase in flow area of ~2.7 times. This observation of extensive dissolution confirmed what was expected given the known high calcite content of the rock. This was important to demonstrate the vulnerability of carbonate caprocks that, if fractured, can erode quickly and may jeopardize sealing integrity when hydrodynamic conditions promote flow of CO_2-acidified brine.

Additional important findings were revealed by post-experiment scanning electron microscopy (SEM). Complex geometric alterations of the fracture were created by preferential dissolution patterns, as shown in Figure 7. For example, where the relatively fast reacting calcite is banded with slower reacting dolomite, preferential dissolution of calcite created ‘comb-tooth’ shaped roughness (Figure 7a). In contrast, where calcite is homogeneously mixed with dolomite or non-reactive clay minerals and quartz, very porous calcite-depleted areas were formed, which we refer to as ‘degraded zones’ (Figure 7a). This suggested that increases in fracture permeability due to mineral dissolution may be offset by unaltered constrictions along the flow path and increases in surface roughness. Thus, the evolution of fracture permeability will depend in complex ways on the carbonate content as well as the heterogeneity of the minerals and their spatial patterning.

To examine the effects of evolving surface roughness on fracture hydrodynamics, we used computational

fluid dynamics (CFD) to simulate flow in this experimental fractured core, before and after reaction, and to compare these simulations results with predictions from simpler models. The relationship between fracture roughness and fluid flow has been represented with models of different levels of complexity. One-dimensional models based on the distribution of local apertures account for roughness by using a weighted average or standard deviation of apertures (Tsang and Witherspoon 1981; Renshaw 1995; Zimmerman and Bodvarsson 1996). The Local Cubic Law (LCL) assumes that the cubic law for smooth parallel wall fractures holds locally, and solves Reynolds' equation locally (O'Brien et al. 2003; Chaudhuri et al. 2008; Cvetkovic et al. 1999; Ghassemi and Kumar 2007; Yasuhara and Elsworth 2006). These models have been shown to under-estimate the impact of roughness on fracture flow at relatively high, yet realistic roughness (Nicholl et al. 1999; Petchsingto and Karpyn 2009; Crandall et al. 2010). CFD simulations have been shown to provide accurate calculations for flow in fractures across a range of relevant values for fracture roughness (Petchsingto and Karpyn 2009; Crandall et al. 2010; Javadi et al. 2010). While CFD simulations have shown that increased roughness generally results in more tortuous flow and lower transmissivity, Deng et al. (2013) was the first to observe this relationship by coupling SEM and xCT images showing the spatial distribution of minerals and resulting dissolution patterns in CFD simulations of the core-flooding experiments. The impact of increasing roughness on tortuosity can be seen in Figure 7b, where the inclusion of 'degraded zones' in the CFD simulations clearly increases the tortuosity of the streamlines. Therefore, while calcite dissolution greatly increased the fracture volume, the geometric alterations increased roughness, which in turn reduced the impact of fracture volume increase on transmissivity. Noiriel et al. (2007) similarly observed a decrease in permeability that they attributed partly to the increase of fracture roughness even though flowing acidified brine had dissolved calcite in a fractured argillaceous limestone rock.

While the banding of soluble and insoluble minerals is a common type of sedimentary feature that can result in increased fracture roughness, a lens of relatively insoluble minerals can also create a contiguous transverse stricture that controls fracture transmissivity no matter how much calcite dissolution is occurring throughout the fracture. Figure 7c shows the cross-sections of the fracture along the flow direction where such a transverse sedimentary layer of insoluble clay and silicates has maintained a mechanical aperture roughly equivalent to the fracture in the unreacted core. Deng et al. (2013) point out that sharp changes in fracture geometry such as fracture closure may occur if the geomechanical strength of the non-reactive bands is compromised.

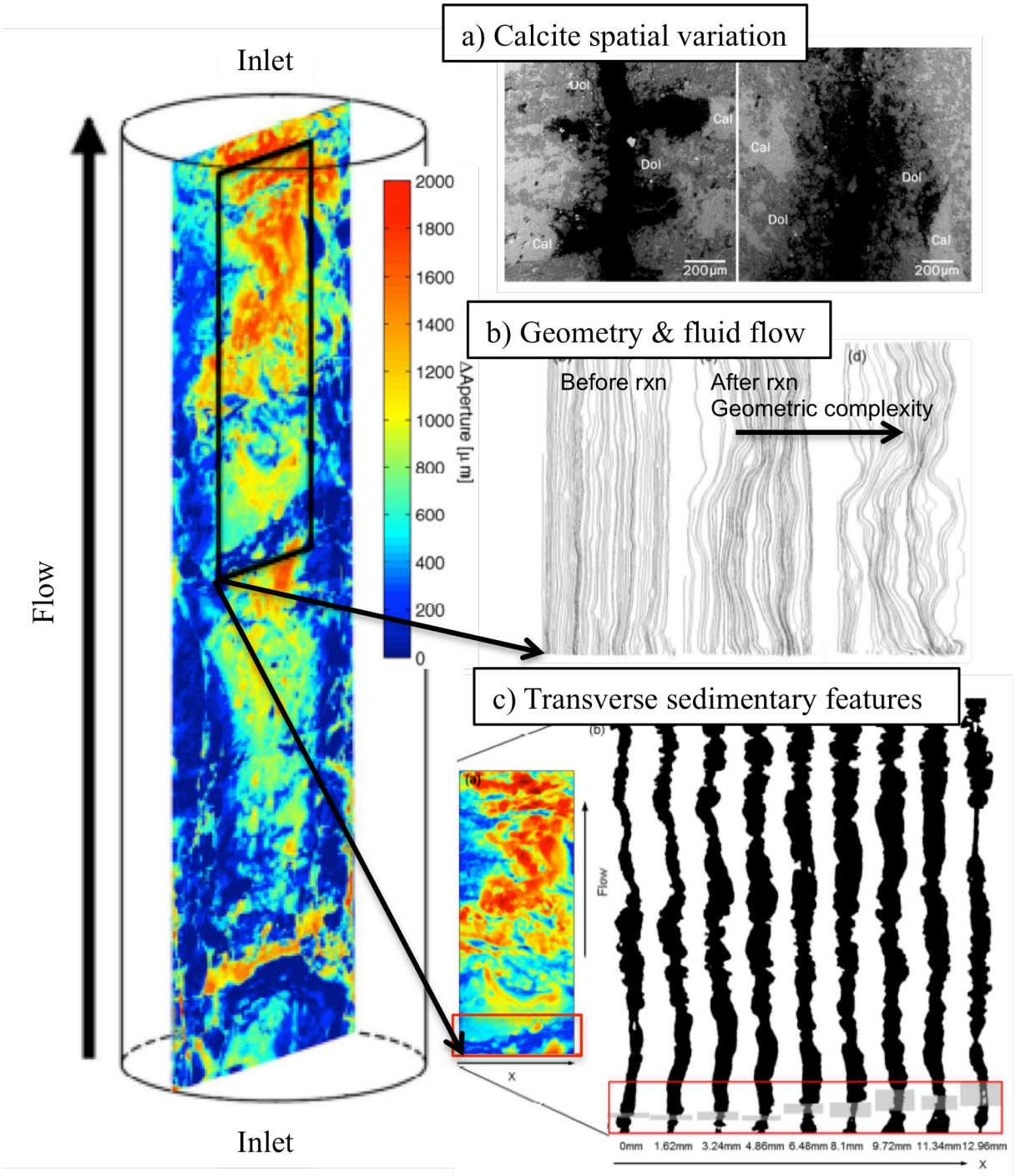

Figure 7. Delta aperture map showing the increase in aperture resulting from calcite dissolution along a fractured core from the Amherstburg formation: (a) Scanning electron microscopy images of two thin sections from the reacted core showing the two most common patterns of calcite dissolution observed in the reacted fracture, (b) streamlines of the velocity fields of fluid flow calculated from CFD simulations comparing the unreacted fracture with the post-reacted geometry with and without considering 'degraded zones' as part of the rock, and (c) vertical cross-sections of the reacted fracture highlighting the transverse sedimentary feature stricture in gray at the bottom. [Adapted from Deng et al. (2013)].

Evidence that dissolution can initiate mobilization and physical rearrangement of less soluble minerals has been observed in core-flooding experiments with acidified brines (Noiriel et al. 2007; Andreani et al. 2008; Smith et al. 2013; Ellis et al. 2013). Andreani et al. (2008) and Noiriel et al. 2007 were the first to observe dissolution of calcite that created a clay matrix with 40-50% increased porosity at the fracture boundary. The breakup, rearrangement and mobilization of this porous clay matrix resulted in complex and contradictory changes to permeability – flushing of the clay matrix increased permeability while fracture closure and clogging reduced permeability. Similarly, Ellis et al. (2013) presented imaging evidence for calcite dissolution that led to the release of less soluble feldspar and dolomite particles. These particles went on to occlude regions of the fracture, demonstrating that extensive dissolution may sometimes lead to a reduction in fracture permeability.

The final complexity that we consider is the development of preferential flow paths due to acid-driven mineral dissolution. There is a growing body of imaging studies investigating the development of preferential flow paths, ranging from studies of reactive flow through idealized fractures (Szymczak and Ladd 2012) to core-flooding experiments with rock cores (Noiriel et al. 2007). The studies with idealized parallel plate geometry and homogeneous mineralogy have observed a transition from uniform dissolution to channelization with increasing Damkohler number and decreasing Peclet number (Detwiler 2008; Detwiler et al. 2003). Furthermore, Szymczak and Ladd (2009) found that channelization occurs above a roughness threshold and is favored under the conditions of high reaction rates and intermediate Peclet number. Detwiler and Rajaram (2007) were able to predict channelization along an idealized single fracture surface using a depth-averaged model of fracture flow and reactive transport that explicitly calculates local dissolution-induced alterations of fracture apertures. Mineral spatial heterogeneity and variation present serious challenges to the application of these relationships beyond homogeneous mineralogy, especially in any realistic field setting.

Given the complexities observed in experimental observations, how does one mathematically relate permeability evolution to the porosity change that results from mineral reactions? A power law relationship has been most widely applied to relate changes in permeability to changes in porosity:

$$k = k_o \left(\frac{\phi}{\phi_o}\right)^{\alpha} \qquad (2)$$

where k_o and Φ_o represent initial permeability and porosity, respectively, and α is the power law parameter. While many experimental observations and theoretical studies suggest a cubic relationship is appropriate, a number of recent studies of CO_2-acidified brine driven permeability evolution have observed a much larger range of values for the power law parameter. Nogues et al. (2013) simulated permeability evolution in a pore network that contained heterogeneous distribution and abundance of calcite (ref. Figure 8), and found that appropriate α values ranged from 4 to 10. Although Carroll et al. (2013) fit the power law to experimental observations of permeability evolution driven by CO_2-acidified brine flow through limestone cores, they observed a similarly strong dependence of the power law parameter on initial pore connectivity and mineralogy. They found the highest α values for the samples with greatest anisotropy of pore space, connectivity and mineral heterogeneity.

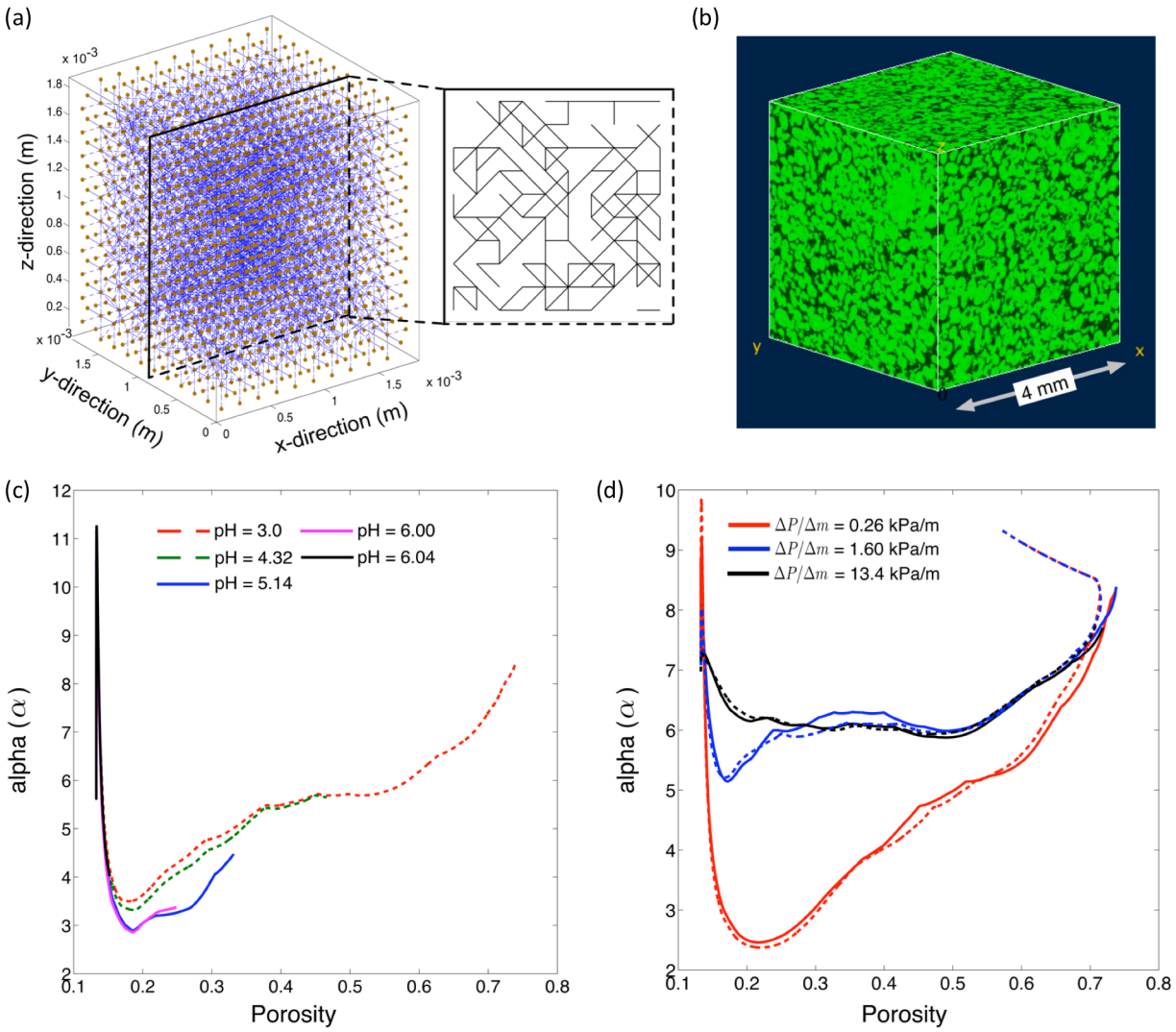

Figure 8. (a) Ball and stick representation of the pore network with a cross-sectional slice of the pore-to-pore connectivity derived from (b) dolomitized oolithic grainstone from Biswal et al. (2009), and used to model permeability changes due to calcite dissolution and derive values of power law parameter as a function of network porosities, for (c) different inflowing chemistries and (d) different pressure gradient conditions, where solid lines correspond to an inflowing pH=3 and dashed lines for an inflowing pH=5. [Adapted from Nogues et al 2013].

The greatest challenge to predicting permeability evolution in flow paths will be to account for this diverse set of factors unique to the unprecedented geochemical burdens while developing computationally efficient continuum, hybrid continuum-numerical and fully numerical models.

1.9 Concluding Remarks

Caprock formations are known to be reliable in containing buoyant fluids, including natural hydrocarbon and CO_2 reservoirs (*e.g.*, Bravo Dome, Sheep Mountain, McElmo Dome), stored natural gas, as well as injected CO_2 in numerous demonstration projects. Caprocks perform well because they are compacted matrices of fine particles, have undergone diagenic cementation, or are solid evaporite precipitates.

However, the large volumes of CO_2 that will need to be injected and stored to meaningfully mitigate climate change will exert unprecedented burdens on caprocks and their potential flow paths. Stringent caprock performance standards will likely be required to overcome economic and commercial barriers to GCS implementation and to facilitate regulatory compliance and public acceptance.

Allowable leakage rates of 1% are generally believed to be an acceptable target for GCS projects. Evidence to date indicates that leakage risks will be manageably low at properly sited storage reservoirs. However, there are challenges in predicting leakage rates for individual geologic strata. One such challenge comes from the plausibility of geochemical alterations of caprock flow paths given the acidity of CO_2-saturated brines and the reactivity of calcite present in most caprocks. Dissolution of caprock minerals in flow paths can conceivably increase the permeability and transmissivity and promote CO_2 and brine leakage. That is, if a flow path exists or is created during the injection process, flow of acidified brine through this flow path can adversely alter its hydrodynamic properties and promote leakage.

The single most important reactive mineral in the context of permeability evolution of flow paths is calcite because it has the necessary criteria of being soluble and fast-reacting, and it is ubiquitous in tight sedimentary rocks and in some formations is sufficiently abundant that dissolution would lead to important porosity changes. Therefore, we recommend that caprock calcite content be viewed as a critical siting assessment metric. Furthermore, because calcite dissolution is promoted not only by low pH (high carbonic acid concentration) but also by low concentration of dissolved calcium, the calcium concentration of formation brines is also a critical siting assessment metric.

Prediction of permeability evolution of a caprock flow path resulting from acid perturbation requires a reactive transport model that couples Darcy or fracture flow with geochemical speciation and reaction. Normally such a model would be computationally complex and not amenable to practical analytical leakage risk assessments. However, given the rationale for focusing on calcite as the most important mineral, we argue that simplified reactive transport models can be developed that limit the geochemical equations to those relating to pH, calcium, and the carbonate system. Furthermore, there are good arguments for using local equilibrium assumptions for calcite dissolution, rather than including the complexity of kinetic limitations. Such a model would vastly simplify the range of complexity ordinarily considered in geochemical reactive transport modeling, and would be computationally tractable for application in large-scale leakage risk models.

In this chapter, we presented a simple example of such a model simulation for one-dimensional reactive transport through a reactive flow path in a calcite-bearing caprock. We showed that it is conceivable that permeability could triple over the course of a century if the conditions are favorable to drive calcite dissolution. Even with plausible simplifying assumptions, the chemistry is sufficiently complex that the simulation results reveal a non-monotonic relationship between permeability change and calcite content.

Recent experimental and modeling activities at Princeton and elsewhere have revealed additional levels of complexity that are not currently accounted for in any reactive transport model. As an example, reactive evolution of fracture surfaces in rocks with mixtures of calcite and dolomite produces roughness and calcite-depleted porous zones. This makes it difficult to predict permeability evolution using conventional fracture flow models such as the Local Cubic Law model. Furthermore, vertical transport is orthogonal to sedimentary bedding layers so contiguous transverse features may remain undissolved and constrict flow

even when there is extensive calcite dissolution. Another complexity that has been observed is the case of reduced fracture permeability resulting from calcite dissolution, explained by the mobilization of clay particles that clog the flow path downstream. Finally, pore-network reactive transport modeling revealed a broad range of possibilities for the power law that relates changes in permeability to changes in porosity, which often is assumed to be a cubic law. Clearly, the process of reaction-induced permeability evolution in caprock flow paths is fraught with complexities that make it difficult to develop computationally tractable models of permeability evolution.

The following list highlights the experimental and modeling research priorities to reduce prediction uncertainties.

- Develop simple permeability evolution models based on calcite as the only reactive mineral, and conduct laboratory core-scale flow experiments and field tests to determine the extent to which such simplified geochemical reactive transport models are effective in predicting permeability change.
- Advance x-ray and electron microscopy and image processing methods to enable i) more accurate and precise quantification of pore space, pore-to-pore connectivity, and mineral spatial heterogeneity and variation; ii) real-time imaging of interfacial processes at flow path boundaries during acidified brine and multi-phase flow at caprock P/T conditions.
- Conduct more controlled experiments to explore the complex processes that accompany acid-driven mineral dissolution and contribute to flow path permeability evolution, including: i) the effects of mineral spatial heterogeneity and variation on the complex evolution of flow path geometry and surface roughness, ii) the importance of strictures resulting from relatively insoluble transverse sedimentary features, iii) the mobilization and physical rearrangement of less soluble minerals, iv) the initiation and development of preferential flow paths.
- Develop the means of representing these phenomena in reactive transport models that predict permeability evolution.

1.10 References

Andreani, M, Gouze, P, Luquot, L, Jouanna, P (2008) Changes in seal capacity of fractured claystone caprocks induced by dissolved and gaseous CO_2 seepage. Geophysical Research Letters DOI: 10.1029/2008GL034467

Aydin, A (2000) Fractures, faults, and hydrocarbon entrapment, migration and flow. Marine and Petroleum Geology 17(7): 797-814

Bachu, S (2008) CO_2 storage in geological media: Role, means, status and barriers to deployment. Progress in Energy and Combustion Science 34(2): 254-273

Battelle, (2011). Michigan Basin Phase II Geologic CO_2 Sequestration Field Test, Battelle, Columbus, OH.

Benson, SM, Cole, DR (2008) CO_2 Sequestration in Deep Sedimentary Formations. Elements 4(5): 325-331

Bickle, M, Chadwick, A, Huppert, HE, Hallworth, M, Lyle, S (2007) Modeling carbon dioxide accumulation at Sleipner: Implications for underground carbon storage. Earth and Planetary Science Letters 255(1-2): 164-176

Bielicki, JM, Pollak, MF, Wilson, EJ, Fitts, JP, Peters, CA (2013) A Methodology for Monetizing Basin-Scale Leakage Risk and Stakeholder Impacts Energy Procedia In press

Birkholzer, JT, Nicot, JP, Oldenburg, CM, Zhou, Q, Kraemer, S, Bandilla, K (2011) Brine flow up a well caused by pressure perturbation from geologic carbon sequestration: Static and dynamic evaluations. International Journal of Greenhouse Gas Control 5(4): 850-861

Birkholzer, JT, Zhou, Q (2009) Basin-scale hydrogeologic impacts of CO_2 storage: Capacity and regulatory implications. International Journal of Greenhouse Gas Control 3(6): 745-756

Biswal, B, Held, RJ, Khanna, V, Wang, J, Hilfer, R (2009) Towards precise prediction of transport properties from synthetic computer tomography of reconstructed porous media. Physical Review E 80(4): 041301

Bonnet, E, Bour, O, Odling, NE, Davy, P, Main, I, Cowie, P, Berkowitz, B (2001) Scaling of fracture systems in geological media. Reviews of Geophysics 39(3): 347-383

Carey JW (2013) Geochemistry of Wellbore Integrity in CO2 Sequestration: Portland Cement-Steel-Brine-CO2 Interactions. Rev Mineral Geochem 77:505-539.

Carroll, S, Hao, Y, Smith, M, Sholokhova, Y (2013) Development of scaling parameters to describe CO_2–rock interactions within Weyburn-Midale carbonate flow units. International Journal of Greenhouse Gas Control 16S: S185-S193

Celia, MA, Nordbotten, JM, Court, B, Dobossy, M, Bachu, S (2011) Field-scale application of a semi-analytical model for estimation cif CO_2 and brine leakage along old wells. International Journal of Greenhouse Gas Control 5(2): 257-269

Chaudhuri, A, Rajaram, H, Viswanathan, H (2008) Alteration of fractures by precipitation and dissolution in gradient reaction environments: Computational results and stochastic analysis. Water Resources Research 44(W10410): 1-19

Chiaramonte, L, Zoback, MD, Friedmann, J, Stamp, V (2008) Seal integrity and feasibility of CO_2 sequestration in the Teapot Dome EOR pilot: geomechanical site characterization. Environmental Geology 54(8): 1667-1675

Cihan, A, Birkholzer, JT, Zhou, Q (2013) Pressure Buildup and Brine Migration During CO2 Storage in Multilayered Aquifers. Ground Water 51(2): 252-267

Crandall, D, Bromhal, G, Karpyn, ZT (2010) Numerical simulations examining the relationship between wall-roughness and fluid flow in rock fractures. International Journal of Rock Mechanics and Mining Sciences 47(5): 784-796

Crandell, LE, Ellis, BR, Peters, CA (2010) Dissolution Potential of SO_2 Co-Injected with CO_2 in Geologic Sequestration. Environmental Science & Technology 44(1): 349-355

Curtis, JB (2002) Fractured shale-gas systems. Aapg Bulletin 86(11): 1921-1938

Cvetkovic, V, Selroos, JO, Cheng, H (1999) Transport of reactive tracers in rock fractures. Journal of Fluid Mechanics 378: 335-356

Deng, H, Ellis, BR, Peters, CA, Fitts, JP, Crandall, D, Bromhal, GS (2013) Modifications of carbonate fracture hydrodynamic properties by CO_2-acidified brine flow. Energy & Fuels DOI: 10.1021/ef302041s

Detwiler, RL (2008) Experimental observations of deformation caused by mineral dissolution in variable-aperture fractures. Journal of Geophysical Research-Solid Earth DOI: 10.1029/2008JB005697

Detwiler, RL, Glass, RJ, Bourcier, WL (2003) Experimental observations of fracture dissolution: The role of Peclet number on evolving aperture variability. Geophysical Research Letters 30(12): 1648−1651

Detwiler, RL, Rajaram, H (2007) Predicting dissolution patterns in variable aperture fractures: Evaluation of an enhanced depth-averaged computational model. Water Resources Research DOI:10.1029/2006WR005147

Elliot, TR, Celia, MA (2012) Potential Restrictions for CO_2 Sequestration Sites Due to Shale and Tight Gas Production. Environmental Science & Technology 46(7): 4223-4227

Ellis, BR, Crandell, LE, Peters, CA (2010) Limitations for brine acidification due to SO_2 co-injection in geologic carbon sequestration. International Journal of Greenhouse Gas Control 4(3): 575-582

Ellis, BR, Fitts, JP, Bromhal, GS, McIntyre, DL, Tappero, R, Peters, CA (2013) Dissolution-Driven Permeability Reduction of a CO_2 Leakage Pathway in a Carbonate Caprock. Environmental Engineering Science 30(4): 187-193

Ellis, BR, Peters, CA, Fitts, JP, Bromhal, GS, McIntyre, DL, Warzinski, RP, Rosenbaum, EJ (2011) Deterioration of a fractured carbonate caprock exposed to CO_2-acidified brine flow. Greenhouse Gases Science and Technology 1(3): 248-260

Emberley, S, Hutcheon, I, Shevalier, M, Durocher, K, Gunter, WD, Perkins, EH (2004) Geochemical monitoring of fluid-rock interaction and CO_2 storage at the Weyburn CO2-injection enhanced oil recovery site, Saskatchewan, Canada. Energy 29(9-10): 1393-1401

Gaus, I, Azaroual, M, Czernichowski-Lauriol, I (2005) Reactive transport modelling of the impact of CO_2 injection on the clayey cap rock at Sleipner (North Sea). Chemical Geology 217(3-4): 319-337

Ghassemi, A, Kumar, GS (2007) Changes in fracture aperture and fluid pressure due to thermal stress and silica dissolution/precipitation induced by heat extraction from subsurface rocks. Geothermics 36(2): 115-140

Gherardi, F, Xu, TF, Pruess, K (2007) Numerical modeling of self-limiting and self-enhancing caprock alteration induced by CO_2 storage in a depleted gas reservoir. Chemical Geology 244(1-2): 103-129

Gor, GY, Elliot, TR, Prevost, JH (2013) Effects of thermal stresses on caprock integrity during CO_2 storage. International Journal of Greenhouse Gas Control 12: 300-309

Gouze, P, Noiriel, C, Bruderer, C, Loggia, D, Leprovost, R (2003) X-ray tomography characterization of fracture surfaces during dissolution. Geophysical Research Letters 30(5): 1267

Griffith, CA, Dzombak, DA, Lowry, GV (2011) Physical and chemical characteristics of potential seal strata in regions considered for demonstrating geological saline CO_2 sequestration. Environmental Earth Sciences 64(4): 925-948

Gupta, N, Ball, D, Sminchak, J, Gerst, J, Kelley, M, Place, M, Bradbury, J, Cumming, L (2011) Geologic storage field tests in multiple basins in Midwestern USA–Lessons learned and implications for commercial deployment. Energy Procedia 4: 5565-5572

Harrington, JF, Noy, DJ, Horseman, ST, Birchall, DJ, Chadwick, RA (2009) Laboratory study of gas and water flow in the Nordland Shale, Sleipner, North Sea. In: Grobe, M., Pashin, J.C., Dodge, R.L. (Eds.), Carbon dioxide sequestration in geological media. State of the science: AAPG Studies in Geology, pp. 521-543.

Heath, JE, Dewers, TA, McPherson, BJOL, Nemer, MB, Kotula, PG (2012) Pore-lining phases and capillary breakthrough pressure of mudstone caprocks: Sealing efficiency of geologic CO_2 storage sites. International Journal of Greenhouse Gas Control 11: 204-220

Hepple, RP, Benson, SM (2005) Geologic storage of carbon dioxide as a climate change mitigation strategy: performance requirements and the implications of surface seepage. Environmental Geology 47(4): 576-585

Iding, M, Ringrose, P (2010) Evaluating the impact of fractures on the performance of the In Salah CO_2 storage site. International Journal of Greenhouse Gas Control 4(2): 242-248

Javadi, M, Sharifzadeh, M, Shahriar, K (2010) A new geometrical model for non-linear fluid flow through rough fractures. Journal of Hydrology 389(1-2): 18-30

Karpyn, ZT, Grader, AS, Halleck, PM (2007) Visualization of fluid occupancy in a rough fracture using micro-tomography. Journal of Colloid and Interface Science 307(1): 181-187

Knauss, KG, Johnson, JW, Steefel, CI (2005) Evaluation of the impact of CO_2, co-contaminant gas, aqueous fluid and reservoir rock interactions on the geologic sequestration of CO_2. Chemical Geology 217(3-4): 339-350

Little, MG, Jackson, RB (2010) Potential Impacts of Leakage from Deep CO_2 Geosequestration on Overlying Freshwater Aquifers. Environmental Science & Technology 44(23): 9225-9232

Liu, F, Lu, P, Griffith, C, Hedges, SW, Soong, Y, Hellevang, H, Zhu, C (2012) CO_2-brine-caprock interaction: Reactivity experiments on Eau Claire shale and a review of relevant literature. International Journal of Greenhouse Gas Control 7: 153-167

Long, JCS, Ewing, RC (2004) Yucca Mountain: Earth-science issues at a geologic repository for high-level nuclear waste. Annual Review of Earth and Planetary Sciences 32: 363-401

Lu, C, Sun, Y, Buscheck, TA, Hao, Y, White, JA, Chiaramonte, L (2012) Uncertainty quantification of CO_2 leakage through a fault with multiphase and nonisothermal effects. Greenhouse Gases-Science and Technology 2(6): 445-459

Manga, M, Beresnev, I, Brodsky, EE, Elkhoury, JE, Elsworth, D, Ingebritsen, SE, Mays, DC, Wang, C-Y (2012) Changes In Permeability Caused By Transient Stresses: Field Observations, Experiments, And Mechanisms Reviews of Geophysics 50 DOI: 10.1029/2011RG000382

Michael, K, Golab, A, Shulakova, V, Ennis-King, J, Allinson, G, Sharma, S, Aiken, T (2010) Geological storage of CO_2 in saline aquifers-A review of the experience from existing storage operations. International Journal of Greenhouse Gas Control 4(4): 659-667

Morris, JP, Detwiler, RL, Friedmann, SJ, Vorobiev, OY, Hao, Y (2011) The large-scale geomechanical and hydrogeological effects of multiple CO_2 injection sites on formation stability. International Journal of Greenhouse Gas Control 5(1): 69-74

Neufelder, RJ, Bowen, BB, Lahann, RW, Rupp, JA (2012) Lithologic, mineralogical, and petrophysical characteristics of the Eau Claire Formation: Complexities of a carbon storage system seal Environmental Geosciences 19: 81-104

Nicholl, MJ, Rajaram, H, Glass, RJ, Detwiler, R (1999) Saturated flow in a single fracture: Evaluation of the Reynolds equation in measured aperture fields. Water Resources Research 35(11): 3361-3373

Nogues, JP, Court, B, Dobossy, M, Nordbotten, JM, Celia, MA (2012a) A methodology to estimate maximum probable leakage along old wells in a geological sequestration operation. International Journal of Greenhouse Gas Control 7: 39-47

Nogues, JP, Celia, MA, Peters, CA (2012b) Pore Network Model Development to Study Dissolution and Precipitation of Carbonates. XIX International Conference on Water Resources, University of Illinois, http://cmwr2012.cee.illinois.edu/SubsurfaceBiogeochemReactiveTrans(Proceedings).html

Nogues, JP, Fitts, JP, Celia, MA, Peters, CA (2013) Permeability evolution due to dissolution and precipitation of carbonates using reactive transport modeling in pore networks. Water Resources Research, Vol 49: 6006-6021, doe:10.1002/wrcr.20486

Noiriel, C, Made, B, Gouze, P (2007) Impact of coating development on the hydraulic and transport properties in

argillaceous limestone fracture. Water Resources Research 43(9) DOI:10.1029/2006WR005379
Noiriel, C, Renard, F, Doan, M-L, Gratier, J-P (2010) Intense fracturing and fracture sealing induced by mineral growth in porous rocks. Chemical Geology 269(3-4): 197-209
Nordbotten, JM, Celia, MA, Bachu, S (2005b) Injection and storage of CO_2 in deep saline aquifers: Analytical solution for CO_2 plume evolution during injection. Transport in Porous Media 58(3): 339-360
Nordbotten, JM, Celia, MA, Bachu, S, Dahle, HK (2005a) Semianalytical solution for CO_2 leakage through an abandoned well. Environmental Science & Technology 39(2): 602-611
O'Brien, GS, Bean, CJ, McDermott, F (2003) Numerical investigations of passive and reactive flow through generic single fractures with heterogeneous permeability. Earth and Planetary Science Letters 213(3-4): 271-284
Oldenburg, CM, Doughty, C, Peters, CA, Dobson, PF (2012) Simulations of long-column flow experiments related to geologic carbon sequestration: effects of outer wall boundary condition on upward flow and formation of liquid CO_2. Greenhouse Gases-Science and Technology 2(4): 279-303
Palandri, JL, Kharaka, YK (2004) A Compilation of Rate Parameters of Water-Mineral Interaction Kinetics for Application to Geochemical Modeling, U.S. Geological Survey, Menlo Park, CA.
Petchsingto, T, Karpyn, ZT (2009) Deterministic Modeling of Fluid Flow through a CT-scanned Fracture Using Computational Fluid Dynamics. Energy Sources Part a-Recovery Utilization and Environmental Effects 31(11): 897-905
Pollak, MF, Bielicki, JM, Dammel, JA, Wilson, EJ, Fitts, JP, Peters, CA (2013) The Leakage Impact Valuation (LIV) Method for Leakage from Geologic CO_2 Storage Reservoirs Energy Procedia In press
Renshaw, CE (1995) On the relationship between mechanical and hydraulic apertures in rough-walled fractures. Journal of Geophysical Research-Solid Earth 100(B12): 24629-24636
Rubin, ES, Chen, C, Rao, AB (2007) Cost and performance of fossil fuel power plants with CO_2 capture and storage. Energy Policy 35(9): 4444-4454
Shukla, R, Ranjith, P, Haque, A, Choi, X (2010) A review of studies on CO_2 sequestration and caprock integrity. Fuel 89(10): 2651-2664
Singurindy, O, Berkowitz, B (2005) The role of fractures on coupled dissolution and precipitation patterns in carbonate rocks. Advances in Water Resources 28(5): 507-521
Smith, MM, Sholokhova, Y, Hao, Y, Carroll, SA (2013) Evaporite caprock integrity: an experimental study of reactive mineralogy and pore-scale heterogeneity during brine-co_2 exposure. Environmental Science & Technology 47(1): 262-268
Sonnenthal, EL, Spycher, NF, Conrad, M, Apps, J (2004) A Conceptual and numerical model for thermal-hydrological-chemical processes in the yucca mountain drift scale test. *In*: Coupled Thermo-Hydro-Mechanical-Chemical Processes in Geo-Systems, Fundamentals, Modelling, Experiments and Applications. Elsevier Geo-Engineering Book Series. Vol. 2. Stephansson O., Hundson JA, Jing L (eds) Elsevier, pp. 347-352
Suekane, T, Soukawa, S, Iwatani, S, Tsushima, S, Hirai, S (2005) Behavior of supercritical CO_2 injected into porous media containing water. Energy 30(11-12): 2370-2382
Szymczak, P, Ladd, AJC (2009) Wormhole formation in dissolving fractures. Journal of Geophysical Research-Solid Earth 114 DOI: 10.1029/2008JB006122
Szymczak, P, Ladd, AJC (2012) Reactive-infiltration instabilities in rocks. Fracture dissolution. Journal of Fluid Mechanics 702: 239-264
Tsang, YW, Witherspoon, PA (1981) Hydromechanical Behavior of a deformable rock fracture subject to normal stress. Journal of Geophysical Research 86(NB10): 9287-9298
USEPA (2012) Criteria and Standards Applicable to Class VI Wells. 40 CFR 146.81. Retrieved June 01, 2013 from www.ecfr.gov.
Werth, CJ, Zhang, CY, Brusseau, ML, Oostrom, M, Baumann, T (2010) A review of non-invasive imaging methods and applications in contaminant hydrogeology research. Journal of Contaminant Hydrology 113(1-4): 1-24
Wildenschild, D, Sheppard, AP (2013) X-ray imaging and analysis techniques for quantifying pore-scale structure and processes in subsurface porous medium systems. Advances in Water Resources 51: 217-246
Wood, CP, Brathwaite, RL, Rosenberg, MD (2001) Basement structure, lithology and permeability at Kawerau and Ohaaki geothermal fields, New Zealand. Geothermics 30(4): 461-481
Xu, T, Apps, JA, Pruess, K, Yamamoto, H (2007) Numerical modeling of injection and mineral trapping Of CO_2 with H2S and SO_2 in a sandstone formation. Chemical Geology 242(3-4): 319-346
Xu, TF, Apps, JA, Pruess, K (2004) Numerical simulation of CO_2 disposal by mineral trapping in deep aquifers. Applied Geochemistry 19(6): 917-936
Yasuhara, H, Elsworth, D (2006) A numerical model simulating reactive transport and evolution of fracture permeability. International Journal for Numerical and Analytical Methods in Geomechanics 30(10): 1039-1062

Zimmerman, RW, Bodvarsson, GS (1996) Hydraulic conductivity of rock fractures. Transport in Porous Media 23(1): 1-30

Zoback, MD, Zinke, JC (2002) Production-induced normal faulting in the Valhall and Ekofisk oil fields. Pure and Applied Geophysics 159(1-3): 403-420

Chapter 2. Estimation and statistical analysis of hydraulic properties of sedimentary formations underlying Ottawa County, Michigan

2.1 Abstract

Comprehensive site characterizations are required for selection and performance evaluation of CO2 geological storage sites. Thickness, porosity and permeability of reservoir rock and overlying formations are critical inputs of hydrodynamic models. These parameters of the subsurface are difficult to collect, and often have large uncertainties attached. In the current study, using publicly available geophysical well logs, a primary site characterization was conducted for a potential CO2 storage site Ottawa County, Michigan, targeting Mount Simon Sandstone. A 3D geological model was constructed, providing thickness information of all 24 geological units. Porosity was estimated from neutron logs and density logs; whereas permeability was estimated from porosity or resistivity/conductivity logs using four different methods. Large variability across different formations is evident. Within one geological unit, large lateral and vertical variations were also observed. But the relationships between depth and porosity are not well-defined. Lognormal and generalized extreme value (GEV) distribution functions can be used to describe the uncertainties in permeability, and the latter captures the maximum and minimum tails better.

2.2 Introduction

Carbon Capture and Sequestration (CCS) has been identified as a key carbon mitigation technology (Pacala and Socolow, 2004; IPCC Report, 2007). Geological CO_2 storage in deep saline aquifers is particularly promising, because of the low cost (Anderson and Newell, 2004), accessible suitable geological formations and large storage capacities (Hepple and Benson, 2005; IPCC special report). However, CCS application at large scale is subject to several challenges (IPCC special report; Bachu, 2008), most notable of which is uncertainty for potential leakage of injected CO_2 through diffusion, fault and fracture zones, and abandoned wells into overlying formations or back to the atmosphere (Celia and Nordbotten, 2009), which can offset mitigation efficiency (Hepple and Benson, 2005), and have adverse effects on subsurface natural resources (e.g. potable water) and human health (Lewicki *et al*., 2007).

Knowledge of the likelihood of CO_2 leakage and consequences associated is crucial for site selection and design of proper operative guidelines.

Various investigations have conducted simulations through numerical (Ebigbo *et al*., 2006; Doughty, 2007; Pruess, 2008; Iding and Ringrose 2010), semi-analytical and analytical (Nordbotten *et al*., 2004; Nordbotten *et al*., 2005a; Nordbotten *et al*., 2005b; LeNeveu, 2008; Nordbotten *et al*., 2009; Celia and Nordbotten, 2009) methods to quantitatively assess the leakage possibility of (potential) storage sites under different injection scenarios. Regardless of the modeling approach used, high-quality input data are desirable. Lack of detailed information on subsurface hydraulic properties such as porosity and permeability, and large uncertainties associated are recognized as issues that require further studies (Maul *et al*., 2007; Celia and Nordbotten, 2009).

Comprehensive CCS site characterization is critical for risk assessment in the immediate subsurface environment to account for CO_2 migration and in the far field for pressure field and brine migration. A site characterization includes a 3D geological model of the subsurface, hydraulic property estimates of the storage reservoir and the overlying formations, and an assessment of the potential evolution of hydraulic properties during both injection and post-injection periods. Information of subsurface hydraulic properties is predominantly from (1) geophysical borehole logs (Zhang and Brusseau, 1998; Moreton *et al*., 2002), (2) production, injection, pumping and slug tests (Haimson and Doe, 1993; Zhang and Brusseau, 1998; Moreton *et al*., 2002), (3) whole core studies (Shipton *et al*., 2002), and (4) borehole-probe permeameter (Moreton *et al*., 2002; Shipton *et al*., 2002). Geophysical well logs are preferential for early stage site characterization given the following traits. Firstly, a large amount of geophysical log data is available in the public domain. Secondly, low costs and large coverage of borehole data allow a geostatically-extendable characterization of hydraulic properties of not only the target formation, but also the overlying formations, which are equally important for CCS risk assessment. In this respect, whole core studies and pumping tests are disadvantageous owing to the high cost associated with core sample recovery and the tests (Naoaki, 1999; Gallardo and Marui, 2007). Further to which, the fine vertical resolution provided by borehole data is favorable considering the variable nature of subsurface hydraulic properties caused by complex geological processes (Dafflon *et al.* 2009), which when combined with the lateral continuity of formations in the Michigan Basin provides a good basis for geological model development. Last but not least, borehole data provide in situ measurements of the subsurface hydraulic properties, and hence is not subject to errors caused by core relaxation and deviations from subsurface conditions, such as confining pressure (Shipton *et al*., 2002), in lab studies. Admittedly, deriving hydraulic properties from geophysical borehole data is based on the appropriate application of evidence-based porosity-permeability relationships and geostatistics, which introduces some uncertainty into the estimates. Furthermore, interpretation of publicly available borehole data helps identify spatial regions that require complementary data from whole core studies and pumping tests, and thus enhances economic efficiency of site characterization.

The objectives of our study are to (1) estimate hydraulic properties from available borehole data, and (2) provide statistically meaningful understandings of the estimates, including probabilistic distributions of permeability and uncertainties introduced in the process, which will be crucial for parameterization of large-scale models. Our study focuses on a potential CO_2 injection site – Ottawa County of the State of Michigan, targeting the Cambrian Mount Simon Sandstone. A 3-D geological model of the subsurface was constructed, providing thickness and depth information of all the major geological formations.

Porosity and permeability were derived from geophysical well logs and documented in detail for each geological unit. Systematic analyses were applied to investigate the statistical behavior of permeability and associated uncertainties.

2.3 Study area, data and methodology

2.3.1 Study area and target formation

Mt Simon Sandstone, deposited in the Cambrian period, has been identified as a highly potential reservoir for CO_2 sequestration (MRCSP report, 2005; Barns *et al.*, 2009; Medina *et al.*, 2010). It is medium- to coarse-grained quartz sandstone, with high porosity and permeability, large depth and thickness, overlain by a relatively non-permeable formation – Eau Claire. Its storage capacity in Michigan State alone is estimated to be >600,000 MM tons (Medina *et al.*, 2010). Mt Simon has a large areal coverage, as well as significant spatial variations. Its depth and thickness range from 900m to more than 5000m, and 50m to 400m respectively (Medina *et al.*, 2010). Ottawa County in the State Michigan (see Figure 1) was chosen as a potential injection site due to its large thickness, around 250m, and preferable depth of 1900m, enough to keep CO_2 in supercritical phase, yet not subject to the influences of compaction and overgrowth of quartz (Barns *et al.*, 2009; Medina *et al.*, 2010).

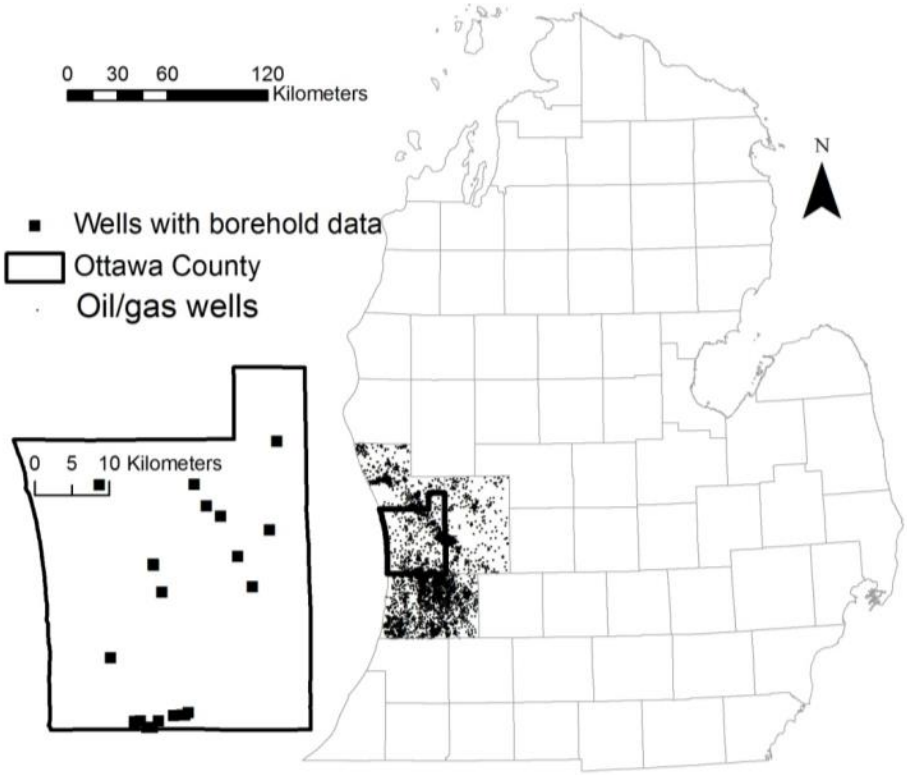

Figure 1 Geographical location of Ottawa County in state Michigan, and oil and gas wells.

2.3.2 Data

Formation depth data and geophysical well logs were obtained from the Department of Natural Resources and Environment of the State Michigan, while lithology information was collected from the stratigraphic cross-sections of the Michigan Basin – Report of Investigation 19 (RI19) prepared by Michigan department of environmental quality geological and land management division, and supplemented by the density and neutron porosity cross-plots derived from the geophysical well logs (figure 2), which are considered as useful tools for lithology identification (Labo *et al.*, 1987; Rider, 1996), and other geological documentations (Ells, 1978; Wylie and Wood, 2005).

Geophysical well logs, including gamma logs, density logs, neutron logs, and resistivity/conductivity logs from 22 wells were digitized at an interval of 10 ft (3.084m) and used to infer porosity and estimate permeability. Errors introduced during digitization are considered as random and normally distributed.

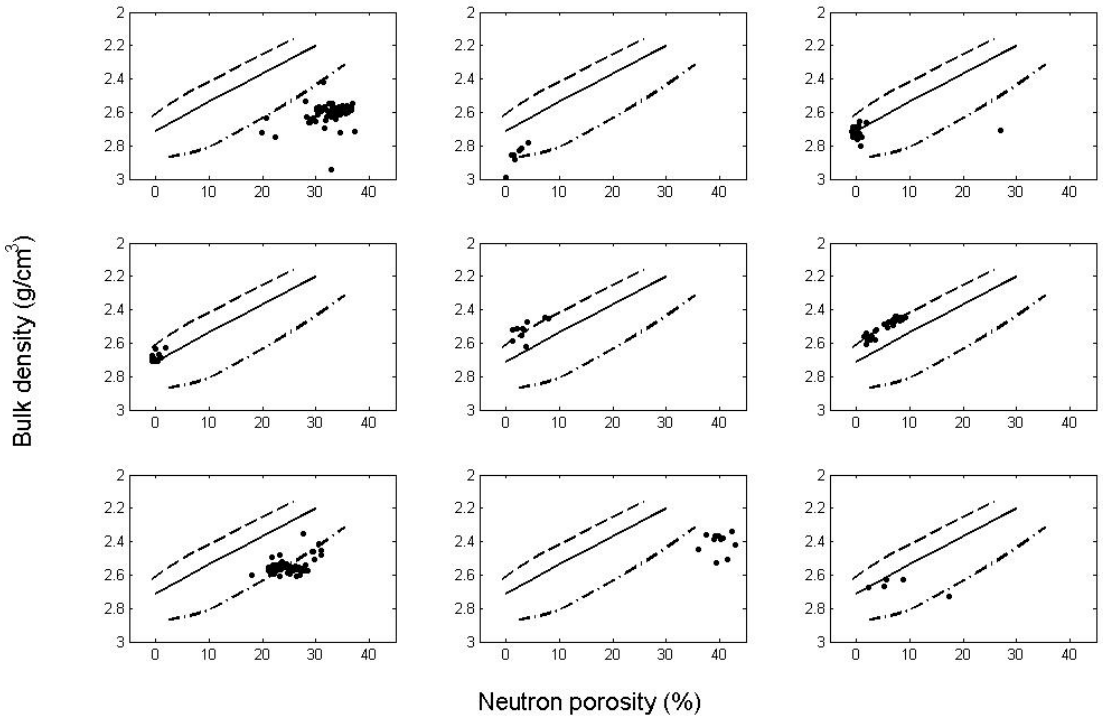

Figure 2 Neutron porosity - density crossplot for (a) well 34885, Coldwater Shale;(b) well 34885, Bass Island Group; (c) well 34885, Trenton Formation; (d) well 34885, Black River Formation; (e) well 34885, Dresbach Sandstone; (f) well 34885, Mount Simon Sandstone; (g) well 56203, Niagara Group; (h) well 30814, Antrim Shale; and (i) well 30814, Dundee Limestone. The solid line is for limestone matrix, dashed line for sandstone, and dash-dotted line for dolomite.

2.3.3 Geological reconstruction

The dataset of formation depth consists of information from 5759 wells, including brine disposal, observation, oil and gas wells. The depth of the wells ranges from 25m to 2500m. Among them, 936 wells are located in Ottawa County. Data from wells in the neighboring counties – Muskegon, Kent and Allegan, were included to improve the reconstruction of geological formations around the county boundary. Abnormal values either come from bad data, lenses or interbedding were treated as outliers and excluded. An outlier test for uniform samples was conducted (Barnett and Lewis, 1994). The statistic for testing h lower and k upper outliers is

$$T = \frac{[x(n)-x(n-k)+x(h+1)-x(1)](n-k-h-1)}{[x(n-k)-x(h+1)](k+h)} \qquad \text{eqn (1)}$$

with test distribution $F(2(k+h), 2(n-k-h-1), \alpha)$, $\alpha = 0.01$ in this case. Then, the data were imported into ArcGIS (Version 9.3, ERSI, 2008) to construct a 3D model of the subsurface of Ottawa County. Kriging, shown to be capable of providing high accuracy (Venteris and Carter, 2009), was used for spatial interpolation.

2.3.4 Porosity correction

Neutron porosity (ϕ_N) is a measure of the abundance of hydrogen, and thus an indicator of water content in the formation. It is commonly used to infer conventional porosity (ϕ). In the current study, conversion relations from Rider (1996) were adopted. As calibrations of the detectors were based on limestone, neutron porosity is equal to real porosity in clean limestone (eqn(2)), whereas matrix effects of sandstone and dolomite are accounted for using eqn(3) and (4) respectively. Volume of shale (V_{sh}) estimated from gamma logs (eqn (6) and (7)) is incorporated (eqn(5)) to eliminate the impacts of bound water in shaly formations.

$$\phi = \phi_N \qquad eqn(2)$$

$$\phi = \phi_N + 4 \qquad eqn(3)$$

$$\phi = \phi_N - 6 \qquad eqn(4)$$

$$\phi = \phi_N - V_{sh}H_{sh} \qquad eqn(5)$$

H_{sh} is the hydrogen index for shale. The value 0.37 (Rider, 1996) was used in this case.

$$V_{sh} = 0.33(2^{2V_{sh}^*} - 1) \qquad eqn(6)$$

$$V_{sh}^* = \frac{GR-GR(min)}{GR(max)-GR(min)} \qquad eqn(7)$$

where *GR*(min) is gamma ray reading for clear formation and *GR*(max) for pure shale given in the geophysical logs.

Porosity estimated from density logs (ϕ_{den}) is given by:

$$\phi_{den} = \frac{\rho_{ma} - \rho_b}{\rho_{ma} - \rho_f} \qquad eqn(8)$$

where ρ_{ma}, ρ_b, and ρ_f are density of the matrix, bulk (2.71 g/cm^3 as in limestone) and fluid (1.0 g/cm^3 as in fresh mud) respectively. Arithmetic averages of density and neutron porosity were taken.

2.3.5 Permeability estimations

Four approaches were adopted to estimate permeability, (*k*). Katz-Thompson relation (Katz and Thompson, 1986) (eqn(9)) describes *k* as a function of two parameters - the characteristic length scale of pore size (l_c), and the ratio of conductivity of the matrix saturated with a single fluid (σ) over conductivity of the fluid (σ_f), which is a measure of connectivity among pores.

$$k = \frac{1}{226} {l_c}^2 (\sigma/\sigma_f) \qquad eqn(9)$$

The other three methods relate permeability to porosity. Kozeny-Carman equation (Carman, 1956) (eqn(10)) includes grain diameter (d), and an empirical constant (c) that is dependent on the type of rocks. Values used here were from Rose and Bruce (1949). Grain sizes and characteristic length scale of pores for different rocks were collected from previous studies (table 1).

$$k = \frac{\phi^3}{36c(1-\phi)^2} d^2 \qquad eqn(10)$$

Kozeny-Carman relation was developed for granular matrix, and has been widely used for sandstones. However, similar as the Katz-Thompson relationship, it does not explicitly address specific factors such as fabrics of carbonate formations and shale content in shaly rocks. For this reason, two empirical approaches were applied on carbonates and shales accordingly, and the results were compared with estimates from K-T and K-C methods.

Lucia (1995) grouped limestone and dolomite rocks into three permeability fields according to rock fabrics, and provided empirical porosity-permeability relationships for each class. Though lacking of detailed fabric information makes it impossible to classify the formations and apply the corresponding porosity-permeability relationship, Lucia's equations allow estimation of permeability ranges of the carbonate formations by considering the two extreme cases – coarse (eqn(11)) and fine (eqn(12)) fabrics.

$$Coarse\ Fabric: k = (45.35 \times 10^8) \times \Phi^{8.537} \qquad eqn(11)$$

$$Fine\ Fabric: k = (2.884 \times 10^3) \times \Phi^{4.275} \qquad eqn(12)$$

For shales, the relationship proposed by Yang and Aplin (2009) was applied. It addresses directly the impacts of clay content (CF by weight) on permeability (eqn(13)). CF is calculated by $CF = \rho_{clay} V_{sh}/\rho_b$, where ρ_{clay} is the average clay density (2.7 g/cm^3, Rider 1996).

$$ln(\kappa) = -69.59 - 26.79CF + 44.07CF^{0.5} + (-53.61 - 80.03CF + 132.78CF^{0.5})\left(\frac{\phi}{100-\phi}\right) + (86.61 + 81.91CF - 163.61CF^{0.5})\left(\frac{\phi}{100-\phi}\right)^{0.5} \quad \textit{eqn(13)}$$

Table 1 Grain sizes and pore throat sizes

	Grain size (μm)	Notes	Reference	Value used in this study	Pore throat size (μm)	Notes	Reference	Value used in this study
Sandstone	150-300	St Peter	Kelly et al 2007	250	2-5	Mt. Simon	Barnes et al 2009	10
	86-297	Mt. Simon	Odom 1975		9-23 (16.67)	Medium-grained sandstone, worldwide	Nelson 2009	
	85-266	Galesville	Odom 1975		4-30 (15.5)	fine-grained sandstone, worldwide	Nelson 2009	
	99-322	Berea Sandstone	Churcher et al 1991					
Carbonates	5-100		Arns et al, 2005	10	1-10		Lucia, 1995	1
	70-100	Eau Claire	Odom 1975		10-35		Ausbrooks et al 1999	
					0.1-0.65	Red River Formation	Tanguay and Friedman, 2001	
Shales	0.1-80		Aplin and Macquaker, 2011	1	0.0028-1.4034		Yang and Aplin (2007)	0.01
	0.76-25.6		Daigle and Dugan, 2011		0.008-0.03		Aplin and Macquaker, 2011	
					0.008-0.05	Averages for various shales	Nelson 2009	

2.4 Results and discussions

2.4.1 3D reconstruction

Twenty four geological units were identified and reconstructed in the subsurface of Ottawa County, as listed in Table 2. Jurassic system and the Grand River formation of the Upper Pennsylvanian series are

missing and other formations in the Upper Pennsylvanian series are scarcely present under Ottawa County. Frequently encountered formation immediately underlying the Quaternary glacial drift is Michigan formation. However, it is predominantly recorded in the northeast part of Ottawa County and wedges out towards southwest. Beneath the Michigan formation are the Lower Mississippian series – Marshall Sandstone, Coldwater Shale and Sunbury Shale. Compared to Coldwater Shale, which has an average thickness of about 190 meters, Sunbury Shale is thin, of 14 m thick, consistent with documentations of its thinning westwards in the Michigan State (Ells, 1978), possibly due to its pinching out into Ellsworth Shale (RI19). Besides Ellsworth Shale, other formations/groups in the Devonian system (Antrim Shale, Traverse Group, Dundee Limestone and Detroit River Group) are all present in the subsurface of Ottawa County. Ellsworth shale is approximately 156 m thick, and Antrim has an average thickness of 49m, both within the range documented in the western Michigan (400-600 and 150-300 feet respectively) previously by Ells (1978) and references cited therein. Traverse Group is normally further divided into Traverse Formation, Traverse Limestone and Bell Shale (RI19). In the case of Ottawa County, Traverse Limestone is well-developed, while the other two formations are rarely encountered. Among the three units of Detroit River Group – Lucas Formation, Amhersburg Formation, and Sylvania Sandstone, only Amhersburg is well-defined. The Silurian rock sequence in the underground of Ottawa County includes, in descending order, Bass Island Group, Salina Group, Niagara Group and Cataract Group. Though Traverse Group, Dundee Limestone, Detroit River Group and Bass Island Group are well-developed in the northern part of the State and often identified as potential reservoir for CO_2 (Kirschner and Barnes 2009; Sminchak *et al.* 2009), they are relatively thin in the southwestern county Ottawa. In the stratigraphically older Ordovician system, from the youngest to the oldest are the Cincinnati (or Richmond) group, the Trenton formation, the Black River formation, St. Peter Sandstone and the Prairie du Chien Group. St. Peter has been identified as a potential storage reservoir in the MRCSP region (Hololick *et al*., 1984; MRCSP report, 2005), where the average thickness is around 30-60 m (Hololick *et al*., (1984)). However, St Peter Sandstone is less than 10m in the subsurface of Ottawa, in contrast with the thick Prairie du Chien Group. This contrast is consistent with previous findings (RI19 and cited work therein) that St. Peter Sandstone is often the thinnest where the Prairie du Chien Group is the thickest. The Cambrian strata, in descending order, is composed of Trempealeau formation, Franconia Formation, Dresbach (also called Galesville) Sandstone, Eau Claire Formation, and Mount Simon Sandstone. The averaged depth of the top of Eau Claire Formation and its thickness are about 1860m and 75m respectively, larger compared with the studies (1483.5m and 57m) of Barnes *et al*. (2009). The depth of Mount Simon Sandstone ranges from <800m to >6000m in the MRCSP region (Medina *et al*., 2011), and from 914m to 4572m in the state of Michigan (Barnes *et al*., 2009). Its thickness shows a range from 15m to 762m in the MRCSP region, and no more than 396m in the Michigan basin. In the subsurface of Ottawa County, Mount Simon has an average depth of 1935m, and average thickness of 236m, comparable to the value of 258.4m from Barnes *et al* (2009).

Table 2. Twenty four Geological units in the subsurface of Ottawa County (Fm: Formation, Gr: Group)

Time-stratigraphic unit (System)	Formation	Formation Code	Top Depth (m)	STD(m)	Thickness (m)
Quaternary	Glacial Drift	GCDF	0	17.5	55.4
Mississippian	Michigan Fm	MCGN	55.4	17.9	22.5
	Marshall Sandstone	MRSL1	77.9	12.6	24.0
	Coldwater Shale	CLDR3	101.9	46.8	193.7
	Sunbury Shale	SNBR1	295.5	51.9	13.8
Devonian	Ellsworth Shale	ELSR1	309.4	43.5	156.1
	Antrim Shale	ANRM	465.5	59.0	49.3
	Traverse Gr	TRVR	514.7	22.0	110.7
	Dundee Limestone	DUND	625.4	95.6	19.5
	Detroit River Gr	DRRV	644.9	50.1	156.1
Silurian	Bass Islands Gr	BILD	801.0	56.7	4.4
	Salina Gr	SLIN	805.4	42.4	271.9
	Niagara Gr	NGRN	1077.3	117.8	38.6
	Cataract Gr	CTRC	1115.9	119.3	22.4
Ordovician	Cincinnati Gr (Richmond Gr)	CNCN	1138.3	124.2	136.5
	Trenton Fm	TRNN	1274.8	131.5	92.8
	Black River Fm	BKRV	1367.6	134.4	49.2
	St. Peter Sandstone	STPR	1416.8	140.1	5.6
	Prairie du Chien Gr	PRDC	1422.5	148.6	272.7
Cambrian	Trempealeau Fm	TMPL	1695.1	108.8	82.5
	Franconia Fm	FRNC	1777.6	113.8	48.6
	Dresbach (Galesville) Sandstone	DRBC	1826.2	116.9	33.3
	Eau Claire Fm	ECLR	1859.5	116.0	75.2
	Mount Simon Sandstone	MNSM	1934.8	104.0	236.0

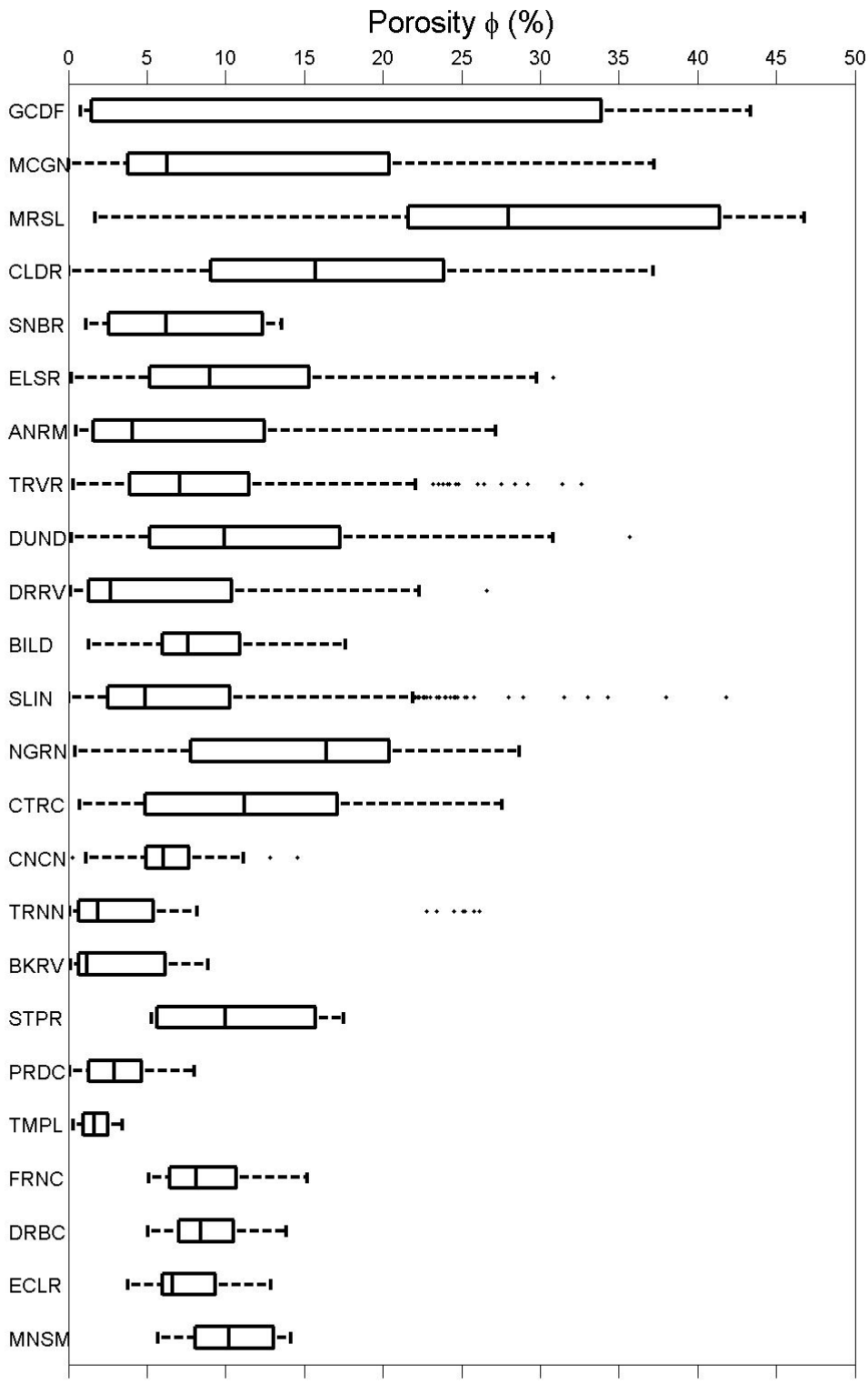

Figure 3 Porosity for each geological unit. The box shows the 25% and 75% quartiles, black lines indicate the range of the data, and the dots are statistical outliers.

2.5.1 Porosity

Porosity derived from neutron and density logs for each geological unit is plotted in figure 3. Large variations across the sedimentary rock sequence are evident. Generally, shallower formations are more porous, while deeper formations have lower porosity due to compaction. Shaly formations, i.e. Coldwater, Sunbury, Ellsworth, Antrim Shale, and Cincinnati Group, even after corrections for the effects of bound water, still show porosities up to more than 20%. Such high values are not unusual. It has been reported that for relatively shallow shaly formations, porosity generally falls between 10-25% (Rider, 1996). The reason for the relatively high porosity in shales is the inherent layered structures of clay minerals and significant amount of void spaces in between. Sandstones (Marshall, St. Peter, Franconia, Dresbach and Mt. Simon) also have high porosities, generally between around 5-15%. Formations dominated by carbonates, such as Trenton Formation, Black River Formation, Prairie du Chien Group and Trempealeau Formation have lower porosity compared with sandstones that are dominated by quartz and siliciclastic materials, for carbonates are more reactive and hence more inclined to be modified by cementation at depth (Ehrenberg and Nadeau, 2005).

Variability in porosity within each geological unit is obvious as well, indicating non-uniformity within one geological unit. In the case of Glacial Drifts, large variations may due to various forces, natural and anthropogenic on the land surface, and the fact that no high pressure alteration has happened. The other two shallower formations, Michigan and Marshall Sandstone also demonstrate large variations. Large variations may also be an indicator of sub-divisions, as in the case of the Salina Group, for which different units have been reported in previous studies (RI19), and identified in the geophysical logs.

The average porosity estimated for Traverse Group is about 8.5%, consistent with the reported 9% average (RI19), whereas the mean of 8.6% for Bass Island Group is much lower than that of the Otsego County, a CO_2 injection test site in the northern part of the State. St Pete Sandstone shows relatively high porosity, ranging from 5-17.5%, with an average of 10.7%. The potential injection reservoir Mt. Simon has comparably large porosity. Though the average value (10.5%) is slightly lower than the average of 12.89% reported by Barnes *et al*. (2009), the documented data (5.7-14%) fall into the range estimated for the Michigan Basin (Medina *et al*., 2010), and are close to what has been reported for Mt. Simon Sandstone in the Illinois Basin (8-18%, Hololick *et al*., 1984). Average porosity for Eau Claire Formation (7.5%) is mildly higher than the value of 5.9 reported by Barnes *et al*. (2009).

Large variability in the porosity data can also be caused by uncertainties other than the heterogeneous nature of the subsurface formations. Uncertainties of the porosity estimates can come from three sources – precision of the detector, digitization and correction. Correction of neutron porosity and conversion of density into porosity depends largely on the homogeneity of the rock and the 'correctness of the matrix assumption' (Labo *et al*., 1987). It may generate larger errors than the first two sources. Considering the worst scenario, occasional presence of dolomites blocks or fragments in sandstones was not differentiated, and hence the error introduced in the correction process for those data points can be 10% higher than the true values. For shales, the correction is majorly controlled by the goodness of the shale fraction value and the assumption of hydrogen index. Assume large errors for both the estimation of shale fraction (±50%) and hydrogen index of shale (0.2), the error propagated to porosity can reach 10%. However, the procedures taken in this study followed the standard guidelines in petroleum practices, and

such extreme cases are rare. The sporadic large errors may contribute to statistical outliers observed, but the porosity estimations are able to preserve the major characteristics.

The relationship between porosity and depth of sedimentary rocks has been extensively studied by Athy (1930) using more than 2000 samples, and documented for various sedimentary basins and formations (Hololick *et al*., 1984; Ehrenberg and Nadeau 2005; Barnes *et al*., 2009; Medina *et al*., 2010). Porosity of sedimentary rocks can be modified by physical compaction and chemical alterations after deposition. As depth increases, hydrostatic pressure builds up and temperature rises, causing elevated compaction, diagenesis and cementation that lead to porosity decrease. Though improved reactivity at high temperature also favors dissolution that may result in porosity increase with depth, this effect is regarded as insignificant compared with the other processes (Ehrenberg and Nadeau 2005). Therefore, porosity is often thought to be decreasing as depth increases, and the relationship can be expressed by the exponential function, also called Athy's equation (Athy, 1930) (eqn(13)).

$$\phi = ae^{-bd} \qquad eqn(13)$$

where *a* and *b* are fitted parameters.

In previous studies, decreasing porosity with increasing depth was found for St. Peter Sandstone (Hololick *et al*., 1984) and the Mt. Simon Sandstone (Hololick *et al*., 1984; Medina *et al*., 2010). In the current study, the relationships between porosity and depth are not undiversified in all geological units. Slight increase of porosity with depth can be found for the Glacial Drift, Antrim Shale, Trempealeau Formation, Franconia Formation, Dresbach Sandstone, and Eau Claire Formation, while other formations demonstrate porosity decrease with depth. However, only for the Salina Group, the Cataract Group and the Black River Formation the fitting of Athy's equations are bearable (adjusted R^2>0.5). For St Peter Sandstone (adjusted R^2=0.34) and Mt. Simon Sandstone (adjusted R^2<0.1), the fittings are too poor to have any statistical significance.

The poor relationships between porosity and depth in some formations serve as another indicator of the complicated geological processes, revealing porosity heterogeneity and the possibility of sub-layers. For example, Mt. Simon has been shown as clean sandstone (figure 2(f)), yet systematic variations in porosity along depth can be observed, suggesting that there might be different units. In the Illinois basin, different units for Mt Simon were observed (Leetaru and McBride, 2009). Electrofacies in St Peter was also documented (Gelhar 1986). However, sub-divisions cannot be achieved with porosity data, more information is required.

2.5.2 Permeability

Across the geological units, permeability estimates from both the K-T and K-C methods vary significantly for about 10 orders of magnitude (figure 4(a)). The pattern of variation among formations correlates well between the two approaches. Formations dominated by shales, such as coldwater, Sunbury, Ellsworth and Antrim, are the least permeable, with permeability around 10^{-8} to 10^{-2} mD, whereas Sandstone formations have permeability approximately 1 to 10^4 mD, and permeability of carbonate formations range from 10^{-4} to 1 mD.

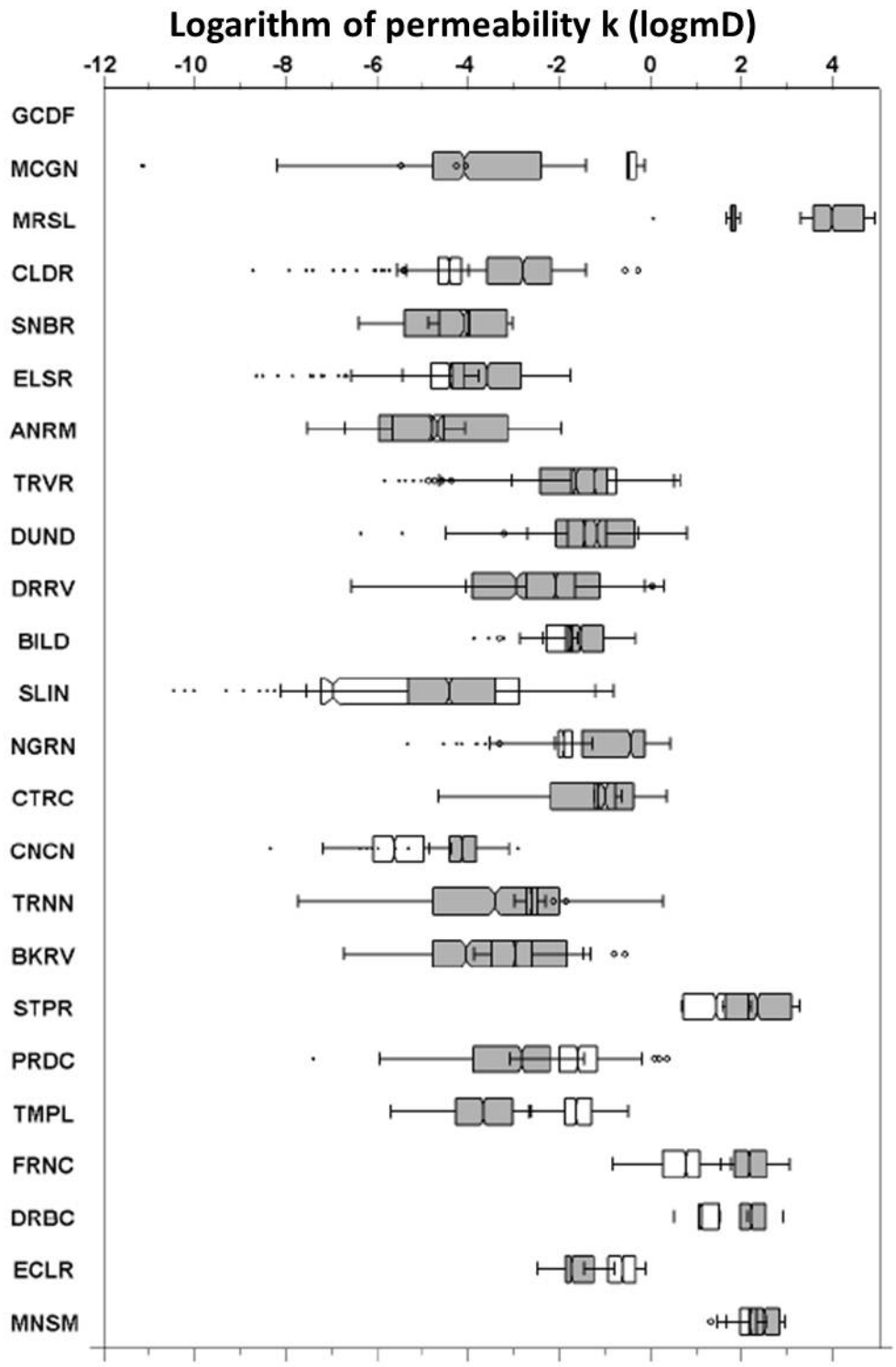
Logarithm of permeability k (logmD)
-12
-10
-8
-6
-4
-2
0
2
4
GCDF
MCGN
MRSL
CLDR
SNBR
ELSR
ANRM
TRVR
DUND
DRRV
BILD
SLIN
NGRN
CTRC
CNCN
TRNN
BKRV
STPR
PRDC
TMPL
FRNC
DRBC
ECLR
MNSM

Figure 4a

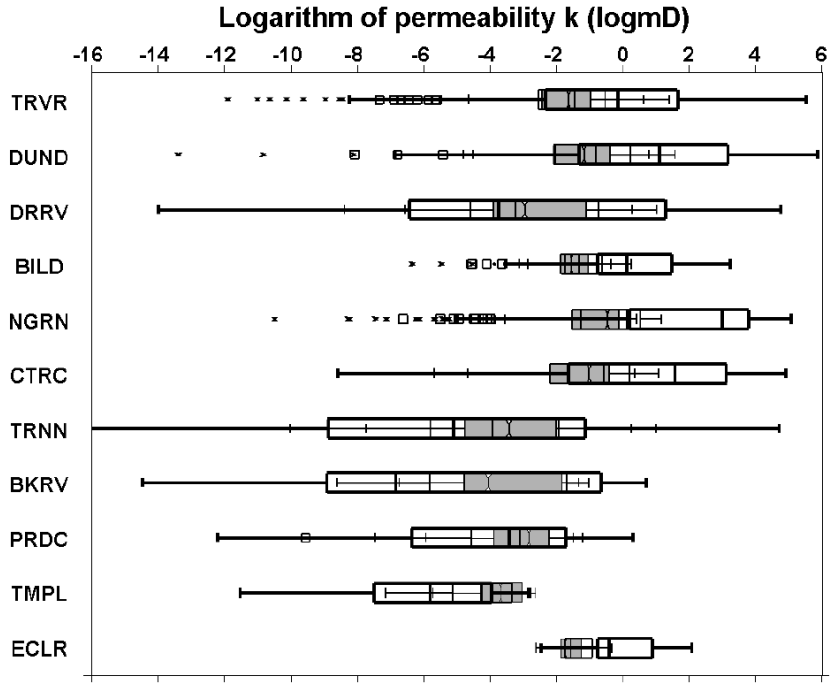

Figure 4b

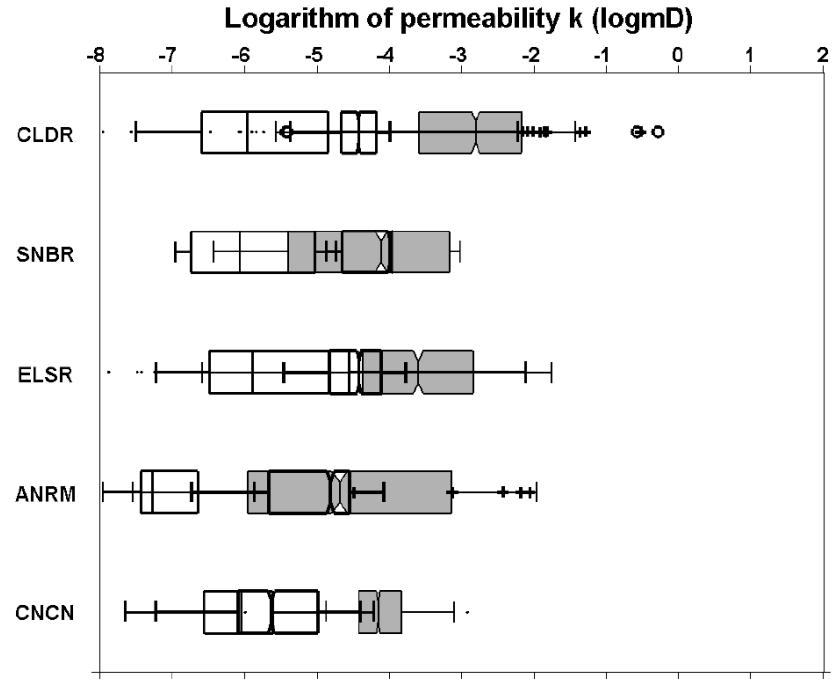

Figure 4 (a) Boxplots for permeability estimates from the K-C (filled notched box) and K-T (void notched box) methods; (b) permeability estimates from K-C method (filled notched box), Lucia's equation for fine fabrics (box with fine lines, outliers square), and Lucia's equation for coarse fabrics (box with thick lines, outliers x) for carbonate formations; (c) permeability estimates from K-C, K-T methods, and YA relationship (void box).

Comparing the K-C and K-T methods, the K-T estimates exhibit a weaker variation across the geological sequence. For sandstones, estimates using the K-T method are generally smaller than those from the K-C method. The discrepancy is caused by the underlying difference in their treatments of length scale. Whereas the characteristic length required in the K-T method is acquired from mercury injection test (Katz and Thompson, 1986), equivalent to pore throat size, the K-C method uses grain sizes that are about one order of magnitude larger (table 1). However, despite that for carbonate formations length scales used in the K-T method are one order of magnitude smaller than those used in the K-C estimation as well; the resultant permeability estimates from the K-T method are higher. A possible explanation for this difference is that in carbonate formations, fractures are often prevalent (Ehrenberg and Nadeau, 2005). Since the conductivity ratio term in the K-T relationship accounts for connectedness among pores, the K-T method is, to some extent, capable of accounting for the effectiveness of fractures as flow path. For shaly geological units, the results from the two approaches display some overlap, but the K-T estimates in general show a narrower range and lower values.

Similar as K-C method, Lucia's equations estimate permeability from porosity for carbonate formations. In the case of coarse fabrics, results from Lucia's equation display stronger sensitivity to changes in porosity (figure 4(b)), while the estimates for the fine rock fabrics agree quite well with the K-C estimates. As the fine rock fabrics correspond to the less than 20 μm permeability field, it is close to the average grain size used in the K-C estimation. These results to some degree reflect the good agreement between Lucia's empirical relationship and the K-C equation. The YA estimates of shaly formations have a range of 10^{-4} to 10^{-7} mD, lower than estimates using K-T method. The relatively high values estimated by the K-T method are possibly a consequence of the fact that shales have high conductivities owing to the bound water, and thus the conductivity ratios are also overestimated.

The average permeability of Mt Simon is 2.45 logmD and 2.08 logmD from the K-C and K-T methods respectively, quite close to the value of 2.0687 logmD from the core measurements (Barnes *et al*., 2009). The results from K-C and K-T methods are also compared with results estimated using the empirical porosity-permeability equations fitted in Medina *et al.* (2010) and Barnes *et al.* (2009) (figure 5). The estimates using Medina's equation is much lower, with average of 1.17 logmD, while the Barnes' equation provides estimates closer to the K-T estimates. However, due to the low goodness-of-fitting, the applicability of such empirical porosity-permeability relationship is limited.

The K-C estimates are controlled by grain size, the scaling constant (c), and porosity. Though no grain size information is directly available from borehole well logs (Zhang and Brusseau, 1998), the tabulated average grain sizes from different sources (table 1) for a given rock type are often of the same order of magnitude. The scaling constant depends on the type of rocks, and varies from 5 for sandstone and about 100 for shaly rock samples (Rose and Bruce, 1949). However, it was also reported that the scaling constant may disperse over two orders of magnitude for a relatively uniform rock (Walker and Glover, 2010), owing to the fact that the K-C method doesn't account for connectedness among pores. For the K-T method, uncertainties in permeability estimates are associated with the goodness of the scaling constant, characteristic length and the conductivity ratio. The scaling constant used here (1/226) is the theoretical value derived in the original paper for cylindrical pore geometry. Though other studies have reported different theoretical and experimental values, the variation is relatively small, and independent of length scale (Walker and Glover, 2010) and mineralogy (Bauget *et al*., 2005).

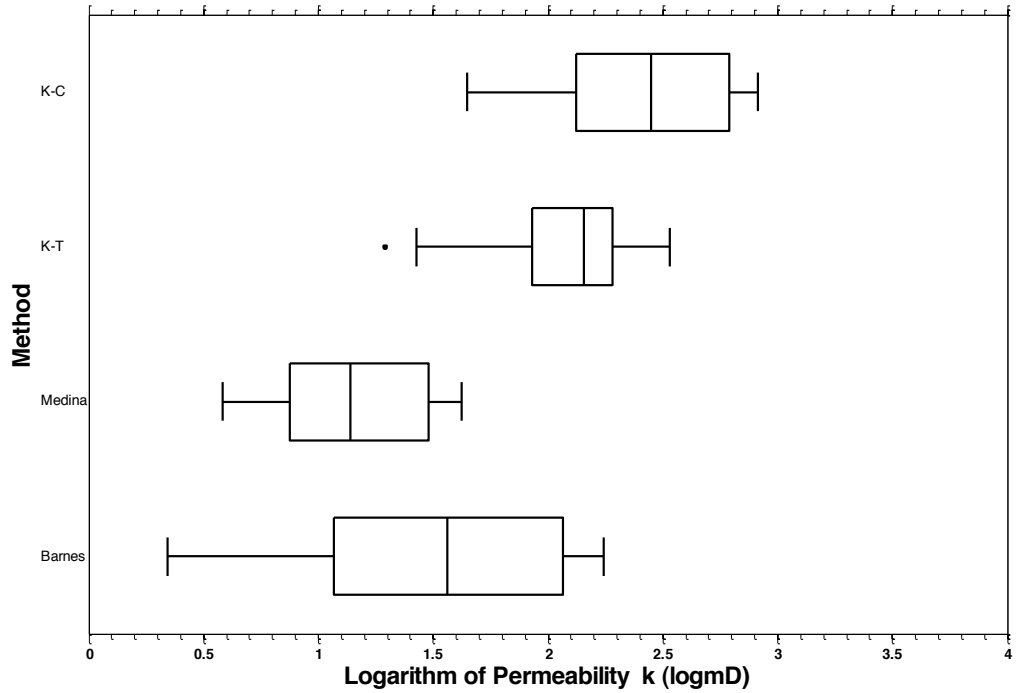

Figure 5 Comparisons of permeability estimates from the four methods, and demonstration of the large variability among different formations

As shown in figure 4(a), within one geological unit, variation of permeability can range over 4-5 orders of magnitude. Such large variations were also documented in previous studies (Gelhar 1986; Moline and Bahr 1995). In the current study, it was assumed that for each geological unit, mineralogy and grain size are uniform. Given the assumption, variation of permeability within one formation is solely attributable to spatial variations in porosity. Owing to the invariant scaling constant of the K-T method with respect to mineralogy and grain size, the K-T estimates are more reliable under the assumption, and more suitable for studies of permeability variability within formations.

For a given geological structure, it was argued that its hydraulic properties can be described by a single PDF (Jussel *et al*., 1994), and lognormal distribution has been widely used for permeability or hydraulic conductivity in previous studies (Gallardo and Marui, 2007). For permeability data in each geological unit, different probabilistic distribution types were explored. Both lognormal and generalized extreme value (GEV) distributions passed Kolmogorov-Smirnov test (α=0.01). Lognormal distribution implies that the effective permeability of a formation can be calculated as the geometric mean. This implication also reflects the physical reality of fluid flowing through a layered structure. Therefore, geometric mean provides a single value that is representative of the hydraulic properties of a formation and used in large-scale models, assuming the vertically stratified structure. However, other than vertical variations along depth, lateral variations among spatially dispersed wells are also contributing to the large variability of permeability within one geological unit. For formations where multiple well logs are available, statistically significant (α=0.05) differences among datasets from different wells were found (figure 6),

indicating that in characterizing matrix hydraulic properties within one formation, lateral variation must be taken into consideration. Presence of large lateral variations undermines the physical soundness of using a single value as geometric mean to represent the hydraulic property of a geological unit. Alternatively, sampling from permeability distributions can be introduced into large scale model, which provides a way to fully account for the large variability in hydraulic properties. As shown in figure 7, lognormal distribution fails to capture the extremely minimum and maximum values, whereas GEV distribution provides better fittings at the two tails. Hence, GEV distribution is an alternative to lognormal distribution in describing permeability variation, especially when extreme scenarios are to be considered.

2.6 Summary and Conclusions

To summarize, in the current study a primary site characterization was conducted for Ottawa County, Michigan with publicly accessible borehole data. A 3D geological model was constructed for the subsurface of Ottawa County, in which 24 geological units were identified. Hydraulic properties, porosity and permeability, for each geological unit were estimated from geophysical well logs. Large variabilities across the sequence of geological formations are evident, as well as variations within one geological unit. The latter can be described by lognormal and generalized extreme value (GEV) distribution, and further attributed to lateral variation among different wells and vertical variation along depth, but no good relationships between porosity and depth were found. Such large variation indicates the complexity of geological processes that control these properties, and insufficiency of using the geometric mean as representative value in large-scale modeling. Alternatively, permeability distribution can be sampled, and GEV distribution is recommended to capture the tails.

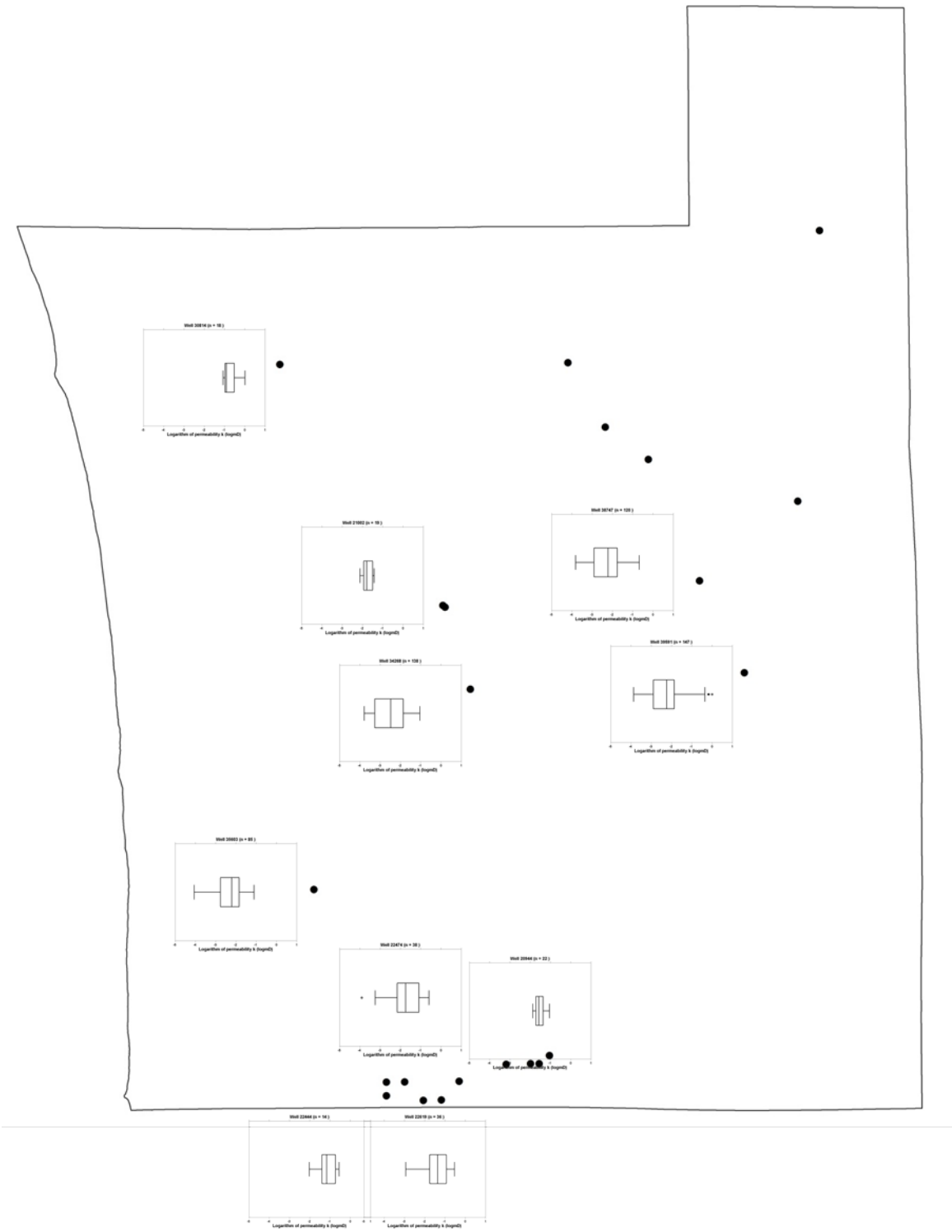

Figure 6 Lateral variability of permeability within the Detroit River Group. Not all box plots are shown in the figure due to the constraint of space. For each box plot, the range of the permeability is -5~1 logmD, n in the parenthesis gives the sample number in the corresponding well.

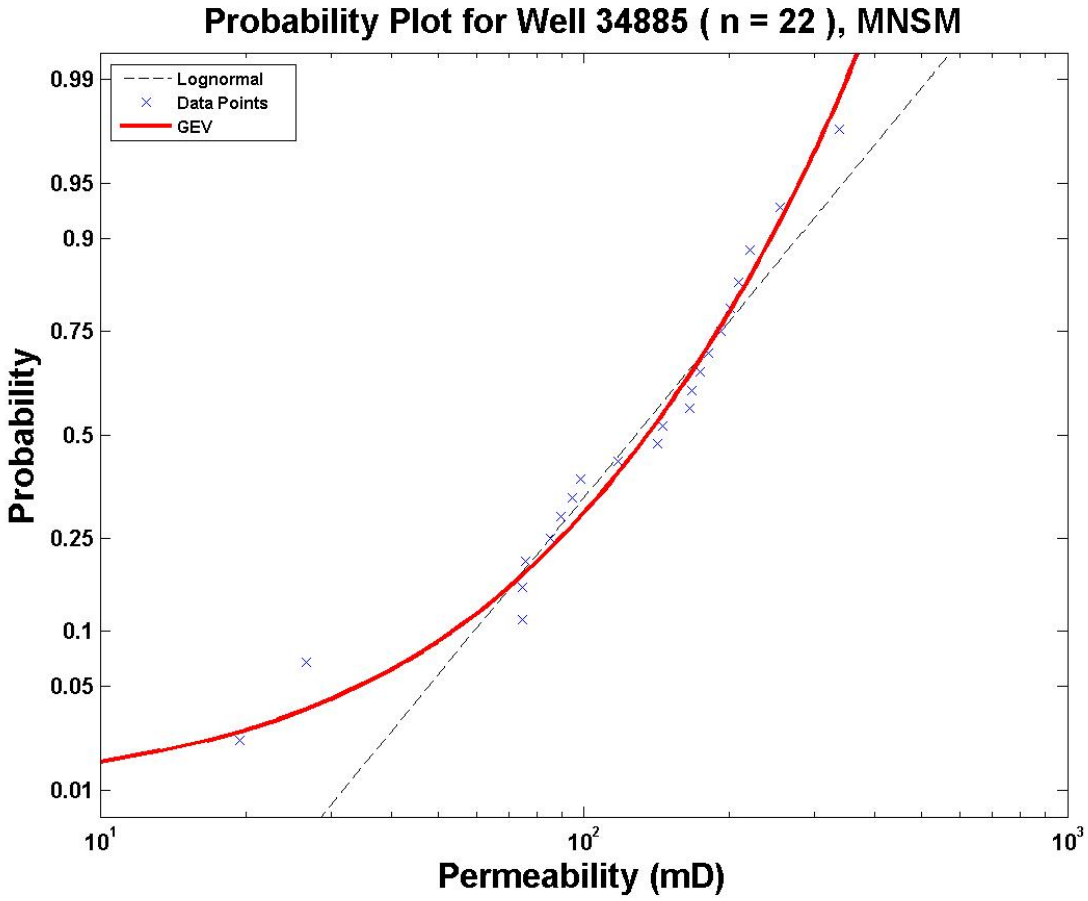

Figure 7 Probability plot for Mount Simon, well 34885.

2.7 References

Anderson, S. and R. Newell (2004), Prospects for carbon capture and storage technologies, *Annual Review of Environment and Resources, 29*, 109-142.

Athy, L. F. (1930), Density, porosity, and compaction of sedimentary rocks, *American Association of Petroleum Geologists -- Bulletin, 14*, 1-24.

Bachu, S. (2008), CO_2 storage in geological media: Role, means, status and barriers to deployment, *Progress in Energy and Combustion Science, 34*, 254-273.

Barnes, D. A., D. H. Bacon, and S. R. Kelley (2009), Geological sequestration of carbon dioxide in the Cambrian Mount Simon Sandstone: Regional storage capacity, site characterization, and large-scale injection feasibility, Michigan Basin, *Environmental Geosciences, 16*, 163-183.

Barnett, V. and T. Lewis (1994), Outliers in Statistical Data, 3rd Edition, John Wiley & Sons Ltd.

Bauget, F., C. H. Arns, M. Saadatfar, A. P. Sheppard, R. M. Sok, M. L. Turner, W. V. Pinczewski, and M. A. Knackstedt (2005), What is the characteristic length scale for permeability? Direct analysis from microtomographic data, SPE Annual Technical Conference and Exhibition, ATCE 2005, October 9, 2005 - October 12, 2005.

Carman, P.C. (1956), Flow of gases through porous media, New York, Academic Press.

Celia, M. A. and J. M. Nordbotten (2009), Practical Modeling Approaches for Geological Storage of Carbon Dioxide, *Ground Water, 47*, 627-638.

"Characterization of Geologic Sequestration Opportunities in the MRCSP Region." Phase I Task Report Period of Performance: October 2003 – September 2005. Prepared by the Ohio Division of Geological Survey under subcontract to Battelle Memorial Institute, 505 King Avenue, Columbus, OH 43201. Submitted by Battelle under DOE Cooperative Agreement No. DE-PS26-05NT42255, the Midwest Regional Carbon Sequestration Partnership (MRCSP).

Dafflon, B., J. Irving, and K. Holliger (2009), Use of high-resolution geophysical data to characterize heterogeneous aquifers: Influence of data integration method on hydrological predictions, *Water Resour. Res., 45*.

Doughty, C. (2007), Modeling geologic storage of carbon dioxide: Comparison of non-hysteretic and hysteretic characteristic curves, *Energy Conversion and Management, 48*, 1768-1781.

Ebigbo, A., H. Class, and R. Helmig (2007), CO_2 leakage through an abandoned well: problem-oriented benchmarks, *Computational Geosciences, 11*, 103-115.

Ehrenberg, S. N. and P. H. Nadeau (2005), Sandstone vs. carbonate petroleum reservoirs: A global perspective on porosity-depth and porosity-permeability relationships, *AAPG Bull., 89*, 435-445.

Ells, G. D. (1978), Stratigraphic Cross Sections Extending from Devonian Antrim Shale to Mississippian Sunbury Shale in the Michigan Basin, 212.

Gallardo, A. H. and A. Marui (2007), Hydraulic characteristics of sedimentary deposits at the J-PARC proton-accelerator, Japan, *Earth Sciences Research Journal, 11*, 140-155.

Gelhar, L. W. (1986), STOCHASTIC SUBSURFACE HYDROLOGY FROM THEORY TO APPLICATIONS., *Water Resour. Res., 22*, 135-145.

Haimson, B. C. and T. W. Doe (1983), State of stress, permeability, and fractures in the Precambrian granite of northern Illinois, *Journal of Geophysical Research, 88*, 7355-71.

Hepple, R. P. and S. M. Benson (2005), Geologic storage of carbon dioxide as a climate change mitigation strategy: performance requirements and the implications of surface seepage, *Environ. Geol., 47*, 576-585.

Hoholick, J. D., T. Metarko, and P. E. Potter (1984), Regional variations of porosity and cement: St. Peter and Mount Simon sandstones in Illinois Basin, *Am. Assoc. Pet. Geol. Bull., 68*, 753-764.

Iding, M. and P. Ringrose (2010), Evaluating the impact of fractures on the performance of the In Salah CO(2) storage site, *International Journal of Greenhouse Gas Control, 4*, 242-248.

IPCC (Intergovernmental Panel on Climate Change) (2005), "Special Report on Carbon Dioxide Capture and Storage." Metz. B., Davidson, O., de Coninck, H., Loos, M. and Meyer, L. (eds). *Cambridge University Press*.

Jussel, P., F. Stauffer, and T. Dracos (1994), Transport modeling in heterogeneous aquifers: 1. Statistical description and numerical generation of gravel deposits*, Water Resour. Res., 30*, 1803-1817.

KATZ, A. and A. THOMPSON (1986), QUANTITATIVE PREDICTION OF PERMEABILITY IN POROUS ROCK*, Physical review.B, Condensed matter, 34*, 8179.

Kirschner, J. P. and D. A. Barnes (2009), Geological sequestration capacity of the Dundee Limestone, Michigan Basin, United States*, Environmental Geosciences, 16*, 127-138.

Labo, J, H. M. Samuel, and A. C. Charles (1987), A Practical Introduction to Borehole Geophysics: an Overview of Wireline Well Logging Principles for Geophysicists. Tulsa, Okla.: Society of Exploration Geophysicists.

Leetaru, H. E. and J. H. McBride (2009), Reservoir uncertainty, Precambrian topography, and carbon sequestration in the Mt. Simon Sandstone, Illinois Basin*, Environmental Geosciences, 16*, 235-243.

LeNeveu, D. M. (2008), CQUESTRA, a risk and performance assessment code for geological sequestration of carbon dioxide*, Energy Conversion and Management, 49*, 32-46.

Lewicki, J. L., J. Birkholzer, and C. Tsang (2007), Natural and industrial analogues for leakage of CO_2 from storage reservoirs: identification of features, events, and processes and lessons learned*, Environ. Geol., 52*, 457-467.

LUCIA, F. (1995), ROCK-FABRIC PETROPHYSICAL CLASSIFICATION OF CARBONATE PORE-SPACE FOR RESERVOIR CHARACTERIZATION*, AAPG Bull., 79*, 1275.

Maul, P. R., R. Metcalfe, J. Pearce, D. Savage, and J. M. West (2007), Performance assessments for the geological storage of carbon dioxide: Learning from the radioactive waste disposal experience*, International Journal of Greenhouse Gas Control, 1*, 444-455.

Medina, C., J. Rupp, and D. Barnes (2011), Effects of reduction in porosity and permeability with depth on storage capacity and injectivity in deep saline aquifers: A case study from the Mount Simon Sandstone aquifer*, International journal of greenhouse gas control, 5*, 146.

Moline, G. R. and J. M. Bahr (1995), Estimating spatial distributions of heterogeneous subsurface characteristics by regionalized classification of electrofacies*, Math. Geol., 27*, 3-22.

Moreton, D. J., P. J. Ashworth, and J. L. Best (2002), The physical scale modelling of braided alluvial architecture and estimation of subsurface permeability*, Basin Research, 14*, 265-285.

Naoaki, S. (1999), Study on methodology of practical parameter estimation for groundwater modeling based on hydrogeological classification*, Journal of Geosciences*, 21-43.

Nordbotten, J. M., M. A. Celia, and S. Bachu (2004), Analytical solutions for leakage rates through abandoned wells*, Water Resour. Res., 40*, W04204.

Nordbotten, J. M., M. A. Celia, and S. Bachu (2005), Injection and storage of CO_2 in deep saline aquifers: Analytical solution for CO_2 plume evolution during injection*, Transp. Porous Media, 58*, 339-360.

Nordbotten, J. M., M. A. Celia, S. Bachu, and H. K. Dahle (2005), Semianalytical solution for CO_2 leakage through an abandoned well*, Environ. Sci. Technol., 39*, 602-611.

Nordbotten, J. M., D. Kavetski, M. A. Celia, and S. Bachu (2009), Model for CO_2 Leakage Including Multiple Geological Layers and Multiple Leaky Wells*, Environ. Sci. Technol., 43*, 743-749.

Pacala, S. and R. Socolow (2004), Stabilization wedges: Solving the climate problem for the next 50 years with current technologies*, Science, 305*, 968-972.

Pruess, K. (2008), On CO_2 fluid flow and heat transfer behavior in the subsurface, following leakage from a geologic storage reservoir*, Environ. Geol., 54*, 1677-1686.

Rider, M.H. (1996), The geological interpretation of well logs (2^{nd} edtition). Houston: Gulf Publishing.

Rose, W. and W. A. Bruce (1949), Evaluation of capillary character in petroleum reservoir rock*, American Institute of Mining and Metallurgical Engineers -- Journal of Petroleum Technology, 1*, 127-142.

Shipton, Z. K., J. P. Evans, K. R. Robeson, C. B. Forster, and S. Snelgrove (2002), Structural heterogeneity and permeability in faulted eolian sandstone: Implications for subsurface modeling of faults*, Am. Assoc. Pet. Geol. Bull., 86*, 863-883.

Sminchak, J., N. Gupta, and J. Gerst (2009), Well test results and reservoir performance for a carbon dioxide injection test in the Bass Islands Dolomite in the Michigan Basin*, Environmental Geosciences, 16*, 153-162.

"Stratigraphic Cross-Sections of the Michigan Basin – Report of Investigation 19", Michigan Department of Environmental Quality Geological and Land Management Division.

Venteris, E. R. and K. M. Carter (2009), Assessing spatial uncertainty in reservoir characterization for carbon sequestration planning using public well-log data: A case study*, Environmental Geosciences, 16*, 211-234.

Walker, E. and P. W. J. Glover (2010), Permeability models of porous media: Characteristic length scales, scaling constants and time-dependent electrokinetic coupling*, Geophysics, 75*, E235-E246.

Wylie, A. S. and J. R. Wood (2005), Well-log tomography and 3-D imaging of core and log-curve amplitudes in a Niagaran reef, Belle River Mills field, St. Clair County, Michigan, United States*, AAPG Bull., 89*, 409-433.

Yang, Y. and A. Aplin (2010), A permeability-porosity relationship for mudstones*, Mar. Pet. Geol., 27*, 1692.

Zhang, Z. H. and M. L. Brusseau (1998), Characterizing three-dimensional hydraulic conductivity distributions using qualitative and quantitative geologic borehole data: Application to a field site*, Ground Water, 36*, 671-678.

Chapter 3. Summary of relevant policies, laws, and regulations affecting the subsurface

3.1 Introduction

Geologic storage of carbon dioxide (CO2) in the Michigan Basin will be another activity added to the long history of subsurface usage in the state of Michigan. These activities provide a context into which carbon dioxide capture and storage (CCS) will be deployed, and the extant regulatory oversight and legal frameworks relevant to them provide foundations that are to varying degrees relevant to the geologic storage of CO2. The absence of experience resolving actual geologic storage disputes dictates that closely-related current activities (natural gas storage, waste injection, and oil and gas production) must be used as analogies, albeit with important distinctions with potentially far-reaching implications. This report provides a summary of current subsurface activities in Michigan, relevant federal and state regulatory agencies and laws, and applicable subsurface property law.

3.2 Interviews Conducted

Approximately fifteen interviews were conducted, as listed in Table 1. The interviewees include attorneys, law professors, industry personnel, and regulatory employees. The interviews were conducted over e-mail and with phone conversations. The general topics are grouped below, with a short description of the interview parties, the type of interview, and a summary of the findings.

Table 1. Fifteen interviews conducted to gather information for this report.

Interviewee and date	Interview details
a. Michigan Organizations, Regulations, and Statutes	
1 Mar. 2010, Tom Godbold, MI Office of Geological Survey (OGS), e-mail	Mr. Godbold answered questions about the annual budget of his office, which handles oil and gas permitting in Michigan and provided contacts regarding other individuals within the MI government to speak with about their organizational capacity. In a subsequent e-mail, he also confirmed that the majority of the office is staffed by oil and gas program employees (53/55 employees in OGS) and that the public service commission has some regulatory overlap with his office. Finally, he answered a query about how CCS might be handled and predicted that EOR would be covered by the oil and gas program and storage in saline aquifers by the mineral well program in OGS. He expected an increase of 1-2 staff in that program, but thought it could be covered by a shift in staff, not necessarily new hires.
11 Mar. 2010, David Davis, Supervisor, Petroleum Geology & Production Unit, OGS, e-mail	Mr. Davis answered questions regarding different subsurface uses and their governance in Michigan. Specifically, he clarified different goals between OGS and public commission permitting and regulation in gas wells and storage. He also confirmed that EPA and the OGS regulate solution mining separately. Finally, he confirmed that OGS regulates gas storage wells, regardless of whether FERC or the state commission regulates their production/commodity aspects.
16 Mar. 2010, Eva Rowe, UIC Branch, USEPA, e-mail	Answered questions regarding the role of state regulators in injection wells, since they have not asserted primacy over EPA under the UIC program. She responded that UIC only regulates injection well activities and there are exclusions in 40 CFR 144 that exclude injection of pipeline quality hydrocarbons – basically, there is an exemption for these wells.
29 Mar. 2010, Ray Vugrinovich, Senior Geologist, OGS, e-mail	Assisted in answering questions regarding mineral well regulation in MI. Gave the MI laws that control mineral wells, confirmed that the program is independent of UIC, and provided a list of current solution mining operations in the state. Finally, he said that he didn't know of any state agency that had production data, but did provide a spreadsheet for mineral well depths.
b. Attorney Interviews on Michigan Subsurface Disputes and CCS	
21 June 2010, Larry Elkus, Law Offices of Lawrence M. Elkus, PC, e-mail	Mr. Elkus provided answers to questions I had e-mailed attorneys from across the state. He said that subsurface disputes are not commonly litigated in the state and that he had not participated in one. Also did not know of settlement data nor a list of cases on the issue. Stressed that facts and circumstances and the cost of litigation as major factors and recommended several other attorneys.
26 June 2010, Jack Lynch, Lynch, Gallagher, Lynch, Martineau & Hackett, PLLC, e-mail	Had only run into subsurface interference on two occasions – one was regarding salt water disposal in sandstone (the matter settled shortly and the owner of the disposal well paid to drill another well). The others involved gas storage migration and gas production disputes where stored gas migrates into a production field and the producer "steals" the stored gas [this gets into the rule of capture]. Proof of harm is important, as always, and he does not have any settlement data regarding subsurface trespass and stressed its confidentiality.
2 July 2010, William Horn, Mika Meyers Beckett & Jones PLC, phone	Discussed some cases he had heard about, but not many. Provided a copy of draft CCS legislation and talked a little about the process of creating the draft.
c. Bonds and Financial Assurance	
19 July 2010, James Duszynski, Bond Specialist, OGS, e-mail	Provided information regarding the types of bonds posted by operators for oil and gas wells. Also forwarded a queried list of bonds issued by MI OGS since 1983 with data regarding bond type and forfeiture rate.
11 Aug. 2010, Kevin Frederick & Dan Clark, Wyoming DEQ, e-mail	Responded to questions about the state of CCS in Wyoming. Provided an update as well as detailed spreadsheets used in the state's report on financial assurance mechanisms and CCS.
1 Sept. 2010, Bob Green, GM Sustainable Development and External Relations, Cloud Peak Energy Resources LLC, phone & e-mail	Discussed underlying assumptions of the working group report. Made distinctions from coal/oil/gas risk analysis and the CCS analysis they performed. Talked about state of financial assurance in WY compared to provisions in the UIC rulemaking process. Spoke generally about bonds and cost estimate assumptions.

3.3 Overview of subsurface activities, relevant agencies and lawa

3.3.1 Subsurface Activities

A number of subsurface activities are presently occurring in Michigan. Oil and natural gas wells are found throughout the Lower Peninsula of the state, which has the most substantial natural gas reserves of any state in the Great Lakes region (U.S. Energy Information Administration, 2010a). In addition, the natural gas storage capacity in Michigan is the largest of any state in the country, supplying nearby states with natural gas during the winter months (U.S. Energy Information Administration, 2010a). Other subsurface activities include the injection of hazardous and non-hazardous waste, solution mining, wastewater disposal, and groundwater supply. Other practices – namely coal mining and copper mining – fall outside of the scope of this inquiry, but are significant nonetheless. Coal mining is no longer practiced in Michigan and the controversial nickel-copper Kennecott Eagle mine is located in the Upper Peninsula – outside the focus area of this project. Regulation of these subsurface activities has ties to both historical practice and subsequent laws that governs how federal and state agencies protect the environment and manage its resources.

3.3.2 Agencies and Laws

The United States Environmental Protection Agency (EPA) is the main federal regulatory agency for subsurface activities. The Underground Injection Program (UIC) within the EPA regulates injection wells across the country to protect groundwater supplies. The program traces its origins to the injection of wastewater (consisting of oil field brines and other waste products) into depleted reservoirs by oil companies in the 1930's. Over the next few decades, more industries began to inject waste into the subsurface and incidents of wells leaking into water supplies increased. Awareness of this growing problem ensued, and Congress responded by enacting the Safe Drinking Water Act in 1974. Under the Act, EPA sets requirements for protecting underground sources of drinking water. The UIC program was formed in 1980. Subsequent regulations, codified in 40 C.F.R. § 144, define five classes of wells based on the similarity in the fluids injected, activities, construction, injection depth, design, and operating techniques concerning the well. The SDWA lets states to apply for primary enforcement responsibility (called "primacy") if they choose. Forty states have established complete or partial primacy with regard to these wells (U.S. Environmental Protection Agency, 2001). Michigan has not applied for primacy; its wells are regulated by EPA Region 5 staff, though some legacy state programs and permits are run, at times concurrently, by state agencies.

In addition to the EPA, the other federal agency with jurisdiction of subsurface activities in Michigan is the Federal Energy Regulatory Commission (FERC), an independent agency that regulates the interstate transmission of electricity, oil, and natural gas, including its production and storage (Federal Energy Regulatory Commission, 2009). FERC's regulation of natural gas storage levels is the only activity it regulates relevant to this report.

The Michigan Department of Natural Resources and Environment (MDNRE) is the state regulatory agency for subsurface activities. Within the MDNRE, the Office of Geological Survey (OGS) issues permits for oil and gas, mineral wells, waste injection, and mining activities. The OGS has a staff level of 60 and an appropriated budget of $10.8 million (T. Golbold, Personal Communication, 3/3/2010). The Michigan Public Service Commission (MPSC) regulates energy, telecommunications, and transportation

services for residents of the state. MPSC's role in the subsurface is analogous to FERC's role as it sets in-state production levels for natural gas for the wells under its jurisdiction. Most of Michigan's environmental acts, including those related to subsurface activities, have been combined in the Natural Resources and Environmental Protection act (NREPA), P.A. 451, as amended. Another relevant state law is the Safe Drinking Water Act of 1976, P.A. 399, which authorizes state agencies to take enforcement action regarding water problems.

3.3.3 Subsurface Property Rights

The ancient legal principle of c*uius est solum, eius est usque ad caelum et ad inferos* ("for whoever owns the soil, it is theirs up to Heaven and down to Hell") was limited in regard to airspace ownership early in the 20th Century and will likely be limited with regard to subsurface ownership as well, as geologic storage legislation develops. Designating subsurface property rights, however, will not be as straightforward as airspace ownership. Furthermore, due to the scope, complexity, and relative isolation to geologic storage in comparison to other subsurface activities, pore space owners will likely need to show that an actual harm occurred to receive compensation, either through eminent domain or tort theories of trespass or nuisance.

An important distinction in subsurface ownership is the difference between owning a pore space and owning a commodity (Klass, 2010). Subsurface water rights, oil and gas rights, hard-rock mining rights, and coal-bed methane gas ownership are examples of activities where ownership, development, or extraction, are at stake for a resource or commodity. The unitization of oil fields and secondary oil and gas recovery that interferes with subsurface interests, subsurface waste injection, and natural gas storage are situations in which the ownership of pore space and competing interests (surface owner, operator, the public) present a similar set of facts as geologic storage (Klass, 2010).

3.3.4 Effort to Implement Regulatory and Legal Oversight for Geologic Storage of CO_2 in Michigan

Michigan has not enacted any state laws governing geologic storage of CO_2. In 2009, State Rep. Joseph Haveman, a Republican from Ottawa County, introduced HB 5253,which would have established a permitting system for geologic storage of CO_2 and authorized the Department of Environmental Quality (DEQ) to issue these permits. HB5253 also enumerated requirements of the permitting system, such as the appropriateness of storage boundaries and whether or not the storage would be in the public's interest. The bill also would have provided the DEQ with the authority to require financial assurance along with the permit, though no specific guidance was discussed. Eminent domain was also addressed. The bill would have established a trust fund to be used for monitoring, remediation, repair, plugging, and paying claims; this trust fund would be financed by a one-time fee of $1 per ton of CO_2 injected. The bill would have given state- or federally-financed projects conceived for the purpose of geologic storage a waiver of liability (it is assumed by the state) after the CO_2 is injected—this aspect of the bill was presumably present to encourage funding of such projects and developer buy-in. Finally, the bill would have given operators immunity from nuisance or trespass causes of action. HB5253 was referred to the Committee on Energy and Technology and stalled in committee.

3.4 Subsurface Activities, Regulatory Structure, and Applicable Subsurface Property Law

3.4.1 Oil and Gas Production

Geology and Resources

Oil and natural gas production are two fossil-based subsurface activities in the Michigan basin. Reserves are found in rocks from the Cambrian through Mississippian formations and production focuses on the Silurian pinnacle-reef trend around the margin of the basin (Wickstrom, 2005). Oil and gas are currently produced at varying depths; from the shallow Devonian Antrim Shale in the northwestern part of the basin to the Glenwood and Prairie Du Chein Formations at depths reaching 11,500 feet in central Michigan (Wickstrom, 2005). In 2009, an estimated 5.9 million barrels (33 million cubic feet) of crude oil were produced from approximately 3,600 wells across the Lower Peninsula (U.S. Energy Information Administration, 2010b) (Michigan Public Service Commission, 2008). Natural gas production in Michigan is substantial and supplies approximately 20 percent of the state's demand, with 802 billion cubic feet produced from 10,000 wells in 2007 (Michigan Public Service Commission, 2008). A dense concentration of natural gas wells stretches across the northern part of the state in Antrim, Otsego, and Montmorency counties (Michigan Public Service Commission, 2008).

Regulatory Structure

The exploration, drilling, and operating of oil and gas wells are regulated by OGS. Part 615 of NREP and rules promulgated by DNRE form the basis for regulation of these wells.[1] OGS sets production levels on oil wells and the MPSC sets production levels for gas, or non-liquid hydrocarbon-producing wells (D. Davis, Personal Communication, 3/16/10). The Oil and Gas Program is the largest division at OGS with has a staff level of 53 and a budget of approximately $8 million (T. Golbold, Personal Communication, 3/3/10). This department also regulates oil and gas disposal and natural gas storage, described in more detail in sections below.

Michigan has a long history of oil and gas exploration and production. The first oil and gas permits were issued by the OGS in 1927. Since then, almost 60,000 permits have been issued by the state (Michigan Department of Natural Resources and Environment, 2010b). Figure 1 shows a schematic of the well permitting process. The agency issues permits pursuant to MCL 324.61525 and Rule 324.201. When an applicant submits a permit application, it is logged into an oil and gas well database managed by OGS. The Permit Coordinator then completes an initial review and forwards to an Area Geologist for an on-site inspection. Depending on the potential impact, other DNRE programs may perform inspections as well. Upon completion of the site inspection, the District Supervisor completes the review and forwards a recommendation to the Permit Coordinator. The process takes approximately 60 days from receipt. In the event a violation occurs, the OGS may take action to enforce the rules, including suspending operations at a well.[2]

[1] Specifically, Part 615 of the NREPA concerns the well permit process, spacing and location, drilling and well construction, production, disposal, and injection.

[2] Rule 324.1301, "Authority of supervisor."

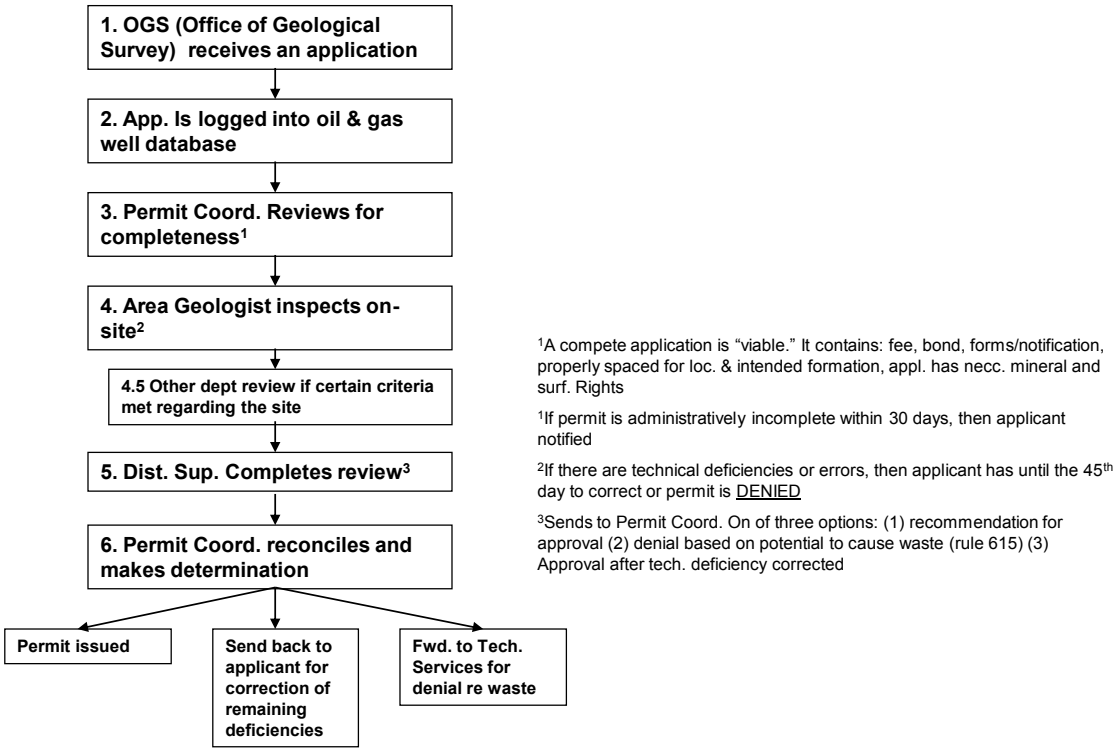

Figure 1 The Oil and Gas Well Permitting Process in Michigan.

Subsurface Property Law

Oil and gas production has a long history of jurisprudence. The majority view is that for native formations, the rule of capture applies. The rule of capture traces its property law origins back to English common law, which applied to the "capture" of wild game. The rule of capture has been translated to the oil and gas sector to mean that native oil and gas is not owned until a person "captures" it and brings it to the surface. Michigan has adopted the rule of capture, *see* ("ANR Pipeline Co. v. 60 Acres of Land," 2006). To mitigate the "harshness" of the rule of capture, the court in ANR Pipeline Co. advocated the traditional "fair share" principle, which provides each landowner an opportunity to produce a proportionate share of the oil and gas from the common formation. It appears as though state legislatures have attempted to limit these types of disputes while also advocating a policy goal of reducing waste and benefiting the economy by unitizing oil and gas fields. While such and activity has utility for oil and gas applications, unitization for geologic storage might be significantly more complex, potentially involving thousands of property interests (Fish, 2008).

3.4.2 Oil and Gas Waste Disposal

The production of oil and gas creates waste that must be disposed. A common waste product is brine, or salt water, brought to the surface in the process of extracting oil and gas. After the brine is separated from the hydrocarbon, it is often injected back into the formation. Brine is also injected into an oil-bearing formation to aid in the recovery of residual hydrocarbons. This process, called Enhanced Oil Recovery (EOR), is widely used, especially in Texas, California, Oklahoma, and Kansas (U.S. Environmental Protection Agency, 2010b). EOR is also practiced in Michigan, with 8 existing sites and 3 proposed projects in 2008 (Koottungal, 2008). EOR and brine injection activities are regulated by state and federal agencies.

Oil and gas related injection wells are classified as Class II wells in the UIC program. There are approximately 144,000 Class II wells in operation in the U.S. with approximately 1,500 active in Michigan (U.S. Environmental Protection Agency, 2009a). OGS is responsible for the state regulation of this type of well. Part 15 of the NREPA and rules R 324.101 – R 324.1301 specify the requirements for parties seeking a well permit.

3.4.3 Natural Gas Storage

Overview

Natural gas storage acts as a warehouse from which energy consumers can withdraw during times of high demand. In states with cold climates, like Michigan, natural gas has traditionally been injected into underground storage fields during summer months and withdrawn in winter for home heating use. The seasonal impact on storage has decreased, however, as market forces exert more influence on storage patterns over the past decade (U.S. Energy Information Administration, 2004). Michigan has abundant natural gas storage; approximately 12.5 percent of the total natural gas storage capacity in the United States at over 1,000 billion cubic feet and a working gas capacity of over 660 billion cubic feet, primarily in depleted oil and gas fields,[3] is contained in Michigan (U.S. Energy Information Administration, 2010d). Many of the depleted fields are located in the Niagaran Formation, first utilized as production fields in the 1960's and productive through the 1980's (Michigan Public Service Commission, 2009b) (Michigan Public Service Commission, 2009a). In 2008, over 563 billion cubic feet of natural gas was exported from Michigan (representing over half of the exports of natural gas in the U.S.), 467 billion cubic feet of gas was injected and 492 billion cubic feet of gas was withdrawn (U.S. Energy Information Administration, 2010c).

Regulatory Structure

Natural gas storage is regulated by federal and state agencies. The state OGS regulates the non-commercial environmental and geological components of natural gas storage wells pursuant to Part 615 of NREPA and regulations, even though their storage from a commodity perspective is regulated by a federal agency (FERC) or a state agency (MPSC). In other words, OGS regulates the storage wells from

[3] Working gas is gas available to the marketplace. A reservoir has a larger total capacity, but it must keep a certain volume of "base gas" or "cushion gas" to maintain adequate pressure and deliverability rates. Working gas is total capacity minus base gas and, in Michigan, it varies from 30% to 85%, depending on the storage field.

an environmental and geological standpoint while FERC or MPSC regulate the natural gas from storage wells as a commodity.

The EPA does not regulate the storage wells as a Class II well[4] under its UIC program because of the exception found in 40 C.F.R. § 144.1(g)(2)(iv) which excludes, "Injection wells used for injection of hydrocarbons which are of pipeline quality and are gases at standard temperature and pressure for purposes of storage." The OGS instead works with the MPSC and FERC to record gas storage and production data and regulates non-commerce activities relating to the transport of gas in and out of the storage reservoir (Michigan Department of Natural Resources and Environment, 2010a).

FERC regulates the "transmission or sale of natural gas in interstate commerce," including storage, as established by the Natural Gas Act of 1938. FERC does not regulate the sale of natural gas to *consumers*, this responsibility is left to the MPSC (Federal Energy Regulatory Commission, 2009). In Michigan, 17 storage fields fall within FERC jurisdiction, comprising almost half of the total storage capacity in the state at 430 billion cubic feet (working gas capacity is 280 billion cubic feet) (Federal Energy Regulatory Commission, 2010). These federally regulated storage sites are managed within FERC by the Office of Energy Market Regulation.

The Michigan Public Service Commission (MPSC) regulates intrastate storage of natural gas pursuant to Act No. 9 of the Public Acts of 1929. The Commission regulates storage fields across the state with a total capacity of 700 billion cubic feet and a working gas capacity of 422 billion cubic feet (Michigan Public Service Commission, 2009b).

Subsurface Property Law

Subsurface storage of natural gas is an important activity to investigate both for its similarity with geologic storage and for its prevalence in Michigan, which has approximately 12.5 percent of the natural gas storage capacity in the United States (U.S. Energy Information Administration, 2010) . There is extensive case law dedicated to natural gas storage operations across the country, helping to delineate different approaches different jurisdictions may take. There are several distinctions between natural gas storage and the storage of CO_2. Natural gas is stored in cycles, responding to supply and demand of energy markets, whereas CO_2 storage permanence is the overarching purpose of geologic storage. The liability of long-term storage will thus be a topic not generally covered by working natural gas storage operations. Perhaps more importantly, natural gas is a commodity and CO_2 may be seen as a waste product (Anderson, 2009). This distinction has two important implications:

1. Regulation under the 1976 Resource Conservation and Recovery Act (RCRA) is invoked when a substance is classified as a waste. Additionally, the 1980 Comprehensive Environmental Response, Compensation, and Liability Act (CERCLA, more commonly known as Superfund) applies for a hazardous waste, which, unless hazardous substances (e.g., H_2S) are present in the injected fluids.
2. Compensation for interest-holders is easier for a commodity like natural gas, in part because it has a market value.

[4] Oil & Gas Injection Wells

These distinctions are perhaps less important, however, than the similarities between the two activities (Anderson, 2009). The regulatory framework for natural gas storage could be a useful analog for geologic storage. The federal Natural Gas Act gives FERC the authority to issue certificates of "public convenience and necessity" to natural gas storage operators, allowing them to utilize the power of eminent domain to take land (Klass, 2010). This regulatory taking provides compensation to both surface and subsurface interest holders at a fair market value and based on the harm they suffer. Some commentators have questioned whether the burden of proving actual harm would bar many interest holders from receiving compensation (CCSReg Project, 2009). Interestingly, interest holders who allow for the storage of natural gas within their property often receive rent payments of approximately $20/ac/yr. For geologic storage operators who wish to store CO_2 in natural gas storage reservoirs, the question of whether the loss of rent payments from natural gas storage is reasonable and foreseeable –thus compensable use for these interest holders—is crucial. If it is compensable, geologic storage operates might face a prohibitory cost. These operators who would make payments to property owners on the scale of $13 million/yr in perpetuity for a sequestration project of 1,000 square miles (Fish, 2008). In addition, mineral estates have traditionally been given dominance over natural gas storage interests when there is still an economically recoverable resource in the formation. Such a decision could incentivize other non-mineral formations, such as saline aquifers, to be sought as CO_2 storage reservoirs (CCSReg Project, 2009) (Fish, 2008).

3.4.4 Underground Waste Injection

Overview

Class I wells inject hazardous and non-hazardous wastes deep into isolated rock formations thousands of feet below drinking water supplies. The wells are designed and constructed to prevent the infiltration of waste into drinking water aquifers by using concentric layers of pipe and careful siting (U.S. Environmental Protection Agency, 2001). Michigan has 28 active injection wells (9 hazardous) at depths between 1,800 ft and 6,700 ft (U.S. Environmental Protection Agency, 2009b).

Regulatory Structure

Permits for Class I waste injection wells are issued by EPA and are valid for ten years. Hazardous waste for the purposes of this waste injection is defined in 40 C.F.R. 261 and injection is regulated pursuant to rules in 40 C.F.R. 146 and 148. Criteria for issuance of permits address siting, construction, operation, monitoring and testing, reporting and record keeping, and closure of wells (U.S. Environmental Protection Agency, 2010a). In addition to geologic and potential impact studies, a party seeking to inject a prohibited, hazardous waste in 40 C.F.R. 148(B) must file a "no-migration" petition that shows the injected waste will be contained for 10,000 years and that by the time such movement occurs, if at all, the waste will be transformed into a more benign form. No-migration petitions are costly and time-consuming, often requiring up to 11,000 hours of work done by geologists, engineers, and other scientists and upwards of $2 million to complete (U.S. Environmental Protection Agency, 2001). While the well is operating, quarterly reports on the physical, chemical, and other relevant characteristics must be complied and submitted to EPA. Upon closure of the well, a plugging and abandonment report must be submitted to EPA.

Waste injection wells are also regulated by the Supervisor of Wells at OGS and the Waste and Hazardous Materials division of the MDNRE. Parts 111 ("Hazardous Waste Management") and Part 625 ("Mineral Wells") in the Michigan NREPA specify permit requirements for waste injection. Permits are issued on a timeline similar to the UIC permitting process – six months to a year (Michigan Department of Environmental Quality & Michigan Department of Labor and Economic Growth, 2008).

Subsurface Property Law

The regulatory framework, especially for hazardous waste, may be the closest analog to the type of regulation that might be created for geologic storage, since the injection is meant to be permanent and CO_2 is not supposed to migrate. The "no-migration" petition seeks to ensure that these two objectives are met. In other federal matters, RCRA allows citizen suits for injunctive relief in order to compel remediation of a leak that becomes an imminent and substantial danger to human health and the environment (Klass, 2008). If CO_2 is classified as a waste, this remedy could be available for injunctive relief. If CO_2 is classified as a *hazardous* waste, CERCLA can allow for the private recovery of money, but this recovery is limited to money spent on investigation and remediation (Klass, 2008). Traditional state tort remedies discussed below may provide one alternative for individuals harmed by migration of geologically stored CO_2. A tension exists, however, between limiting the liability of operators to spur development of the technology and the ability for an individual to recover from harm under current proposals which could preclude state tort actions.

3.4.5 Solution Mining

Overview

Solution mining utilizes the injection of fluids to dissolve and extract minerals like salt, copper, and sulfur. Michigan's solution mines produce salt and potash[5] (U.S. Geological Survey, 2009). In 2006 nonfuel raw mineral production in Michigan, including salt and potash, had a value approaching $1 billion[6] (U.S. Geological Survey, 2009). Currently, three mines utilize solution mining techniques. They are the Morton Salt Company in Manistee, Mosaic Potash Hersey in Hersey, and Cargill, Inc. in St. Clair (R. Vugrinovich, Personal Communication, 3/29/10). Mining occurs in the rocks of the Salina group, typically A-1 or B Evaporite at depths ranging from 2,100 ft. to 8,000 ft below ground (*Id.*).

Regulatory Structure

The EPA's UIC program and the MDNRE's Mineral Wells Management program regulate solution mining in Michigan. Mining wells fall within the Class III designation of the UIC, which regulates only the injection of solution into the subsurface (not the extraction of material from the wells). In 2008, there were 53 Class III wells operating at 5 sites in Michigan (U.S. Environmental Protection Agency, 2009a).

[5] "Potash" is used as an agricultural fertilizer because it contains potassium , one of the three primary plant nutrients (U.S. Geological Survey, 2010).

[6] In addition to salt and potash value, this sum includes bromine, iron ore (usable shipped), iron oxide pigments (crude), lime, magnesium compounds, stone (crushed marl, dimension dolomite, sandstone), and "withheld" values, but not cement, clays, gemstones, peat, sand and gravel, or crushed stone (U.S. Geological Survey, 2009).

The Permits and Bonding Unit and the Mineral Wells Management program of the OGS regulates solution mining separately from EPA's UIC program and includes extraction as well as injection wells. The federal and state agencies do coordinate activities and requirements to avoid giving conflicting instructions to applicants (R. Vugrinovich, Personal Communication, 3/29/10). Injection wells classified as "artificial brine" under Part 625 of the NREPA. A permit applicant must submit a well location description, information regarding proximity to surface water or other environmentally sensitive areas, an environmental impact assessment, an organization report, geologic and hydrologic information of the site, and other information required by rule. After submission of the permit application, the supervisor of mineral wells has 60 days to review the application and, if it is found to be incomplete, 30 days after receipt of the additional information to issue or deny the permit. Part 625 of the NREPA and the promulgated rules R 299.2301 – R 299.2531 cover the scope of the state regulatory scheme, which does not include collecting production data from mines.

3.4.6 Groundwater Withdrawal and Discharge

Regulatory Structure

The Michigan Safe Drinking Water Act, enacted in 1976, gives the MDNRE Water Programs division primary enforcement authority for the Federal Safe Drinking Water Act. Groundwater discharge is regulated by the Groundwater Program under Part 31, Water Resources Protection, of the NREPA and the promulgated rules 323.2201 – 323.2241. Permits to discharge are issued on a sliding scale based upon the risk of impact by activity. EPA also oversees the shallow injection of non-hazardous fluids as Class V wells through the UIC program, though it rarely issues permits (U.S. Environmental Protection Agency, 2007). There are 20 subtypes of Class V wells identified by EPA. These include aquifer recharge/recovery, in-situ fossil fuel recovery, and storm water drainage. Michigan had over 3,000 Class V wells in 2008 (U.S. Environmental Protection Agency, 2009a).

3.4.7 Summary of Subsurface Activities and Regulatory Oversight in Michigan

Table 2. Summary of Subsurface Activity Regulation in Michigan

Subsurface Activity	Agency	Rules
Deep injection of hazardous and non-hazardous waste	USEPA Region 5	UIC Class I 40 C.F.R. 144
Oil and Gas		
Oil and gas production (permitting)	MDEQ/OGS/Oil and Gas	MI Admin. Code: R 324.101 – 324.1301
Gas production (safety & quantity)	MSPC	MI Admin. Code: R 460.851-460.875
Waste fluid disposal & Injection for Enhanced Oil Recovery (subject to both state and federal rules)	USEPA Region 5	UIC class II 40 C.F.R. 144
	MDEQ/OGS/Oil and Gas	MI Admin. Code: R 324.101 – 324.1301

Natural Gas Storage	MSPC	MI Admin. Code: R 460.851-460.875
Solution Mining		
Fluid injection	USEPA Region 5	UIC class III 40 C.F.R. 144
Mineral extraction	MDEQ/OGS/Mineral Mining Group	MI Admin. Code: R 299.2301 to 299.2531
Groundwater withdrawal	MDEQ/Waters Group	Part 327 and 328 of the Natural Resource and Environmental Protection Act and the Safe Drinking Water Act

3.5 Subsurface Property Law and Pore Space Ownership

3.5.1 Center of the Earth Theory

In a 2008 UCLA Law Review article, Professor John Sprankling declared the end of the center of the earth theory of property law (Sprankling, 2008). The article looks at cases encompassing the above-mentioned subsurface activities and concludes that most states have rejected the theory, if only implicitly. These cases can be divided into two main categories:

1. Disputes involving activities at or a few feet below the surface (tree roots, sewer lines, etc.).
2. Disputes involving activities extending from a few feet to two miles below the surface.

The first category uses the center of the earth theory to justify ownership and Sprankling argues that this justification is shorthand for providing the surface owner reasonable control over the subsurface. The rights afforded to the surface owner decrease in the second category and continue to decrease as the depth below the surface increases. Sprankling recommends that courts recognize a surface owner's right to the subsurface extending from the surface to a depth of 1,000 feet, with an exception for competing mineral estates. Others have advocated that the federal carbon sequestration legislation include language stating the public interest in sequestering CO_2—similar to the declaration of airspace as public decades ago—thus limiting ownership to a depth commensurate with the "reasonable expectations" of the owner (CCSReg Project, 2009).

Important differences between the air and subsurface exist, though, and these differences could influence the practicability of such a proposal (Klass, 2010). The "bundle of sticks" that make up subsurface property rights have been scattered throughout the past century-and-a-half. As a consequence, a plot of land could have multiple owners beneath it, and each of these owners could have their own independent but competing interests. In contrast, airspace was relatively devoid of private interests when it was declared public. A strong public interest in using airspace (for commerce) exists. While there is a public interest in using the subsurface, the real actors are private companies and developers, not the typical citizen. Furthermore, encompassing both of these issues is the fact that the subsurface is traditionally been a private entity in the United States. It would be a "seismic" shift to declare it generally, or at least

substantially, a public space. While the end of the center of the earth theory of property ownership may be in sight, such a demise presents the larger question: if not the surface owner, than whom?

3.5.2 Pore Space Ownership

Law related to pore space ownership is not settled, and because of the new and potentially widespread activity set to take place in the subsurface, pore space ownership could have far-reaching implications for takings, torts, and long-term liability. Despite the above advocacy for the demise of the center of the earth theory, surface owners still likely "own" the pore space below their property, at least in the majority of jurisdictions (Fish, 2008). In short, a property right not expressly conveyed is retained, the mineral estate, though dominant, cannot use the subsurface in a way that interferes with the surface owner's existing uses, and even though agencies could issue permits for pore space *use*, the permit does not convey title (Anderson, 2009). The overarching theme is thus related to the issue of how the rights inherent to ownership of the pore space should be prescribed.

If it is assumed that the surface owner has an interest in the pore space, then the question becomes: what are their current or reasonably foreseeable uses for the pore space? If no reasonable foreseeable uses exist, then surface owners are unlikely to receive compensation for either a taking or for a trespass or other tort-based claim. If each surface owner had a right to receive compensation for a use that did not interfere with their current or expected uses, it would be a prohibitively expensive and complex analysis to parse out their "share" of the compensation. Such an approach is also inconsistent with the "no harm, no foul" tradition of other subsurface dispute resolutions. If there is some current or reasonably foreseeable use, then the surface owner may be entitled to some form of compensation, but it is unclear what this would be. It is further unclear whether pore space rental, as suggested in the Fish article, would be compensable (Fish, 2008). While the specifics will no doubt be addressed in the courts, it is reasonable to expect that ownership rights will extend so far as they are compensable only if the surface owner is actually harmed by either the taking of their subsurface property or by a migration of the CO_2 plume.

Another unresolved aspect of pore space ownership involves short- and long-term liability of the injected CO_2. Some proposals seek to encourage development of geologic storage by relieving operators of liability after a short post-closure period. The IOGCC proposal approaches liability in a two-stage framework. The first stage is a 10-year post-closure period where the geologic storage operator maintains liability and responsibility for continued monitoring. After that period, the operational bond is released and liability transfers to the state with funding for the state monitoring system coming from a trust fund created for this purpose and funded by an injection fee (Hayano, 2009). The Wyoming CCS laws (HB 89 & 90) reject this approach; liability remains with the operator into perpetuity and is unlikely to ever transfer to the state (Hayano, 2009). Others have advocated for limiting corporate liability to further the policy goal of removing CO_2 from the atmosphere (CCSReg Project, 2009). Some advocate for the preservation of existing state and federal liability regimes (as opposed to transferring liability to states) to provide for important risk management tools and to provide a safeguard in the event of harm (Klass, 2008). The final makeup of federal CCS legislation likely depends on how competing interests fare during the drafting stage; corporations and developers will no doubt push for the transfer of liability to the states. Such a result could encourage lax environmental practices during the operational and closure phases; because the operator has no liability should a leak occur. Strong regulation during operation and closure could limit poor practices while the state, with funds from injector fees, would be in a better

position anyway to handle long-term liability; conceivably, the state would continue to exist even if the injection operator goes bankrupt or no longer exists when a harm occurs.

3.5.3 Potential Remedies

For many years, traditional remedies rooted in state tort law have been used to resolve subsurface disputes and to remedy harms. Subsurface trespass and nuisance are the common tort theories used by allegedly harmed parties. Trespass is more applicable because its function is to remedy harm to a party as opposed to nuisance, which concerns impairment of one's enjoyment of their land or an activity that interferes with some public interest. Trespass also appears to be the more common cause of action in other analogous cases (gas storage, oil and gas production, waste injection). Typically, as described above, a party must show actual harm to their property or show some other reason why the balance between public good (sequestering gas) and private interests should tip in their favor. A party may bring a nuisance claim against an operator even if that operator is acting within permitted guidelines but, again, the likelihood of success is tied closely to a balancing of public benefits and the alleged harm. One reason commentators advocate for the preservation of tort claims (and CCS legislation) is the way the traditional tort remedies interact with statutes. One of these is negligence per se. If a party can prove that an operator had a statutory duty to act in a certain way and that they violated this duty, that party can seek negligence per se relief (Klass, 2008). What form does this relief take? Aside from injunctive relief (which prevents a party from performing some action), monetary damages would be the reward. Courts usually uphold significant damages for widespread contamination and the company faces the additional prospect of an environmental stigma (Klass, 2008). Furthermore, while the preservation of tort liability for operators could seem to create significant room for litigation before geologic storage is adopted, traditional subsurface disputes have hinged significantly whether or not the property owner can show actual harm or impairment.

3.6 References

Anderson, O. L. (2009). Geologic CO2 Sequestration: Who Owns the Pore Space? *Wyoming Law Review, 9*(1).

ANR Pipeline Co. v. 60 Acres of Land, 418 933 (U.S. District Court for the Western District of MI 2006).

CCSReg Project. (2009). Policy Brief: Governing Access to and Use of Pore Space for Deep Geologic Sequestration. Pittsburgh, PA: Carnegie Mellon University.

Federal Energy Regulatory Commission. (2009). About FERC. Retrieved March 28, 2010, from http://www.ferc.gov/about/ferc-does.asp

Federal Energy Regulatory Commission. (2010). Jurisdictional Storage Fields in the United States by Location. Retrieved March 15, 2010, from http://www.ferc.gov/industries/gas/indus-act/storage/fields-by-location.pdf

Fish, J. R. W., Thomas R. (2008). *Geologic Carbon Sequestration: Property Rights and Regulation.* Paper presented at the Proceedings of the Rocky Mountain Mineral Law Fifty-Fourth Annual Institute, Westminster, CO.

Hayano, D. (2009). Guarding the Viability of Coal & Coal-Fired Power Plants: A Road Map for Wyoming's Cradle to Grave Regulation of Geologic CO2 Sequestration. *Wyoming Law Review, 1*(9).

Klass, A. B. W., Elizabeth J. (2008). Climate Change and Carbon Sequestration: Assessing a Liability Regime for Long-term Storage of Carbon Dioxide. *Emory L.J., 58*(1).

Klass, A. B. W., Elizabeth J. (2010). Climate Change, Carbon Sequestration, and Property Rights. *U. Ill. Law Rev., 2010*(2).

Koottungal, L. (2008). Special Report: 2008 Worldwide EOR Survey. *Oil and Gas Journal, 106*(15), 47-59.

Michigan Department of Environmental Quality & Michigan Department of Labor and Economic Growth. (2008). Michigan Manufacturers' Guide to Environmental, Health, and Safety Regulations. Retrieved March 15, 2010, from http://www.michigan.gov/deq/0,1607,7-135-3310_4148-15820--,00.html

Michigan Department of Natural Resources and Environment. (2010a). Injection Well Data. Retrieved March 15, 2010, from http://www.michigan.gov/deq/0,1607,7-135-3311_4111_4231-214727--,00.html

Michigan Department of Natural Resources and Environment. (2010b). Permits Issued By Year. Retrieved March 15, 2010, from http://www.michigan.gov/deq/0,1607,7-135-3311_4111_4231-130396--,00.html

Michigan Public Service Commission. (2008). Michigan Energy Overview. Retrieved March 15, 2010, from //www.dleg.state.mi.us/mpsc/reports/energy/energyoverview/

Michigan Public Service Commission. (2009a). About Michigan's Natural Gas Industry. Retrieved March 15, 2010, from http://www.dleg.state.mi.us/mpsc/gas/about1.htm.

Michigan Public Service Commission. (2009b). Michigan Natural Gas Storage Field Summary. Retrieved March 15, 2010, from http://www.dleg.state.mi.us/mpsc/gas/storage.htm

Sprankling, J. G. (2008). Owning the Center of the Earth. *UCLA L.R., 55*(4).

U.S. Energy Information Administration. (2004). The Basics of Underground Natural Gas Storage. Retrieved March 15, 2010, from http://www.eia.doe.gov/pub/oil_gas/natural_gas/analysis_publications/storagebasics/storagebasics.html

U.S. Energy Information Administration. (2010a). Michigan Energy Profile. Retrieved March 15, 2010, from http://tonto.eia.doe.gov/state/state_energy_profiles.cfm?sid=MI

U.S. Energy Information Administration. (2010b). Monthly Michigan Field Production of Crude Oil. Retrieved March 15, 2010, from http://tonto.eia.doe.gov/dnav/pet/hist/LeafHandler.ashx?n=PET&s=MCRFP_SMI_1&f=M

U.S. Energy Information Administration. (2010c). Natural Gas Summary (Michigan). Retrieved March 15, 2010, from http://tonto.eia.doe.gov/dnav/ng/ng_sum_lsum_dcu_SMI_a.htm

U.S. Energy Information Administration. (2010d). Underground Natural Gas Storage Capacity. Retrieved March 15, 2010, from http://tonto.eia.doe.gov/dnav/ng/ng_stor_cap_a_EPG0_SAC_Mmcf_a.htm

U.S. Environmental Protection Agency. (2001). Study of the Risks Associated with Class UIC Wells. Retrieved March 15, 2010, from http://www.epa.gov/ogwdw000/uic/pdfs/study_uic-class1_study_risks_class1.pdf

U.S. Environmental Protection Agency. (2007). Frequent Questions (about Class V Wells). Retrieved March 15, 2010, from http://www.epa.gov/safewater/uic/class5/frequentquestions.html

U.S. Environmental Protection Agency. (2009a). Annual Inventory of Underround Injection Wells in Region 5. Retrieved March 15, 2010, from http://www.epa.gov/reg5oh2o/uic/final_inventory.htm.

U.S. Environmental Protection Agency. (2009b). Class I Underground Injection Wells in Region 5. Retrieved March 15, 2010, from http://www.epa.gov/reg5oh2o/uic/cl1sites.htm

U.S. Environmental Protection Agency. (2010a). Industrial & Municipal Waste Disposal Wells (Class I). Retrieved March 15, 2010, from http://www.epa.gov/safewater/uic/wells_class1.html

U.S. Environmental Protection Agency. (2010b). Oil and Gas Related Injection Wells (Class II). Retrieved March 15, 2010, from http://www.epa.gov/safewater/uic/wells_class2.html.

U.S. Geological Survey. (2009). *2006 Minerals Yearbook: Michigan*. Washington.

U.S. Geological Survey. (2010). Potash Statistics and Information. Retrieved March 15, 2010, from http://minerals.usgs.gov/minerals/pubs/commodity/potash/

Wickstrom, L. H., Venteris, E.R., Harper, J.A., McDonald, J., Slucher, E.R., Carter, K.M., ... Greb, S.F. (2005). *Characterization of Geologic Sequestration Opportunities in the MRCSP Region* (Phase I Task Report). Columbus: Midwest Regional Carbon Sequestration Partnership.

Chapter 4. Three-Dimensional Geospatial Model of the Michigan Sedimentary Basin, Subsurface Activities, and Well Leakage Pathways

4.1 Michigan Basin Geology and Subsurface Activities

We created a three-dimensional model of the Michigan sedimentary basin underlying the lower peninsula of Michigan (USA). This model depicts the topography of the geologic units and the locations of wells as leakage pathways and subsurface activities. Section 4.2 documents how well and borehole data are used to characterize the location and nature of current subsurface activities as well as potential leakage pathways for geologically injected CO_2 or the brine displaced by this CO_2. Section 4.3 presents the methodology and procedure regarding how the three-dimensional model was constructed.

Section 4.1.1 documents the data sources and describes how they are used in the model. The stratigraphy and structure of the Michigan Basin, as interpreted for this study, are described in Section 4.1.2 and Section 4.1.3, respectively.

4.1.1 Data Sources

Table 1 lists our data sources, describes the type of data obtained from each source, and indicates how the data was used. Section 4.3 provides additional details on how the data were cleaned.

4.1.2 Stratigraphy

Our stratigraphic system closely follows the USGS hydrostratigraphic system, as shown in Table 2. Adjustments to the USGS hydrostratigraphic system are explained in the Section 4.3.1. The Mt. Simon Sandstone (capped by the Eau Claire Formation) and the St. Pater Sandstone (capped by the Prairie du Chien Formation) are the primary targets for CO_2 injection for storage in the Michigan Basin (Wickstrom, et al., 2005). Other formations, such as the Galesville Sandstone, or formations within the Silurian-Devonian Unit, could be injection targets in some areas, but they do not have CO_2 storage capacity throughout the basin.

Table 1: Summary of Data Sources

Data Source	Data Type	Use
MI DEQ oil and gas online database[a]	API well number, depth, producing formation, top surface, well type and status, latitude and longitude	Stratigraphy, structure, subsurface activities, leakage pathways
MI DEQ oil and gas well location database[b]	API well number, well depth, slant, objective formation, deepest formation, well type, well status, latitude and longitude.	Stratigraphy, structure, subsurface activities, leakage pathways
MI DEQ oil and gas wells Formation Tops & Elevations database[c]	Formation top elevations, surface reference elevation, reference code and method obtained by various sources for top surface of data	Stratigraphy, structure
EPA Region 5 Underground Injection Control Program	Class I and III wells including: API well number, formation, depth, well type, well status, latitude and longitude.	Subsurface activities, leakage pathways
Michigan geographic data library County drinking water well files[d]	Drinking water wells for each county: depth, type, latitude and longitude	Subsurface activities, leakage pathways
USGS Hydrogeologic Framework for the Lake Michigan Basin	Grid points containing bottom elevations for formations in Michigan basin.	Stratigraphy, structure
MRCSP Geologic Characterization	Raster files for isopach and structure of St. Peter and Mt. Simon Formations	Stratigraphy, structure

[a] MDEQ (2011a); [b] MDEQ (2011b); [c] MDEQ (2011c); [d] MiGDL (2011)

Table 2: Michigan Sedimentary Basin Hydrostratigraphic Units Summary

Hydrogeologic Unit	Basin: Thickness (m)	Ottawa Co.: Thickness (m)	Group/Formation[a]	USGS Hydrogeologic Unit[b]
Quaternary	0 - 338	10 - 125	Glacial Drift	Quaternary
Jurassic	0 - 59	absent	Ionia Fm	Jurassic
Upper Pennsly.	0 - 183	absent	Grand River Fm	Upper Pennsly.
Lower Pennsylvanian	0 - 161	absent	Saginaw Fm	Lower Pennsylvanian
			Parma Ss	
			Bayport Fm	
Michigan	0 -219	0 - 77	Michigan Fm	Michigan
Marshall	0 - 150	0 - 88	Marshall Ss	Marshall
Devonian-Mississippian	0 - 623	320 - 445	Coldwater Sh	Devonian-Mississippian
			Sunbury Sh	
			Ellsworth Sh	
			Antrim Sh	
Traverse-Dundee	6 – 942	206 - 325	Squaw Bay Ls	Silurian-Devonian
			Traverse Gr	
			Dundee Ls	
			Detroit River Gr	
Silurian-Devonian	46 - 1475	242 – 614	Bois Blanc Fm	Silurian-Devonian
			Garden Island Fm	
			Bass Islands Gr	
			Salina Gr	
			Niagara Gr	
			Manistique Gr	
			Burnt Bluff Gr	
			Cataract Gr	
Richmond-Collingwood	38 - 659	95 - 246	Richmond Gr	Maquoketa
			Collingwood Sh	
Trenton-Black River	0 - 534	45 - 284	Trenton Fm	Sinnipee
			Black River Fm	
			Glenwood Fm	St. Peter
St. Peter	0 - 352	2 - 48	St. Peter Fm	
Prairie du Chien	4 - 569	88 - 338	Prairie du Chein Gr	Prairie du Chien-Franconia
			Trempealeau Fm	
			Franconia Fm	
Galesville	4 - 131	26 - 37	Galesville Ss	Ironton/Galesville
Eau Claire	21 - 235	57 - 99	Eau Claire Fm	Eau Claire
Mt. Simon	4 - 390	201 - 253	Mt. Simon Ss	Mt. Simon
			Pre Cambrian Clastics	
			PreCambrian Crystalline Basement	

4.1.3 Geologic Structure

The Michigan Sedimentary Basin is a nearly circular feature centered in the lower peninsula of Michigan (USA). This basin has bowl-shaped sedimentary formations that are deepest near the center of the lower peninsula. Previous geologic studies depict the structure of many of the sedimentary formations (Barnes, et al., 2009; Catacosinos, et al., 1990; Wickstrom, et al., 2005). We created a custom model that adopted the USGS hydrostratigraphic system (Lampe, 2009) for units above the St. Peter Sandstone, and used ESRI Arc-GIS to model the St. Peter Sandstone and deeper units. We chose this hybrid approach after comparing interpolations of formation tops for Ottawa County (based on proximal well records), with the USGS structural model projections. The two models were comparable for units above the St. Peter, but diverged significantly from the St. Peter down. The discrepancies are likely due to the fact that the USGS model includes the entire Lake Michigan hydrogeologic basin, including data from western Wisconsin. The Wisconsin data appears to have exaggerated the thickness of the deeper units in western Michigan. Since the Mt. Simon Sandstone and the St. Peter Sandstone at the base of the sedimentary sequence are the primary targets for CO_2 injection, we decided to interpolate formation tops for the deeper units where the results of the USGS model departed from the results of our Michigan-only approach. We also interpolated the top of the Traverse-Dundee formation because the USGS model did not include this horizon.

Formation structures and thicknesses were interpolated using Geostatistical Analyst in ArcGIS. Elevations of formation tops were obtained from the Michigan Department of Environmental Quality (MI DEQ) "Formation Tops & Elevations database." In cases of apparent inconsistencies, preference was given to data confirmed by multiple methods (for example by the MI geological survey, the company log, and by a sample).

Since the elevations of the tops and bottoms of the formations are stacked on each other and are thus not independent, three-dimensional kriging to interpolate the subsurface formations is the ideal methodology. These algorithms can be expensive and computationally cumbersome, however, and they were not available to us. Other analyses, including the USGS, have used two-dimensional approaches. Consequently we investigated two different 2-D kriging approaches to interpolate unit structure and thickness:

1. *Kriging the top and the bottom surfaces for each formation independently (two-layer method):* Thicknesses are calculated by subtracting the bottom elevations from the top elevations. This method is advantageous because errors in the interpolations of tops and bottoms of a formation are independent and do not additively propagate to deeper formations. If data are sparse or the functional form is overly curvy where the formation is thin, the subtraction might produce negative values. Consequently, this method may be more sensitive to the number of lags and lag distances that are used in the interpolation.

2. *Kriging the thickness for each formation directly:* The thickness of a formation at each data point is calculated and interpolated. This thickness is then subtracted from the elevation of the top of the formation to get the elevation of the bottom of the formation. One disadvantage of this approach is that errors from the shallowest interpolation propagate to deeper formations. This method can produce results with lower root mean square errors (RMSE) for each formation, but it

artificially treats formations as independent of each other. For this approach, we utilized the method that minimized the RMSE and avoided negative thicknesses.

The two-layer method (1) is preferred, because it allows the user to krig the formation tops and bottoms as they depend on each other and on other formations in the stratigraphic column. For example, the number of lags and lag distances in the interpolation can be chosen to represent a trend through the stratigraphic column. Top- and bottom-kriging (1) was used where there were sufficient control points and the results did not produce negative thicknesses. Thickness-kriging (2) was used as necessary.

For each interpolation, the dataset was checked for a trend and if present, the best trend was fitted and removed from the data. Experimental variograms were calculated and variogram models were fitted. Variograms were calculated by changing lag size and lag distance. A spherical fit was used for all formations. The best variogram with the lowest RMSE was chosen for the final kriging model, summarized in Table 3. Section 4.3.2 describes the procedures and parameters used for each formation.

Table 3: Formation Modeling Parameters

Formation	Type of Kriging	Trend	Lag Size	Lag Number	Nugget	Partial Sill	RMSE
Surface	kriging	Obtained from USGS					
Quaternary	kriging						
Jurrasic	kriging						
Upper Pennslyvanian	kriging						
Lower Pennsylvanian	kriging						
Michigan	kriging						
Marshall	kriging						
Devonian Mississippian	kriging						
Bottom of Travers-Dundee	Local Polynominal	NA	NA	NA	NA	NA	101
Silurian-Devonian	kriging	Obtained from USGS					
Richmond	kriging						
Trenton-Black River	kriging						
Top of St. Peter	Ordinary Kriging	Second	109220	12	0	202104.5	194
Top of Prairie du Chien	Ordinary Kriging	Second	115930	12	0	280387.9	201
Top of Galesville	Ordinary Kriging	Second	109220	12	0	1265519	462
Thickness of Galesville	Ordinary Kriging	Second	87340	12	0	1769	57
Thickness of Eau Claire	Ordinary Kriging	NO	117930	12	0	45641.4	121
Thickness of Mt. Simon	Ordinary Kriging	NO	112760	12	0	150245.7	347

Table 2 shows the results of our model for the minimum and maximum thickness of each unit in Ottawa County and in the entire Michigan Basin. Three-dimensional representations in cross-section are shown in Figure 1. Overall, the structure and thickness of formations in our model are consistent with other studies of the Michigan Basin (Barnes, et al., 2009; Catacosinos, et al., 1990; Wickstrom, et al., 2005).

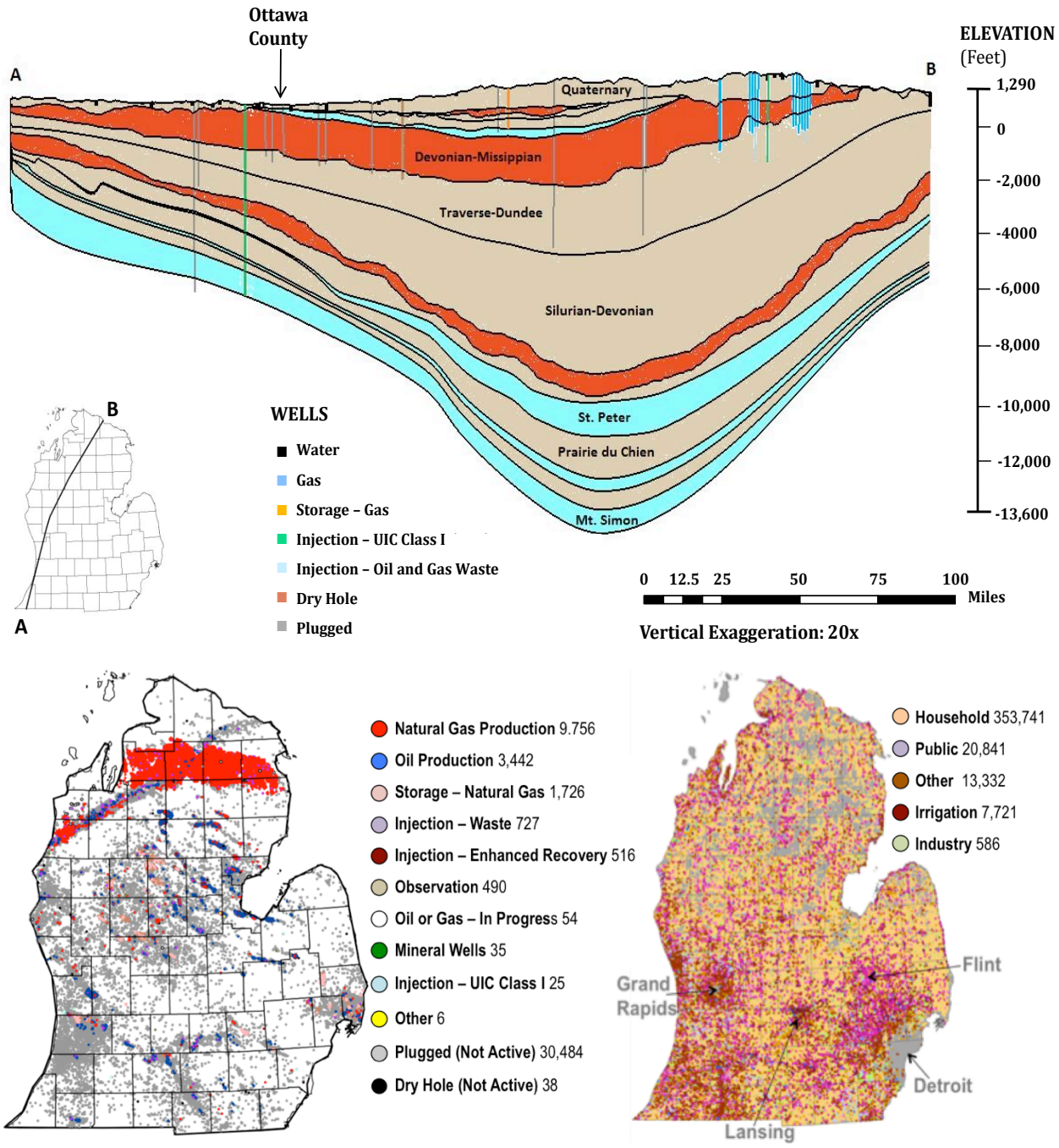

Figure 1: The Michigan Sedimentary Basin in Cross-Section with Active and Inactive Wells Shown

4.2 Subsurface Activities and Leakage Pathways

4.2.1 Active and Inactive Wells for Subsurface Activities Except Groundwater Withdrawals

The database catalogs the location, total depth, and hydrostratigraphic unit associated with wells and boreholes in the Michigan sedimentary basin. Wells and boreholes can have at least two roles in leakage from CO_2 storage reservoirs. First, all active and inactive or plugged wells and boreholes can potentially be pathways for CO_2 or brine leakage. Imperfections in well construction, cementing, or plugging can leave gaps that allow these fluids to leak, and geochemical reactions between water, CO_2, and cement can create or open gaps. Second, active wells locate current subsurface activities. These activities could be impaired if leakage interferes with them.

The Michigan basin presents an interesting case study of potential leakage interference because of the wide variety and significant extent of subsurface activities, including 1) energy production, 2) energy storage, 3) waste disposal, 4) minerals production and 5) water production. Oil and gas production have a long history in Michigan. Oil was discovered in 1886, followed by natural gas in1911. Approximately 60,000 permits have been issued since 1927, when oil and gas permitting began. (Michigan Department of Natural Resources and Environment, 2010). Michigan currently produces 5.9 Mbbl of oil and 272 Bcf of gas per year, which represents 0.3% and 1.3% respectively, of total U.S. production (U.S. EIA, 2010a, 2010b). Development of shale gas plays, such as the established Antrim shale play and the newly discovered Collingwood shale play, could be significant sources of natural gas (Lynch, 2010; NETL, 2009). Michigan has more seasonal natural gas storage capacity than any other state, with 12.5% of the total in the United States, mostly in depleted oil and gas reservoirs (U.S. EIA, 2010c). Waste from manufacturing and from oil and gas production is injected underground under the auspices of the EPA Underground Injection Control Program, and salt and potash are produced using solution mining techniques that circulate fluids deep underground to dissolve the minerals and bring them to the surface. Finally, groundwater supplies 37% of the state's drinking water, and 64% of its irrigation needs (Kenny, et al., 2009).

Table 4 shows the well-type classification for wells in the database that are associated with subsurface activities but not for groundwater withdrawal. This database includes the total number of each well type and the number for which complete data is available (location, depth, formation). For a subset of the data, location is known but not depth and/or formation. In compiling our model database we excluded permitted wells (PW) and terminated permits (TP) because these wells had not been drilled at the time of our construction of the database. Table 5 lists well type and status codes.

Table 4: Wells Associated with Subsurface Activities (not including groundwater withdrawals) in the Michigan Sedimentary Basin

	Well Category	Wells with depth and formation	Description	MI DEQ*/ EPA Well Types
Active	**Gas**	9,756	Active gas and gas condensate wells	GAS; GC
	Oil	3,442	Active oil wells	OIL;
	Oil or gas in progress	54	Oil or gas wells not yet completed	LOC;
	Injection -waste from oil and gas	727	Wells that inject fluids associated with oil and gas production, including: brine, drilling fluids, gas, or CO_2 for enhanced oil production. Classified as UIC Class II	BDW; GBD
	Storage - gas	1,726	Injection and extraction wells associated with underground storage of natural gas	GS; LPG
	Injection- EHR	516	Injection of water, CO_2, or another gas for secondary recovery of oil or gas	WIW; GIW; OTI
	Mineral wells	35	Injection and extraction wells associated with solution mining, permitted either as EPA UIC class III wells, or under Michigan's part 625 permit system	M; MNB; UIC Class III
	Injection -waste UIC class I	25	Wells that inject hazardous or non-hazardous waste. Permitted as EPA UIC Class I.	UIC Class I
	Observation	490	Observation or monitoring wells	OBS; GSO
	Other	6	All other types of wells or boreholes	OTH, LHL
Inactive	**Plugged**	30,484	Wells or boreholes of any type that have been plugged	Any type with status *PB, PLA or PLC*
	Dry hole	38	Dry holes not recorded as plugged	DH with status not *PB, PLA or PLC*

* MI DEQ database classifies wells and boreholes by both type and status. Our classification combines these factors. Well type abbreviations are noted in capital letters, and well status abbreviations are noted in italics. Active wells are those with any status other than *PB, PLA* or *PLC.* Records of permitted wells (*PW)* and terminated permits *(TP)* are not included in this model, as these wells have not been drilled. MI DEQ key to well types and status is included in the Table 5.

Table 5: Michigan Department of Environmental Quality (MNDEQ) Well Type and Status Codes

Well Type	
BDW	Brine Disposal Well
DH	Dry Hole
GAS	Gas
GBD	Gas & Brine Disposal
GC	Gas Condensate
GIW	Gas Injection Well
GS	Gas Storage
GSO	Gas Storage Observation
LHL	Lost hole
LOC	Location only - not yet completed
LPG	Liquid Petroleum Gas
M	Mineral well (any starting with an "M")
MNB	Mineral Well
OBS	Observation
OIL	Oil
OTH	Other
OTI	Other Injection
WIW	Water Injection Well

Well Status	
ACT	Active
DC	Drilling Complete
PB	Plugged Back
PLA	Plugging Approved (Properly plugged and site restored)
PLC	Plugging Completed (Plugged but site needs restoration and approval)
PR	Producing
PW	Permitted Well - not yet drilled
SI	Shut In
SUS	Suspended
TA	Temporarily Abandoned
TP	Terminated Permit
WC	Well Complete

The distribution of active and inactive wells is shown in Figure 1, along with a basin cross-section showing the subsurface hydrostratigraphy across the state. **Error! Reference source not found.** and 3 detail the incidence of pathways and subsurface activities associated with the modeled hydrostratigraphic units, including just wells for which depth and hydrostratigraphic unit are known.

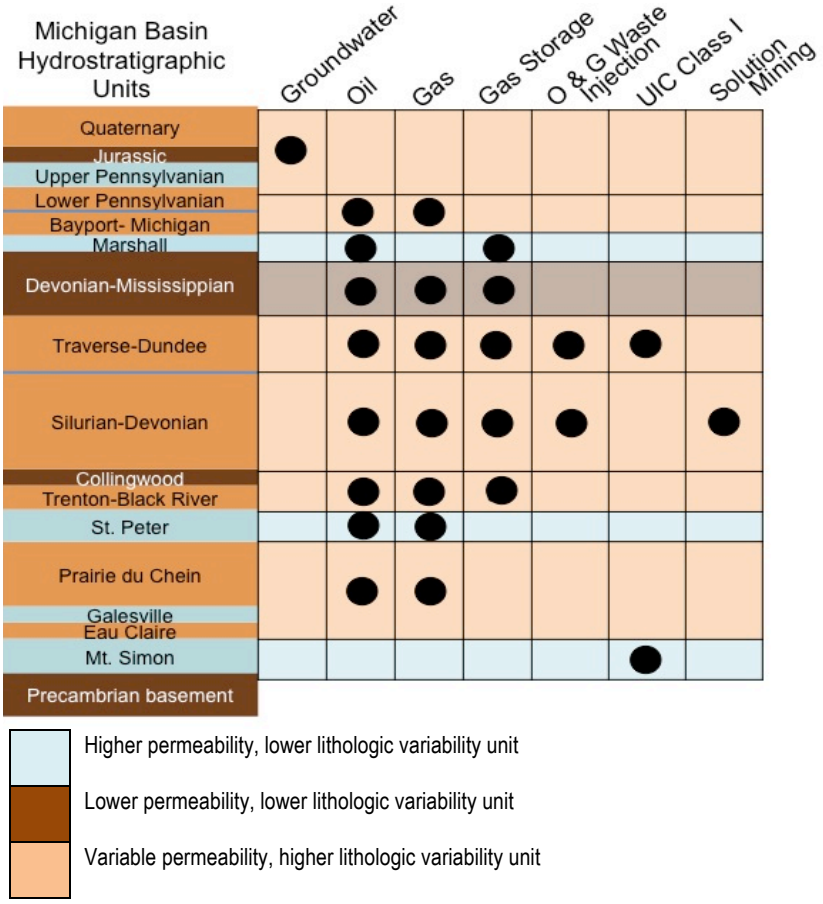

Figure 2: Summary of Subsurface Activities in the Michigan Basin

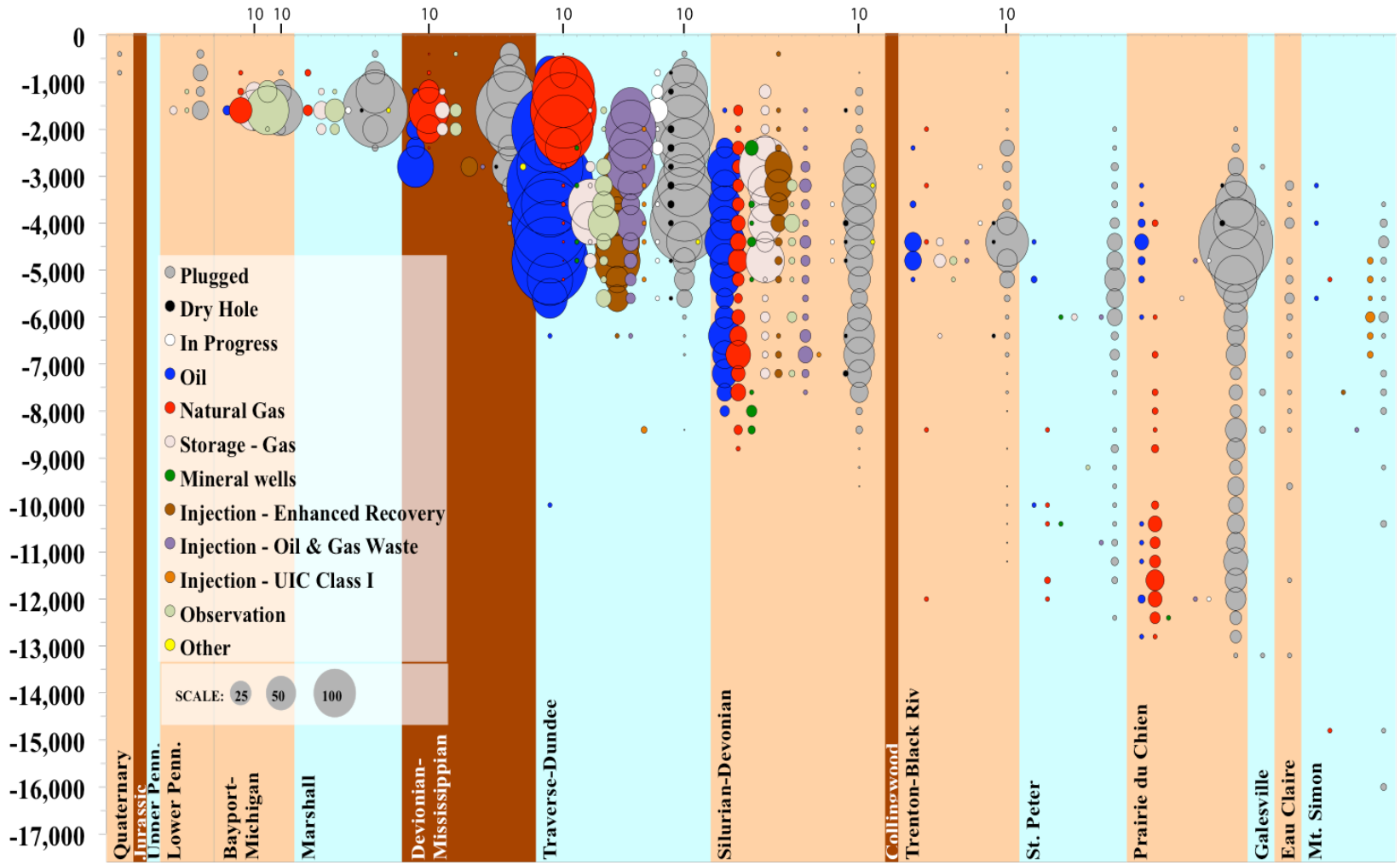

Figure 3: Incidence of Subsurface Activities and Pathways by Geologic Unit

4.2.2 Groundwater Wells

Table 6 shows the numbers and types of water wells in the Michigan basin. This data, from the Michigan Geographic Data Library County water well files, includes all wells drilled since the year 2000. The extent to which earlier wells are included varies by county, and also by well type. Older household wells are probably significantly under-reported. Figure 14 shows water well locations and distribution with depth. Water wells are widespread and generally shallow, with 90% less than 200 feet deep and 99% less than 350 feet deep.

Table 6: Summary of Water Wells in the Michigan Sedimentary Basin

Well Type	# of wells[a]	2005 withdrawals (Mgal/day)[b]	Description
Household	353,741	251	Private residential water supply (largely rural)
Public	20,842	260	Type I, II, or III public water supply
Other	13,332	39	Includes wells for livestock, aquaculture, small businesses, mining, and thermoelectric power cooling
Irrigation	7,721	198	Wells for irrigation
Industry	580	89	Industrial wells

[a]MI geographic data library, county water well files
[b]Kenny et al., 2005

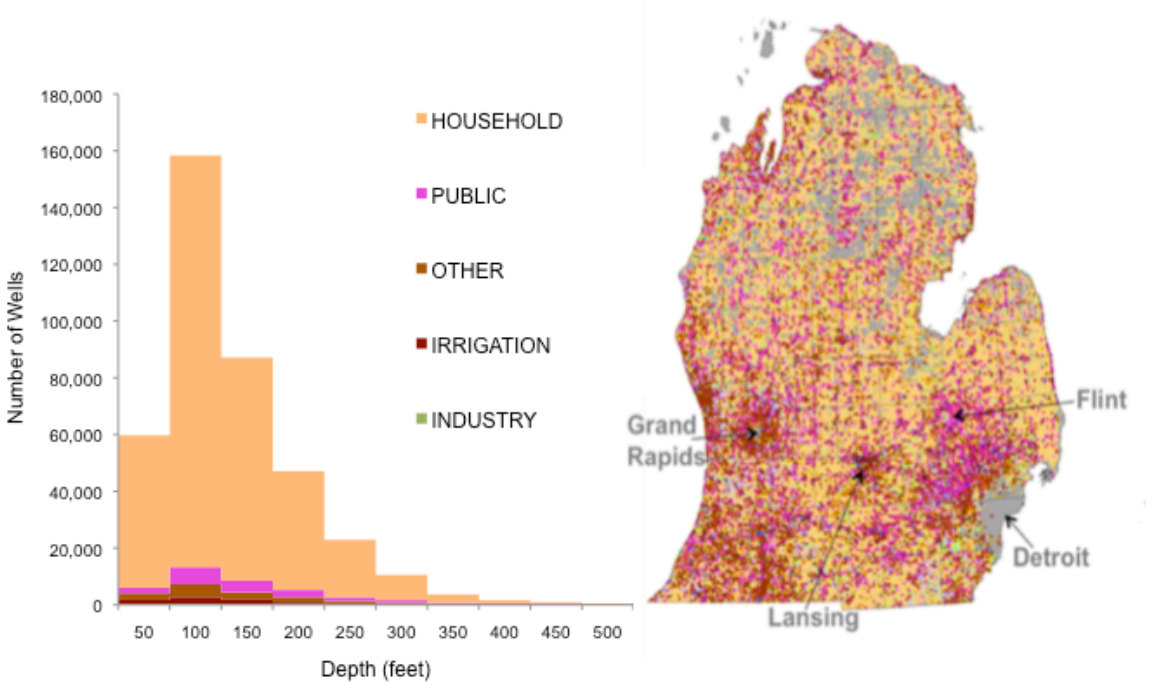

Figure 4: Water Wells: Depths and Locations

4.3 Three-Dimension Construction of Michigan Sedimentary Basin

Section 4.3.1 explains adaptations to the USGS hydrostratigraphic system. Section 4.3.2 describes modeling procedures for each geologic unit.

4.3.1 Adjustments to the USGS Hydrostratigraphic System

We made several minor adaptations to the USGS hydrostratigraphic system:

- Several unit names were changed to reflect current stratigraphic lexicon in Michigan, as defined by Fitch (2000).
- For the subsurface use database, the Bayport limestone is grouped with the Michigan formation, because they host similar subsurface activities at similar depths. The GIS model adopts the USGS formation boundary, which groups the Bayport with the Lower Pennsylvanian units. While this inconsistency is not ideal, it has very little effect on the questions being asked by this study; these units are quite shallow and a great distance above the units targeted for geologic sequestration. Consequently, the effort to model the top of the Bayport was deemed nonessential.
- The Bayport/Michigan Unit is classified as a variable permeability unit rather than a confining unit. There are locations in the state where subsurface activities occur in the Bayport/Michigan unit, indicating at least moderate permeability.
- The USGS classifies the upper portion of the Silurian Devonian unit as an aquifer. We reclassify it as a variable permeability unit, because oil and gas deposits are found at varying depths within

the unit. These deposits indicate that lower permeability horizons are present to trap the buoyant hydrocarbons.

4.3.2 Modeling Procedures

Travers-Dundee Formation: To split the Silurian-Devonian formation, we interpolated the top of Bois Blanc formation as the bottom of Travers-Dundee formation:

1. Wells that have Bios-Blanc top were selected from "The Formation Tops & Elevations database". The elevation for Bios-Blanc Formation was calculated based on the top surface and reference surface for each well.
2. Wells described in Number 1 were imported into ArcGIS.
3. The validity of the data was checked using semivariograms. Bad data[1] were removed.
4. The top surface of Bios-Blanc Formation was kriged using the data in Section 3.
5. Results were converted to points.
6. The top of Bios-Blanc formation was subtracted from the bottom of Devonian-Mississippian formation to get the thickness of Travers-Dundee formation.

NOTE: Various kriging approaches to the interpolations, with different lag sizes and numbers, were used. Some results had negative thicknesses in some portions of the basin or other erroneous results. We found that the Local Polynomial method had the lowest RMSE and no negative thicknesses.

St. Peter Sandstone: The steps of kriging for the top and bottom of St. Peter Formation are as follows:

1. Wells that have a top for the St. Peter formation were selected from "The Formation Tops & Elevations database". The elevation for St. Peter formation was calculated based on the top surface and reference surface for each well.
2. Wells with the top of Prairie du Chien Formation (the bottom of the St. Peter) were selected from "The Formation Tops & Elevations database". The elevation for Prairie du Chien formation was calculated based on the top surface and reference surface for each well.
3. Wells in Numbers 1 and 2 were imported into ArcGIS.
4. Wells in Numbers 1 and 2 were joined and those that have both the top of the St. Peter formation and Prairie du Chien formation were selected.
5. The thickness at each well was calculated and calculations producing negative thicknesses were removed. The semivariogram was used to remove bad data.
6. The top surface for St. Peter sandstone was interpolated using the data in Number 5. In other words, the top surface of St. Peter was interpolated using the wells that both have the top and bottom of the St. Peter.
7. The top surface of Prairie du Chien formation (the bottom of the St. Peter) was interpolated using the data in Number 5.
8. The interpolated surfaces in Numbers 6 and 7 were converted to points using Geostatistical Analyst.

[1] Bad data means one point was not correlated with the surrounding points in its vicinity or one point has more than one data from different method so the bad one was removed.

9. The thickness was calculated by subtracting the top and bottom surfaces. The southern part of Michigan Basin had negative thicknesses. In these regions we assigned the elevation of the top of St. Peter to be the same as the top of Prairie du Chien formation.

NOTE: The thickness of Trenton-Black River formation was checked with the new St. Peter surface. A few places in southwest and north had negative thicknesses, because the USGS data are influenced by Lake Michigan. To compensate, we replaced these data with the average of neighboring points.

Prairie du Chien Formation: The top of the Galesville formation was interpolated in order to calculate the thickness of Prairie du Chien formation.

1. Wells for the top surface of Galesville Formation were selected from "The Formation Tops & Elevations database" database. The elevation of Galesville Formation was calculated based on the top surface and reference surface for each well.
2. Data in Number 1 were imported into ArcGIS.
3. Data were checked using the semivariogram and bad data were removed.
4. The top surface of Galesville formation was kriged using the data in Number 3.
5. The result was converted to points.
6. The top of Prairie du Chien formation was subtracted from the bottom of Prairie du Chien Formation (the top of Galesville) to get the thickness of Prairie du Chien Formation.

Galesville Formation: To calculate the thickness of Galesville Formation, the bottom of Galesville Formation (the top of the Eau Claire Formation) was interpolated.

1. Wells with the bottom surface of Galesville Formation were selected from "The Formation Tops & Elevations database" database. The elevation of Galesville Formation was calculated based on the top surface and reference surface for each well.
2. Wells in Number1 were imported into ArcGIS.
3. Wells that both have the top of Galesville and bottom of Galesville were chosen and the thickness at each wells were calculated.
4. Wells with negative thicknesses were removed from the data and the bad data were also removed using the semivariogram.[2]
5. A "artificial points" were added to the data in Number 4 from USGS dataset.
6. The thickness of Galesville formation (data in Number 5) was interpolated.
7. Data were converted to points.
8. The points in Number 7 were added to the top of Galesville to get the bottom of the Galesville Formation.

Eau Claire Formation: There were not enough wells with data for the top and bottom of Eau Claire formation; we could not use the two-layer method. As a result, we interpolated the thickness of the Eau

[2]Due to the scarcity of controlling points for the bottom of Galesville formation, we interpolated the thickness of the Galesville formation. In addition, artificial points from USGS dataset were added. These artificial points were selected from northeastern and northern parts of Michigan and were not influenced by data for Lake Michigan and Wisconsin.

Claire formation. Some "artificial points" in northern and northeastern part of the Michigan were added from USGS data.

1. The wells for the bottom surface of Eau Claire formation were selected from "The Formation Tops & Elevations database" database. The elevation of Eau Claire formation was calculated based on the top surface and reference surface for each well.
2. Data in Number 1 were imported to ArcGIS.
3. Wells that both have the top and bottom of the Eau Claire formation were selected and the thickness at each wells were calculated.
4. Data with negative thicknesses were removed and the semivariogram was used to remove bad data.
5. A few "artificial points" were added to the data in section 4 from USGS data.
6. The thickness of Eau Claire Formation (data in Number 5) was kriged.
7. Data were converted to points.
8. The points in Number 7 were added to the top of Eau Claire formation to get the bottom of the Eau Claire formation (the top of Mt. Simon).

Mt. Simon Formation: The process used to determine the thickness of the Eau Claire formation was the also used to determine the thickness of the Mt. Simon formation. Control points for the Mt. Simon formation were not dispersed enough throughout Michigan to use the two-layer method. As with the Eau Claire formation, "artificial points" were added from the USGS data.

1. Data for the bottom surface of Mt. Simon Formation were selected from "The Formation Tops & Elevations database" database. The elevation of Mt. Simon formation was calculated based on the top surface and reference surface for each well.
2. Data from Number 1 was imported into ArcGIS.
3. The wells that both have the top Mt. Simon and bottom of Mt. Simon Formation were selected and the thickness at each wells were calculated.
4. Wells with negative thicknesses were removed from the data and bad data were removed using semivariograms.
5. A few "artificial points" from the USGS data were added to the data in Number 4.
6. The thickness of the Mt. Simon formation (data in Number 5) was interpolated.
7. Data were converted to points.
8. The points in Number 7 were added to the top of Mt. Simon formation to get the bottom of the Mt. Simon formation.

4.4 References

Barnes, D. A., Bacon, D. H., and Kelley, S. R. (2009). "Geological Sequestration of Carbon Dioxide in the Cambrian Mount Simon Sandstone: Regional Storage Capacity, Site Characterization, and Large-Scale Injection Feasibility, Michigan Basin." *Environmental Geosciences, 16*(3), 163-183.

Catacosinos, P. A., Daniels, P. A., and Harrison, W. B. (1990). Chapter 30: Structure, Stratigraphy, and Petroleum Geology of the Michigan Basin *Selected Interior Analog Cratonic Basins* (Vol. II): AAPG Special Volumes.

Core Energy (2007). *Class V Underground Injection Control Permit Application: State-Charlton #4-30 CO2 sequestration test well Otsego County Michigan.*

Fitch, H. (2000). *Stratigraphic Nomenclature for Michigan*. MI DEQ and Michigan Basin Geological Society. Retrieved 20 April 2011, from http://www.deq.state.mi.us/documents/deq-gsd-info-geology-Stratigraphic.pdf.

Kenny, J. F., Barber, N. L., Hutson, S. S., Linsey, K. S., Lovelace, J. K., & Maupin, M. A. (2009). *Estimated use of water in the United States in 2005* (No. Circular 1344). U.S. Geological Survey Retrieved 14 April 2011, from http://pubs.usgs.gov/circ/1344/.

Lampe, D. C. (2009). *Hydrogeologic Framework of Bedrock Units and Initial Salinity Distribution for a Simulation of Groundwater Flow for the Lake Michigan Basin* (No. U.S. Geological Survey Scientific Investigations Report 2009-5060). Retrieved 17 March 2010, from http://pubs.usgs.gov/sir/2009/5060/pdf/sir20095060.pdf.

MDEQ (2011a). "Online Oil and Gas Information System Online." Michigan Department of Environmental Quality. Online database available at: http://ww2.deq.state.mi.us/mir/. Last accessed May 17, 2013.

MDEQ (2011b). "Locations - Oil & Gas wells - download database." Michigan Department of Environmental Quality. Online database available at: http://www.michigan.gov/deq/0,1607,7-135-3311_4111_4231-97870--,00.html, last accessed May 17, 2013.

MDEQ (2011c). "Formation Tops and Elevation Database." Online database available at: http://www.michigan.gov/deq/0,4561,7-135-3311_4111_4231-143855--,00.html, last accessed May 17, 2013.

MiGDL (2011). "Drinking Water Wells Geographic Data Theme." Michigan Geographic Data Library. Available at: http://www.mcgi.state.mi.us/mgdl/?rel=thext&action=thmname&cid=2&cat=Drinking+Water+Wells

Wickstrom, L. H., et al., 2005, Characterization of geologic sequestration opportunities in the MRCSP region, phase I task report of performance, October 2003 – September 2005: U.S. Department of Energy Cooperative Agreement No. DE-PS26-05NT42255, 152 p

Chapter 5. Causes and Financial Consequences of Geologic CO_2 Storage Reservoir Leakage and Interference with other Subsurface Resources

This chapter has been published as:

J.M. Bielicki; M.F. Pollak; J.P. Fitts; C.A. Peters, E.J. Wilson. (2014) "Causes and Financial Consequences of Geologic CO_2 Storage Reservoir Leakage and Interference with other Subsurface Resources". *International Journal of Greenhouse Gas Control*. Vol. 20: 272-284.

An earlier version of the LIV method was presented at The 11th International Conference on Greenhouse Gas Technologies in Kyoto, Japan, November 18th–22nd, 2012 (Pollak, M., Bielicki, J., Dammel, J., Wilson, E., Fitts, J., Peters, C., 2013. The leakage impact valuation (LIV) method for leakage from geologic CO_2 storage reservoirs. *Energy Procedia* 37, 2819–2827).

5.1 ABSTRACT

Leakage from geologic carbon dioxide (CO_2) storage reservoirs used in CO_2 capture, utilization, and storage (CCUS) technologies could trigger costs to a variety of stakeholders, including operators of other subsurface activities, such as oil and gas recovery and groundwater withdrawal. We identify the drivers of these costs and the resulting financial consequences of leakage. Costs could be incurred even in the absence of legal action or if the leakage does not affect other subsurface activities, groundwater resources, or reach the surface. In a case study of leakage potential for CO_2 injection in the Michigan Sedimentary Basin, we find that the majority of leakage costs arise from activities to "Find and Fix a Leak" and from "Injection Interruption". We also found that these costs will be influenced by regulator decisions specific to a leakage event and depend on the developmental state of the CCUS industry. Estimated costs for an Nth-of-a-Kind (NOAK) project range from $2.2MM for a low-cost event with only leakage to $154.7MM for a high-cost event that reaches the surface. Leakage from First-of-a-Kind (FOAK) projects incurs approximately 1.6–3.0× more costs than equivalent leakage from an Nth-of-a-Kind (NOAK) project

across all of the storylines we develop. Multiple stakeholders will incur leakage costs, and such externalities must be managed lest they impede the development of the CCUS industry.

5.2 Introduction

The accumulation of atmospheric carbon dioxide (CO_2) is altering the climate (IPCC, 2007), and CO_2 capture, utilization, and storage (CCUS) is a technological approach to mitigate the emission of CO_2 from anthropogenic sources (IPCC, 2005; Pacala and Socolow, 2004). With CCUS, geologic reservoirs are the final location for CO_2 in an integrated system that captures CO_2 from large point sources, transports it, and injects it deep into the subsurface where it should remain isolated from the atmosphere. But injected CO_2 will be buoyant in the subsurface and the CO_2 or pressure-driven brine may leak out of the geologic reservoir through natural or manmade pathways. This leakage may migrate from the injection formation through the subsurface, encounter other subsurface activities or sources of groundwater, or reach the surface. Studies of leakage from geologic CO_2 reservoirs typically focus on the physical mechanisms by which leakage may occur (e.g., Ellis et al., 2011; Presig and Prevost, 2011) or migrate (e.g., Nordbotten et al.,2005; Celia and Nordbotten, 2009; Oldenburg et al., 2012), or ways to avoid, manage, or remediate that leakage (Espisito and Benson,2010). Fewer efforts have sought to understand how much leakage may cost (Industrial Economics, 2012), or focused on risk-based information for financial responsibility for the injection operator (Trabucchi et al., 2010) or the technical costs associated with environmental remediation (U.S. EPA, 2001). In addition to operator liability and remediation, leakage could trigger costs for a variety of stakeholders. While the regulatory framework for CCUS in the United States does not allow injected CO_2 to leak into Underground Sources of Drinking Water (USDW, with total dissolved solids <10,000 mg/l), this framework does not manage interference with other subsurface activities like oil and gas production or natural gas storage.[1] Given the many past, current, and future uses of the subsurface, understanding the possibility and scale of the potential financial consequences of CCUS interference with other subsurface activities will be important factor for siting and operating CCUS projects.

In this work, we estimate the possible financial causes and con-sequences of leakage from geologic CO_2 storage reservoirs. This leakage could also interfere with other subsurface resources or be released to the atmosphere. Identifying the economic costs of leakage to injection operators is important to understand the costs in the supply chain (e.g., Al-Juaied and Whitmore, 2009; McCoy, 2008; McCoy and Rubin, 2008; Eccles et al., 2009), evaluate market diffusion (Bistline and Rai, 2010) and model future pathways for energy portfolios (e.g., McFarland and Herzog, 2006). Ultimately, this quantitative information is necessary for injection operators to acquire the insurance needed to develop CO_2 injection projects.

Leakage from geologic CO_2 storage reservoirs, however, will affect a number of stakeholders outside of a classic operations-cost analysis, creating an externality that is borne by other members of society—many of whom are not involved with the industry—arising from a variety of activities initiated by the leakage event. For example, diagnostic monitoring activities such as drilling, equipping monitoring wells, and soil or water surveys are technical costs, but the extent of the requirements for diagnostic monitoring will be a matter of regulatory discretion; consequently, regulator's labor will be necessary to assess the specifics of each leakage case and deter-mine if a leak has been satisfactorily remedied or if the site must close prematurely. Similarly, if CO_2 migrates into a natural gas storage reservoir and increases the CO_2 content of the stored natural gas above maximum pipeline specifications, technical costs will be incurred to install and operate equipment to strip CO_2 from the natural gas. The natural gas storage operator might choose to pursue legal action against the injection operator to recover some of these damages—costs that are

[1] The U.S. Environmental Protection Agency (EPA) has regulatory authority for injection of CO_2into saline formations under the Safe Drinking Water Act. This authority is managed under the Underground Injection Control (UIC) Program andCO_2could be injected under a Class VI injection well, which lays out siting, operational and closure requirements for CO_2injection into saline formations. If a CO_2injection project is linked to an enhanced-oil recovery (EOR) well, these projects would be managed under the UIC Program Class II Enhanced Oil Recovery wells and not be subject to the Class VI framework, but managed under the laws governing injection for EOR.

imposed on the activity operator by the imperfect integrity of the reservoir chosen by the injection operator. Identifying externalities from potential interference—those affected, how, and to what extent—fully accounts for the variety of ways in which leakage may incur costs to different stakeholders.

The financial and operational performance of geologic CO_2 reservoirs is tied in part to the extent of the CO_2 pipeline transportation network. The financial consequences of leakage depend on the maturity of CCUS and the availability of a transportation and injection infrastructure. Early in the development of the CCUS industry, it is likely that geologic CO_2 reservoirs will receive CO_2 by a pipeline directly from a CO_2 source. In the event of a detected leak, CO_2 injection may be temporarily interrupted or permanently halted if a reservoir is deemed unsuitable for storage. As a consequence, for First-of-a-Kind (FOAK) projects, options to dispose of the CO_2 will be minimal and venting CO_2 to the atmosphere maybe the only option. In this case, the injection operator will likely violate terms of the contract to receive CO_2, and the geologic CO_2 site will become a source of CO_2 emissions. At later stages of CCUS development, when the CO_2 pipeline system is more extensive and integrates multiple reservoirs (Middleton and Bielicki, 2009; Kubyet al., 2011; Middleton et al., 2012), CO_2 destined for a leaking reservoir could be routed to another injection site. Costs incurred by not being able to dispose of CO_2 in the intended geologic reservoir could be reduced or avoided, even if a different company operates the new injection site. Financial exposure to leakage will be shaped by infrastructure-dependent costs, and other costs arising from technical, legal, and regulatory drivers.

We present the Leakage Impact Valuation (LIV) method to investigate the drivers of costs incurred by leakage from geologic CO_2 storage reservoirs, and the financial consequences of this leakage and interference, LIV is applied to a case study of CO_2 injection into the Mt. Simon Sandstone in the Michigan Sedimentary Basin. The following section introduces the LIV methodology and our Michigan Sedimentary Basin case study. Results are presented in Section 3. A discussion follows in Section 4, and Section 5 provides a brief conclusion.

5.3 The Leakage Impact Valuation (LIV) method

The Leakage Impact Valuation (LIV) method was developed to estimate the financial consequences of leakage from geologic CO_2 storage reservoirs; LIV is a systematic approach that uses transparent and internally consistent low- and high-cost storylines for potential outcomes of leakage, identifies the broad array of stake-holders who may be affected by that leakage, and estimates the numerous costs these stakeholders may incur (Fig. 1). In so doing, LIV identifies the physical, infrastructural, institutional, and regulatory mechanisms by which costs may be incurred. An earlier description of the LIV method appears in Pollak et al. (2013); here we explain the approach in more detail. In the description that follows, we use the term “storyline” rather than “scenario” to emphasize that the cost estimates arise from narratives that are developed for low- and high-cost results of leakage; “scenario” is reserved for quantifiable properties, such as the permeability by which a pathway leaks. We also use the term “outcome” to identify the result of leakage, in broad terms (e.g., leakage contaminates groundwater).

The LIV method assumes that Injection Operator is responsibly meeting state and federal regulations and the requirements for EPA UIC Class VI wells for CO_2 injection (U.S. EPA, 2010a). This cost-estimating process is driven by transparent and internally consistent storylines that are developed from leakage outcomes and the stakeholders in order to assess the full extent of the impact of leakage. For each outcome, narratives are developed for low- and high-cost situations and the mechanisms by which the stakeholders are affected by the leakage, and focus on the possible ways in which leakage may evolve, affect the subsurface and other activities, groundwater, the surface, and the stakeholders involved. These storylines are not end points; they are reasonable descriptions of the issues that may occur near the lower and upper ends of the scale of leakage.

The LIV method relies on storylines because such an approach avoids suggesting that there is more a priori information about the combined natural and manmade system than is possible to know. Probabilistic cost-estimations may appear to be more straightforward than those based on storylines, but probabilistic approaches must address the likelihood that costs are unlikely to be independent. Further, because many of the probabilities are likely to be contingent, it is difficult to acquire reliable data on the distributions and extents of leakage outcomes without geophysical modeling. This modeling is beyond the scope of this paper, but the LIV method is designed to be incorporated into modeling frameworks that include site-specific geophysical modeling.

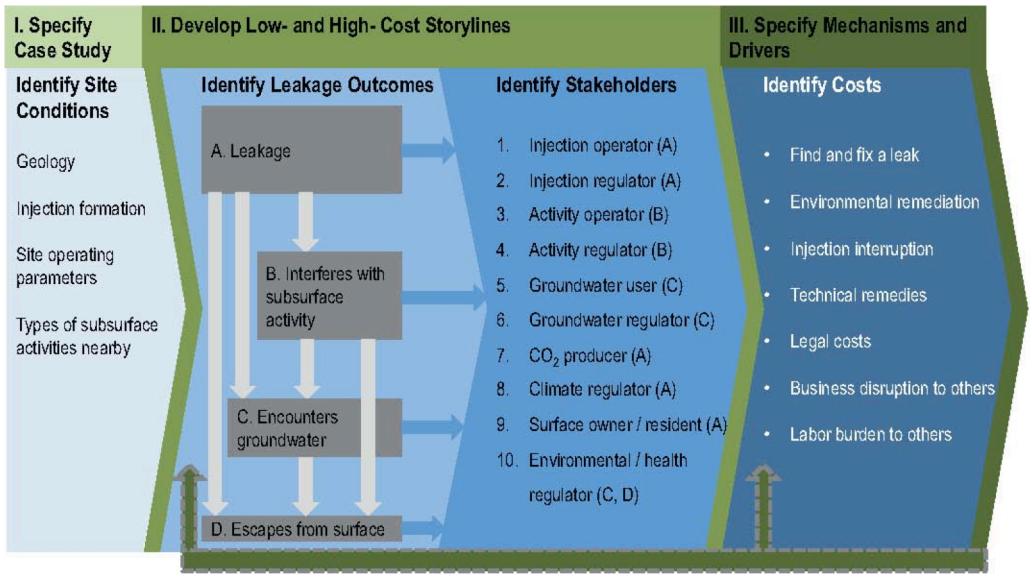

Fig. 1. Summary of the thorough process and feedbacks in the Leakage Impact Valuation (LIV) method. (For interpretation of the references to color in the text, the reader isreferred to the web version of the article.)

The LIV method begins by identifying a CO_2 storage site and its operating characteristics, the features of the geology and of the leakage event, and the presence of other nearby activities that could be encountered by leakage. These items determine the ways in which leakage may occur, how that leakage may propagate through the subsurface, and how costs may be incurred by the physical characteristics the site and the leakage event.

After the site has been assessed, the next step in the LIV method involves the four categories of leakage outcomes that are listed in Fig. 1. These outcomes identify what can happen as a result of leakage, and the potential combinations of these outcomes (e.g., leakage that encounters a subsurface activity and reaches groundwater) shown by the light gray arrows result in a collectively exhaustive list of potential outcomes of leakage.

The blue arrows emanating from each individual outcome indicate pathways to then consider which stakeholders may directly incur costs due to a leakage event. This list enumerates the variety of stakeholders who could incur costs as a result of leakage, and the storylines describe the ways in which these costs could be incurred as a result of the outcomes. Since the LIV method focuses on those stakeholders that may incur costs directly as the result of leakage, other stakeholders that have a secondary involvement, such as insurers, are not included in the assessment. For example, detailing the amount of costs that could be recovered by insurance claims is outside the scope of valuing the impacts of leakage. Table 1 details ten different stakeholder groups may incur economic costs from the leakage of CO_2 or brine from geologic CO_2 storage reservoirs. These stakeholder groups have financial exposure to leakage from a variety of drivers and mechanisms, and Table 1 presents example costs that these

stakeholders may incur as a result of leakage.

In Fig. 1, the letters after each stakeholder indicate that stakeholder's possible exposure to the leakage outcome corresponding to that letter. Injection Operators, for example, incur costs any time leakage (A) occurs. Since all other potential outcomes follow from leakage, the Injection Operator may incur costs regardless of what combinations of outcomes follow from the leakage event (A). In contrast, Activity Operators will incur costs when leakage interferes with their subsurface activity (Outcome B), such as natural gas production. If leakage interferes with a subsurface activity (B) and escapes from the surface (Outcome D), only those stakeholders that have exposure as a result of Outcome C, leakage that encounters groundwater, will not incur costs: Groundwater Users and Groundwater Regulators.

Table 1. Stakeholder groups and example cost exposure identified by the Leakage Impact Valuation method (as presented in Pollak et al., 2013).

Stakeholders	Example of potential costs
CO_2 injection operator	Expenses for diagnostic monitoring, containment activities, and environmental remediation. Legal expenses to defend against lawsuits and negotiate settlements.
CO_2 injection regulator	Regulatory oversight of leakage related activities.
Subsurface activity operator	Expenses for technical remedies if a subsurface activity is affected by leakage. Legal expenses to seek compensation from the CO_2 injection operator.
Subsurface activity regulator	Regulatory oversight if leakage affects regulated subsurface activity.
Groundwater user	Time and trouble dealing with alternate water source if groundwater is contaminated by leakage. Expenses for alternate water as well.
Groundwater regulator	Regulatory oversight is leakage affects groundwater.
CO_2 producer	Labor burden involved with redirecting CO_2 to an alternate geologic storage site if CO_2 injection must be interrupted due to leakage.
CO_2 regulator	Regulatory oversight if leakage complicates emissions reporting.
Surface owner/resident	Time and trouble to stay abreast of the leakage situation. Time spent on arrangements for new monitoring wells or containment activities.
Environmental/health regulator	Regulatory oversight if leakage affects ecosystems. Legal expenses to force environmental remediation.

Including the complete list of leakage outcomes, a full array of stakeholders that may directly incur costs from leakage events, and a thorough exploration of the means by which financial expo-sure is incurred is necessary in order to understand the potential effect of technical, economic, and social issues pertaining to leakage. These issues will influence CCS deployment at multiple scales: at the injection location, in the community proximal to that injection location, and in to the incorporation of CCS into the broader energy system.

The last phase of the LIV method, as indicated in Fig. 1, involves assessing costs over multiple categories. These categories assure a thorough exploration of the mechanisms that may lead to costs for all of the stakeholders who are directly exposed to the financial consequences of leakage. Examples of this broader array of costs include the expenditures for activities that would not occur without leakage, and time and labor that might be required for these activities. The seven cost categories emphasize their drivers and externalities, and are explained in Section 2.3.

Fig. 1 shows the two feedbacks within the LIV process. The first feedback indicates the reflective nature of estimating costs over the categories to assure that this estimating process thoroughly includes the mechanisms that may affect all stakeholders with financial exposure to leakage. The second feedback cycles back to the outcomes and the initial development of the storylines. This feedback indicates that what is learned by the identification of the stakeholders that are exposed to costs and the mechanisms underlying these costs and exposure is considered in the storyline development. This consideration may lead to revisions of the storylines to assure internal consistency and the identification of the multiple ways in which numerous stakeholders may incur costs from leakage.

We capitalize the costs incurred by these stakeholder groups for the storylines we have developed for our application in the Michigan Sedimentary Basin. The following sections present the storylines, the cost categories, and the causes of the costs in these categories. Estimating the economic costs triggered by leakage from geologic CO_2 storage reservoirs requires that the storylines be based on the specifics of the case study. As a consequence, the descriptions below refer to our case study in the Michigan Sedimentary Basin, which we introduce prior to describing the storylines and cost categories.

5.3.1 Case study: Michigan Sedimentary Basin

The Michigan Sedimentary Basin has been extensively developed (Fig. 2). Approximately 450,000 wells penetrate the subsurface, 400,000 of which (not show in Fig. 2) are shallow and provide groundwater for drinking (37% of demand), irrigation (64%of demand), and industrial uses (Kenny et al., 2009). Roughly 48,000 wells are permitted for activities other than water production, and about one-third of these wells are active: for oil and gas production, natural gas storage, waste injection, and solution mining to produce salt and potash. In 2009, 5.9Mbbl of oil and 272 BSCSF of natural gas—0.3% and 1.3% of the United States total, respectively—was produced from the basin (U.S. EIA, 2010a,b). Shale gas plays, in the Antrim and Collingwood formations, could also be major sources of natural gas in the future (Lynch, 2010; NETL, 2009b). Michigan has 12.5% of the seasonal natural gas storage capacity, mostly in depleted oil and gas reservoirs, the most of any state in the United States (U.S. EIA, 2010c). Waste from industrial processes (e.g., pickle solution from metal surface treatments) and from oil and gas production is also injected into the subsurface under the auspices of the U.S. Environmental Protection Agency (EPA) Underground Injection Control (UIC) Program. The basin may store up to 15 GtCO2 (NETL,2010), almost 200x the 76 MtCO2 emitted from Michigan's power sector in 2007 (U.S. EPA, 2012). The majority of this storage capacity is located in the Mt. Simon and St. Peter aquifers (NETL, 2010).

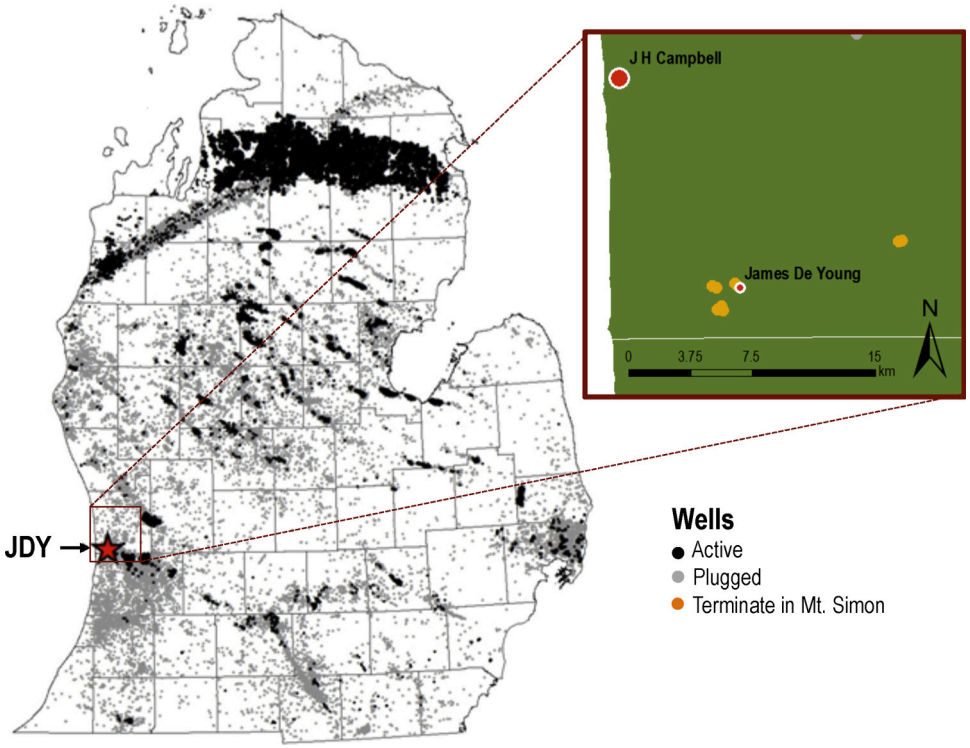

Fig. 2. The Michigan Sedimentary Basin and the James De Young (JDY) case study location.

These wells and activities are present amidst the sixteen hydrostratigraphic units that comprise the Michigan Sedimentary Basin (Table 2). To estimate the characteristics of CO_2 injection, migration, and leakage in the basin, we use a model that estimates leakage semi-analytically (ELSA) (Nordbotten et al., 2005; Celia and Nordbotten, 2009) to simulate injection beneath the James De Young (JDY) power plant in Ottawa County in western Michigan (Fig. 2). This model requires that CO_2 injection be modeled in an aquifer-aquitard sequence, which we construct based on the permeabilities of the hydrostratigraphic units and presence of sub-surface activities within these units (Table 2).

Our ELSA simulation injects 9.5 MtCO2/yr, into the Mt. Simon sandstone. This CO_2 is captured from JDY and the J.H. Campbell power plants (0.6 and 8.9 MtCO2/yr, respectively, assuming an 85% capacity factor and 90% capture efficiency). The JDY injection location is chosen because the properties of the Mt. Simon make it amenable for CO_2 storage. The primary confining unit (Eau Claire) is thick with significant lateral continuity, and multiple secondary confining units are present (Prairie du Chien, Richmond-Collingswood). Moreover, the area is seismically stable. In addition, the case study assumes significant transverse faults or fractures would be detected during pre-siting seismic surveys and appropriate preventative measures would be undertaken to not site an injection well in proximity. The JDY location is also within 1.8 km of eight UIC Class I wells (Fig. 2), which when modeled as leakage pathways, provide an upper bound on the potential for CO_2 to escape from the Mt. Simon.

Table 2. Geologic sequence and ELSA representation in the Michigan Sedimentary Basin underlying the James De Young power plant in Ottawa County.

Hydrostratigraphic Unit	Depth to Top (m)	ELSA Sequence
Quatternary	0	
Jurassic	Absent	
Upper Pennsylvanian	Absent	
Lower Pennsylvanian	Absent	
Bayport-Michigan	Absent	
Marshall	Absent	Aquifer
Devonian-Mississippian	65	Aquitard
Traverse-Dundee	426	
Silurian-Devonian	647	Aquifer
Richmond-Collingwood	904	Aquitard
Trenton-Black River	1,052	
St. Peter	1,222	Aquifer
Prairie du Chien	1,236	Aquitard
Galesville	1,480	Aquifer
Eau Claire	1,511	Aquitard
Mt. Simon	1,604	Aquifer
PreCambrian Basement	1,853	
Permeability	Low	Mixed / High

5.3.2 Leakage storylines

We developed six potential leakage outcomes, three of which arise from interaction with subsurface activities, and base our storylines on those presented in Pollak et al. (2013). The elements of the storylines were developed from risk assessments for geologic CO_2 storage (U.S. DOE, 2007; Walke et al., 2011; U.S. EPA,2008; Oldenburg, 2005; Yamaguchi et al., 2011; Duncan et al.,2009; Hnottavange-Telleen et al., 2009), consequences of leakage (Keating et al., 2011; Siirila et al., 2012), lay and expert opinion of leakage risk (Mander et al., 2011), modeling of CO_2 injection and leakage for the case study in the Michigan Sedimentary Basin, and input from local experts, oil and gas engineers, academics, attorneys, and other environmental professionals who are knowledgeable about the Michigan Sedimentary Basin. The low-cost storylines are based on leakage through a well-defined pathway, in our case a well neighboring the CO_2 injection well. The high-cost storylines are based on leakage due to geologic factors (e.g., faults, fractures), which were poorly defined or hydraulically re-activated by the CO_2 injection process. These storylines are plausible but not exhaustive, and we summarize a few major points for our storylines below. (Full storyline details are provided in Table 3):

Table 3. Summary storylines for the leakage outcomes (from Pollak et al., 2013).

Leakage outcome	Cost storyline	Storyline summary
Leakage only	Low	Leakage is detected when the plume is small. | Leakage is contained below formations in which other subsurface activities are present. | CO_2 injection is halted for five days while the leaky well is reworked.
	High	Leakage is detected when the plume is large. | Neither subsurface activities nor the lowermost USDW are affected. | An accumulation of CO_2 above the caprock is detected and extracted. | A nearby natural gas storage operator files suit claiming decreased injectivity, but the suit is dismissed. | CO_2 injection is halted for nine months while a pressure management system is installed.
Interference with subsurface activities		
Natural gas production and storage	Low	A small amount of CO_2 migrates into a natural gas storage reservoir causing minor damage to fittings and tubing. The CO_2 content in the resulting mixture is below pipeline standards of 2%. | The natural gas storage facility misses one month of operation while damages are repaired and sues the geologic CO_2 storage operator for the costs of damages and business interruption. | CO_2 injection is halted for five days while leaky well is reworked.
	High	The CO_2 content of produced natural gas in a nearby natural gas storage operation increases. | Unable to meet pipeline requirements, the natural gas storage operator misses one heating season while an amine separation facility is installed to reduce the CO_2 content in the stored produced natural gas below pipeline standards. The natural gas storage operator sues the geologic CO_2 storage operator for damages and business interruption. | CO_2 injection is halted for nine months while a pressure managements system is installed.
Oil production	Low	Leakage causes a temporary pressure increase in the oil bearing formation, inducing increased oil production. The oil production operator takes no action against geologic CO_2 storage operator. | CO_2 injection is halted for five days while the leaking well is reworked.
	High	A nearby oil production operator finds elevated CO_2 in the produced oil and detects damage in fittings and downhole tubing. | The remaining value of the oil reserves is worth less than the cost of technical remedies to resume production. The oil production operator sues the geologic CO_2 for the value of the remaining reserves. | CO_2 injection is halted for nine months while pressure management system is installed.
Waste injection[2]	Low	A nearby waste injection operator experiences decreased injectivity due to increased formation pressure, but projects that capacity and rates will be adequate for the expected life of the operation. | Legal action results in a settlement for the value of the lost injection capacity. | Injection is halted for five days while a leaking well is reworked.
	High	Increased formation pressure renders an existing waste injection well unable to inject the required volume of fluid. | An additional waste injection well is installed, and the waste injection operator sues the geologic CO_2 storage operator for damages and business interruption. | CO_2 injection is halted for nine months while a pressure management system is installed.
Affects groundwater	Low	A small amount of CO_2 migrates into a deep formation that has a total dissolved solids (TDS) level of ~9000 ppm. This unit is technically a USDW, but the state has abundant water resources and there are no foreseeable uses for water from this unit. | U.S. Environmental Protection Agency (EPA) Underground Injection Control (UIC) regulators require that two monitoring wells be drilled into the affected USDW and three monitoring wells be drilled into the lowermost potable aquifer (TDS <1000 ppm) to verify the extent of impacts from the leak. No legal action is taken. | Injection is halted from the time the leak is discovered until monitoring confirms that containment is effective (nine months). The UIC regulator determines that no additional remedial actions are necessary.
	High	A community water system reports elevated levels of arsenic. Monitoring suggests that native arsenic may have been mobilized by pH changes from the presence of CO_2 in the aquifer. | A new water supply well is installed to serve the community, and the former water supply wells are plugged and capped. Potable water is provided to the affected households during the six months it takes for the new wells to be installed | Groundwater regulators sue the geologic storage operator to force remediation ofvaffected USDW using pump and treat technology | UIC regulators require remedial action to remove, through a CO_2 extraction well, an accumulation of CO_2 accumulation that has the potential to affect drinking water. | A nearby natural gas producer files suit alleging that leakage has damaged his natural gas reservoir. The suit is dismissed, but both parties incur significant legal expenses. | CO_2 injection is halted for a year.
Reaches surface	Low	A leaking well provides a pathway whereby CO_2 discharges directly to the atmosphere. Neither CO_2 nor brine leaks into subsurface formations outside the injection formation in significant quantities. | The leaking well is promptly plugged, and CO_2 injection is halted for five days.
	High	This storyline includes the high-cost storyline where groundwater. In addition, a hyperspectral survey completed during the diagnostic monitoring program identifies surface leakage in a sparsely populated area. | Elevated CO_2 levels are detected by a soil gas survey and by indoor air quality sampling in the basements of several residences. Affected residents are housed in a local hotel for several nights while venting systems are installed in their basements. | A soil venting system is installed. | CO_2 injection is halted for a year.

[2] Applicable to injection of hazardous waste, non-hazardous waste, or produced fluids.

• *Remediation*—Containment activities for all low-cost storylines include fixing the leaking well through re-entry and any necessary actions (e.g., pump and treat, perforate and re-seal). All high-cost storylines include installing a pressure management system (brine extraction and re-injection wells) in addition to relocating CO_2 injection wells that are near the poorly defined leakage pathway. High-cost storylines assume leak-age is large enough to require remediation of the subsurface environment.

• *Human Harm*—We did not include cost estimates for human harm in either low- or high-cost storylines because extrapolations of our simulations of CO_2 injection, migration, and leakage using the ELSA model (Nordbotten et al., 2005; Celia and Nordbotten, 2009) showed surface releases—even from our extreme probabilistic leakage scenarios—that never amounted to levels known to cause financial impacts from human harm. Probabilistic simulations using ELSA for the most extreme leakage scenarios, whereby every existing well leaks continuously over uninterrupted injection of 9.5 MtCO2/yr for 30 years, estimated leakage rates that release 3.6 t/d at the surface. As Fig. 3 shows, this leakage rate is below natural analogs for surface leakage of CO_2 (Lewicki et al.,2007), and most importantly, is 20× less than the case with the lowest release rate with documented financial impacts associated with human harm. Furthermore, plausible dispersion and mixing scenarios at this leakage rate result in CO_2 concentrations in the ambient air that are below regulatory limits and guide-lines set by the U.S. Center for Disease Control, National Institute for Occupational Safety and Health, and the American Society of Heating, Refrigeration, and Air-Conditioning Engineers (additional information is provided in Chapter 4). Although these results did not justify including costs of human harm in our application of the LIV method, our results cannot be used to rule out the possibility of CO_2 leakage resulting in human harm, as this evaluation is beyond the scope of our ELSA simulations. (See Chapter 4 for more information and results of the ELSA modeling.)

• *Industry Buildout*—We model two possibilities for the state of the CCUS industry: First-of-a-Kind (FOAK) projects and Nth-of-a-Kind (NOAK) projects. These FOAK sites would need to refuse CO_2 delivery or vent CO_2 to the atmosphere if injection must be temporarily or permanently stopped. In contrast, NOAK sites are part of an integrated CO_2 pipeline system that connects multiple geologic CO_2 storage sites. If leakage renders an NOAK project temporarily or permanently unable to inject CO_2, the pipeline system could redirect the CO_2 to another injection site. We assume that the new injection site will accept this extra CO_2 fora modest fee, even if a different operator owns the new injection site.

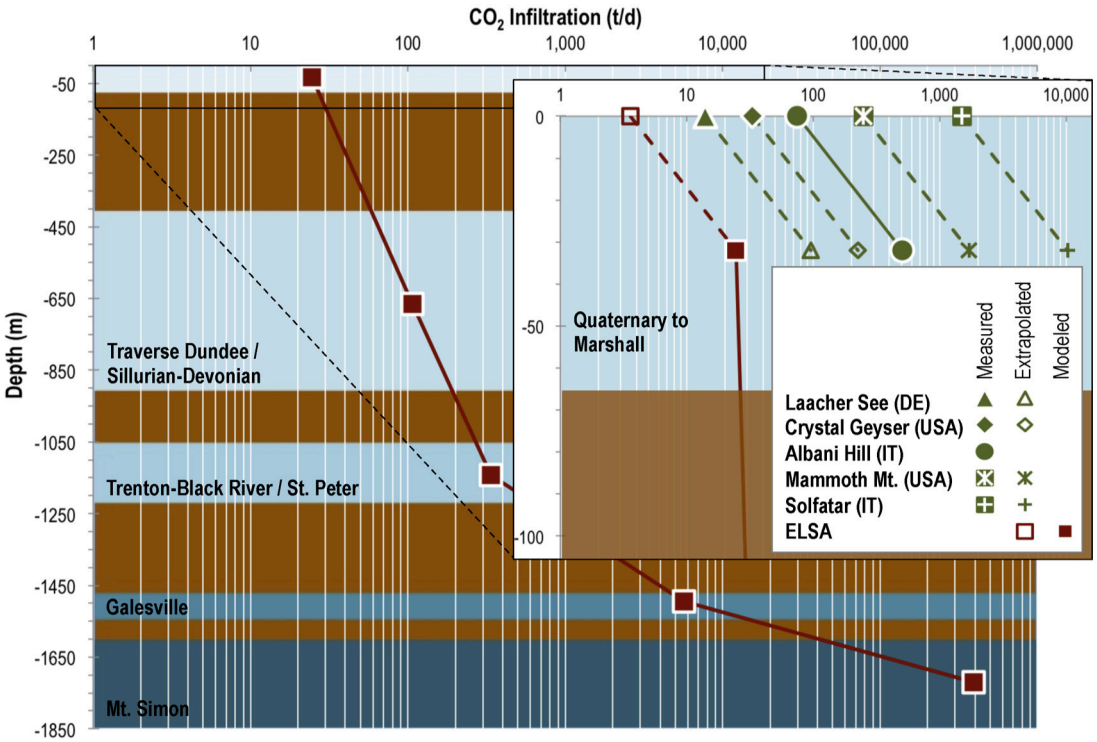

Fig. 3. Infiltration of CO_2 through geologic sequence after 30 years of continuous CO_2 injection and unabated leakage in relation to natural analogs for CO_2 leakage (basedon Lewicki et al., 2007).

5.3.3 Estimating economic costs

The LIV method estimates numerous costs distributed across multiple cost categories. The general methods behind the cost estimations for our storylines are presented below, and full details of the cost algorithms and data sources are available in Chapter 4.

1. ***Find and Fix a Leak***—These costs are based on U.S. Environmental Protection Agency (EPA) estimates that itemize costs for diagnostic monitoring and containment (U.S. EPA, 2010a).

2. ***Environmental Remediation***—These costs are based on EPA estimates that itemize costs for remediation techniques (U.S. EPA ,2001).

3. ***Injection Interruption***—An Injection Regulator could require that CO_2 injection be suspended if a CO_2 storage reservoir leaks. Injection Interruption costs depend on the duration of the suspension and the terms of the contract between the CO_2 Emitter and the CO_2 Injection Operator. The duration of the Injection Interruption depends on the circumstances of the leakage (e.g., the time necessary to find and fix the leak) and on regulatory discretion (the labor burden to the Injection Regulator is included in Category #7). We use values that range from five days (a minimum amount of time to rework a leaking well) to one year. An Injection Operator that cannot inject into a reservoir must refuse delivery and pay a penalty to the CO_2 Emitter, depending on the terms of a "Take or Pay" contract, of either $20/tCO2(FOAK) or $5/tCO2(NOAK). The penalty to the Injection Operator is higher for FOAK projects because of the absence of pipeline infrastructure to reroute CO_2 to other injection locations. The financial exposure for Injection Interruption is shared between the Injection Operator (included in this category) and the CO_2 Emitter (included in Category #7), but weighted toward the Injection

Operator.

This category also includes costs for climate program compensation. We assume that CCUS is occurring because of a policy incentive that imposes costs on facilities that emit CO_2. We assume that this "carbon price" for an FOAK project ($30/tCO2) is less than that of an NOAK project ($50/tCO2), because NOAK projects result from stronger political commitments to CO_2 emissions mitigation that have encouraged the build-out of CCUS infrastructure. Climate Compensation is triggered by surface leakage and venting (consistent with EPA reporting requirements: U.S. EPA, 2010b) and tailored to the specifics of each storyline. We note that the choice of the CO_2 price for an NOAK project is in the range of CO_2 allowance price forecasts for policy scenarios designed to stabilize atmospheric CO_2 levels at under 600 ppm (Nordhaus, 2010) and in the range projected for the cost of capturing CO_2 (Al-Juaied and Whitmore, 2009).

4. ***Technical Remedies for Damages***—The cost of technical remedies is specific to the storyline and based on the itemized costs in U.S. EPA (2001, 2010c). These costs may result from outcomes such as leakage that interferes with subsurface activities or groundwater supply systems or reaches the surface.

5. ***Legal Costs***—We address the components of a typical legal case (e.g., attorney's fees, technical remedies, business interruption costs) in order to estimate damages related to a storyline. This category focuses on the Injection Operator's legal expenses to defend against such suits. Effort by attorneys to bring a claim (Category #7) or defend a claim (this category) is estimated by the time typically required for each stage of litigation, valued at $300/h (LexisNexis, 2011). Costs that might be recovered from the Injection Operator by legal action are included in other cost categories. For example, technical remedies are included in Category #4, and the costs for business disruption are included in Category #6. Stakeholders' additional labor burden involved with damage claims is included in Category #7. We assume a well-managed project and do not consider punitive damages.

6. ***Business Disruption to Others***—These costs are specific to the storyline. An example cost in this category is the value to a natural gas storage operator (Activity Operator) for losing the ability to provide stored natural gas during a heating season. This outcome could occur, for example, if CO2 leakage increases the CO_2 content of stored natural gas above pipeline specifications. The magnitudes of these costs depend on the degree to which leakage infiltrates the stored natural gas and the resulting amount of effort necessary to necessary to mitigate the disruption.

7. ***Labor Burden to Others***—These costs relate to the time necessary for stakeholder groups to address issues associated with leakage, such as the effort by Regulators of all varieties (Injection, Sub-surface Activities, Groundwater, Environment and Health), those bringing legal action, and Surface Residents to stay abreast of the leakage situation.

The LIV method estimates the economic costs of leakage based on storylines that detail the characteristics of the leakage and the outcomes of that leakage. Table 3 shows a summary of the story-lines that were developed for the Michigan Sedimentary Basin.

5.4 Results

Before presenting the results of our application of the LIV method to the case study within the Michigan Basin, we briefly summarize the results of the ELSA simulations of migration and leakage resulting from CO_2 injection. These results inform some of the cost estimation procedures, as described in Section 2.3, and the LIV results presented below. The ELSA predictions of the amount of CO_2 accumulating within each aquifer of the aquifer-aquitard stratigraphic sequence were conducted for an extreme leakage situation at the case study site: (1) continuous 9.5 MtCO2/yr injection for 30 years, (2) every well in the

basin is a potential leakage path-way, (3) no action is taken to mitigate any of the leakage pathways, and (4) eight UIC Class I injection wells—leakage pathways—that penetrate into the Mt. Simon are located within a 5700 feet radius of the CO_2 injection well.

The red squares in Fig. 3 show the average rate of CO_2 accumulating in each aquifer from four hundred probabilistic simulations. (See Chapter 4 for more details on the probabilistic approach.) The CO_2 plume in the Mt. Simon has a radius of approximately 15 km. Our modeling of the extreme leakage scenario estimates 5660 tCO2/d migrating into the Galesville, 339 tCO2/d into the Trenton-Black River/St. Peter, 107 tCO2/d into Traverse Dundee /Sillurian-Devonian, and 24.5 tCO2/d into the unconfined shallow aquifer—including the hydrostratigraphic units from Quaternary to Marshall. Since ELSA does not predict the surface release of CO_2, the inset in Fig. 3 puts this 24.5 t/d leakage rate in the context of some major analogs for natural CO_2 leakage by presenting extrapolations in order to facilitate the comparisons.

Data from natural CO_2 leakage analogs in Lewicki et al. (2007) were used to extrapolate the ELSA results for leakage to the unconfined aquifer into estimates for CO_2 releases to the atmosphere. The major natural analogs for CO_2 leakage include measurements of CO_2 naturally leaking to the atmosphere for Laacher See (DE) (14 tCO2/d), Crystal Geyser (USA) (33 tCO2/d), Albani Hill (IT)(74 tCO2/d), Mammoth Mountain (USA) (250 tCO2/d), and Solfa-tar (IT) (1500 tCO2/d). The Albani Hills (IT) analog also includes measurements for the rate of CO_2 accumulating in the shallow groundwater (506 tCO2/d). Using this ratio from Albani Hills, (74/506) the extrapolated amount of CO_2 reaching the surface for the extreme leakage situation at the case study site is 3.6 tCO2/d. This extrapolated leakage rate is shown by the hollow square marker in the inset of Fig. 3. The solid green markers in the inset correspond to the measured CO_2 leakage rates from the natural analogs. The hollow green markers indicate extrapolations of these measured surface leakage rates to the shallowest aquifer that ELSA can model. In all cases, the extrapolated leakage rates for the natural analogs (extrapolated from the surface to the shallow aquifer) are much greater than those for the ELSA modeling (extrapolated from the shallow aquifer to the surface). This estimated amount of CO_2 to be released from the surface in the extreme leakage scenario is clearly less than leakage rates observed at natural sites with high CO_2 release rates (see Chapter 4 for more details). We further note that such a leakage rate resulting from the extreme leakage scenario that we modeled is minimal compared to documented instances of catastrophic releases, which may be the focus of public concern; for example, 3.6 tCO2/d after 30 years is quite small relative to the eruptive event on one day in August 21, 1986 when approximately 240,000 tCO2was suddenly released from Lake Nyos (Lewicki et al., 2007; Baxter et al., 1989). In addition to the substantial differences in magnitudes and time-lines, the physical mechanisms underlying abrupt releases such as these are quite different from the potential for CO_2 leakage from an engineered and actively managed storage reservoir through greater than 800 m of sedimentary formations.

We determined the cost drivers from the activities triggered by leakage from geologic CO_2 storage reservoirs. Table 3 shows the full results by cost categories and by stakeholder exposure for FOAK projects, and Table 5 shows these results for NOAK projects. In addition to the total costs of leakage, Tables 4 and 5 also include the estimated costs by stakeholder and category as well as the percentage of the total that these costs comprise. These costs and their percentages are shown in order to directly provide the magnitude and the percentage of the financial exposure. In addition, the entries in Tables 4 and 5 that are italicized indicate where the costs differ between FOAK and NOAK projects.

Table 4
Financial consequences of leakage for FOAK projects.

Scenario	Leakage		Interference with gas storage		Interference with groundwater		Migration to surface	
	Low	High	Low	High	Low	High	Low	High
First-of-a-Kind (FOAK) Cost ($MM 2010 USD)	4.8	251.6	7.0	268.0	216.0	340.4	4.9	343.8
Find and Fix a Leak	0.700 (14.8%)	39.530 (15.7%)	0.705 (10.1%)	41.062 (15.3%)	1.040 (0.5%)	39.956 (11.7%)	0.710 (14.4%)	40.401 (11.8%)
Environmental remediation	0.000 (0.0%)	0.763 (0.3%)	0.000 (0.0%)	0.763 (0.3%)	0.000 (0.0%)	12.929 (3.8%)	0.004 (0.1%)	15.184 (4.4%)
Injection interruption	3.904 (82.0%)	210.822 (83.8%)	3.904 (55.7%)	210.822 (78.7%)	214.726 (99.3%)	285.000 (83.7%)	3.904 (79.2%)	285.000 (82.9%)
Technical remedies for damages	0.000 (0.0%)	0.000 (0.0%)	0.500 (7.1%)	7.459 (2.8%)	0.000 (0.0%)	0.438 (0.1%)	0.000 (0.0%)	0.451 (0.1%)
Legal costs	0.001 (0.0%)	0.090 (0.0%)	0.091 (1.3%)	0.735 (0.3%)	0.614 (0.0%)	0.900 (0.3%)	0.007 (0.1%)	1.055 (0.3%)
Business disruption to others	0.000 (0.0%)	0.000 (0.0%)	1.623 (23.1%)	6.490 (2.4%)	0.000 (0.0%)	0.000 (0.0%)	0.000 (0.0%)	0.000 (0.0%)
Labor burden to others	0.154 (3.2%)	0.426 (0.2%)	0.193 (2.7%)	0.654 (0.2%)	0.407 (0.2%)	1.208 (0.4%)	0.307 (6.2%)	1.682 (0.5%)
Injection operator	*3.957 (83.1%)*	*216.023 (85.9%)*	*4.004 (57.1%)*	*217.840 (81.3%)*	*180.024 (83.3%)*	*291.091 (85.5%)*	*3.974 (80.6%)*	*293.918 (85.5%)*
Injection regulator	0.002 (0.1%)	0.005 (0.0%)	0.002 (0.0%)	0.006 (0.0%)	0.010 (0.0%)	0.023 (0.0%)	0.003 (0.1%)	0.029 (0.0%)
Activity operator	0.001 (0.0%)	0.071 (0.0%)	2.206 (31.5%)	14.454 (5.4%)	0.001 (0.0%)	0.071 (0.0%)	0.001 (0.0%)	0.071 (0.0%)
Activity regulator	0.000 (0.0%)	0.000 (0.0%)	0.000 (0.0%)	0.002 (0.0%)	0.000 (0.0%)	0.000 (0.0%)	0.000 (0.0%)	0.000 (0.0%)
Groundwater user	0.000 (0.0%)	0.084 (0.0%)	0.000 (0.0%)	0.084 (0.0%)	0.0083 (0.0%)	0.973 (0.3%)	0.000 (0.0%)	0.973 (0.3%)
Groundwater regulator	0.000 (0.0%)	0.001 (0.0%)	0.000 (0.0%)	0.001 (0.0%)	0.026 (0.0%)	0.159 (0.1%)	0.000 (0.0%)	0.159 (0.1%)
CO_2 emitter	*0.651 (13.7%)*	*35.144 (14.0%)*	*0.651 (9.3%)*	*35.144 (13.1%)*	*35.788 (16.6%)*	*47.506 (14.0%)*	*0.651 (13.2%)*	*47.507 (13.8%)*
Climate regulator	0.000 (0.0%)	0.001 (0.0%)	0.000 (0.0%)	0.001 (0.0%)	0.000 (0.0%)	0.001 (0.0%)	0.000 (0.0%)	0.001 (0.0%)
Surface owner/resident	0.151 (3.2%)	0.303 (0.1%)	0.151 (2.2%)	0.454 (0.2%)	0.304 (0.1%)	0.606 (0.2%)	0.303 (6.1%)	1.091 (0.3%)
Environmental/health regulator	0.000 (0.0%)	0.000 (0.0%)	0.000 (0.0%)	0.000 (0.0%)	0.000 (0.0%)	0.000 (0.0%)	0.000 (0.0%)	0.031 (0.0%)

Table 5
Financial consequences of leakage for NOAK projects.

Scenario	Leakage		Interference with gas storage		Interference with groundwater		Migration to surface	
	Low	High	Low	High	Low	High	Low	High
Nth-of-a-Kind (NOAK) Cost ($MM 2010 USD)	2.2	111.1	4.4	127.4	73.1	150.4	2.3	154.7
Find and Fix a Leak	0.700 (32.6%)	39.530 (35.6%)	0.705 (16.0%)	41.062 (32.2%)	1.040 (1.4%)	39.956 (26.6%)	0.710 (30.5%)	40.401 (26.1%)
Environmental remediation	0.000 (0.0%)	0.763 (0.7%)	0.000 (0.0%)	0.763 (0.6%)	0.000 (0.0%)	12.929 (8.6%)	*0.007 (0.3%)*	*16.134 (10.4%)*
Injection interruption	1.301 (60.3%)	70.274 (3.3%)	1.301 (29.5%)	70.274 (55.1%)	71.575 (97.9%)	95.000 (63.2%)	1.301 (55.8%)	95.000 (61.4%)
Technical remedies for damages	0.000 (0.0%)	0.000 (0.0%)	0.500 (11.3%)	7.459 (5.9%)	0.000 (0.0%)	0.438 (0.3%)	0.000 (0.0%)	0.451 (0.3%)
Legal costs	0.001 (0.1%)	0.090 (0.1%)	0.091 (2.1%)	0.735 (0.6%)	0.614 (0.1%)	0.900 (0.6%)	0.007 (0.3%)	1.055 (0.7%)
Business disruption to others	0.000 (0.0%)	0.000 (0.0%)	1.623 (36.8%)	6.490 (5.1%)	0.000 (0.0%)	0.000 (0.0%)	0.000 (0.0%)	0.000 (0.0%)
Labor burden to others	0.154 (7.1%)	0.426 (0.4%)	0.193 (4.4%)	0.654 (0.5%)	0.407 (0.6%)	1.208 (0.8%)	0.307 (13.2%)	1.682 (1.1%)
Injection operator	*2.005 (92.8%)*	*110.632 (99.6%)*	*2.052 (46.5%)*	*112.429 (88.2%)*	*72.661 (99.4%)*	*148.591 (98.8%)*	*2.024 (86.8%)*	*152.368 (98.5%)*
Injection regulator	0.002 (0.1%)	0.005 (0.0%)	0.002 (0.1%)	0.006 (0.0%)	0.010 (0.0%)	0.023 (0.0%)	0.003 (0.1%)	0.029 (0.0%)
Activity operator	0.001 (0.0%)	0.071 (0.1%)	2.206 (50.0%)	14.454 (11.3%)	0.001 (0.0%)	0.071 (0.1%)	0.001 (0.0%)	0.071 (0.1%)
Activity regulator	0.000 (0.0%)	0.000 (0.0%)	0.000 (0.0%)	0.002 (0.0%)	0.000 (0.0%)	0.000 (0.0%)	0.000 (0.0%)	0.000 (0.0%)
Groundwater user	0.000 (0.0%)	0.084 (0.1%)	0.000 (0.0%)	0.084 (0.1%)	0.082 (0.1%)	0.973 (0.6%)	0.000 (0.0%)	0.973 (0.6%)
Groundwater regulator	0.000 (0.0%)	0.001 (0.0%)	0.000 (0.0%)	0.001 (0.0%)	0.026 (0.0%)	0.159 (0.1%)	0.000 (0.0%)	0.159 (0.1%)
CO_2 emitter	*0.000 (0.0%)*	*0.004 (0.0%)*	*0.000 (0.0%)*	*0.004 (0.0%)*	*0.000 (0.0%)*	*0.004 (0.0%)*	*0.000 (0.0%)*	*0.004 (0.0%)*
Climate regulator	(0.0%)	(0.0%)	(0.0%)	(0.0%)	(0.0%)	(0.0%)	(0.0%)	(0.0%)
Surface owner/resident	0.151 (7.0%)	0.303 (0.3%)	0.151 (3.4%)	0.454 (0.4%)	0.304 (0.4%)	0.606 (0.4%)	0.303 (13.0%)	1.091 (0.7%)
Environmental/health regulator	0.000 (0.0%)	0.000 (0.0%)	0.000 (0.0%)	0.000 (0.0%)	0.000 (0.0%)	0.000 (0.0%)	0.000 (0.0%)	0.031 (0.0%)

The costs triggered by leakage events for a FOAK project vary from approximately $4.8MM for the lo cost storyline for the leak-age only outcome to approximately $343.8MM for the high-cost storyline where leakage migrates to the surface, affects ground-water, and causes ecosystem damages. These numbers decrease to $2.0MM and $155MM, respectively, as the CCUS system is significantly built ou (an NOAK project) primarily because the infrastructure is in place to avoid venting CO_2 by diverting i a reservoir that is not leaking. Leakage impacts for FOAK projects are 1.6–3.0× as costly as NOAK projects.

The costs for outcomes where leakage encounters other sub-surface activities will vary by the type of subsurface activity (e.g. natural gas production or storage). The low-(high-) cost storyline for interferi with natural gas production or storage is $7.0MM ($268.0MM); with oil production the value is moderately lower at $4.8MM ($254.7MM), and with waste injection the low-cost storyline is higher, b the high-cost storyline is slightly smaller at $9.8MM ($256.5MM) for FOAK projects. For an NOAK project, these costs decrease to $4.4MM ($127.4MM), $2.2MM ($114.2MM), and $3.3MM ($116.0M for each of the three possibilities examined, respectively. Costs associated with all other outcomes are within 0.1% of those for natural gas production or storage.

5.4.1 Cost allocation

Costs arising from Finding and Fixing the Leak and Injection Interruption account for most of the cost leakage—at least 93.5% of the costs for an FOAK project and 86.2% for a NOAK project. The only exception is for the low-cost storyline where leakage encounters another subsurface activity, and consequently Business Disruption to Others (the operators of the affected subsurface activity) compris 23.1% (FOAK) or 36.8% (NOAK). Including this cost category with Finding and Fixing a Leak and Injection Interruption increases the total for the three categories to 88.8% (FOAK) or 82.2% (NOAK); over all leakage outcomes, the remaining four cost categories comprise at most 18% of the costs of leakage.

Legal Costs and the Labor Burden to Others are relatively minor contributors to the total cost, but they may be significant from an individual stakeholder's perspective: Legal Costs range from $1200 (Leaka Only, Low-Cost) to $1.1MM (Surface Release, High-Cost) and Labor Burden to Others varies from $154,000 to $1.68MM. These values are insensitive to whether or not the leak occurs in an FOAK or a NOAK project.

Fig. 4 shows the costs incurred by the CO_2 Injection Operator, which comprise between 57.1% and 85 of the total costs of leak-age for a FOAK project, or 46.5% and 99.6% of the total costs of leakage fro an NOAK project, depending on the storyline and the outcome. The columns indicate the results for ar FOAK project, and the black inset lines show the amounts that these costs are reduced for an NOAK project. The y-axis is on a log scale so that costs that are small relative to the maximum are visible. Th presentation format (columns = FOAK, inset lines = NOAK, log scale) is consistent from Figs. 4–6 in order to facilitate easy visual comparison.

Leakage from geologic CO_2 injection can impose significant financial externalities on stakeholders oth than the Injection Operator, from $805,000 to $49.8MM (FOAK), or from $154,000 to$2.4MM (NOA Fig. 5 shows the total costs incurred by all stake-holders except the Injection Operator. The financial impacts on all of the Regulators are combined into one category. The inset black lines show the resulti costs for NOAK projects; only the CO_2 emitters have different costs for FOAK and NOAK projects. C emitters incur a fair amount of FOAK leakage costs (between 9.3% and 16.6%), but their financial exposure is substantially reduced for NOAK projects. For NOAK projects, Subsurface Activity Operat and Surface Owners/Residents are the two stakeholder groups affected the most. Costs to a Subsurface

Activity Operator include Business Interruption, Technical Remedies for Damages, and Legal Costs, whereas costs to Surface Owners stem largely from the value of their time when addressing activities that could be triggered by leakage (e.g., attending a community information meeting, reading mailings to stay informed, arranging access for monitoring activities on their property). These total costs may be significant, despite the modest times assigned to these activities (1–6 h per household overlying the CO_2 plume). For NOAK projects, these stakeholder groups bear at least 71.8% of these externalities in all storylines except for the low-cost storylines where leakage affects groundwater or reaches the surface; herein the primary two stakeholder groups incur a total 36.8% and 49.2%, respectively. For FOAK projects, these same stakeholder groups incur 0.8–78.3% of the costs imposed on other stakeholders over the range of outcomes and associated storylines.

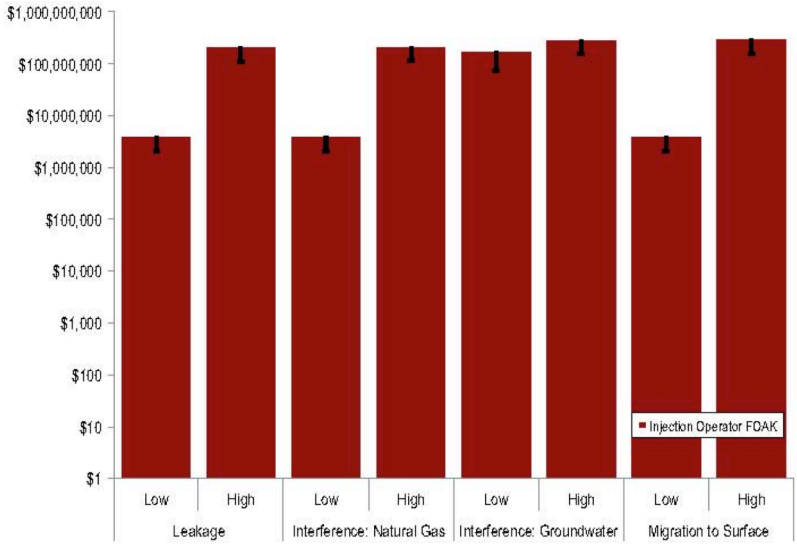

Fig. 4. Financial impacts incurred by CO2injection operators from FOAK projects(columns) to NOAK projects (black inset lines).

As with the Labor Burden to Others and Legal Costs, the costs imposed on Subsurface Activity Operators and Surface Owners/Residents do not depend on whether or not the leaking geologic CO_2 injection project is FOAK or NOAK. Injection Interruption is the only cost category that differs between FOAK and NOAK projects across all storylines (Fig. 6), and Environmental Remediation costs only differ in the outcome where CO_2 migrates to the surface (Tables 4 and 5). In addition, only the costs incurred by Injection Operators and CO_2 Emitters decrease from FOAK to NOAK projects (see Tables 4 and 5 and Figs. 4 and 5). All of these costs are less for an NOAK project than a FOAK project. In fact, costs incurred by CO_2 emitters are close to zero for NOAK projects and arise only from the Labor Burden necessary to manage the switch to an alternate CO_2 injection reservoir.

These distinctions will likely affect the relative social acceptance of FOAK projects compared to NOAK projects. Given limited resources, stakeholders may set aside money in budgets or take insurance against the possibility of reservoir leakage incurring future costs. For example, the Labor Burden to Regulators never exceeds 0.15% of the total leakage cost, but the expenditures may be significant, from $2400 (low-cost, leakage only) to $189,000 (high-cost, leakage reaches surface) and potentially strain tight agency budgets. In contrast, contracts between the Injection Operator and the CO_2 Emitter will likely change if the industry builds out.

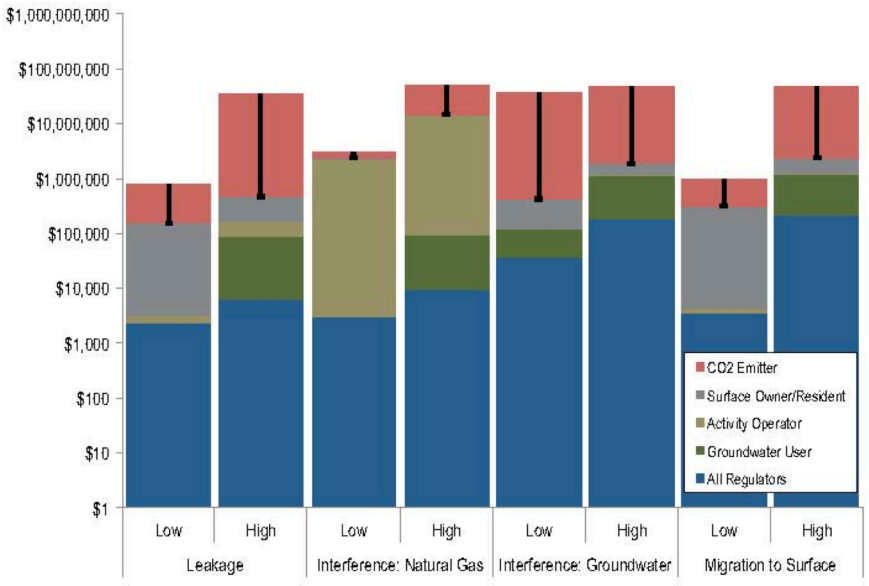

Fig. 5. Financial impacts imposed on others from a leaking geologic CO_2 storage from FOAK projects (columns) to NOAK projects (black inset lines, where only CO_2 emitters incur different costs).

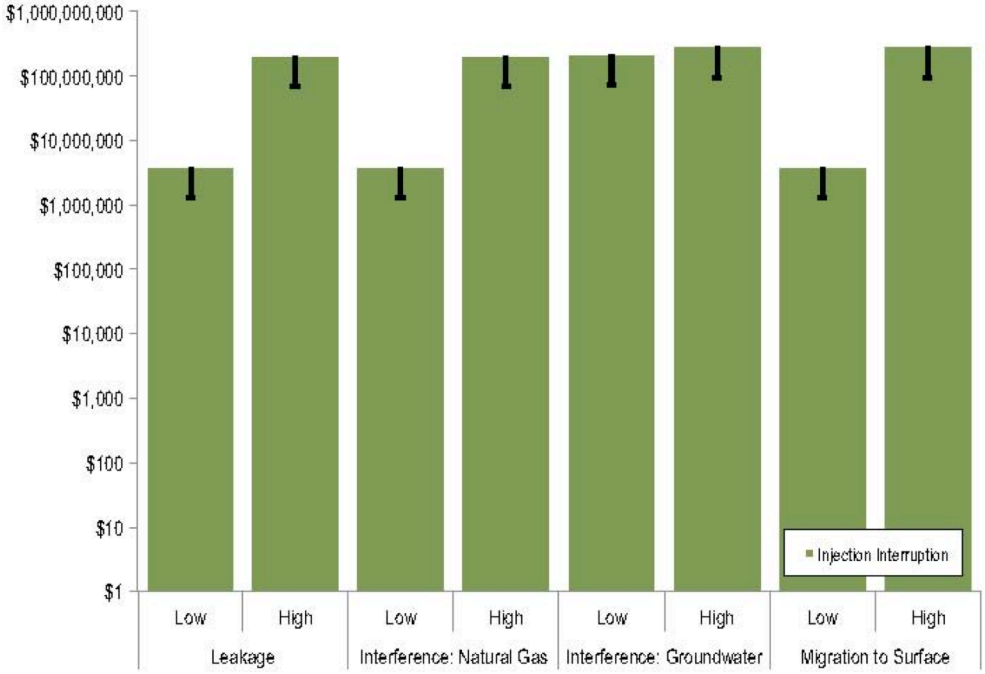

Fig. 6. Injection interruption differs substantially between FOAK (columns) and NOAK (black inset lines) projects.

5.4.2 Financial buffering

Setting aside financial resources to buffer against leakage maybe difficult for an Injection Operator whose revenue is tied to the amount of CO_2 injected into the geologic CO_2 storage reservoir because normalized leakage costs vary widely due to uncertainty in the timing and extent of a leak. Using our storylines for the annual 9.5 MtCO2 injection, a low-cost "leakage only" outcome that occurs at the end of a project lifetime of 30 years costs less than a penny per tonne of CO_2 injected, in present terms, discounted at 8%. In contrast, consider a reservoir with a high-cost leak that reaches the surface and occurs just after the first year of injection. If the leak cannot be successfully remediated, the site must close prematurely, effectively forgoing CO_2 injection for the remaining 29 years of the project life. In addition to the premature site closure costs, which the LIV method can estimate but are not included in the storylines for this case study, leakage costs for this extreme situation are $33.51/tCO2 injected for an FOAK project and $15.08/tCO2 injected for an NOAK project. Costs such as these may be prohibitive for potential project developers, but if best-practices siting procedures are followed, it is extremely unlikely that a leak will either be this severe or occur so early in a project life. In fact, if we assume that any leak can be successfully remedied within a year, then all of the leakage outcomes can be treated as equally likely at any point in time, and, leakage costs would be at most $1.25/tCO2 (FOAK) and $0.56/tCO2 (NOAK) without discounting. For comparison, NOAK CO_2 capture costs are estimated to be $35–70/tCO2 (Al-Juaied and Whitmore, 2009), CO_2 transportation costs are estimated to be less than $5/tCO2 and decrease as the industry builds out (Middleton and Bielicki, 2009; Kuby et al., 2011; Middleton et al., 2012), and CO_2 storage costs are approximately $5/tCO2 (McCoy, 2008).

5.5 Discussion

By applying the LIV method, we determined that the cost to Find and Fix a Leak are largely driven by technical factors related to site geology and the specifics of the leakage event, and to a lesser extent regulatory discretion that determines the extent of Diagnostic Monitoring and the nature of Containment activities. Appropriate site characterization and operation, and conventional financial assurance mechanisms (e.g., bonding and insurance: U.S.EPA, 2011) may reduce an Injection Operator's exposure to these costs, and policy may be further developed to overcome barriers to deployment created by these costs. Table 6 shows the relationships between the cost categories presented here and the technical, legal, and regulatory drivers of these costs, as well as the influence of the infrastructure external to the geologic CO_2 storage site, namely the presence of CO_2 pipeline networks.

Table 6
Cost drivers for the financial consequences of leakage from geologic CO_2 reservoirs.

	Cost drivers			
	Technical	Legal	Regulatory	Infrastructure
Legal costs		X		
Labor burden to others	X	X	X	
Technical remedies for damages	X	X	X	
Business disruption to others	X	X		
Injection interruption		X	X	X
Find and Fix a Leak	X		X	
Environmental remediation	X	X	X	

Injection Interruption costs are driven by legal components of the contracts between CO_2 Emitters and Injection Operators, regulatory discretion regarding required Diagnostic Monitoring and Containment Activities to Find and Fix a Leak, and the degree of extant CO_2 transportation and storage infrastructure. Venting CO_2 and paying Climate Compensation is more likely to occur in the early build-out of the CCUS industry, when the scale of CO_2 pipeline development is embryonic. The duration of an injection

interruption is uncertain a priori, as is the Injection Regulators interpretation of the EPA UIC Class VI rules that govern CO^2 injection for storage. At present, these rules state that injection must stop if leakage that may endanger a USDW is detected, and injection may resume if the Injection Operator can demonstrate that leakage will not endanger a USDW (sec 146.94(b,c)). A simple leakage event may take only a few days to remedy and satisfy regulators, whereas a complicated event with multiple impacts may take months or years. Uncertainty regarding the duration of injection interruptions could be reduced if the EPA UIC Class VI permitting process incorporated clear criteria for Diagnostic Monitoring and Containment. Another option could be to limit the liability for Climate Compensation when an operator must vent CO_2.

Injection Operators may also have a strong incentive to protect against the possibility of Injection Interruption by designing sites with multiple injection wells and excess injection capacity. An Injection Operator can offset the cost of an extra injection well by avoiding venting CO_2 for a few days or avoid diverting it for a few months. For example, an Injection Operator injecting 9.5 MtCO2 per year can afford a $6MM injection well more than it can afford five days of venting or a month and a half of diverting CO_2 to another reservoir. Since Injection Interruption is more costly for FOAK projects than NOAK projects, early projects may seek to incorporate more spare injection capacity than later projects. Early in the development of the industry, as technological learning that reduces costs is occurring (Bielicki, 2009) and uncertainties are being narrowed, operational costs are likely to be higher than later in the development of the industry. Early projects are likely to be more expensive than later projects because of the lack of commercial experience, and policy may be necessary to provide the impetus to overcome cost barriers. To gain commercial experience that generates such learning and resolves uncertainties, it may be necessary to provide more financial incentives for early projects than for late ones in order to facilitate the Injection Operator's ability to buffer against the possibility of injection interruption.

The financial consequences of leakage will vary based on geologic settings and outcomes, but our results permit several generalized points:

- Leakage can be costly even if it causes no subsurface damage, triggers no legal action, and needs no environmental remediation: The obligation to Find and Fix a Leak and the potential for the Injection Interruption incur the most significant portions of the cost for any leakage event, regardless of where the CO2or brine leakage migrates and what it encounters.

- Regulators' decisions strongly influence costs: Choices made by regulators regarding the duration of Injection Interruption, the requirements for Diagnostic Monitoring, and the need for Environmental Remediation have a major influence on the total cost of leakage. Injection Interruption can trigger penalties specified in the contracts between CO_2 Emitters and Injection Operators and incur Climate Compensation costs for the CO_2 that must be vented to the atmosphere.

- The normalized cost of leakage is very likely to have marginal impact on the total cost of CCUS: For sites that successfully remedy leakage and are able to inject for their intended lifetime, the cost of leakage is very small compared to other costs in the CCS value chain.

- Widespread deployment of CCUS decreases the financial consequences of leakage: The financial consequences of leakage are less when CO_2 originally intended to be injected into a reservoir that is leaking can be diverted to an alternate CO_2 storage site instead of being vented to the atmosphere; CO_2 will not need to be vented if it can be re-routed through an integrated pipeline system to another injection reservoir, and thus Climate Compensation costs will not be incurred.

- The financial consequences of leakage imposed on stakeholders other than the Injection Operators comprise a relatively small portion of the total, but these costs may have several important

implications for public and institutional acceptance of CCUS: Concern over the time and trouble that leakage could impose on Surface Residents/Owners may impede public acceptance of geologic CO_2 storage and will need to be addressed with well-designed stakeholder engagement processes (e.g., WRI, 2010). In addition, adequate funding for Injection Regulators will be crucial. Regulators will need training and support to accurately interpret scientific evidence during leakage in order to make decisions about Diagnostic Monitoring, Injection Interruption, and Environmental Remediation that balance environmental protection, development of the industry, and cost. Regulators will also need adequate funding for regulatory oversight made necessary by leakage.

Our study shows that the cost of leakage at the last step in the integrated CCUS system, while very likely to be very low, depends in part of the development of the entire CCUS industry. Early projects bear more exposure to larger potential costs than do later projects, in a manner unrelated to the normal expectations that costs decrease with experience. As a consequence, in order to motivate future CCUS development, it may be necessary for policy to be designed in a manner that is adaptive to the development of the industry, with earlier projects receiving more liability limits or financial incentives than later projects.

Risk is defined as the probability of an outcome multiplied by the impact of that outcome. Our study investigates the financial impacts of leakage. These monetary impacts must be considered in tandem with the likelihoods, or probabilities, of these outcomes. Geophysical models of subsurface CO_2 injection and leakage (e.g., appropriate use of analytic, semi-analytic and numerical simulation options: Nordbotten et al., 2005; Celia and Nordbotten, 2009) are required to assess the probabilities of these leakage outcomes, determine the possible extent of the leaks, and anticipate when this leakage may occur. Combining understanding of the causes and consequences of leakage from geologic CO_2 reservoirs with probabilities derived from geophysical modeling provides a quantitative measure of risk, and does so in a manner that can be compared with the performance of other technologies and the options for other investments.

The LIV results for the Michigan Basin case study highlight the need to consider other subsurface activities when siting and operating CCUS projects. The LIV results also underscore the importance for comprehensive public policy necessary to deploy emerging technologies like CCUS. As markets do not currently price CO_2 emissions, any CCUS demonstration and deployment requires policy incentives (e.g., Newell et al., 2006) or synergistic opportunities for revenue (e.g., Bachu et al., 2004; Randolph and Saar, 2011; Buschecket al., 2013). As our analysis shows, the barriers to deployment can be larger than simply achieving the price parity that makes CCUS a viable option for facilities that emit CO_2 or that equalizes the levelized cost of electricity for different electricity generation options. Encouraging CCUS deployment requires additional policy incentives as well as a comprehensive integration with past, present,and future subsurface activities.

5.6 Conclusions

Leakage of CO_2 or brine from geologic CO_2 reservoirs may occur from different physical mechanisms, and the costs triggered by this leakage will result from different technical, legal, and regulatory drivers. We have identified where and how these leakage costs will arise and applied the LIV method to investigate the consequences and implications of leakage costs for detailed storylines of CO_2 storage in the Michigan Sedimentary Basin. The LIV method can be adapted to any sedimentary basin, injection scheme, and regulatory system to estimate potential costs triggered by leakage from geologic CO_2 reservoirs.

Using this systematic approach, we found that the majority of costs triggered by leakage arise from activities to “Find and Fix a Leak” and from “Injection Interruption”. Economic costs triggered by leakage are dictated by geology and the nature of the leakage event, regulatory discretion, and the degree of build-out of the CCUS industry; financial consequences of leakage are significant even in the absence

of subsurface damages, legal action, and environmental remediation. The build-out of the CCUS industry would provide CO_2 disposal options that would otherwise be injected into a leaking reservoir. Consequently, significant difference in cost exists between early FOAK projects and later NOAK projects due to options to inject elsewhere and avoid venting CO_2 that incurs losses in carbon credits. We also identify the financial externalities of leakage, namely events that would affect many stakeholders and impose costs on them that may not be recoverable through legal action. Overall, costs triggered by leakage are driven by technical, legal, and regulatory factors, and these costs are heavily influenced by the state of development of the CCUS industry.

References

Al-Juaied, M., Whitmore, A., 2009. Realistic Costs of Carbon Capture. Harvard Kennedy School, Belfer Center, Discussion Paper 2009-08. July 2009.

Bachu, S., Shaw, J., Pearson, R., 2004. Estimation of oil recovery and CO2 storage capacity in CO2 EOR incorporating the effect of underlying aquifers. Society of Petroleum Engineers, 89340-MS.

Baxter, P., Kapila, M., Ffonfu, D., 1989. Lake Nyos Disaster, Cameroon, 1986: the medical effects of large scale emission of carbon dioxide? British Medical Journal 298, 1437–1441.

Bielicki, J., 2009. Integrated Systems Analysis and Technological Findings for Carbon Capture and Storage Deployment. Harvard University (Ph.D. thesis).

Bistline, J., Rai, V., 2010. The role of carbon capture technologies in greenhouse gas reduction models: a parametric study of the U.S. Electric Sector. Energy Policy 38, 177–1191.

Buscheck, T., Elliot, T., Celia, M., Chen, M., Sun, Y., Hao, Y., Lu, C., Wolery, T., Aines, R., 2013. Integrated geothermal-CO2 reservoir systems: reducing carbon intensity through sustainable energy production and secure CO2 Storage. Energy Procedia 37, 6587–6594.

Celia, M., Nordbotten, J., 2009. Practical modeling approaches for geological storage of carbon dioxide. Ground Water 47 (5), 627–638.

Duncan, I., Nicot, J.-P., Choi, J.-W., 2009. Risk assessment for future CO2 sequestration projects based CO2 enhanced oil recovery in the U.S. Energy Procedia 1 (1),2037–2042.

Eccles, J., Pratson, L., Newell, R., Jackson, R., 2009. Physical and economic potential of geological CO2 storage in saline aquifers. Environmental Science & Technology 43 (6), 1962–1969.

Ellis, B., Peters, C., Fitts, J., Bromhal, G., McIntyre, D., Warzinski, R., Rosenbaum, E., 2011. Deterioration of a fractured carbonate caprock exposed to CO_2-acidified brine flow. Greenhouse Gases: Science and Technology 1 (3), 248–260.

Espisito, A., Benson, S., 2010. Remediation of possible leakage from geologic CO2 storage reservoirs into groundwater aquifers. Society of Petroleum Engineers, 133603-MS.

Hnottavange-Telleen, K., Krapac, I., Vivalda, C., 2009. Illinois Basin-Decatur Project: initial risk-assessment results and framework for evaluating site performance. Energy Procedia 1 (1), 2431–2438.

Industrial Economics, 2012. Value of Human Health and Ecological Risks Arising from Carbon Capture and Storage (CCS): Final Study Observations. A Report prepared for the CCS Project Sponsor Group, prepared by Trabucchi, C., Donlan, M., Huguenin, M., Konopka, M., and Bolthrunis, S., Available at: http://www.globalccsinstitute.com/publications/valuation-potential-risks-arising-model-commercial-scale-ccs-project-site?highlight=pdf

IPCC, 2005. Special report on carbon dioxide capture and storage. In: Metz, B., Davidson, O., Coninck, H., Loos, M., Meyer, J.P. (Eds.), Intergovernmental Panel on Climate Change. Cambridge University Press, Cambridge, p. 431.

IPCC, 2007. Climate Change 2007: Mitigation. Contribution of Working Group III to the Fourth Assessment Report of the Intergovernmental Panel on Climate Change. Cambridge University Press, Cambridge, United Kingdom and New York,NY, USA.

Keating, E., Hakala, J., Viswanathan, H., Capo, R., Stewart, B., Gardiner, J., Guthrie, G., Carey, J., Fessenden, J., 2011. The challenge of predicting groundwater quality impacts in a CO2 leakage

scenario: results from field, laboratory, and modeling studies at a natural analog site in New Mexico, USA. Energy Procedia 4, 3239–3245.
Kenny, J.F., Barber, N.L., Hutson, S.S., Linsey, K.S., Lovelace, J.K., Maupin, M.A., 2009. Estimated use of water in the United States in 2005 (No. Circular 1344). U.S. Geological Survey. Retrieved 14 April 2011 from http://pubs.usgs.gov/circ/1344/
Kuby, M., Bielicki, J., Middleton, R., 2011. Optimal spatial deployment of CO2 capture and storage given a price on carbon. International Regional Science Review 34(3), 285–305.
Lewicki, J., Birkholzer, J., Tsang, C., 2007. Natural and industrial analogues for leakage of CO2 from storage reservoirs: identification of features, events, and processes and lessons learned. Environmental Geology 52, 457–467.
LexisNexis, 2011. How, and How Much, Do Lawyers Charge?, Lawyers.com. Available at: http://research.lawyers.com/How-and-How-Much-Do-Lawyers-Charge.html. Last accessed: 22 January 2013.
Lynch, J., 2010. Auction of Drilling Rights Fizzles. The Detroit News, October 28.
Mander, S., Polson, D., Roberts, T., Curtis, A., 2011. Risk from CO2 storage in saline aquifers: a comparison of lay and expert perceptions of risk. Energy Procedia 4, 6360–6367.
McCoy, S., 2008. The Economics of Carbon Dioxide Transport by Pipeline and Storage in Saline Aquifers and Oil Reservoirs. Carnegie Mellon University (Ph.D. thesis).
McCoy, S., Rubin, E., 2008. An engineering-economic model of pipeline transport of CO_2 with application to carbon capture and storage. International Journal of Greenhouse Gas Control 2 (2), 219–229.
McFarland, J., Herzog, H., 2006. Incorporating carbon capture and storage technologies in integrated assessment models. Energy Economics 28, 632–652.
Middleton, R., Bielicki, J., 2009. A scaleable infrastructure model for carbon capture and storage; SimCCS. Energy Policy 32, 1052–1060.
Middleton, R., Kuby, M., Bielicki, J., 2012. Generating candidate networks for optimization: the CO2 capture and storage optimization problem. Computers, Environment, and Urban Systems 36, 18–29.
NETL, 2009b. Modern Shale Gas Development in the United States: A Primer. National Energy Technology Laboratory.
NETL, 2010. 2010 Carbon Sequestration Atlas of the United States and Canada – Third Edition (Atlas III). National Energy Technology Laboratory, United States Department of Energy, Available at: http://www.netl.doe.gov/technologies/carbonseq/refshelf/atlasiii/
Nordbotten, J., Celia, M., Bachu, S., Dahle, H., 2005. Semianalytical solution for CO2 leakage through an abandoned well. Environmental Science & Technology 39(2), 602–611.
Nordhaus, W.D., 2010. Economic aspects of global warming in a post-Copenhagen environment. Proceedings of the National Academy of Sciences of the United States of America, http://dx.doi.org/10.1073/pnas.1005985107.
Oldenburg, C.M., 2005. Health, Safety, and Environmental Screening and Ranking Framework for Geological CO2 Storage Site Selection; LBNL 58873. LawrenceBerkeley National Laboratory, Earth Sciences Division, pp. 29, September 20,2005.
Oldenburg, C., Doughty, C., Peters, C., Dobson, P., 2012. Simulations of long-column flow experiments related to geologic carbon sequestration: effects of outer wall boundary condition on upward flow and formation of liquid CO2. Greenhouse Gases: Science and Technology 2 (4), 279–303.
Pacala, S., Socolow, R., 2004. Stabilization wedges: solving the climate problem for the next 50 years with current technologies. Science 305, 968–972.
Pollak, M., Bielicki, J., Dammel, J., Wilson, E., Fitts, J., Peters, C., 2013. The leakage impact valuation (LIV) method for leakage from geologic CO2 storage reservoirs. Energy Procedia 37, 2819–2827.
Presig, M., Prevost, J.H., 2011. Coupled multi-phase thermo-poromechanical effects. Case study: CO2 injection at In-Salah, Algeria. International Journal of Greenhouse Gas Control 5 (4), 1055–1064.
Randolph, J., Saar, M., 2011. Combining geothermal energy capture with geologic carbon dioxide sequestration. Geophysical Research Letters (38), L10401.

Siirila, E., Navarre-Sitchler, A., Maxwell, R., McCray, J., 2012. A quantitative methodology to assess the risks to human health from CO2 leakage into groundwater. Advances in Water Resources 36, 146–164.

Trabucchi, C., Donlan, M., Wade, S., 2010. A multi-disciplinary framework to monetize financial consequences arising from CCS projects and motivate effective financial responsibility. International Journal of Greenhouse Gas Control 4 (2),388–395.

U.S. DOE, 2007. Final Risk Assessment Report for the FutureGen Project Environmental Impact Statement, Contract No. DE-AT26-06NT42921. Revision 2 October 2007.

U.S. EIA, 2010a. Crude Oil Production, Retrieved 14 November 2010, from http://www.eia.gov/dnav/pet/pet_crd_crpdn_adc_mbbl_a.htm

U.S. EIA, 2010b. State Energy Profiles: Michigan, Retrieved 15 December 2010, from http://www.eia.gov/state/state energy profiles.cfm?sid=MI

U.S. EIA, 2010c. Underground Natural Gas Storage Capacity: Michigan, Retrieved 15 December 2010, from http://www.eia.gov/dnav/ng/ng_storcap_dcu_SMI_a.htm .

U.S. EPA, 2001. Remediation Technology Cost Compendium – Year 2000. United States Environmental Protection Agency, Solid Waste and Emergency Response (5102G). EPA 542-R-01-009.

U.S. EPA, 2008. Vulnerability Evaluation Framework for Geological Sequestration of Carbon Dioxide. United States Environmental Protection Agency, EPA 430-R-08-009.

U.S. EPA, 2010a. Federal Requirements Under the Underground Injection Control (UIC) Program for Carbon Dioxide (CO2) Geologic Sequestration (GS) Wells, F.R. vol. 75, no. 237, Friday 10 December 2010; vol. 40 CFR Parts 124, 144,145, 146, and 147, pp. 77230–77303. Available at: https://federalregister.gov/a/2010-29954, last accessed 15 August 2013.

U.S. EPA, 2010b. Final Mandatory Reporting of Greenhouse Gases from Carbon Dioxide Injection and Geologic Sequestration, In 40 CFR Part 98.440, Wednesday 1 December 2010 ed.; FR vol. 75 no. 230 2010; pp 75060–75089.

U.S. EPA, 2010c. Geologic CO2 Sequestration Technology and Cost Analysis. United States Environmental Protection Agency. Office of Water (4606M), EPA 816-R10-008. November 2010. Available at: http://water.epa.gov/type/groundwater/uic/class6/upload/geologicco2sequestrationtechnologyandcostanalysisnov2010.pdf, last accessed 15 August 2013.

U.S. EPA, 2011. Geologic Sequestration of Carbon Dioxide: Underground Injection Control (UIC) Program Class VI Financial Responsibility Guidance. United States Environmental Protection Agency. Office of Water (4606M), 816-R-11-005.

U.S. EPA, 2012. Emissions & Generation Resource Integrated Database (eGRID). U.S. Environmental Protection Agency, Available at: http://www.epa.gov/cleanenergy/energy-resources/egrid/index.html, last accessed November 27, 2013.

Walke, R., Metcalfe, R., Limer, L., Maul, P., Paulley, A., Savage, D., 2011. Experience of the application of a database of generic features, events and processes (FEPs) targeted at geological storage of CO2. Energy Procedia 4, 4059–4066.

Yamaguchi, K., Takizawa, K., Komaki, H., Hayashi, E., Murai, S., Ueta, S., Tsuchiya, M., 2011. Scenario analysis of hypothetical site conditions for geological CO2 sequestration in Japan. Energy Procedia 4 (0), 4052–4058.

Chapter 6. Parameters and Cost Algorithms for Michigan Sedimentary Basin Case Study

This chapter has been published as:

J.M. Bielicki; M.F. Pollak; J.P. Fitts; C.A. Peters, E.J. Wilson. (2014) "Supplemental Information: Parameters and Cost Algorithms for Michigan Sedimentary Basin Case Study Conducted" for "Causes and Financial Consequences of Geologic CO_2 Storage Reservoir Leakage and Interference with other Subsurface Resources". *International Journal of Greenhouse Gas Control*. Vol. 20: doi:10.1016/j.ijggc.2013.10.024

6.1 Introduction

This chapter presents the details on the parameters and cost algorithms that were used for the case study presented in the Leakage Impact Valuation (LIV) analysis in the previous chapter. Also included are the details of the geophysical model and the parameters assumed in the leakage estimation. Finally, we include a discussion of human health impacts from exposure to inhaled CO_2 and how this applies to releases of CO_2 at the land surface.

6.2 Parameters and Cost Algorithms

Table 1: James De Young Case Study Parameters

Case Study		Notes
Injection rate ($MtCO_2$/yr)	9.5	Yearly emissions from James De Young and J.H. Campbell power plants (0.6 MtCO2/yr and 8.9MtCO2/yr, respectively)
Storage facility injection life (years)	30	
Plume area at 5 years (km^2)	255	ELSA simulations
Plume area at 30 years (km^2)	707	ELSA simulations
Depth of injection wells (m)	1,845	Base of Mt. Simon formation. Stratigraphic sequence at case study location. Adapted from Lampe et al. (2009) using well logs from case study area.
Depth to top of injection formation (m)	1,605	Top of Mt. Simon Formation
Thickness of primary confining zone (m)	93	Eau Claire formation
Depth of lowest USDW (m)	65	Quaternary aquifer.
Depth of lowest potable aquifer (m)	65	Quaternary aquifer.
Depth to water table (m)	10	Best professional judgment
Depth of standard monitoring wells (m)	1,500	Monitoring in Galesville above confining unit
Number of monitoring wells	6	U.S. EPA (2010a), p. 3-9
Scenario Assumptions		**Notes**
Depth to CO_2 accumulation (m)	450	Accumulation in Traverse Dundee
Depth of impacted activity (m)	1,100	Petroleum production from Trenton-Black River Formation
Depth of produced water disposal well (m)	550	Disposal to Traverse Dundee
Population density (households/km^2)	27	68.77 households/mi^2 (U.S. Census Bureau, 2011a)
Groundwater domestic use density (households/km^2)	13	50% of households use groundwater (GWAC, 2006)

6.3 CO_2 Leakage and Human Exposure to Elevated CO_2 Levels

The U.S. Center for Disease Control (CDC) National Institute for Occupational Safety and Health (NIOSH) defines the level of CO_2 the Immediately Dangerous to Life or Health (IDLH) to be 40,000 ppm. This level is based upon studies and statements that 30-minute exposure to 50,000 ppm CO_2 produces indications of intoxication, and exposure to 70,000 ppm and 100,000 ppm produces unconsciousness within a few minutes (NIOSH, 1994). For the allowable level of indoor exposure, the American Society of Heating, Refrigeration, and Air-Conditioning Engineers (ASHRAE) Standard 62.1–2007 summarizes regulatory and recommended levels of CO_2 from a variety of agencies and organizations involved with setting standards for indoor environments. Enforceable, Regulatory, and Non-Enforceable Guidelines for allowable continuous exposure are set at 5,000 ppm. The Deutsche

Forschungs Gemeinschaft (similar in purpose to the U.S. National Institutes of Health and NIOSH) has one regulatory limit of 10,000 ppm exposure for one hour, and NIOSH and ACGH have non-enforced guidelines of 30,000 ppm for 15 minutes.

The amount of CO_2 that could be released to the surface depends on the amount of leakage as it percolates through leakage pathways and hydrostratigraphic units. The ELSA model assumes that wells are the only potential leakage conduits across aquitard formations (see Norbotten et al, 2005; Watson and Sullivan, 2012 for justification), and predicts CO_2 and brine migration rates into overlying confined aquifers and finally leakage rates into the topmost, or unconfined aquifer in the stratigraphic sequence. The ELSA model, however, does not model surface release. Therefore, the maximum amount of CO_2 that can be released to the surface equals the maximum amount that reaches this unconfined aquifer.

We used the ELSA model to simulate 9.5 $MtCO_2$/yr injection and leakage for an extreme situation where injection is located within 5,700 ft of eight wells that perforate the Mt. Simon and are all leaking. The red squares in Figure 3 (Chapter 3) show the average rate of CO_2 accumulating in each aquifer from four hundred simulations where Mt. Simon porosity (φ) and permeability (κ) are drawn from the empirical distribution $\kappa = (5x10^{-18})\ \varphi^{3.911}$, where $\varphi = logN(0.13, 0.04)$ and $\kappa = logN(2.25, 3.11)x10^{-13}\ m^2$. One hundred simulations each assign existing wells leakage permeabilities (κ_{leak}) of $10^{-10}\ m^2$, $10^{-12}\ m^2$, $10^{-14}\ m^2$, and $10^{-16}\ m^2$. The CO_2 plume in the Mt. Simon has a radius of approximately 15 km. The most extreme leakage results are for the situation where 9.5 $MtCO_2$/yr is continuously injected and leakage through every well encountered by CO_2 continues unabated for 30 years. If all of the CO_2 getting into the shallow aquifer passes through it and is released from the surface, 332,000 m^3/d of air would need to mix with the 24.5 t/d leakage. If this CO_2 is released from a 1 m^2 surface area and mixes with air within 1 m of the surface, 8.7 mph wind would reduce the concentration in air to 4%.

The inset in Figure 3 (Chapter 3) and

Table 2 put this 24.5 t/d leakage rate in the context of some of the leakage analogs presented in Lewicki et al (2007), by presenting extrapolations of these leakage rates to facilitate the comparisons. The ELSA model can only model leakage to the shallowest aquifer, and all but one of the natural analogs have CO_2 leakage measurements at the surface. Albany Hills (IT) is the exception; the data contains measurements at the surface and in the groundwater aquifer. To estimate the amount of the CO_2 flux infiltrating groundwater that may be released from the surface, we use the data for Albani Hill (IT), where approximately 1/7 of the CO_2 that reaches groundwater gets to the surface. Applying this factor to the simulation results suggests that 3.6 t/d could reach the surface for the most extreme leakage scenario. In addition to the visual representation in Figure 3 (Chapter 3),

Table 2 presents the simulation results and extrapolation in the contexts and the measurements of natural analogs and extrapolations of these analogs.

To dilute the 3.6 tCO_2/d that are extrapolated from the simulation results to 4% concentration in air requires 48,600 m^3/d of air, or a 1.3 mph breeze moving through a cubic meter of air (1 m^2 surface area, 1 m high). Air blowing at 5.1 mph through the cubic meter would dilute this leakage to 1%, and air blowing at 1.3 mph through a 4 m^3 volume of CO_2 would also dilute the CO_2 concentration to 1%.

Table 2: Modeled Leakage CO_2 Leakage Results and Select Analogs of CO_2 Leakage – Rates of CO_2 leakage from the subsurface for analogs are taken from Lewicki et al, (2007).

Location	**CO_2 Leakage** (t/d)		**Surface Flux**	**Notes**[c]
	Groundwater	Surface	(kg/d/m^2)	
Solfatara (IT)	10,257[a]	1,500	6.0[b]	Recreational Area: vegetation absent in degassing area.
Mammoth Mountain, CA (USA)	1,709[a]	250	0.5[b]	Recreational Area: Tree kills, one asphyxiation, four deaths. CO_2 concentrations and fluxes being monitored (temporally and spatially) in tree kill areas; Groundwater chemistry measurements of groundwater chemistry; public education
Paradox Basin, UT (USA): Crystal Geyser	226[a]	33		Rural: Measurements of atmospheric CO2 concentrations
Laacher See (DE)	96[a]	14		Monitoring CO2 fluxes and concentrations from lake surface and shore
Albani Hill (IT)	506	74	1.2[b]	Urban: High residential CO_2 concentrations, past deaths
Ma´traderecske (HU)			0.2-0.4	Rural Village: CO2 detection and control devices installed in homes, demolition of homes with hazardous CO2 levels, public education
Paradox Basin, UT (USA): Soil			0.1	Rural
James De Young, MI (USA)	24.5	3.6[a]		Estimate after 30 years of continuous 9.5 $MtCO_2$/yr injection and unabated leakage.

[a]Estimated based on relationship for Albani Hill (IT); [b]Calculated data in from Lewicki et al (2007); [c]Presented in Lewicki et al (2007).

6.4 Michigan Sedimentary Basin Case Study: Economic Parameters, Cost Algorithms, and Data Sources

This section presents the details of the economic parameters, cost algorithms and data sources used for the Leakage Impact Valuation (LIV) analysis of the Michigan sedimentary basin presented in Chapter 3.

Table 3: Michigan Sedimentary Basin Case Study Economic Parameters

Economic Assumptions ($/tCO$_2$)		**Notes**
Injection Operator's revenue	5	UIC class VI rule quotes the cost of CO_2 as \$3.80/tCO_2. (U.S. EPA, 2010a). Added return on investment.
FOAK CO_2 price	30	Relatively weak policy drivers such as tax incentives
NOAK CO_2 price	50	CO_2 capture cost estimated at \$35 -\$70/tCO_2 for NOAK plants. (Al-Juaied and Whitmore, 2009).
FOAK penalty for refusing delivery	20	
NOAK penalty for refusing delivery	5	
FOAK financial exposure to CO_2 Emitter	5	CO_2 price - Revenue - Penalty
Discount rate	8%	
Labor Rates ($/hr)		**Notes**
Geoscientist/engineer	109	U.S. EPA (2010a)
Activity Operator	109	Equal to geoscientist/engineer labor
Injection Operator	109	Equal to geoscientist/engineer labor
Regulator	50	Average of state and federal rates (U.S. EPA, 2010a: p 5-34)
Surface Owner time	22	Median income for MI household is \$46,597. (U.S. Census Bureau, 2011)
Water Utility	109	Equal to geoscientist/engineer labor
CO_2 Emitter	109	Equal to geoscientist/engineer labor
Attorney Legal Fees including paralegal and secretary	300	(LexisNexis, 2011)

Table 4: Michigan Sedimentary Basin Case Study Cost Algorithms and Data Sources

Diagnostic Monitoring Costs		
Cost item	**Cost algorithm**	**Data sources and notes**
Geochemical and pressure sampling at monitoring wells	$200/sample and 4 samples per well plus 0.5 hours of engineer labor for sampling per well	U.S. EPA (2010b: p. 27, #B-12)
Seismic survey	($40,150/km^2) over CO_2 plume	U.S. EPA (2010b: p. 28. #B-17)
Hyperspectral or lidar survey	$2,400/km^2 plus $5,000 mobilization	U.S. EPA (2010b: p. 28. #B-15b&c)
Additional fluid flow modeling	Geoscientist labor	U.S. EPA (2010b: p. 28. #B-18)
Additional analysis and reporting	Geoscientist labor	U.S. EPA (2010b: p. 28. #B-19)
Injection operator's time	equal to geoscientist/engineer labor	
Additional monitoring well		
Monitoring well(s) right-of way	$10,400 per well	U.S. EPA (2010b: p. 27. #B-4)
Monitoring well(s) engineering	$5,200 per well	U.S. EPA (2010b: p. 27. #B-3)
Monitoring well(s) drilling and installation	$656/m plus $20,800 for downhole equipment	U.S. EPA (2010b: p. 27. #B-8)
Monitoring well water table		
Monitoring well(s) right-of way	$10,400 per well	U.S. EPA (2010b: p. 27. #B-4)
WT monitoring well(s) drilling and installation	40 hr for plan plus $8,000/well	U.S. EPA (2010b: p. 27. #B-4)
Activity geochemical sampling and analysis (based on activity type)	$200/sample plus 0.5 hr to collect	U.S. EPA (2010b: p. 27. #B-12)
Water supply sampling and analysis	$200/sample plus 0.5 hr/sample to collect	Best professional judgment, based on U.S. EPA (2010b: p. 28 #B-12)
Soil vapor or AC survey	65,000 for equipment, 40 hr for plan, 16 hr per survey	
Surface water sampling	10 hr for plan plus 0.5 hr/sample to collect plus $200/sample	Best professional judgment
Well head air sampling	4 samples per survey, $200/sample plus 2 hr for survey	Best professional judgment
Indoor air quality sampling	10 hrs for plan, 3 samples per building, 1 hr/building to collect plus $200/sample	Best professional judgment
Containment Activity Costs		
Cost item	**Cost algorithm**	**Data sources and notes**
Remediate leaking well	$31,200 for clean out, $13,500 to replug and $11,400 to log.	(U.S. EPA, 2010b: p.40 # D-8)
Pressure relief system		
Pressure relief system capital cost	$6,000,000	Wyoming CCS Working Group (2009)
Pressure relief O&M	$8,000,000	Wyoming CCS Working Group (2009)
Brine water treatment	$8,000,000	Wyoming CCS Working Group (2009)
New CO_2 injection wells		
Engineering and design	$41,400/well	(U.S. EPA, 2010b: p. 39 # C-1)
Obtain rights of way	$20,700/well	(U.S. EPA, 2010b: p. 39 #C-2)

UIC permit filing	$2,000/well	(U.S. EPA, 2010b: p. 39 #C-5)
Well construction and installation	$820/m	(U.S. EPA, 2010b: p. 39 #C-6a)
Corrosion resistant tubing and casing	$9.35/m	(U.S. EPA, 2010b: p. 39 # C-7,8)
Cement well from surface to base of lowermost USDW and throughout confining zone	$4.92/m	(U.S. EPA, 2010b: p. 39 # C-9)
Pumps and wellhead control equipment	$338,500/well	(U.S. EPA, 2010b: p..39 # C14,15) average per well
Damage costs		
Cost item	**Cost algorithm**	**Data sources and notes**
Legal fees	(hr) x (Lawyers rate)	
New public water supply well		
Engineering and design	$5,200/well	(U.S. EPA 2010a)
Drilling	18" borehole @ (125/ft) x (250 ft deep)	(Anderson, 2009)
Casing	12" steel @ (60/ft) x (210 ft)	(Anderson, 2009)
Screen	40 foot @ 250/ft	(Anderson, 2009)
Grouting	$500/well	(Anderson, 2009)
Development	$2,500/well	(Anderson, 2009)
Pump and installation	$10,000/well	Ross (2003)
Provision of interim water supply	600 households x (10 gpd) x ($0.70/gal)	
Plugging former water supply wells	20,700 per well	(U.S. EPA, 2010b: p. 40 #D-7)
Install Amine Plant to separate CO_2 from Natural Gas	$1.5M per 35,000 Mcfd capacity	Rented equipment. (Stokes, 2010)
Operate Amine plant	$590M/year, ten years, NPV	(Stokes, 2010)
Value of damaged oil field	reserves in place(9,000bbl) *value of oil($90/bbl)	Proven reserves in MI 33 million barrels, divided by 3655 producing wells. Avg. ~9,000 bbl/well (U.S. EIA, 2011a), (MNDEQ, 2011a)
Damage to tubulars	$500,000	Best professional judgment
Install replacement UIC class I injection well	$2M for well, and $500,000 for new class I permit	Reported cost of 2010 UIC class I well in Antrim Co., MI. (U.S. EPA, 2011b)
Loss of injectivity in UIC class I injection well	$1M	Estimated legal settlement
Basement venting system	$1,500 per building	Adapted from cost of radon remediation systems. radon abatement in MI (MNDEQ, 2011b)
Natural gas business interruption	volume not withdrawn*storage value	Average annual working volume of MI natural gas storage operation: 11.8 Mcf (MIDLEG, 2011); Value of storage: $0.55/Mcf (FERC (2004).
Environmental Remediation Costs		
Cost item	**Cost algorithm**	**Data sources and notes**
CO2 extraction well installation		
Engineering and design	$41,400/well	(U.S. EPA, 2010b: P. 39 #C-1)
Obtain rights of way	$20,700/well	(U.S. EPA, 2010b: P. 39 #C-2)
UIC permit filing	$2,000/well	(U.S. EPA, 2010b: P. 39 #C-5)
Well construction and installation	$656/m	(U.S. EPA, 2010b: P. 39 #C-6a)

Corrosion resistant tubing and casing	$9.35/m	(U.S. EPA, 2010b: P. 39 #C-7,8)
Cement well entire length	$4.92/m	(U.S. EPA, 2010b: P. 39 #C-9)
Pumps and wellhead control equipment	$338,500/well	(U.S. EPA, 2010b: P. 39 #C14,15) Average per well
Continuous measurement/monitoring equipment	$415,500/well	(U.S. EPA, 2010b: P.44 # E-3)
CO2 extraction well operation		
Electricity	(33,000 kWh/yr) x ($.066/kWh)	(U.S. EPA, 2010a: p. 5-18)
Operations a& Maintenance	$20,000/year plus $3.10/foot well depth/yr	(U.S. EPA (2010b: p.44 #E-6) Average cost per well
Groundwater Pump and Treat System		
Capital cost	$5,900,000/system	Costs for 75th percentile pump and treat system for combinations of contaminants including metals (U.S. EPA, 2001a)
Operating cost	$730,000/yr	
Soil venting system		
Installation and operation	$3.25/$m^3$ over 100m x 500m area, depth to water table 5m	(U.S. EPA, 2001b)
Climate compensation costs		
Cost item	**Cost algorithm**	**Data sources and notes**
Emissions from soil gas system and home venting	(0.19 $tCO_2/m^2/yr$) x (50,000 m^2) x (5 years) x (CO_2 Price)	Flux rate at Mammouth Mountain CA (Lewicki et al, 2007)
Emissions from leaking well before it's plugged	(33t/day) x (4 days) x (CO_2 Price)	Discharge rate at Crystal Geyser UT (Lewicki et al (2007)

6.5 References

Al-Juaied, M., and Whitmore, A. (2009). A. "Realistic Costs of Carbon Capture". Harvard Kennedy School, Belfer Center Discussion Paper 2009-08. July 2009.

Anderson (2009). Personal communication with Casey Anderson, Agra Industries, March 12, 2009.

FERC (2004). "Current State of and Issues Concerning Underground Natural Gas Storage." U.S. Federal Electric Regulatory Commisson. Docket No. SD04-11-000.

Groundwater Conservation Advisory Council (2006). *Final Report to the Michigan Legislature in response to Public Act 148 of 2003*. Retrieved 3 February 2010, from http://www.michigan.gov/documents/act148reportlegislature_157533_7.pdf.

Lampe, D. (2009). "Hydrogeologic Framework or Bedrock Units and Initial Salinity Distribution for a Simulation of Groundwater Flow for the Lake Michigan Basin." U.S. Department of Interior, U.S. Geological Survey. Scientific Investigations Report 2009-5060.

LexisNexis (2011). "How, and How Much, Do Lawyers Charge?". Lawyers.com. Available at: http://research.lawyers.com/How-and-How-Much-Do-Lawyers-Charge.html. Last accessed: January 22, 2013.

Lewicki, J., Birkholzer, J., and Tsang, C., (2007). "Natural and Industrial Analogues for Leakage of CO_2 from Storage Reservoirs: Identification of Features, Events, and Processes and Lessons Learned." *Environmental Geology, 52,* 457-467.

MIDEQ (2011a). "Well Type and Status". Michigan Department of Environmental Quality. Available at: http://www.michigan.gov/deq/0,4561,7-135-3311_4111_4231-9311--,00.htm, Last accessed: January 22, 2013.

MIDEQ (2011b) "Reducing Radon Levels." Michigan Department of Environmental Quality. Available at: http://www.michigan.gov/deq/0,4561,7-135-3310_4105_4196-10518--,00.html. Last accessed: January 22, 2013.

MIDLEG (2011). "About Michigan's Natural Gas Storage Industry." LARA Public Service Commission. Michigan Department of Licensing and Regulatory Affairs, available at: http://www.dleg.state.mi.us/mpsc/gas/about3.htm

NIOSH, 1994 NIOSH, Documentation for Immediately Dangerous to Life or Health Concentrations (IDLHs): Carbon Dioxide, 1994, U.S. Center for Disease Control, National Institute of Occupational Safety and Health, . Available at: Available at: http://www.cdc.gov/niosh/idlh/124389.html. Last A. Last accessed January 12, 2012

Nordbotten, J., Celia, M., Bachu, S., and Dahle, H., (2005). "Semianalytical Solution for CO_2 Leakage through an Abandoned Well." *Environmental Science & Technology. 39* (2), 602-611.

Ross, J. (2003) "The Groundwater Contracting Industry: By the Numbers." *Water Well Journal, 57(12),* 22-29.

Stokes W. (2011). Personal Communication with William Stokes. Kinder Morgan. July 30, 2011.

U.S. Census Bureau (2011a). "State & County Quickfacts: Michigan." United States Census Bureau. Available at http://quickfacts.census.gov/qfd/states/26000.html. Last accessed: September 14, 2011.

U.S. Census Bureau. (2011b) "Income: State Median Income." United States Census Bureau. Available at: http://www.census.gov/hhes/www/income/data/statemedian/index.html. Last accessed: September 14, 2011.

U.S. EPA (2001a). "Cost Analyses for Selected Groundwater Cleanup Projects: Pump and Treat systems and Permeable Reactive Barriers." United States Environmental Protection Agency. Solid Waste and Emergency Response (5102G). EPA 542-R-00-013.

U.S. EPA (2001b) "Remediation Technology Cost Compendium - Year 2000". United States Environmental Protection Agency. Solid Waste and Emergency Response (5102G). EPA 542-R-01-009.

U.S. EPA (2010a) "Federal Requirements Under the Underground Injection Control Program for Carbon Dioxide Sequestration Wells (Final GS Rule)." Cost Analysis. United States Environmental Protection Agency. Federal Register / Vol. 75, No. 237 / Friday, December 10, 2010 / Rules and Regulations

U.S. EPA (2010b). "Geologic CO_2 Sequestration Technology and Cost Analysis." Office of Water. (4606-M). EPA 816-R10-008.

U.S. EIA (2011a). "Michigan Crude Oil Proved Reserves, Reserves Changes, and Production." United States Energy Information Administration. Available at: http://www.eia.gov/dnav/pet/pet_crd_pres_dcu_SMI_a.htm. Last Accessed: September 14, 2011.

U.S. EPA (2011b) "Beeland Group - Little Traverse Bay Environmental Project Disposal Well #1 - MI-047-1I-0001". Available at: http://www.epa.gov/r5water/uic/beeland/index.htm. Last Accessed: January 22, 2013.

Watson, T., and Sullivan,T. (2012)/ "Feasibility of a Perfluorocarbon Tracer Based network to Support Monitoring, Verification, and Accounting of Sequestered CO_2." *Environmental Science & Technology, 46,* 1692-1699.

Wyoming CCS Working Group (2009). "Report and Recommendations of the Carbon Sequestration Working Group to the Joint Minerals, Business and Economic Development Committee and the Joint Judicial Committee of the Wyoming State Legislature." September 2009.

Chapter 7. A Methodology for Monetizing Basin-Scale Leakage Risk and Stakeholder Impacts

This chapter has been published as:

J.M. Bielicki, M.F. Pollak, E.J. Wilson, J.P. Fitts, C.A. Peters, "A Methodology for Monetizing Basin-Scale Leakage Risk and Stakeholder Impacts." International Conference on Greenhouse Gas Technologies (GHGT-11), 18th-22nd November 2012, Kyoto International Conference Center, Japan. *Energy Procedia*, 37 (2013) 4665-4672.

7.1 Abstract

Carbon dioxide (CO_2) capture and storage involves injecting CO_2 into permeable geologic reservoirs. Candidate reservoirs will be overlain by an impervious caprock, but CO_2 or brine may leak through this caprock via natural or manmade pathways into overlying units. Such leakage will incur multiple costs to a variety of stakeholders, as mobile fluids may interact with other subsurface activities, reach groundwater, or possibly escape from the surface. We summarize a methodology to monetize leakage risk throughout a basin, based on simulations of fluid flow, subsurface data, and estimates of costs triggered by leakage. We apply this methodology to two injection locations in the Michigan (U.S.A.) Sedimentary Basin, and show that leakage risk is site-specific and may change priorities for selecting CO_2 storage sites, depending on its siting relative to leakage pathways and other subsurface activities.

7.2 Introduction

Carbon [dioxide] capture and storage (CCS) is a process that would involve injecting carbon dioxide (CO_2) into geologic reservoirs. CO_2 is to be "stored" in these reservoirs for hundreds or thousands of years, but the integrity of the seal—a relatively impermeable caprock—may not be perfect, and injected CO_2, or the brine it displaces, may leak through wells, wellbores, existing faults, or fracture networks. Such leakage may incur multiple costs if the mobile fluids interfere with other subsurface activities—water production, energy production, energy storage, and waste disposal—or migrate to the surface. Since many different activities could be affected by leakage, many different stakeholder groups could be affected by leakage events and potential costs or damages could arise from interference with these activities. As a result, site selection for potential CO_2 storage reservoirs must include assessments of leakage risk within a three-dimensional proximity of where CO_2 is being injected and how potential monetary consequences of leakage could differ among stakeholders. Determinations of leakage risk for multiple possible injection locations within a basin are therefore necessary in order to prioritize options for CO_2 storage.

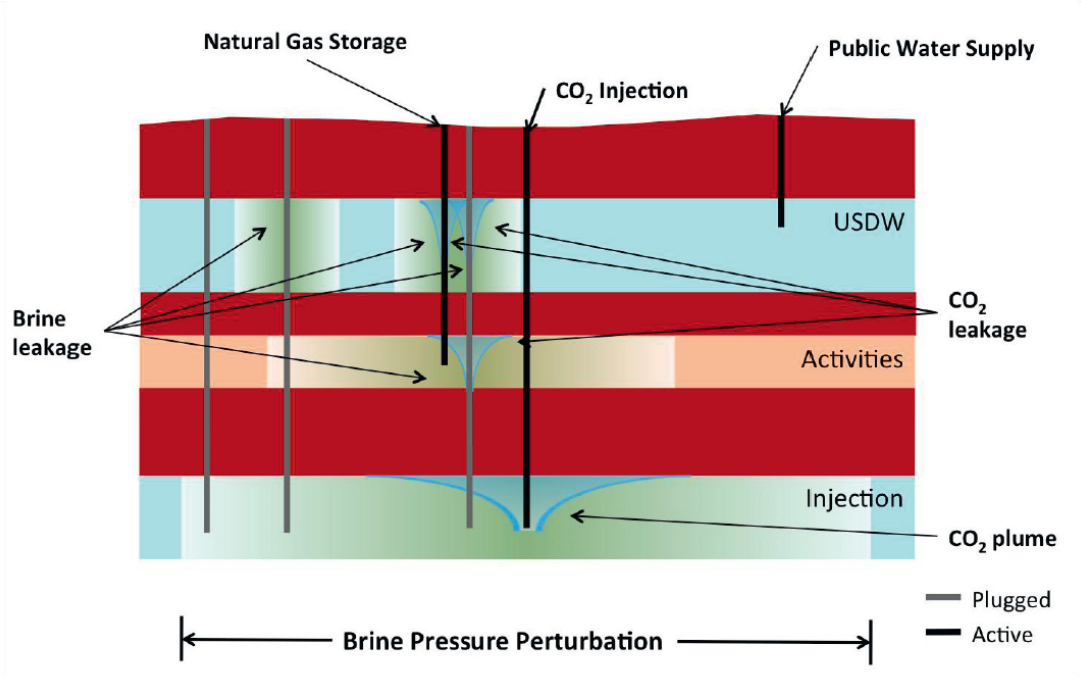

Figure 1: CO_2 Injection and Storage Reservoir Leakage amidst Past and Present Subsurface Activities – Injected CO_2 or displaced brine may leak out of the storage reservoir through leakage pathways (wells are shown here). Such leakage triggers costs and may interfere with other activities, contaminate groundwater (USDW), or migrate to the surface (not shown).

We present a methodology to probabilistically assess leakage risk for geologic CO_2 storage, and demonstrate that methodology on two potential injection locations in the Michigan Sedimentary Basin. This methodology comprises the *RISCS* (Risk Interference Subsurface CO_2 Storage) model, which monetizes leakage risk across a broad range of relevant stakeholders. If CO_2 or brine leaks from the injection formation, interferes with other subsurface activities, migrates into groundwater, or reaches the

surface, *RISCS* monetizes this risk and spatially quantifies how it could differ in magnitude and location across ten different stakeholder groups. We show that leakage risk is site-specific, depending on how CO_2 injection is sited relative to leakage pathways and other subsurface activities.

7.3 Basin Scale Leakage Risk Assessment: Methodology and Example in the Michigan Sedimentary Basin

Determining the potential for a basin to store CO_2 requires that the assessment of multiple potential injection locations. The Michigan Sedimentary Basin is estimated to have up to 15 $GtCO_2$ storage capacity [1] partitioned between the St. Peter and Mt. Simon formations—two of the basin's sixteen major hydrostratigraphic units (**Table 1**). We apply the *RISCS* model on two potential injection locations in the Michigan Sedimentary Basin. The results we present indicate that leakage risk as a function of the three-dimensional proximity to leakage pathways and other subsurface activities.

7.3.1 Risk Interference of Subsurface CO2 Storage (RISCS) Model

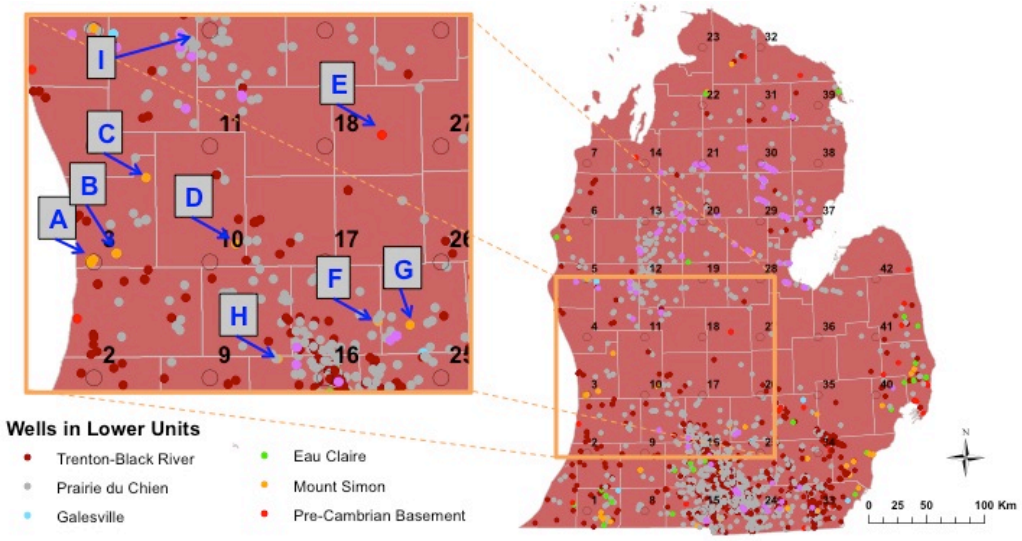

Figure 1: Michigan Sedimentary Basin and Chosen Injection Locations - Two CO_2 Injection locations (11, 17) and Nine Locations (A-I) where CO_2 or Brine May Leak through Existing Wells into the Overlying Galesville Aquifer.

Risk is a function of the probability of an outcome and the impact of that outcome. To monetize leakage risk, the RISCS (Risk Interference Subsurface CO2 Storage) model [2-3] combines (1) probabilistic CO2 and brine leakage magnitudes and spatial extents from simulations of geophysical fluid flow, (2) three-dimensional geospatial data, and (3) estimates of potential costs triggered by leakage. For (1), we use the Estimating Leakage Semi-Analytically (ELSA) model; (2) is compiled from data acquired from the United States Geologic Service (USGS) and the Michigan Department of Environmental Quality; and (3) uses the Leakage Impact Valuation (LIV) method to estimate the financial consequences of leakage. Each of these numbered items is presented next.

RISCS weights the estimated costs triggered by leakage events based on the degree to which CO_2 or brine is present outside the storage reservoir or in an area. These weights are functions of the percentage of the unit thickness that CO_2 occupies, the degree to which brine pressure is elevated above hydrostatic, and the number of leaking wells within a kilometer.

7.3.2 Estimating Leakage Semi-Analytically (ELSA) Model

ELSA simulates CO_2 injected into saline aquifers, and determines where CO_2 and displaced brine flow within the injection formation, through well leakage pathways, and in overlying aquifers and well pathways [4-5]. RISCS can run ELSA using draws from distributions for critical uncertainties (e.g., permeability, porosity, thickness) and numerous well leakage permeabilities. Multiple iterations using values drawn from distributions provide for probabilistic determination of the extents and magnitudes of CO_2 plumes and brine pressure perturbations. We conduct four leakage scenarios wherein we vary the permeability of existing wells the leaking wells. Existing wells are assigned leakage permeabilities of 10^{-10} m^2, 10^{-12} m^2, 10^{-14} m^2, and 10^{-16} m^2, corresponding to each of the leakage scenarios, respectively. For the application presented here, we do not iterate ELSA with values drawn from other distributions. ELSA is used to simulate 4 $MtCO_2$/yr injection continuously for 30 years into the Mt. Simon sandstone, 2.6 and 2.4 km underground (Location 11, and Location 17, respectively). Simulations are conducted with a 200 km radial extent, and data are recorded on a 150 km x 150 km grid at 1 km spacing. For the injection locations chosen for this analysis (11, 17), CO_2 is injected into the center of the recording grid. Consequently, data are recorded on a square grid extending out 75 km horizontally (east and west) and vertically (north and south) from the injection location.

7.3.3 Three-Dimensional Geospatial Data

Three-dimensional geospatial data locates hydrostratigraphic units and the wells that penetrate these units. These wells may serve as leakage pathways, allowing injected CO_2 or displaced brine to migrate into overlying units. Active wells locate existing subsurface activities and may be modeled as leakage pathways in the geophysical fluid flow simulations; inactive wells do not locate existing subsurface activities, but they may also be modeled as leakage pathways in the geophysical fluid flow simulations. The Michigan Sedimentary Basin contains sixteen named hydrostratigraphic units. For ELSA, the hydrostratigraphic sequence must be represented by a layer cake of permeable aquifers and impermeable aquitards. Consequently, the three-dimensional geospatial data must be appropriately combined. For the analysis presented here, high- and mixed-permeability units are combined and modeled as aquifers—except for the Prairie du Chien (low permeability in the chosen injection locations)—and low probability units are modeled as aquitards (**Table 1**).

Table 1: Sixteen Hydrostratigraphic Units Throughout the Michigan Basin and their Representation in ELSA for the Four Chosen Injection Locations.

HYDROSTRATIGRAPHIC UNITS	ELSA SEQUENCE
Quarternary	**Aquifer 1** (Jurassic is absent)
Jurassic	
Upper Pennsylvanian	
Lower Pennsylvanian	
Bayport-Michigan	
Marshall	
Devonian-Mississippian	**Aquitard 1**
Traverse-Dundee	**Aquifer 2**
Silurian-Devonian	
Collingwood	**Aquitard 2**
Trenton-Black River	**Aquifer 3**
St. Peter	
Prairie du Chien	**Aquitard 3**
Galesville	**Aquifer 4**
Eau Claire	**Aquitard 4**
Mt. Simon	**Aquifer 5**
Pre-Cambrian Basement	

7.3.4 Leakage Impact Valuation (LIV) Method

The LIV method [6-8] is a thorough scenario-based approach to identifying the financial costs that are triggered by leakage and the stakeholders that incur these costs. LIV identifies the costs incurred by ten different stakeholders—including the injection operator and regulator, subsurface activity operator and regulator, surface residents and groundwater users, among others. Reasonably plausible storylines are developed for low- and high-cost cases for four broad classes of leakage outcomes: 1.) Leakage only; 2.) Leakage interferes with a subsurface activity; 3.) Leakage reaches an Underground Source of Drinking Water (USDW); or 4.) Leakage reaches the surface. From these storylines and leakage outcomes, multiple costs are estimated across six cost categories: Diagnostic Monitoring, Containment Activities, Environmental Remediation, Damages, Climate Compensation, and Site Closure. Estimates of costs triggered by individual leakage events in the Michigan Sedimentary Basin using the LIV method are detailed elsewhere [7], but, for Nth-of-a-kind projects, estimated costs range from $2.2M for a low-cost leakage only outcome to $154.7M for a high-cost event where CO_2 affects groundwater and migrates to the surface.

7.4 Results

Figure 2 shows the increase pressure in the brine in the bottom two aquifers—Mt. Simon and Galesville—after 30 years of continuous CO_2 injection. CO_2 injected into the Mt. Simon increases the pressure, displacing brine that then leaks along well pathways through the Eau Claire aquitard and into the overlying Galesville aquifer.

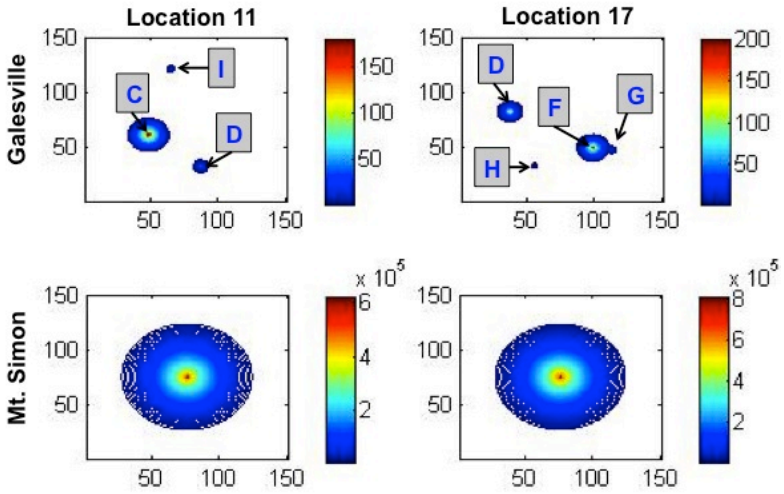

Figure 2: Brine Pressure Elevation in Bottom Two Aquifers, Mt Simon and Galesville after 30 Years of Continuous CO_2 Injection – Brine leaks along well pathways marked by the letters through the impermeable Eau Claire unit into the overlying Galesville aquifer. Units are in Pascals, and the axes are in kilometres.

Figure 3 shows temporal risk profiles for these two locations as monetized by *RISCS*. The monetized values for the extreme leakage cases we present. Three leakage outcomes occur at Location 11. In year 12, a ~$30M brine leakage event occurs through well C. A ~$38M brine leakage event occurs twelve years later, through well D, and a ~$35M brine leakage event occurs two years after that, in year 26, through well I. Location 17 has more leakage events that incur more costs: two ~$40M events in years 15 and 28 (F and H, respectively), and three ~26M events in years 20, 21, and 26 (D, G, and X, respectively). The event labeled "X" on does not occur directly as the result of leakage out of the Mt. Simon. X occurs because brine has migrated up to the Traverse-Dundee / Silurian-Devonian, where it then interferes with oil and gas production.

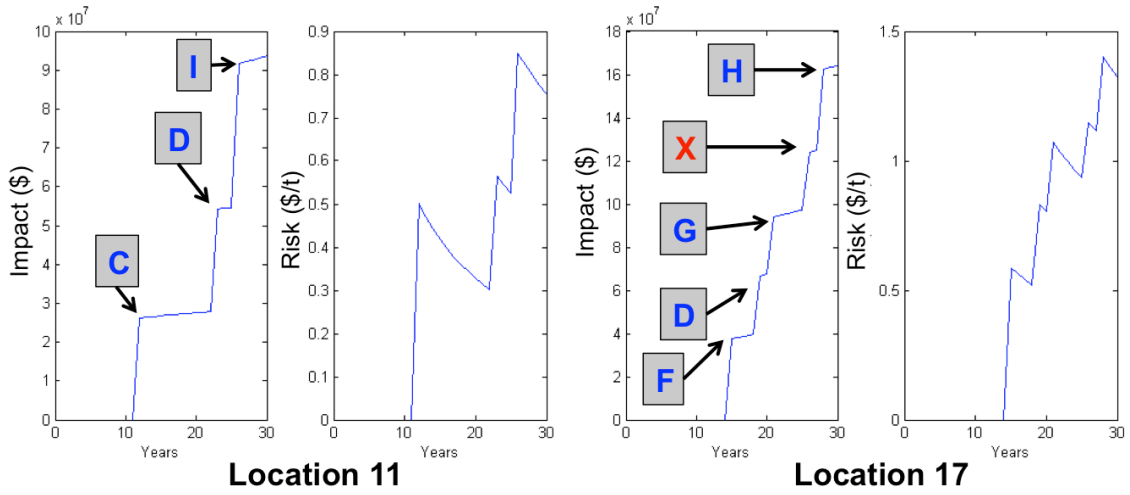

Figure 3: Temporal Risk Profiles for Continuous CO_2 Injection into the Mt. Simon Aquifer at Locations 11 and 17 – The letters identify leakage events and where these leakage events occur. "X" is identifies brine migration that interferes with oil and gas production in the Traverse-Dundee / Silurian-Devionian units. Monetized risk values are high due to the extreme leakage scenarios we present.

The values shown in **Figure 3** may be high for a few reasons. Every existing well in this application leaks, and with a very high permeability. Since we only vary this parameter (well permeability) and run one simulation for each of four values, the probabilities derived by *RISCS* can only be step functions in increments of 25%. More simulations that vary more parameters may reduce the probabilities that enter into the *RISCS* calculations. Further, the values are not discounted to the present; indeed, these values represent costs in present dollars in the year the leakage or interference events occur. Finally, these results are for continuous injection of CO_2 for 30 years, regardless of whether a leakage event has occurred. If leakage occurs and is detected, regulators will likely require that CO_2 injection be halted and the leak remedied. The likelihoods of future leaks and interferences are thus reduced. These values for leakage and interference risk over time should be combined with the increasing probability of time that accumulations of leaked fluids will be detected, and interventions remedy the leakages.

7.5 Conclusions and Discussion

Our approach—the Risk Interference Subsurface CO_2 Storage (RISCS) model—facilitates probabilistic assessment of leakage risk from CO_2 storage reservoirs. *RISCS* monetizes leakage risk by combining geophysical fluid flow simulations, 3D geospatial data, and estimates of costs triggered by leakage. *RISCS* can be used to identify of the potential influence of leakage risk on individual site-selection, and allows for a broader inquiry into how stakeholder groups may be differentially impacted across injection sites. Our results highlight how leakage risk is site-specific, the complicated tradeoffs between injection locations, the dependence of leakage risk on the three-dimensional proximity of injection to pathways and potential interferences, and how past and present uses of the subsurface may constrain the viability of locations for future CO_2 storage projects.

7.6 References

[1] NETL (2010). "Carbon Sequestration Atlas of North America" *Third Edition.* United States Department of Energy, National Energy Technology Laboratory.

[2] Bielicki, J., Bael, D., Pollak, M. Rahimi, M., and Wilson, E., (2011). "RISCS: Risk Interference of Subsurface CO_2 Storage." (2011). with D. Bael,, M. Pollak, M. Rahimi, and E. Wilson. *Sixth Trondheim CCS Conference on CO_2 Capture, Transport, and Storage.* Trondheim, Norway. June 14-16, 2011. Accepted oral presentation.

[3] Bielicki, J., Pollak, M., Wilson, E., Fitts, J., and Peters, C. (2012) "Spatially Integrated Assessment of Leakage Risk from CO2 Storage Reservoirs from Multiple Stakeholder Perspectives". (2012). *DOE-NETL Tenth Annual Conference on Carbon Capture, Utilization, and Sequestration*. Pittsburgh, PA. April 30-May 3, 2012. Accepted Poster Presentation.

[4] Nordbotten, J., Celia, M., Bachu, S., and Dahle, H. (2005). "Semi-Analytical Solution for CO_2 Leakage through an Abandoned Well." *Environmental Science & Technology, 39(2),* 602-6011.

[5] Celia, M., and Nordbotten, J. (2009). "Practical Modeling Approaches for Geological Storage of Carbon Dioxide." *Ground Water, 47(5),* 627-638.

[6] Pollak, M., Bielicki, J., Dammel, J., Wilson, E., Fitts, J., and Peters, C., (2012a). "The Leakage Impact Valuation (LIV) Method for Leakage from Geologic CO2 Storage Reservoirs." *11th International Conference on Greenhouse Gas Technologies*, Kyoto, Japan, November 18-22, 2012.

[7] Pollak, M., Bielicki, J., Fitts, J., Peters, C., and Wilson, E. (2012b). "Causes and Consequences of the Financial Impacts of Leakage from Geologic CO_2 Storage Reservoirs." In preparation for *Energy Policy.*

[8] Pollak, M., Dammel, J., Bielicki, J., Wilson, E., Fitts, J., and Peters, C. (2012c) "Estimating Financial Consequences of Leakage from Geologic Sequestration". (2012c). With Pollak, M. (presenter), Wilson, E., Dammel, J., Fitts, J., and Peters, C.. *DOE-NETL Tenth Annual Conference on Carbon Capture, Utilization, and Sequestration*. Pittsburgh, PA. April 30-May 3, 2012. Accepted Oral Presentation.

Chapter 8. Evaluating the competitiveness of CCS in the U.S. energy market in the context of leakage costs and subsurface liabilities

8.1 Introduction

The potential for fossil energy technologies to remain viable and a significant part of our energy technology mix depends on the development of technically feasible, environmentally safe, and cost-effective carbon capture and sequestration technologies (CCS). A successful CCS approach would require carbon sequestration (CS) to demonstrate low probability of CO_2 leakage, minimal likely impact on health and safety, and the ability to compete in the energy marketplace.

This chapter examines the economic risk of various CCS and CS approaches in a competitive U.S. energy market in comparison with competing energy production and use technologies. To support this analysis, we identified the necessary compliance activities associated with injection, geological storage, and possible leakage. This became the framework for a cost calculator tool we developed called the "Economic and Policy Drivers Module" (EPDM). The EPDM calculates the cost of CS together with the potential costs incurred by CO_2/brine leakage for a particular geologic setting, injection scenario, and CO_2 leakage scenario. This chapter demonstrates the EPDM for the case on injection into the Mt. Simon formation in the Michigan sedimentary basin for an injection site in Ottawa County, Michigan.

In addition, we used MARKAL, an established tool, to assess the costs required in order for CCS to be competitive in the energy systems marketplace. MARKAL is an integrated energy systems analysis model. Using the EPDM together with CCS-MARKAL, we conducted simulations that generate future projections of the energy market competitiveness of CCS in comparison to other energy technologies, and we examined the sensitivity to discount rates and carbon tax. This analysis should be considered preliminary and qualitative, as there remains a high degree of uncertainty about MARKAL model parameters and the lack of available documentation. The exercise did, however, provide valuable conceptual and qualitative findings, which would need to be validated by comparison with other energy systems modeling tools.

Finally, this chapter demonstrates the EPDM in the context of a basin-scale leakage risk model prediction for a hypothetical injection into the Mt. Simon formation underlying Ottawa County in the state of Michigan.

8.2 Development of the Economic and Policy Drivers Module (EPDM)

We developed an "Economic and Policy Drivers Module" (EPDM) for the purpose of compiling the costs and economic drivers of CCS deployment at a specific site, with given geological characteristics, and plausible leakage scenarios. The EPDM is a compilation of algorithms for compliance activities, which multiplies unit costs by quantities from the project type profiles and by the factors appropriate for the project type to produce a project level cost. The EPDM developed for this project incorporates geological formation information from the Mount Simon deep saline aquifer underlying Ottawa County, Michigan. Thus, the results are site specific and dependent on the trade-offs between discounting, leakage rate, and the individual cost module. The EPDM can be used to determine which parameters might be major cost drivers to the overall cost of sequestration approaches, and which are important to estimate CO_2 leakage (e.g. subsurface and atmospheric leakage, permeability, depth, existing wells and others).

The current version of the EPDM accounts for only carbon injection and sequestration costs; it does not account for carbon capture and transport. The online EPDM cost calculator can be downloaded from http://www.subsurfacerisk.umn.edu/. The main sources of data that were used to develop the EPDM are EPA (2008), Rubin et al. (2008), MIT (2009), IPCC (2005), Gresham (2010), Heddle et al. (2003), and Wyoming (2009).

8.2.1 EPDM Unit Cost Modules

The EPDM comprises eight unit cost modules, depicted as green boxes in Figure 1. The unit costs for the Geologic Site Characterization Unit Costs (SC) module are shown in the screenshot in Figure 2. The purpose of geologic site characterization is to determine whether a site is suitable and safe for sequestration, and to compile the necessary data for the permit application. The process includes geologic, geophysical, and engineering evaluation.

The unit costs for the Injection Well Construction (IW) module are shown in the screenshot in Figure 3, and the unit costs for the Well Operation (WO) module are shown in the screenshot in Figure 4. The WO cost category includes cost elements related to the operation of the injection wells, including measuring and monitoring equipment, electricity costs, O&M costs, pore space costs, contribution to a long term monitoring fund, repair and replacement of wells and equipment, and estimated costs for the possibility of failure at the site and the need to relocate a sequestration operation. Figures 5, 6, and 7 show screenshots of the three input modules for the WO module: the costs for Monitoring during Injection (IM), Review Study & Corrective Action (RS), and Mechanical Integrity Tests (MI).

The unit costs for the Post-Injection Monitoring and Verification (MV) module are shown in the screenshot in Figure 8. After the injection phase has ended, it is necessary to prepare the site for long-term

monitoring and eventual closure in a safe and secure manner that protects USDWs. This involves the plugging of injection wells, removal of surface equipment, and land restoration. It also includes long term requirements for monitoring the site to ensure safety and to confirm an understanding of the CO_2 distribution in the subsurface.

The unit cost for Financial & Insurance Considerations (FI) is a single value, as shown in the screenshot in Figure 9. At present, a commercially viable insurance solution against CCS liabilities has not yet emerged. However, there exists on governmental model as an analogue to the issue of long-term catastrophic loss coverage, i.e. the Price Anderson Act for the nuclear industry. While direct extrapolation of this act to the CCS industry is not appropriate, it could still possibly be used as a proxy for monetizing the long-term liability of CCS. This would then represent the upper bound of the cost range. Based on this rationale, the value assumed for the average annual premium for FI is taken to be the premium for a single-unit reactor site, $400,000. Also in the FI category are the General and Administrative Costs (AD), which are shown in the screenshot in Figure 10. The AD costs are included for both the project development and operating phases. The costs are specified as a percentage of either capital costs or annual operating costs. The last in the FI category are the costs associated with Financial Responsibility (FR), as shown in the screenshot in Figure 11. These are the costs needed for the operator to demonstrate and maintain financial responsibility, and have the resources for activities related to closing and remediating GS sites.

The unit costs for Atmospheric Leakage (AL) are determined from the costs associated with over-pressurization of the formation, incomplete sealing, and induced seismicity, as shown in the screenshot in Figure 12.

The unit costs for Subsurface Liabilities (SL) are determined from the costs associated with water quality deterioration, CO_2 and brine migration, and mobilization of contaminants, as shown in Figure 13. At this time only the risks from interference with underground sources of drinking water (USDW) are considered. Future developments of the EPDM should include costs associated with interferences with waste injection (WI) and energy reserves (ER).

Finally, the unit costs for Site Closure and Reclamation (SC&R) are shown in the screenshot in Figure 14. These include the costs for well capping, removal of above-ground facilities, and site reclamation.

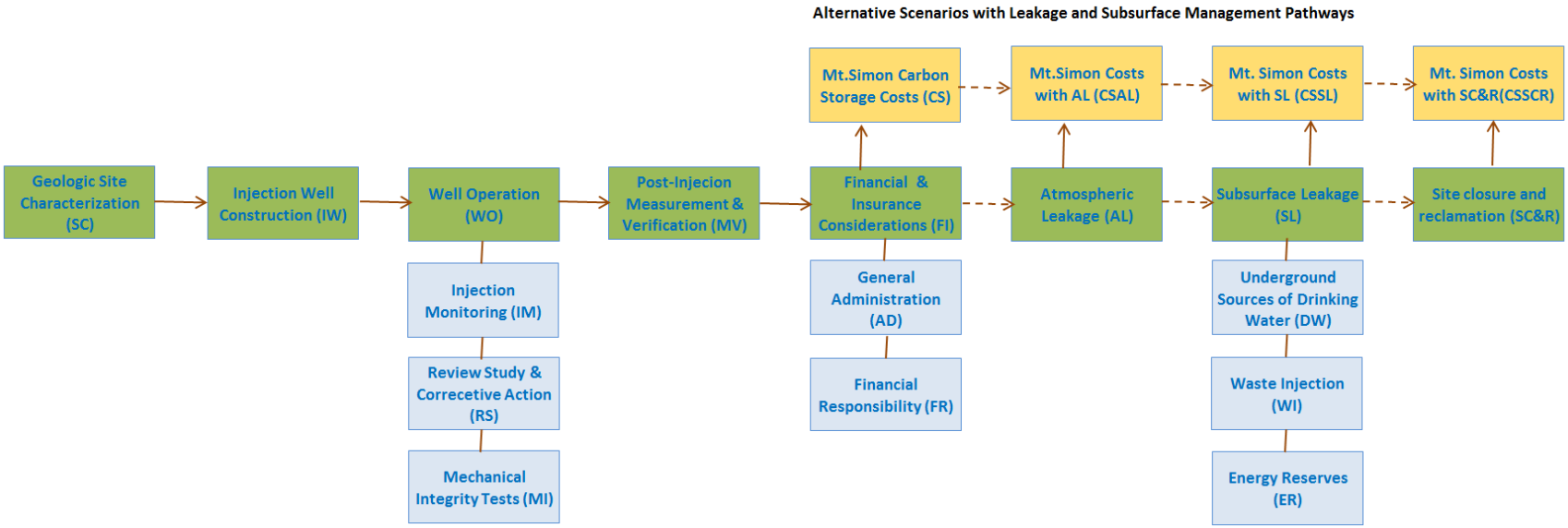

Figure 1. Outline of the Economic and Policy Drivers Module (EPDM). The main cost elements are shown in green, with additional input modules in blue. The four possible output modules represent four alternative scenarios for leakage and subsurface management pathways.

GEOLOGICAL SITE CHARACTERIZATION COST MODULE						
COST ITEM	**UNIT COST**	**QUANTITY**	**COST TYPE**	**TOTAL COST**	**UNITS OF TOTAL COST**	**NOTES**
Mapping	106.31	60	$ per hr	6379	Per site	
Seismic history analysis	106.31	60	$ per hr	6379	Per site	
Data on confining systems	106.31	24	$ per hr	2551	Per site	
Geomechanical research	106.31	120	$ per hr	12757	Per site	
Geomechanical research	3000	1	$ per core	3000	Per core	
Info on aquifers	106.31	60	$ per hr	6379	Per site	
Water-rock-CO2 chemistry	106.31	240	$ per hr	25514	Per site	
Water-rock-CO2 chemistry	10000	1	lab fee	10000	Per site	
Aerial survey of land	3000	1	$ per site	3000	Per site	
USDWs	106.31	24	$ per hr	2551	Per site	
Geologic characterization report	106.31	240	$ per hr	25514	Per site	
Aerial survey of land	400	VAR	$ per sq mile	46332	Per square mile survey	should assume survey is 2x size of site
Geomechanical research	75	VAR	$ per foot	461250	Per foot of test well	
3D seismic survey	75000	VAR	$ per sq mile	4343649	Per square mile	
List injection zone penetrations	106.31	12	$ per hr	1276		
List containment penetrations	106.31	12	$ per hr	1276		
List water wells	106.31	36	$ per hr	3827		
				4961635		
		Annualized Cost		**507374**		

Figure 2. EPDM Cost Calculator screenshot: The elements included in the Geologic Site Characterization (SC) Unit Costs module.

Injection Well Construction (IW)	1					
EPA WELL INJECTION COST MODULE						
COST ITEM	**UNIT COST**	**QUANTITY**	**COST TYPE**	**TOTAL COST**	**UNITS OF TOTAL C**	**NOTES**
Front end engineering/design	200000	2	$ per site	400000	Per site	
Pumps	20000	2	$ per site	40000	Per site	
UIC permit filling	10000	2	$ per site	20000	Per site	
Land use, air emissions, water emissions permits	100000	2	$ per site	200000	Per site	
Wellhead and control equipment	FORMULA	1	$ per well	222961	Per site	$500x(max tons per day injected per well)^0.6
UIC permit filling	5000	VAR	$ per injection we	10000	Per injection well	
Front end engineering/design	40000	VAR	$ per injection we	80000	Per injection well	
Obtain right of way for surface use	20000	VAR	$ per injection we	40000	Per injection	half cost is legal fees for developer, other half is bonus to landowner
Standard injection well cost	210-280	VAR	$ per ft	1537500	Per ft	USUALLY 9000 FT.
Corrosion resistant tubing	1.1	VAR	$ per ft - inch dian	54120	Per ft inch diameter	This is an additional/optional cost
Corrosion resistant casing	1.75	VAR	$ per ft - inch dian	86100	Per ft inch diameter	This is an additional/optional cost
Cement entire length of well	1.15	VAR	$ per ft - inch dian	56580	Per ft inch diameter	
Use CO2 resistant cement	25%	VAR	$ per ft - inch dian	12300	Per ft inch diameter	Adds 25% to total cementing costs
Lease rights for subsurface use	50	VAR	$ per acre/year	3706449.222	Per acre	additional injection fees under O&M costs
Pumps	1500	VAR	$ per HP	18000	Per HP	Assuming 12 HP
All elements of pipeline costs	60000	VAR	$ per inch - mile		Per inch - mile	
Land use, air emissions, water emissions permits	20000	VAR	$ per square mile	1158307	Per square mile	
Set packer no more than 100 above highest perforation	N/A	N/A	N/A		N/A	Affects tubing length
Set packer no more than 300 above highest perforation	N/A	N/A	N/A		N/A	Affects tubing length
Injection pressure limited to 90% of injection fracture pres	N/A	N/A	N/A		N/A	Affects max flow of well & number of wells needed

Figure 3. EPDM Cost Calculator screenshot: The elements included in the Injection Well Construction (IW) Unit Costs module.

Well Operation (WO)						
EPA WELL OPERATION COST MODULE						
COST ITEM	**UNIT COST**	**QUANTITY**	**COST TYPE**	**TOTAL CO**	**UNITS OF TOTAL**	**NOTES**
Develop corrosion monitoring/preventi	53.52	24	$ per hr	1284.48	Per site	
Injection well O & M	75000	2	$ per site	150000	Per site	
Continuous measurement/monitoring e	15000	VAR	$ per well	30000	Per well	
Equipment to add tracers	10000	VAR	$ per well	20000	Per well	
Starndard measuring/monitoring equipr	10000	VAR	$ per well	20000	Per well	
Electricity cost for pump, equipment	0.064	VAR	$ per kWh	3025774.1	Per kWh	
Injection well O & M	3	VAR	$ per ft per well per yr	18450	Per ft per well per yr	
Land use rent, rights of way	5	VAR	$ per acre per yr	185322.46	Per acre per yr	
Pore space use costs	0.35	VAR	$ per metric ton	3325000	Per metric ton	
Property taxes & insurance	0.03	VAR	$ per $1 CAPEX	705000	Per $1 CAPEX	
Tracers in injected fluid	0.05	VAR	$ per ton CO2 injected	475000	Per ton CO2 injected	
Contribution to long term monitoring, i	0	VAR	$ per ton CO2 injected	0	Per ton C02 injected	
Repair, replace wells/equipment	1%	VAR	$ per initial cost		Per initial cost	Assume 1% initial well/equipment cost
Failure of containment - build new site,	0.08%	1%	$ per total capital costs per yr		Per total capital cost	Assume 1% chance of failure over injection life and then 0.083% of total capital costs would cover contingency
				7955831		

Figure 4. EPDM Cost Calculator screenshot: The elements included in the Well Operation (WO) Unit Costs module.

Monitoring during Injection (IM)

Once injection begins, a program for monitoring of CO2 distribution is required.

EPA MONITORING DURING INJECTION COST MODULE

COST ITEM	UNIT COST	QUANTIT	COST TYPE	TOTAL COST	UNITS OF TOTAL COST	NOTES		
Develop geochemical baseline for injection/confining zones	200	4	$ per injection well	1600	Per injection well	Injection plus monitoring well - 07		
Develop baseline of surface air CO2 flux for leakage monitoring	35000	1	$ per station	35000	Per station			
Conduct front-end engineering and deisgn (monitoring wells)	20000	1	$ per site	20000	Per site			
Conduct front-end engineering and deisgn (monitoring wells)	5000	1	$ per shallow monitoring well	30000	Per shallow monitoring well			
Obtain rights of way for surface uses (monitoring wells)	10000	1	$ per monitoring well site	60000	Per monitoring well site			
Obtain rights of way for surface uses (monitoring sites)	5000	1	$ per air monitoring station site	5000	Per air monitoring station site			
Downhole safety shut off valve	15000	1	$ per site	15000	Per site			
Downhole safety shut off valve	2	100	$ per ft	200	Per ft	MUST be at least 100 ft above packer		
Standard monitoring well cost (ABOVE injection zone)	100	VAR	$ per ft	900000	Per ft	Typical for a slim-hole design down to	9000	ft
Standard monitoring well cost (INTO injection zone)	100	VAR	$ per ft	900000	Per ft	Typical for a slim-hole design down to 9000 ft		
Pressure & temperature gauges for monitoring wells	10000	1	$ per well	60000	Per well			
Salinity, CO2, tracer, etc… monitoring equipment	10000	1	$ per well	60000	Per well			
Develop plan and implement surface air/soil monitoring	106.31	80	$ per hr	8504.8	Per site			
Develop plan and implement surface air/soil monitoring	140000	1	$ per monitoring site	140000	Per monitoring site			
Surface microseismic detection equipment	50000	1	$ per site	50000	Per site			
Monitoring well O&M	25000	1	$ per site	25000	Per site			
Annual cost of air/soil surveys & equipment	10000	1	$ per station per yr	10000	Per station per yr			
Annual cost of passive seismic equipment	10000	1	$ per station per yr	10000	Per station per yr			
Periodic 3D seismic surveys	75000	VAR	$ per square mile	4343649	Per square mile			
Complex modeling of fluid flows/migration every 5 years	53.52	204	$ per hr	21836	Per injection well			
Annual reports to regulators	53.52	20	$ per hr	1070	Per report			
Quarterly reports to regulators	53.52	15	$ per hr	803	Per report			
Monthly reports to regulators	53.52	8	$ per hr	428	Per report			
				6698091				
			Annualized Cost	**704963**				

Figure 5. EPDM Cost Calculator screenshot: The elements included in the Monitoring during Injection (IM) Unit Costs module.

Review Study & Corrective Action (RS)						
This aspect of the cost analysis includes fluid flow and reservoir modeling to predict the movement of the injected CO2 and pressure changes during and after injection.						
It also includes those cost elements pertaining to the identification, evaluation, and remediation of existing wells within the area of review.						
EPA REVIEW STUDY & CORRECTIVE ACTION COST MODULE						
COST ITEM	**UNIT COST**	**QUANTITY**	**COST TYPE**	**TOTAL CO**	**UNITS OF TOTA**	**NOTES**
Simple fluid flow calculations to predict CO2 fluid flow	53.52	48	$ per hr	5138	Per injection well	
Complex modeling of CO2 fluid flows & migration over 100 yrs	53.52	204	$ per hr	21836	Per injection well	
Complex modeling of CO2 fluid flows & migration over 10000 yrs	53.52	216	$ per hr	23121	Per injection well	
Search physically for old wells (artificial penetrations)	10800	1	$ per hr per square r	625486	Per site	
Search physically for old wells (artificial penetrations)	5000	1	one time fee (mobili	5000	1 time fee	
Search physically for old wells (artificial penetrations)	13000	VAR	$ per square mile	752899	Per square mile	
Evaluate integrity of wells that penetrate containment system	106.31	24	$ per hr	2551	Per site	
Evaluate integrity of wells that penetrate containment system	53.52	6	$ per hr	321	Per site	
Evaluate integrity of wells that pose a threat to USDWs	53.52	6	$ per hr	321	Per site	
Remediate old wells in AoR that pose a risk to USDWs	74000	1	$ per site	74000	Per site	30000 for clean out, 13000 to replug and 11000 to log 2 cement plugs, water well remediation is 20000
				1510673		
		Annualized Cost		**154481**		

Figure 6. EPDM Cost Calculator screenshot: The elements included in the Review Study & Corrective Action (RS) Unit Costs module.

Mechanical Integrity Tests (MI)

A CO2 injection well will periodically undergo integrity testing to ensure mechanical soundness, lack of corrosion, and ability to sustain pressure.

There are several such tests that are typically used, and they include both pressure tests and wireline logs. These technologies are well established and have been used for decades for underground injection operations.

EPA MECHANICAL INTEGRITY TESTS COST MODULE

COST ITEM	UNIT COST	QUANTITY	COST TYPE	TOTAL COST	UNITS OF TOTA	NOTES
Simple fluid flow calculations to predict CO2 fluid flow	53.52	48	$ per hr	5138	Per injection well	
Complex modeling of CO2 fluid flows & migration over 100 yrs	53.52	204	$ per hr	21836	Per injection well	
Complex modeling of CO2 fluid flows & migration over 10000 yrs	53.52	216	$ per hr	23121	Per injection well	
Search physically for old wells (artificial penetrations)	10800	VAR	$ per hr per square mile	625486	Per site	
Search physically for old wells (artificial penetrations)	5000	1	one time fee (mobilizatio	5000	1 time fee	
Search physically for old wells (artificial penetrations)	13000	VAR	$ per square mile	752899	Per square mile	
Evaluate integrity of wells that penetrate containment system	106.31	24	$ per hr	2551	Per site	
Evaluate integrity of wells that penetrate containment system	53.52	6	$ per hr	321	Per site	
Evaluate integrity of wells that pose a threat to USDWs	53.52	6	$ per hr	321	Per site	
Remediate old wells in AoR that pose a risk to USDWs	74000	1	$ per site	74000	Per site	30000 for clean out, 13000 to replug and 11000 to log 2 cement plugs, water well remediation is 20000
				1510673		

Figure 7. EPDM Cost Calculator screenshot: The elements included in the Mechanical Integrity Tests (MI) Unit Costs module.

Post-Injection Monitoring and Verification (MV)
[Well Plugging, Equipment Removal, Site Care and M&V]
After the injection phase has ended, it is necessary to prepare the site for long-term monitoring and eventual closure in a safe and secure manner that protects USDWs. This involves the plugging of injection wells, removal of surface equipment, and land restoration. It also includes long term requirements for monitoring the site to ensure safety and to confirm an understanding of the CO2 distribution in the subsurface.

EPA POST INJECTION MEASUREMENT & VERIFICATION COST MODULE

COST ITEM	UNIT COST	QUANTITY	COST TYPE	TOTAL COST	UNITS OF TOTAL COST	NOTES
Flush wells with buffer fluid before plugging	500	1	$ per site	500	Per site	
Flush wells with buffer fluid before plugging	0.1	VAR	$ per ft	615	Per ft	
Plug injection wells	24000	1	$ per site	24000	Per site	
Perform an MIT prior to plugging to evaluate cement integrity	2000	1	$ per site	2000	Per site	
Perform an MIT prior to plugging to evaluate cement integrity	4	VAR	$ per ft	24600	Per ft	
Plug monitoring wells	12000	1	$ per site	12000	Per site	
Remove surface equipment, structures, restore vegetation (injection)	25000	VAR	$ per injection v	50000	Per injection well	
Remove surface equipment, structures, restore vegetation (monitoring)	10000	VAR	$ per monitorin	60000	Per monitoring well	
Remove surface equipment, structures, restore vegetation (monitoring)	5000	VAR	$ per monitorin	30000	Per monitoring station	
Document plugging & post injection process	53.52	120	$ per hr	6422.4	Per site	
Post injection monitoring well O&M	25000	1	$ per site	25000	Per site	
Post injection monitoring well O&M	3	VAR	$ ft per well pe	36900	Ft per well per yr	
Post injection air and soil surveys	10000	VAR	$ per station pe	20000	Per station per yr	
Post injection seismic survey (assume every 5 yrs)	75000	VAR	$ per square mi	4343649.469	Per square mile	
Periodic post injection reports to regulators (every 5 years)	53.52	40	$ per hr	2140.8	Per report	
				4637828		
			Annualized Cost	**474262**		

Figure 8. EPDM Cost Calculator screenshot: The elements included in the Post-Injection Monitoring and Verification (MV) Unit Costs module.

Financial & Insurance Considerations (FI)

At present, a commercially viable insurance solution against the CCS liabilities has not yet evolved. However, there exists one governmental model as an analogue to this issue of long term catastrophic loss coverage i.e. the Price- Anderson Act for the nuclear industry. While direct extrapolation of this act to the CCS industry is not appropriate, it could still possibly be used as a proxy for monetizing the long-term liability of CCS. This would then represent the upper bound of the cost range.

The average annual premium for a single-unit reactor site is ($)	**400000**	Source: CCS Risk Pennsylvania, 2009

Figure 9. EPDM Cost Calculator screenshot: The elements included in the Financial & Insurance Considerations (FI) Unit Costs module.

General and Administrative Costs (AD)

General and administrative costs are included as unit costs for both the project development and operating phases. The costs are specified as a percentage of either capital costs or annual operating costs.

EPA GENERAL & ADMINISTRATIVE COST MODULE

COST ITEM	UNIT COST	QUANTITY	COST TYPE	TOTAL COST	UNITS OF TOTAL COST	NOTES
Project development G&A	20%	VAR	Percentage	257774.5404	Per site	20% of initial capital expenditure
Operating G&A	20%	VAR	Percentage	2160041.937	Per site	20% of annual operating costs
			$	2417816		

Figure 10. EPDM Cost Calculator screenshot: The elements included in the General and Administrative (AD) Unit Costs module.

Financial Responsibility

It will be necessary for the operator to demonstrate and maintain financial responsibility, and have the resources for activities related to closing and remediating GS sites.

EPA FINANCIAL RESPONSIBILITY

COST ITEM	UNIT COST	QUANTITY	COST TYPE	TOTAL COST	UNITS OF TOTAL	NOTES
Demonstrate financial ability to close site	53.52	8	$ per hr	428	Per financial report	
Demonstrate financial ability for post-injection	53.52	4	$ per hr	214	Per financial report	
				642		

Figure 11. EPDM Cost Calculator screenshot: The elements included in the Financial Responsibility (FR) Unit Costs module.

Chronic low-level releases to the surface which cause health or ecological damage resulting from	
Mechanical failure of piping or tankage above or below ground	2500000
Orphan wells not discovered prior to injection	5000000
Induced over-pressurization	7500000
Incomplete geological seal resulting from inaccurate characterization of subsurface geology	7500000
Induced seismicity	7500000
TOTAL Cost	**46500000**
Annuitized Cost	4755063
Expected Cost = Prob (event)*cost of event + Prob(No-event)*cost of no-event	**2377531**

Figure 12. EPDM Cost Calculator screenshot: The elements included in the Atmospheric Leakage (AL) unit costs module.

Subsurface Liabilities

[1] Water quality contamination during the fluid phase and resulting from		
Plume migration outside of the permitted area	2500000	This represents the upper bound of the cost range; Source: Wyoming Report, 2009
Unpermitted leakage of CO2 contaminants into aquifer	7500000	Assuming that the contaminated source is heavily utilized for drinking water or by sensitive receptors; Source: Wyoming Report, 2009
Unpermitted leakage of drilling fluid contaminants into aquifer	1000000	Source: Wyoming Report, 2009
Unpermitted rock/acidified water interaction contaminates aquifer by carryover of dissolved contaminants	7500000	Source: Wyoming Report, 2009
[2] Entrained contaminant (non-CO2) releases	5000000	Assuming that the contaminants are released into a drinking water source, mitigation could include establishing a temporary-semi-permanent-permanent replacement drinking source; the contaminated source is heavily utilized for drinking water or by sensitive receptors; Source: Wyoming Report, 2009
[3] Formation fluid and brine removal contingency considerations	5000000	For a mid-range 2Mtpy injection project with a 30-year life, this would set an upper mitigation bound for this risk category at $6M for relief wells, $8M for pumping, and $8M for brine water treatment, totaling $22M. Source: Wyoming Report, 2009
TOTAL Cost	**28500000**	
Annuitized Cost	2914393	
Expected Cost = Prob (event)*cost of event + Prob(No-event)*cost of no-event	**1457197**	

Figure 13. EPDM Cost Calculator screenshot: The elements included in the Subsurface Liabilities (SL) unit costs module.

Site closure and reclamation (SC&R)				
1	**Site Closure and Reclamation Costs ($)**			
		Well Capping	500000	(For a field of 3 injection wells, the total estimated cost is in the range of $.9M to $1.2M with an average of $1M)- Source: Wyoming Report, 2009
		Removal of above-ground facilities	1000000	the range of demolition and disposal costs for a geologic carbon sequestration operation is estimated to be $0.5M to $3.5M is estimated, with an average of $2M
		Site reclamation	1000000	Typical surface reclamation costs average $400 per acre. Surface disturbance reclamation is estimated to range from $0.2M to $4M
	TOTAL Cost		**2500000**	
	Annuitized Cost		255649	
	Expected Cost = Prob (event)*cost of event + Prob(No-event)*cost of no-event		**127824.3**	

Figure 14. EPDM Cost Calculator screenshot: The elements included in the Site Closure and Reclamation (SC&R) unit costs module.

8.2.2 EPDM Total Cost Estimates

For this project, the EPDM was developed and demonstrated for a cost analysis of CO_2 injection and storage in the Mt. Simon deep saline aquifer underlying Ottawa County in the state of Michigan. The EPDM computes costs eight categories (SC, IW, WO, MV, FI, AL, SL, and SC&R) using site details as shown in Table 1 for the Mt. Simon injection analysis considered in this work.

Table 1. EPDM site characterization details used in this project analysis.

Mt. Simon Sandstone (IL)		
Depth (m)	1,845	
Depth (ft)	6150	
Net Thickness (m)	240	
Aerial Survey (mi2)	58	
Injection rate MtCO2/yr	9.5	
Injection rate CO2 bpd	89174629	
Number of Injection Well	2	
Plume Size Estimate(km2)	300	
Plume Size Estimate(acre)	74129	
Pumping & Field Power (7,196 kW)	47277720	
Years of Injection	40	
Monitoring Wells	6	
Pipeline Transport Base Case Parameter	**Unit**	
Pipeline Length (100 km)	miles	62.1
CO2 Inlet Pressure	MPa	15.2
CO2 Outlet Pressure	MPa	10.3
Pressure Drop per Unit Length	Pa/m	49
Pipe Diameter	inches	8
Nominal Pipe Size	inches	8
Capital Cost	Million Dollar	23.5
Annuity Factor @ 10% for 30 years	**0.102**	

The EPDM produces an annual rule cost for each compliance activity in each of the 30 years in the analysis period. The EPDM calculates these annual estimates in non-discounted dollars and in present value and annualized dollars. A screenshot of the calculated output costs is shown in Figure 15, for the case of a 10% discount rate while annuitizing the present value of costs. Four output scenarios are considered as shown in the yellow boxes in Figure 1. Additional results are shown in Table 2 in which two different discount rates were considered: 5% and 10%.

The EPDM can be used to give order of magnitude estimates of costs and determine which parameters might be major cost drivers to the overall cost of sequestration approaches, and which are important to estimate CO_2 leakage (e.g. subsurface and atmospheric leakage, permeability, depth, existing wells and others).

According to the analysis in Figure 15, the impacts of leakage and subsurface liabilities look small. However, at this stage these cost estimates account for only the conventional geological engineering costs

for operation and maintenance of subsurface projects. They do not include the recent findings from the LIV analysis (Chapter 5), which show that the largest costs would come from the need for fixing and finding a leak, or the need for injection interruption (which may require venting). Accounting for these unconventional costs would likely lead to greater financial risk. This analysis remains to be done.

CO2 Sequestration Cost Analysis for Mount Simon deep saline aquifer (Ottawa County, Michigan)

Total CO2 Storage Capacity Tons 9500000

	Carbon Storage Cost - Subcomponents*	Total Cost ($)	Unit Cost ($/Ton CO2)
1	Geologic Site Characterization Unit Costs (SC)	507374	
2	Injection Well Construction (IW)	781499	
3	Well Operation (WO)	7955831	
3.1	*Monitoring during Injection (IM)*	*704963*	
3.2	*Review Study & Corrective Action (RS)*	*154481*	
3.3	*Mechanical Integrity Tests (MI)*	*1510673*	
4	Post-Injection Monitoring and Verification (MV)	474262	
General and administrative costs		2417816	
Finance & Insurance		400000	
A) Carbon Storage Cost without Leakage & Liabilities		***14906899***	***1.5691***
a) Atmospheric Leakage		2377531	0.2503
Carbon Storage Cost with Leakage (A+a)			***1.8194***
b) Subsurface Liabilities		1457197	0.1534
Carbon Storage Cost with Leakage & Liabilities(A+a+b)			***1.9728***
c) Site closure and reclamation		127824	0.0135
Carbon Storage Cost with Leakage, Liabilities & Site closure with reclamation(A+a+b+c)			***1.9863***

Note: * A range of costs will emerge from sensitivity analysis around leakage rates and subsurface liabilities and risks management regimes

Figure 15. EPDM Cost Calculator screenshot: The elements included in the final costs summary module.

Table 2. EPDM cost analysis results for the Mt. Simon injection scenario for two different discount rates.

Disc Rate 5%			Disc Rate 10%		
Items	**Annuitized Cost**	**Unit Cost ($/tCo2)**	**Items**	**Annuitized Cost**	**Unit Cost ($/tCo2)**
Geologic Site Characterization Unit Costs (SC)	524,165		Geologic Site Characterization Unit Costs (SC)	815,902	
Injection Well Construction (IW)	14,217,253		Injection Well Construction (IW)	16,088,722	
Well Operation (WO)	11,191,277		Well Operation (WO)	11,193,530	
Monitoring during Injection (IM)	5,812,079		Monitoring during Injection (IM)	5,440,412	
Corrective Action (CA)	255,620		Corrective Action (CA)	289,268	
Mechanical Integrity Tests (MI)	56,315		Mechanical Integrity Tests (MI)	55,533	
Closure & Post Injection Care (CPIC)	171,386		Closure & Post Injection Care (CPIC)	174,268	
Financial Assurance (FA)	400,000		Financial Assurance (FA)	400,000	
Sub Total Without Leakage	**32,628,095**	**3.435**	**Sub Total Without Leakage**	**34,457,636**	**3.627**
Subsurface leakage	24,407		Subsurface leakage	24,407	
Atmospheric leakage	629		Atmospheric leakage	629	
Sub Total With Leakage	**32,653,131**	**3.437**	**Sub Total With Leakage**	**34,482,672**	**3.630**

8.3 Development and Demonstration of CCS-MARKAL

8.3.1 CCS-MARKAL and Simulations of Interest

MARKAL is a well-established tool for examination of the market competitiveness of energy technologies. It generates least-cost energy path analysis based on life-cycle costs of technologies and competing alternatives (cradle-to-grave). It does so by identifying the most cost-effective pattern of resource use and technology deployment over time. An overview of the elements of MARKAL is shown in Figure 16.

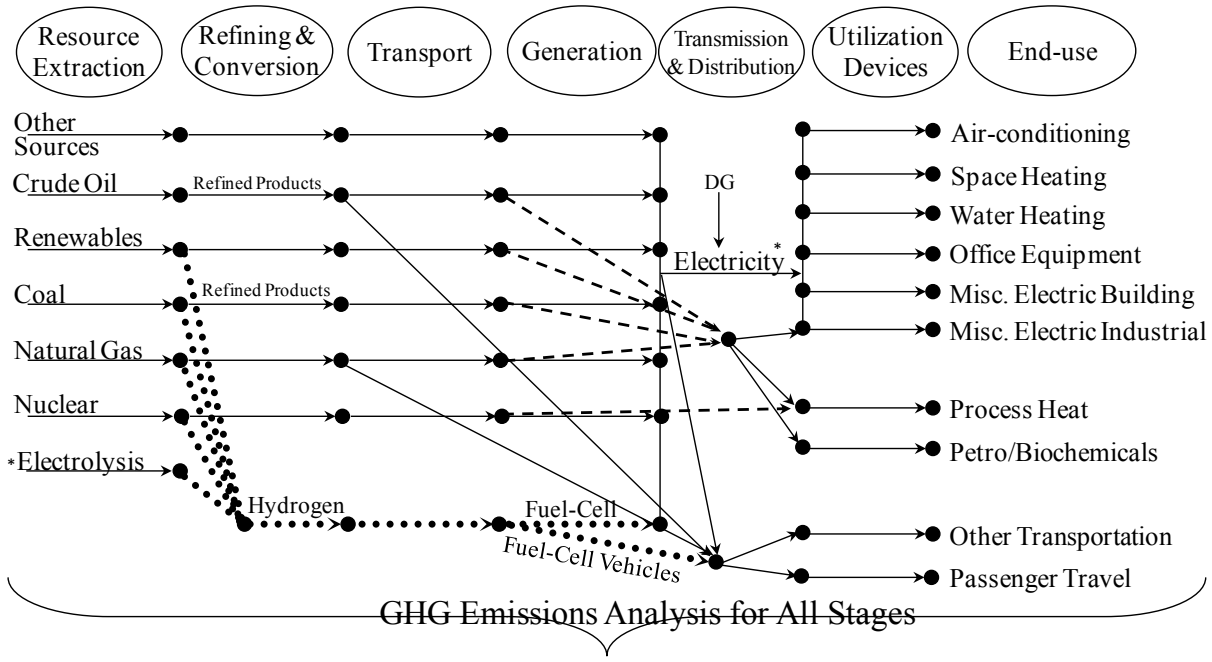

Figure 16. An overview of the MARKAL reference energy system.

The MARKAL methodology for analysis of the U.S. energy System utilizes a state-of-the-art dynamic linear programming framework. It was developed at Brookhaven National Lab in collaboration with the U.S.DOE and IEA. It uses a DOE-accepted and vetted methodology. Over 100 institutions in 55 countries currently use it for energy systems analysis. It is also used at the U.S. DOE Applied R&D Programs (NE, EERE and FE) – GPRA 1993, Office of Policy and International Affairs, Energy-Water Nexus, Hydrogen Economy. MARKAL provides a technology-rich basis for estimating energy dynamics over a multi-period horizon (2010-2050). It allows examination of environmental, technological and policy restrictions.

For this project, we developed a customized national energy systems analysis methodology: CCS-MARKAL. We used it to compare CCS with renewables, and nuclear, for instance, and to examine the effects of alternative policy regimes such as carbon taxes, and high fuel prices. But the customized CCS-

MARKAL allowed us to examine additional costs resulting from leakage pathways and subsurface regimes, taking the EPDM output as input.
To demonstrate CCS-MARKAL, we studied deployment options under various carbon mitigation prices/limits and financial instruments. We specifically applied to model to the case of injection into the Mt. Simon sandstone underlying Ottawa County, Michigan. The sequestration options that are modeled by CCS-MARKAL are sequestration in basalt, depleted gas reservoirs, depleted oil reservoirs, enhanced coal-bed methane recovery, enhanced oil recovery, shale gas, and the Mt. Simon formation.

8.3.2 CCS-MARKAL Simulation Results and Findings

To start, a base case analysis was done based on the DOE Energy Information Agency's (EIA) Annual Energy Outlook (AEO) for 2012. The results are shown in Figure 17. In this basecase scenario, fossil energy provides the majority of all sectoral demands. The market share of renewables remains small and nuclear adds a few plants in addition to announced retirements.

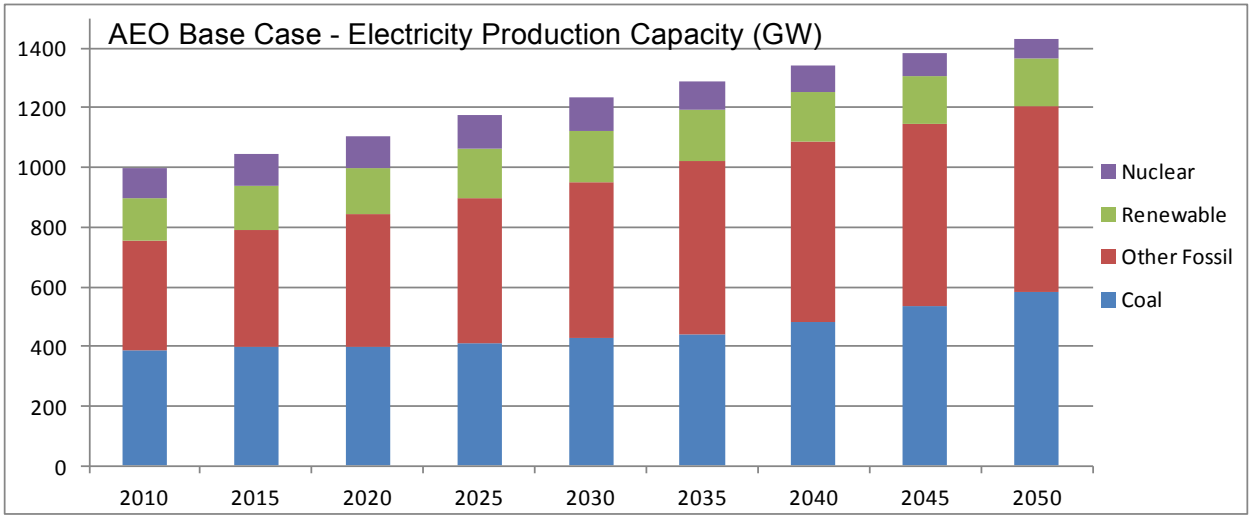

Figure 17. MARKAL predictions of electricity production capacity in GigaWatts (GW) for the base case scenario based on the DOE Energy Information Agency's (EIA) 2012 Annual Energy Outlook (AEO).

CCS-MARKAL was then used to examine the following policy interventions:

- *Financial policies based on sensitivity to discount rates*. In MARKAL, the discount rate reflects both the financial, actuarial and perceptional components (Hurdle rates) of new technology adoption and deployment. Hurdle rates of 10% are used for industrial and electric sectors; Hurdle rates in the range of 1% to 7% can be applied based on technology maturation over time. In this work, discount rates of 10%, 11% and 13% were tested.
- *Environmental policies to incentivize carbon mitigation*. Alternatives for carbon mitigation incentives include imposition of a carbon tax or foster growth of low- or no-carbon emitting technologies. For this work, CO_2 tax schedules between $5 and $100 per ton of CO2 were tested.

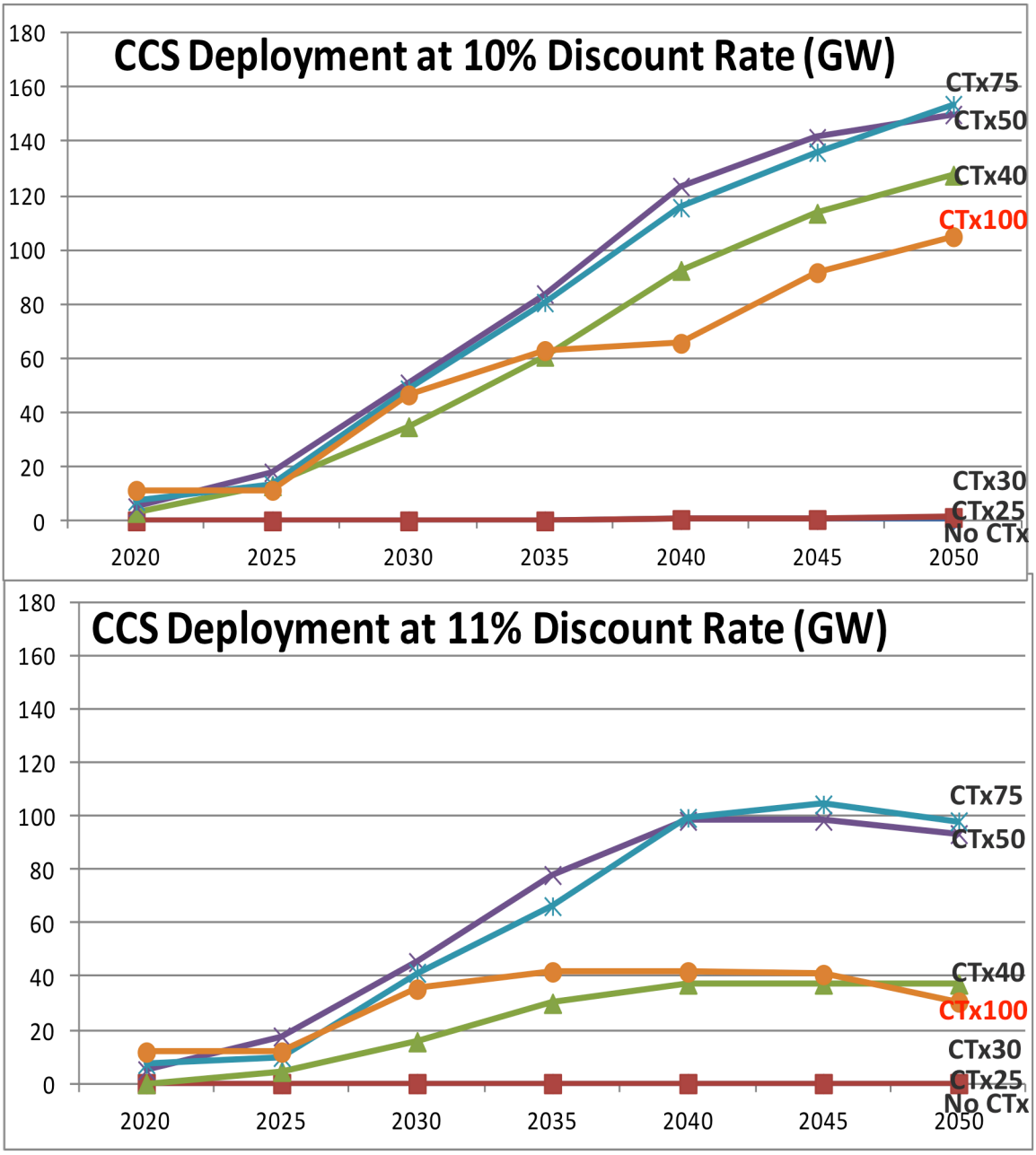

Figure 18 – CCS-MARKAL projections of "CCS" (which means coal combustion with CCS) market deployment expressed as GigaWatts (GW) at two different discount rates and for several different carbon tax (CT) scenarios.

Figure 18 shows CCS-MARKAL simulation results projecting the extent of "CCS" deployment from the year 2020 to 2050, in terms of GigaWatts (GW) produced from coal combustion with CCS.

The effect of the value of a carbon tax is non-monotonic. At CT values of $30 or less, there is no market penetration. When the CT value is $40, there is market penetration and this market penetration increases until it reaches a maximum at $50 or $75 after which the market penetration begins to decline. This reflect the positive effect of incentivization at non-zero but small values of CT, at high values of CT CCS is outpriced and is a less attractive option compared to other energy technologies in the market. That is, there is an optimal carbon tax to maximize CCS market penetration, above which other energy technologies outcompete CCS. Regardless, innovative financial mechanisms are needed for effective deployment.

The effect of increasing discount rate is to diminish market share. At 10% and 11% discount rates, CCS market penetration happens, but CCS does not deploy at 13% discount rate (which is why the plot is not shown).

Figure 19 shows a projection of the sectoral breakdown of the energy market between 2010 and 2050 in the case of a $50 CT scenario with 11% discount rate. This graph should be looked at in comparison with Figure 17, the AEO base case. In this simulation with a carbon tax, net coal market share decreases over time, unlike the base case in which coal market share increases over time. The presence of CCS, however, helps coal to retain significant market share, as is indicated by the growing share of "Coal with CCS". This simulation also shows that CCS faces significant competition from natural gas and renewables. Renewables capture more market share over time, unlike the base case where renewables were roughly constant over time. Natural gas, which is a big portion of "other fossil" increases faster in this scenario than in the base case.

Looking at these simulations another way, Figure 20 examines the resulting CO_2 emissions for the non-zero CT scenarios in comparison with the base case. The basecase results in the highest CO_2 emissions over time, and reductions by a factor of a half are possible with a carbon tax of $100. In this examination, the effect of CO_2 emissions reductions with CT is a monotonic rather than a nonmonotonic relationship. As the CT increases the net use of fossil energy decreases, and nuclear and renewables gain market share.

In conclusion, our market penetration analysis shows that financial incentives, such as a carbon tax, are needed for coal combustion with CCS to gain market share. Furthermore, there is an optimal carbon tax, above which CCS is outpriced and non-coal alternatives become more attractive. These findings make sense conceptually and qualitatively. However, this analysis should be considered preliminary and the quantitative interpretation of the results must be accompanied by consideration of the accompanying uncertainty. The simulation results must first be validated by comparison with other energy system models and the MARKAL model parameterization needs to be carefully checked. Finally, the effects of leakage on market penetration could not be fully examined because of limitations in MARKAL in accounting for unconventional economic risks outside the normal energy market. This would require a detailed accounting of unconventional financial risks, as described in the recent LIV paper (Chapter 5).

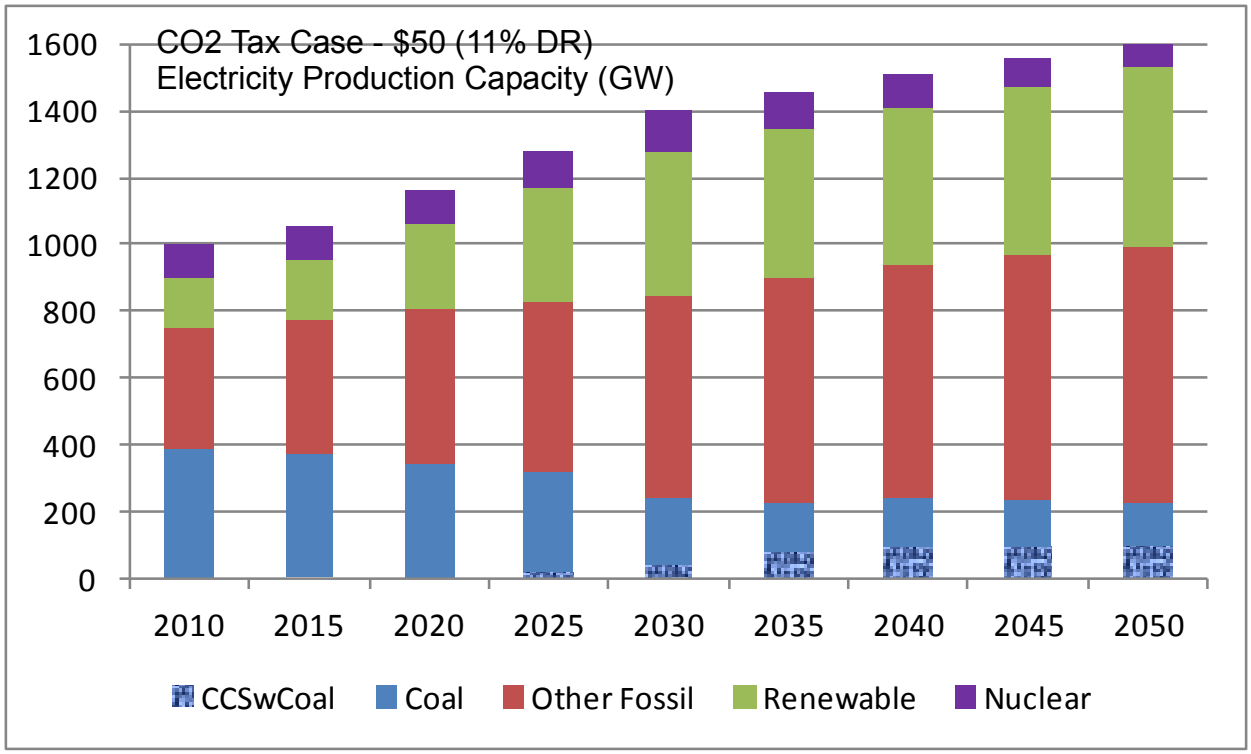

Figure 19. Future projections of energy market sectoral breakdown for the case of a $50 carbon tax and an 11% discount rate.

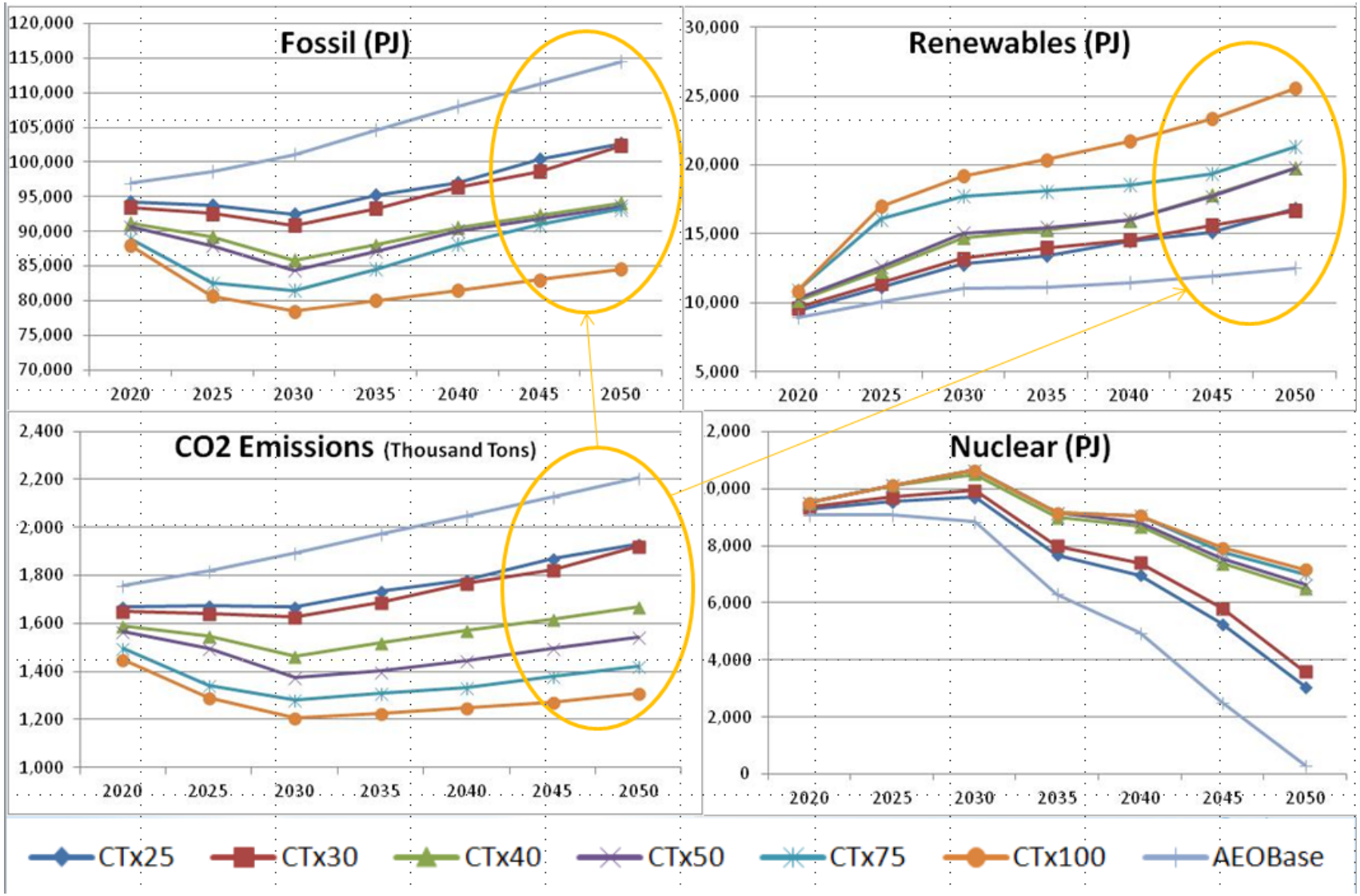

Figure 20. CO_2 emissions projected to 2050 for the scenarios examined in Figures 18 and 19 with a range of CT values and 11% discount rate. Also shown are the market shares for total fossil energy, all renewables and nuclear.

8.4 Basin-scale leakage modeling and demonstration of the EPDM

In this analysis, we conducted basin-scale leakage simulations and used the EPDM to examine costs associated with the sequestration scenarios. We considered storage formations in the Michigan sedimentary basin. The injection scenario was a 50-year injection of CO_2 from James De Young and J.H. Campbell power plants. We used ELSA, a fast semi-analytical model that allows for multiple aquifers and multiple leaky wells to model fluid migration among different formations through existing wells (Celia et al. 2011). We examined alternative assumptions about the permeabilities of the wells, and examined alternative injection site locations underlying Ottawa County, MI (Figure 21).

Figure 21. Ottawa County in the state of Michigan

For a specific injection site, we modeled injection for each of three possible storage formations: the Trenton-Black River and St Peter, the Galesville and the Mt Simon. See Figure 22 for a cross-section of the Michigan sedimentary basin, indicating the location of Ottawa Country, and see Table 1 for a list of the formations with their properties.

It is expected that for a deeper injection case, there is less leakage potential because the number of wells that penetrate the storage formation is smaller, as indicated in Figure 23. Also at deeper formations, CO_2 is denser and this will lead to smaller plume radius and less buoyancy. However, with deeper wells and higher pressure, the cost is higher for well construction and maintenance, CO_2 injection, monitoring and cement integrity evaluation. To examine this tradeoff, we implemented the EPDM to estimate project costs.

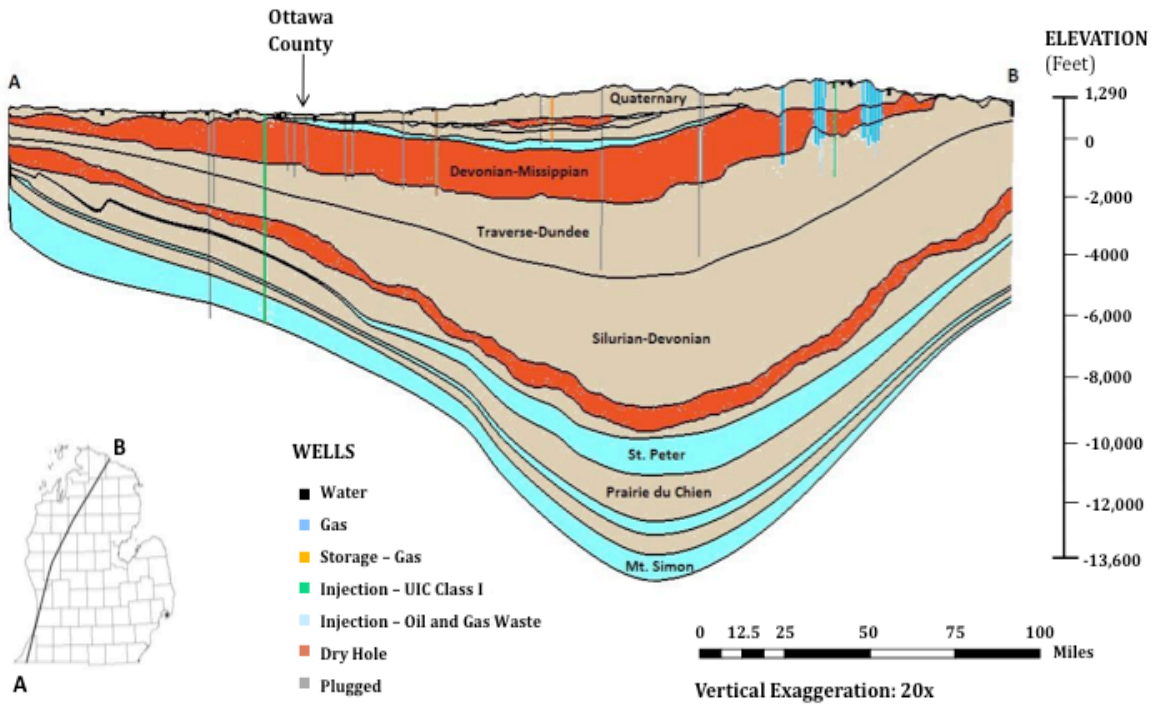

Figure 22. Geological cross-section of Michigan Basin

Table 1. Properties of Formations

Formation	Top Depth (m)	Thickness (m)	Permeability (m^2)	Porosity
Quaternary	0	65	2.36E-16	0.12
Devonian-Mississippian	65	361	—	—
Traverse-Dundee and Silurian-Devonian (TD and SD)	426	479	9.21E-17	0.1
Richmond-Collingwood	905	148	—	—
Trenton-Black River and St Peter (TBR and SP)	1053	183	4.01E-13	0.04
Prairie du Chien	1236	244	—	—
Galesville	1480	31	1.93E-12	0.07
Eau Claire	1512	93	—	—
Mt Simon	1605	240	2.4E-12	0.09

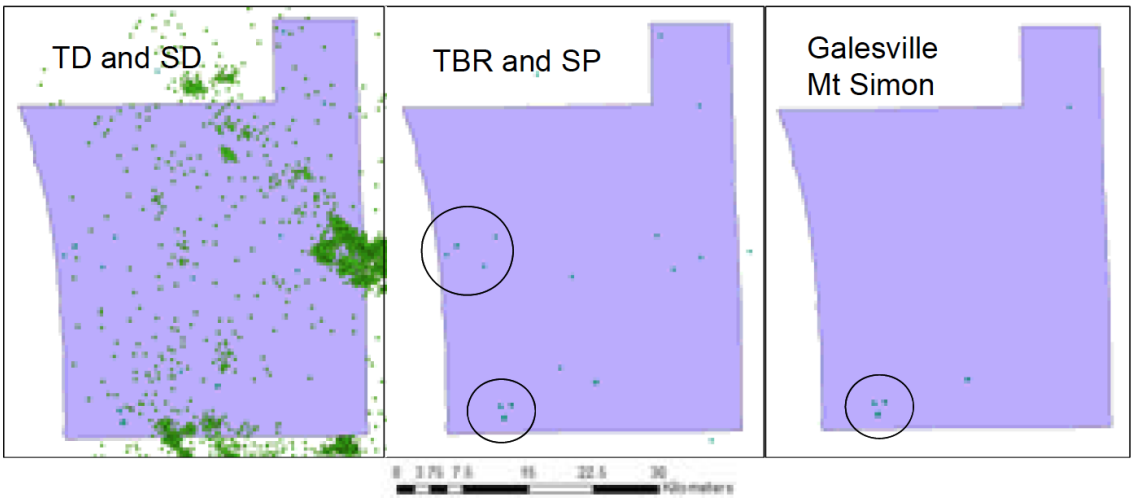

Figure 23. Existing wells in Ottawa County

The injection scenarios that were modeled had a single injection well with an injection rate of 9.5 Mt/yr for 50 years. This represents the sum of the CO_2 produced from the James De Young and J.H. Campbell power plants.

The major uncertainty in the input parameters comes from well permeability. Estimations of abandoned well permeabilities are in the range of 10^{-13} to 10^{-15} m^2, and 10^{-15} m^2 is most likely to be a good estimation with experiment data support. Estimations of well permeability can vary 6 orders of magnitude from 10^{-12} m^2 to 10^{-18} m^2.

In a given simulation, all the wells were set to have the same value of permeability. The range of well permeability conditions was as follows. 1) In the worst case scenario when all wells are very leaky, high permeability is taken to be10^{-11} m^2 . 2) For intermediate case, 10^{-15} m^2 is a good estimation for medium permeability. 3) The case of non-leaking wells occurs if well seals are intact or have been plugged. Low permeability is chosen to be 10^{-18} m^2 , considering that the lower limit of well permeability is 10^{-18} m^2 and shale permeability is 10^{-19} to 10^{-20} m^2.

The simulation results showing the effect of well permeability is shown in Table 3. The cumulative CO_2 and brine leakage is almost proportional to well permeability. Both the proximities and permeabilities of existing wells are major factors that increase the likelihood of CO_2 and brine leakage. For a specific injection site, the amount of CO_2 leakage often decreases as the injection depth increases. The amount of leaked CO_2 (both out of the target formation and to the atmosphere) is relatively small even if we consider the worst scenario, and well permeability has a big impact on the leaked amount.

Table 3. Cumulative CO_2 and brine leakage averaged over all injection sites in Ottawa County

_	injection formation	worst case permeability=10-11 m^2	intermediate case permeability =10-15 m^2	non-leaky case permeability=10-18 m^2
CO2 leakage (Mt)	TBR and SP	1.74E-01	4.87E-05	4.87E-08
_	Galesville	3.28E-01	3.67E-05	3.67E-08
_	Mt Simon	7.80E-02	7.91E-06	7.91E-09
brine leakage (Mt)	TBR and SP	1.18E-01	1.68E-05	1.68E-08
_	Galesville	6.41E-02	2.80E-05	2.80E-08
_	Mt Simon	2.19E-02	2.19E-06	2.29E-09

Table 4. CO_2 leakage into each formation for one injection site near JDY

_	Injection formation	Total leaked (Mt)	Amount of CO_2 leaked into each formation (Mt)	_	_	_
_	_	_	Galesville	TBR and SP	TD and SD	Quaternary
worst case	TBR and SP	5.36E-01	−	−	5.31E-01	4.34E-03
_	Galesville	1.25E+00	−	1.17E+00	8.14E-02	4.12E-03
_	Mt Simon	6.76E-01	4.30E-01	1.75E-01	6.70E-02	4.03E-03
Intermediate case	TBR and SP	1.52E-04	−	−	1.29E-04	2.27E-05
_	Galesville	1.26E-04	−	1.04E-04	3.62E-06	1.90E-05
_	Mt Simon	6.84E-05	4.38E-05	5.36E-06	3.08E-06	1.61E-05
non-leaky case	TBR and SP	1.52E-07	−	−	1.29E-07	2.27E-08
_	Galesville	1.26E-07	−	1.04E-07	3.62E-09	1.90E-08
_	Mt Simon	6.80E-08	4.38E-08	5.36E-09	3.08E-09	1.61E-08

Notice: Total amount of injected CO2 is 475 Mt in 50 years.

The EPDM was used to estimate CO_2 storage cost. Table 6 shows the unit cost of CO2 injection into Trenton-Black River and St Peter, Galesville, Mt Simon, based on the EPDM. The unit cost does not change much, indicating that depth is not a big factor for storage cost. In fact, only some of the cost items are sensitive to depth and the remaining parts are depth-independent. This module uses pumping cost for injecting into Mt Simon. This cost should be lower when injecting into Galesville and TBR and SP. Considering that pumping cost is 0.2 of the total storage cost, the storage cost for injection into TBR and SP should be 6% lower than the estimation. In conclusion, from an economic view, the storage cost increases as the injection formation goes deeper, but it does not change much with a range of 1145m (mean depth of TBR and SP) to 1725m (mean depth of Mt Simon).

Table 6 CO_2 storage cost as estimated by the EPDM

injection formation	Unit cost ($/ton CO_2 /yr)
TBR and SP	1.54
Galesville	1.55
Mt Simon	1.55

8.5 References

Celia, M.A.; Nordbotten, J.M.; Court, B.; Dobossy, M.; Bachu, S. (2011) "Field-scale application of a semi-analytical model for estimation of CO2 and brine leakage along old wells", INTERNATIONAL JOURNAL OF GREENHOUSE GAS CONTROL Vol: 5 Issue: 2 Pages: 257-269.

Environmental Protection Agency. 2008. Geologic CO2 Sequestration Technology and Cost Analysis, EPA 816-B-08-009, June 2008.

Gresham, R. Lee, "Geologic CO_2 Sequestration and Subsurface Property Rights: A Legal and Economic Analysis" (2010). Dissertations. Paper 8. http://repository.cmu.edu/cgi/viewcontent.cgi?article=1007&context=dissertations

Heddle, G.; H. Herzog; and M. Klett. (2003) "The Economics of CO_2 Storage" Publication MIT LFEE 2003-003 RP, Massachusetts Institute of Technology, Cambridge, MA. http://lfee.mit.edu/publications/

IPCC. 2005. IPCC Special Report on Carbon Dioxide Capture and Storage. Prepared by Working Group III of the Intergovernmental Panel on Climate Change [Metz, B., O. Davidson, H. C. de Coninck, M. Loos, and L. A. Meyer (eds.)]. Cambridge University Press, Cambridge, United Kingdom and New York, NY, USA, 442 pp.

Massachusetts Institute of Technology. 2009. Carbon Management GIS: CO_2 Injection Cost Modeling, under contract with U.S. Department of Energy DE-FC26-02NT41622, August 2009.

Rubin, E., Berkenpas, M., McCoy, S. 2008. The Economics of CO2 Transport by Pipeline and Storage in Saline Aquifers and Oil Reservoirs, under contract with US Department of Energy, DE-AC26-04NT41817April 2008.

Wyoming (2009) "REPORT AND RECOMMENDATIONS OF THE CARBON SEQUESTRATION WORKING GROUP TO THE JOINT MINERALS, BUSINESS AND ECONOMIC DEVELOPMENT COMMITTEE AND THE JOINT JUDICIAL COMMITTEE OF THE WYOMING STATE LEGISLATURE", September 2009. Available at http://deq.state.wy.us/out/downloads/1%20FinalReport081909.pdf

Chapter 9. A Tale of Two Technologies: Hydraulic Fracturing and Geologic Carbon Sequestration

This chapter has been published as:

Dammel, J., Bielicki, J., Pollak, M., and Wilson, E. (2011). "A Tale of Two Technologies: Hydraulic Fracturing and Geologic Carbon Sequestration." *Environmental Science & Technology, 45(12) pp 5075-5076.*

Two technologies, hydraulic fracturing and geologic carbon sequestration, may fundamentally change the United States' ability to use domestic energy sources while reducing greenhouse gas emissions. Shale gas production, made possible by hydraulic fracturing and advances in directional drilling, unlocks large reserves of natural gas, a lower carbon alternative to coal or other fossil fuels. Geologic sequestration of carbon dioxide (CO_2) could enable use of vast domestic coal reserves without the attendant greenhouse gas emissions. Both hydraulic fracturing and geologic sequestration are 21st Century technologies with promise to transform energy, climate, and subsurface landscapes, and for both, effective risk management will be crucial. Potential environmental impacts, particularly to groundwater, are key concerns for both activities, because both inject large volumes of fluids into the subsurface. Unless environmental issues and public concerns are actively addressed, public opposition could stall deployment of these two

important technologies.

In the United States, shale gas production increased 8-fold in the past decade, and it is projected to comprise roughly half of domestic production in 2035 (1). Between 2010 and 2011, the U.S. Energy Information Agency (EIA) doubled the estimate of technically recoverable unproven shale gas reserves (1). U.S. energy supply projections have been fundamentally and strategically altered. Hydraulic fracturing, which makes this bounty possible, injects a mix of water, propping agents, and proprietary chemicals at high pressure to create millions of small fractures in low-permeability shale and liberate trapped natural gas. At each well, 2 to 4 million gallons of water are injected and 30 to 70% remains underground. (2)

Geologic sequestration could keep CO_2 out of the atmosphere by capturing it at coal burning power plants or other industrial facilities and injecting it into deep geologic formations. (3) The U.S. Department of Energy, in the 2010 Carbon Sequestration Atlas, estimated that the nation has the capacity to store all CO_2 emissions from large domestic stationary sources for at least 500 years (at 2009 emission rates). Geologic sequestration has great promise, but its role in the U.S. energy future is uncertain; there is no economic driver to do it unless society decides to substantively reduce GHG emissions. A few demonstration projects are underway, scheduled to inject a total of about 10 million tons of CO_2 in the United States. Another 12 million tons of captured CO2 was used for enhanced oil recovery in 2010, but currently, geologic sequestration is a minor player on the U.S. energy stage.

Although hydraulic fracturing and geologic carbon sequestration are distinct technologies, they pose some similar environ- mental risks. Groundwater contamination could occur if injected or mobilized fluids escape from the target formation and migrate upward into drinking water along faults, fractures, abandoned wells, or poorly constructed injection wells. Both technologies can protect groundwater by carefully studying site geology so only appropriate sites are chosen, using best practices for well construction, monitoring site performance, and developing emergency and remedial response plans so all parties are prepared if problems arise.

Despite similarities in their environmental risks, regulations for geologic carbon sequestration and hydraulic fracturing are drastically different; the result is that similar risks are managed quite differently. Ironically, nascent geologic sequestration technology has state-of-the art regulations that were crafted during a decade of federal notice-and-comment rulemaking. The environmental risks of geologic sequestration will be managed by the EPA UIC program, under new Class VI well rules adopted in 2010. As the first injection well class added since 1983, Class VI rules incorporate advances in subsurface technology and modeling, regulatory philosophy, and environmental expectations that have transpired in the intervening quarter century.

In contrast, the Energy Policy Act of 2005 offcially exempted hydraulic fracturing from regulation under the UIC program. The environmental risks of shale gas production are managed through rules established by state oil and gas agencies. These rules reflect historical practices that emphasize production of hydrocarbons for maximum economic gain. These values are so entrenched that federal environmental regulation has grown up around them, often in the form of exemptions. Beyond the UIC exemption, hydraulic fracturing is also effectively exempt from reporting the composition of the hydraulic fracturing fluid to the EPA Toxics Release Inventory and from obtaining stormwater permits that would regulate how hydraulic fracturing fluid is handled at the surface. (2,4) These exemptions are significant because

surface activities associated with hydraulic fracturing can also threaten drinking water. In light of increasing reports of groundwater contamination, some communities are moving to block shale gas projects (5) and bills to remove environmental exemptions have been introduced in Congress. While states struggle to address the environmental risks of hydraulic fracturing, public trust in industry's ability to self-regulate remains low-particularly in the shadow of the 2010 Gulf Oil Spill.

Emerging energy technologies are often held to regulatory standards that incorporate technological advances in management and monitoring, while fossil energy technologies are often exempted from environmental regulation. This double standard can impede the deployment of new technologies and damage the prospects for important energy resources. Overly stringent regulation can damage the business case for important new technologies like geologic sequestration, while environmental exemptions can compromise public acceptance. Further, discussions of regulation, seen recently in the furor over hydraulic fracturing, provoke deeply embedded reactions from both industry and environmental groups. Industry often opposes environmental regulation while environmental groups often decry regulation that falls short of banning particular activities. Neither of these positions is helpful to further the development of valuable and strategic energy technologies. Within this context, appropriate regulation can be seen as a fulcrum to balance community and industry interests.

A shift toward a 21st Century vision of regulation is required. Hydraulic fracturing and geologic sequestration are both technologies that could reduce greenhouse gas emissions, enhance domestic energy security, and fundamentally change trajectories of energy supply and use, not just in the United States but across the world. While both present risks to the environment, appropriate regulatory approaches that equitably and consistently balance risks and benefits can aid in public acceptance and responsible deployment.

REFERENCES

(1) AEO2011 Early Release Overview; Report No. DOE/EIA0383ER(2011); United States Energy Information Administration: Washington, DC, 2010; http://www.eia.gov/forecasts/aeo/pdf/0383er(2011).pdf.
(2) Modern Shale Gas Development in the United States: A Primer; U.S. Department of Energy: Washington, DC, 2009; http://www.netl.doe.gov/technologies/oil-gas/publications/EPreports/Shale_Gas_Primer_2009.pdf.
(3) Special Report: Carbon Dioxide Capture and Storage; Intergovernmental Panel on Climate Change: Geneva, Switzerland, 2005; http://www.ipcc.ch/pdf/special-reports/srccs/srccs_wholereport.pdf.
(4) Drilling Down: Protecting Western Communities from the Health and Environmental E□ects of Oil and Gas Production; Natural Resources Defense Council (NRDC): New York, NY, 2007; http://www.nrdc.org/land/use/down/down.pdf.
(5) Urbina, I., Regulation Lax as Gas Wells' Tainted Water Hits Rivers. New York Times, Feb. 26, 2011, A1.

Chapter 10. Deterioration of a fractured carbonate caprock exposed to CO_2-acidified brine flow

This chapter has been published as:

Ellis, B.R.; Peters, C.A.; Fitts, J.P.; Bromhal, G.S.; McIntyre, D.L.; Warzinski, R.P.; Rosenbaum, E.J. 2011. "Deterioration of a fractured carbonate caprock exposed to CO2-acidifed brine flow". *Greenhouse Gases: Science and Technology*. 1(3): 248.

10.1 Abstract:

A flow-through experiment was performed to investigate evolution of a fractured carbonate caprock during flow of CO_2-acidified brine. A core was taken from the Amherstburg limestone, a caprock formation overlying the Bois Blanc and Bass Islands formations, which have been used to demonstrate CO_2 storage in the Michigan basin. The inlet brine was representative of deep saline brines saturated with CO_2, resulting in a starting pH of 4.4. Experimental conditions were 27 °C and 10 MPa. X-ray computed tomography and scanning electron microscopy were used to observe evolution of fracture geometry and to investigate mineralogical changes along the fracture surface. The initial brine flow corresponded to an average fluid velocity of 110 cm hr^{-1}. After one week, substantial mineral dissolution caused the average cross-sectional area of the fracture to increase from 0.09 cm^2 to 0.24 cm^2. This demonstrates that carbonate caprocks, if fractured, can erode quickly and may jeopardize sealing integrity when hydrodynamic conditions promote flow of CO_2-acidified brine. However, changes to fracture permeability due to mineral dissolution may be offset by unaltered constrictions along the flow path and by increases in surface roughness. In this experiment,

preferential dissolution of calcite over dolomite led to uneven erosion of the fracture surface and an increase in roughness. In areas with clay minerals, calcite dissolution left behind a silicate mineral-rich microporous coating along the fracture wall. Thus, the evolution of fracture permeability will depend in a complex way on the carbonate content, as well as the heterogeneity of the minerals and their spatial patterning.

Secure geologic carbon sequestration requires a caprock that is able to contain CO_2 for long periods of time. Subsurface injection of large volumes of CO_2 may lead to conditions that generate new fractures in the caprock or reopen existing fractures. [1,2] Fractures, regardless of their origin, may serve as conduits for flow if they are hydraulically connected to an overlying aquifer. [3]

CO_2 that dissolves in water will acidify formation brines. [4] Carbonate minerals, such as calcite and dolomite, are known to be reactive when in contact with CO_2-acidified brines. [5] Therefore some degree of erosion is expected along flow paths where CO_2-acidified brine contacts carbonate rock, such as in hydraulically connected fractures in carbonate caprocks. Characterizing and modeling coupled fluid flow and reaction in fractures is challenging due to the interrelationship of these processes and the effects of spatial heterogeneities in fracture geometry and mineral distributions. [6-8] Reaction-induced changes in fracture geometry can alter intrinsic permeabilities and relative permeabilities in ways that are difficult to predict. It is well known that flow permeability increases with fracture aperture, [9] but flow is hindered with increasing roughness of fracture surfaces. [10,11] Furthermore, while mineral dissolution may enlarge the flow path, it is also possible that fracture permeability may decrease due to removal of the asperities holding the fracture open. [12] Finally, mineral dissolution may lead to clogging of the flow path caused by particle decohesion. [13] Therefore, predictions of long-term seal integrity require an understanding of how the complex interplay of CO_2-water-rock interactions and fluid transport will impact fracture evolution.

This paper presents results of an experimental study designed to investigate the micrometer- to centimeter-scale evolution of fracture geometry in an artificially fractured limestone caprock exposed to flow of CO_2-acidified brine. Experiments conducted at this scale are needed to determine the importance of complexities, such as mineral spatial heterogeneity, in controlling flow along fracture pathways. To investigate a relevant case, a caprock specimen was sampled from the drilling core of the injection well at one of the CO_2 injection demonstration sites of the US Department of Energy. The site is the Midwest Regional Carbon Sequestration Partnership's project located in Otsego County, Michigan. Approximately 60,000 tons of CO_2 were injected into the Bass Islands Dolostone between 2008 and 2009. This formation is overlain by the Bois Blanc formation, a cherty carbonate, and above that by the Amherstburg formation, a dense fossiliforous dolomitic limestone. The Amherstburg formation is considered the primary caprock for this injection site. [14] This is one of three existing deep-saline formation CO_2 injection projects that rely on a carbonate caprock as the primary seal for securing the injected CO_2. [15]

A seven-day core-flooding experiment was conducted in which CO_2-acidified brine flowed through an artificially fractured Amherstburg core sample. The brine composition was selected to represent a brine that has had time to react with the injection formation minerals under CO_2-saturated conditions prior to contact with the core. Temperature and pressure conditions were 27°C and 10 MPa. Under these conditions and at equilibrium with CO_2, the brine had a pH of 4.4. The evolution of fracture

aperture was monitored in real-time using an X-ray computed tomography (CT) scanner. Before and after the experiment, 3-D reconstructions of the fracture geometry, aperture, and surface roughness were examined at higher resolution via micro X-ray CT (μCT). Finally, the cores were sectioned and examined with scanning electron microscopy (SEM). The combination of high resolution μCT and SEM analysis provides valuable insight into the mineralogy-dependent alterations of fracture geometry due to flow of reactive fluids. [13,16,17]

10.2 Methods

10.2.1 Sample characterization and brine composition

The Amherstburg sample used in this study came from a 10-cm diameter core that had been collected at a depth of 928 m during the drilling of the injection well at the Otsego County project site. A similar specimen from the Bois Blanc was also obtained, and used to estimate mineralogy of that formation. A 2.54 cm diameter vertical core was cut from the Amherstburg sample using a water-jet cutter to prevent unwanted mechanical degradation of the sample. The sample was artificially fractured prior to the experiment to enable flow. The fracture was induced under normal stress compression with dual knife-edge chisels perpendicular to the horizontal (XY) plane of the core. Prior to fracturing, the core was stabilized by coating the exterior with epoxy. This technique was successful in producing a fracture that propagated the length of the core. After the core was fractured, another coat of epoxy was applied to the core exterior, leaving only the ends exposed, to ensure the integrity of the epoxy coating and prevent lateral flow along the outer boundary during brine flow.

The Amherstburg caprock specimen is primarily composed of calcite and dolomite, in roughly equal proportions. Together, these minerals comprise >90% of the bulk sample, with the remaining rock containing a mixture of quartz, K-feldspar, clay minerals, and pyrite. The Bass Islands formation is predominately composed of dolomite with <10% other minerals including, in descending order of proportion, calcite, anhydrite, quartz, K-feldspar, and clay minerals. To determine these mineral compositions, X-ray diff raction was used to identify the primary minerals present. Then, a section of each sample was cut and polished for SEM analysis. Back-scattered electron (BSE) microscopy was used to differentiate mineral material from pore space, and where possible, differentiate between minerals. These BSE images were then combined with energy dispersive spectroscopy (EDS) elemental maps, such as those for calcium and magnesium. Specific minerals and their percent contribution to the sample area were identified using an algorithm that overlays the BSE gray-scale images with the EDS elemental maps. For example, the BSE images can be used to separate calcite from dolomite. Dolomite is assigned to regions of the EDS map where calcium and magnesium co-occur, with no other metals present, and where the BSE map has a gray-scale intensity corresponding to the range assigned to dolomite. These area estimates are used as a proxy for the percent volume contribution of each mineral and represent a semi-quantitative estimate of bulk mineralogy. Several 2-D images were taken at random locations on the polished section. The analysis of the BSE images builds upon the work of Peters. [18] The samples were examined at the Image Analysis Center at Princeton University using a Bruker X-ray diffractometer and a Quanta environmental scanning electron microscope.

The experimental brine composition shown in Table 1 was selected to represent CO_2-saturated brine that had already reacted with minerals in the injection formation. Specifically, the composition mimicked a CO_2-saturated 1 M NaCl brine reacted with dolomite, calcite, and anhydrite with

saturation indices of approximately -2. Temperature and pressure conditions of 40ºC and 10 MPa were chosen to represent those occurring at a depth of approximately 1 km, which is at the interface between the Amherstburg and the Bois Blanc formations. Brine pH and mineral saturation calculations were made using PHREEQC with the Pitzer.dat database. [19] Aqueous activity coefficients were estimated using the Pitzer model. [20] CO_2 solubility was estimated to be 0.98 mol L^{-1} following the work of Duan *et al*.[21] Thermodynamic constants shown in Table 2 were determined through the use of SUPCRT92 to account for system pressure and temperature conditions. [22]

Table 1. Inlet brine composition.

Species (total)	[mol L^{-1}]
Na^+	1.0×10^0
Cl^-	1.0×10^0
Ca^{2+}	6.4×10^{-3} to 3.5×10^{-2}
Mg^{2+}	1.8×10^{-2}
SO_4^{2-}	1.1×10^{-2}
$CO_{2(aq)}$	9.8×10^{-1}
pH	4.4 to 4.9

10.2.2 Flow-through experiment

Figure 1 shows a simplified depiction of the experimental system that was constructed in the core-flow experimental facility at DOE NETL in Morgantown, WV. The fractured sample was placed in a rubber jacket that was inserted into a TEMCO triaxial carbon-fiber core holder. A confining pressure of 14 MPa was applied to the exterior of the rubber jacket to prevent lateral flow along the core exterior.

A batch of the synthetic brine was prepared in the brine reservoir by mixing deionized water and salts: NaCl (extra pure, Acros Organics), $CaCl_2$ (>96% pure, Acros Organics), $MgCl_2 \cdot 4H_2O$ (reagent grade ACS, Acros Organics), NaOH (>97% pure, Acros Organics), and Na_2SO_4 (>99% pure, Fisher). Then, two separate high-pressure syringe pumps (Teledyne Isco, Inc., Lincoln, NE, USA) delivered CO_2 (99.5% pure, Airgas) and brine to the high-pressure mixing vessel where they were allowed to equilibrate at 40°C and 10 MPa. The resulting CO_2 saturation in the brine was checked by comparing the measured pH to the predicted equilibrium pH. The measured pH values were within the expected range of model pH values shown in Table 1. Inlet brine samples were taken at the beginning of the experiment (higher calcium concentration, higher pH) and after three days (lower calcium concentration, lower pH). Precipitates, likely calcium-bearing, were visible in the brine reservoir early on in the experiment. As such, the day-3 composition is believed to be most representative of the fluid flowed through the fracture over the course of the experiment and is therefore used throughout this paper for the purpose of discussion. The pH measurements were made at system temperature and pressure conditions with use of high-pressure, high-temperature pH probes (Corr Instruments, LLC, San Antonio, TX, USA). Brine samples were treated with nitric acid and diluted before being analyzed via ICP-OES on a Perkin Elmer Optima 3000 XL.

Table 2. Thermodynamic constants (K) for acid-driven dissolution of calcite (Eqn 1) and dolomite (Eqn 2), and the solubility product constant (K_{sp}) for the dissolution of one mole of each mineral at 27 °C and 10 MPa. Saturation indices (SI) correspond to the solution conditions in the inlet brine. Reaction rate constants (k) are estimated following the work of Chou *et al.*[33] for ambient pressure, 25°C and pH = 4.4.

	log(K)	log(K_{sp})	SI	log(k) [mol m^{-2} s^{-1}]
Calcite	1.87	–8.39	–1.99	–4.1
Dolomite	2.54	–17.98	–2.29	–5.0

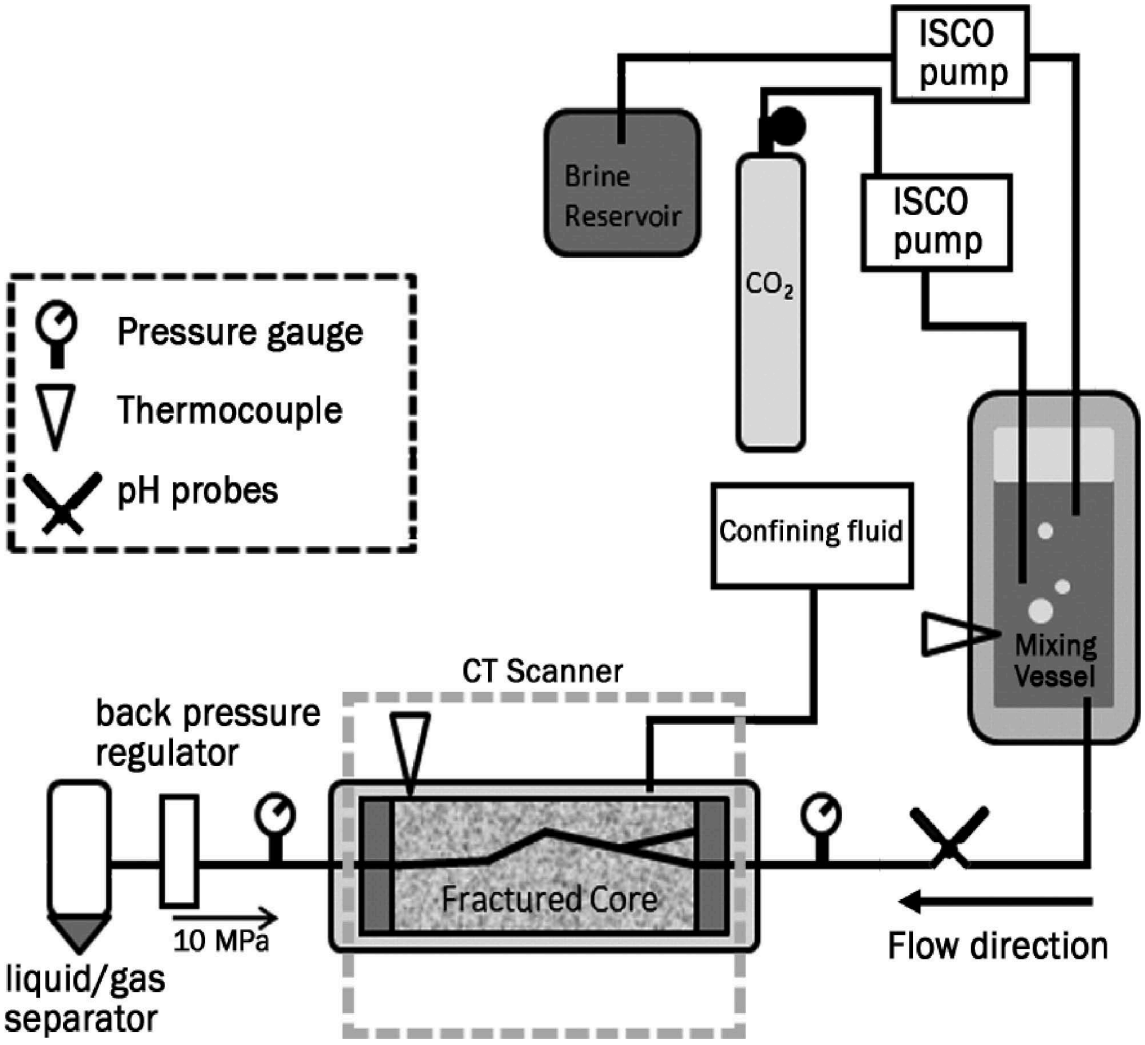

Figure 1. Schematic of the design of the core-flow experiments.

To start the flow experiment, the CO_2 valve was closed and the brine pump was used to push the CO_2-saturated brine through the core. The experiment was designed to have a constant flow rate of 10 mL hr^{-1}, which was chosen such that the pumps would be refilled once every two days. This corresponded to an average initial fluid velocity of 110 cm hr^{-1}, which was calculated as the volumetric flow rate divided by the average initial cross-sectional area of the fracture. The system pressure was controlled at 10 MPa by a back-pressure regulator located near the outlet. Under the flow conditions of the

experiment, there was no measureable pressure differential across the core and as such, there is no discussion of changes in core permeability presented in this paper. A temperature of 40 °C was successfully maintained in the mixing vessel; however, the average temperature measured at the core was 27 °C. This lower core temperature was due to safety limitations in heating of the core holder exterior coupled with heat losses along the upstream flow path and at the core-holder end caps.

10.2.3 X-ray computed tomography

Tomographic imaging of the core

X-ray computed tomography was used in two ways to perform non-destructive imaging of the fractured core before, during, and after the experiment. X-ray attenuation at beam energies greater than 100 keV corresponds to material density with a characteristic CT number that can distinguish mineral and void space.[23,24] The flow-through experiment was conducted within a Universal Systems HD-350E medical CT scanner. This allowed for real-time scans to be taken without disturbing the experiment. Scans were taken twice daily with a beam energy of 140 keV for the duration of the experiment providing information on fracture evolution. The medical scanner produces a series of 2-D slices with a voxel resolution of 250 μm in the plane of the slice and a thickness of 2 mm. This leads to data being averaged over the 2 mm depth of a single slice causing some blurring along areas where the fracture aperture changes within this length. It also means that a fracture aperture of less than 250 μm will only be positively identified as a void space due to a reduction in the CT number for the voxel that captures the fracture.

The fractured core was also imaged prior to and after completion of the experiment with a MicroXCT-400 scanner (Xradia, Inc., Pleasanton, CA, USA). The core was scanned dry and under ambient temperature and pressure conditions. Unlike the medical CT that scans a stationary sample while rotating the X-ray source and detector array, the μCT obtains a series of 2-D images with the sample rotating in a stepwise fashion between a stationary source and detector. Xradia utilizes a proprietary arrangement of scintillators, optics, and high-resolution detector to achieve high-resolution, high-contrast X-ray images.[25] The large size of the core required that the sample be imaged in three sections of approximately 27 mm in length, allowing for some overlap between consecutive sections. The sample was scanned with an X-ray beam energy and power of 150 keV and 10 W, respectively, at rotational increments of 0.06° for the top section and 0.14° for the bottom two sections. The selected optics provided a 3-D reconstructed image with a voxel resolution of 27 μm, representing an order of magnitude improvement in resolution when compared to that achieved by the medical scanner.

Image analysis and aperture measurement

The medical CT scans were adjusted using the image processing Java application, ImageJ, in order to provide a uniform gray-scale image for the given range of CT numbers generated in the reconstruction. This also allowed for balancing of the contrast between consecutive scans, which then made it possible for cross-scan comparison of single 2-mm slices.

Two-dimensional slices of the reconstructed μCT scans were exported as jpeg files and ImageJ was again used to align and uniformly contrast these images. Each 2-D slice contained square pixels (27 μm × 27 μm) and represented a thickness (z-direction) of 27 μm. The field-of-view for these images

was 27 × 27 mm, which is slightly larger than the core diameter. At these settings, the angle of the cone-beam of the μCT X-ray source introduces a wedge-shaped artifact at the top and bottom of the reconstructed images. This artifact can be seen at the top of Fig. 5(a), the bottom of which was cropped for this figure. If detailed whole-core information was required, more sections could have been scanned to provide sufficient overlap between sections to enable elimination of the wedge-shaped artifacts during stitching of the stacked sections. This was not necessary for the purposes of the research reported here. The three sections that were scanned of the 7.06-cm core still yielded ~6.5 cm (92%) of good μCT data for image analysis.

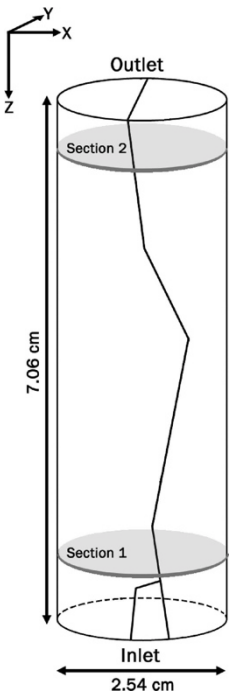

Figure 2. Diagram of fractured core with core dimensions and location of sections used for SEM analysis.

Prior to fracture aperture analysis, the fracture area of the entire set of 2-D images was isolated and the gray-scale contrast enhanced. The gray-scale images were then segmented using a thresholding algorithm in ImageJ based on a normalized histogram of the entire set of images. Fracture aperture was measured as the width of the fracture at every pixel column spanning the fracture. In areas where there were multiple fractures, a volumetric average was calculated to estimate an effective fracture aperture.

10.2.4 Sectioning and SEM imaging

To examine mineralogical alterations of the fracture surface, the core was sectioned and prepared for SEM imaging. After the experiment was finished and the core had been scanned, the core was dried and flooded with epoxy to allow for sectioning and further analysis with the SEM. To do this, the core was first flushed with ethanol and then dried via continuous flow of desiccated air. The core was flooded with epoxy with vacuum-assisted flow.

Figure 2 depicts the fracture orientation and identifies where samples were taken for SEM analysis. The core was sectioned along three planes. Section 1 was taken approximately 15 mm from the core inlet. Section 2 was taken approximately 8 mm from the outlet end of the core. The 15 mm section (core inlet to section 1) was then cut in the flow (Z) direction to bisect the fracture perpendicular to its propagation in the XY plane. The sections were then polished and analyzed using the BSE/EDS image analysis technique previously described to identify the minerals adjacent to the fracture.

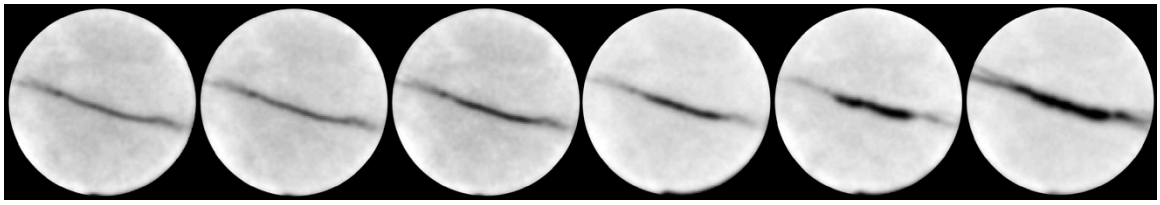

Figure 3. Six-day time series of medical CT scans of 2-mm section taken approximately 2 cm from core inlet. Scans from days 2 through 7 are shown, left to right. Consecutive scans are not precisely 24 hours apart, but show general progression of fracture erosion.

10.3 Results

Results from both the medical and μCT scans show evidence of an increase in fracture aperture throughout the core. Figure 3 shows a series of scans taken near section 1 with the medical CT scanner over the duration of the experiment. Even with the relatively low resolution of the medical CT images, an increase in fracture aperture is observed.

Figure 4 contains aperture maps for the fracture before (a) and after (b) flow of the CO_2-acidified brine. The difference in aperture is shown in Fig. 4(c). Figure 4(f) shows the average fracture aperture along the length of the core from the core inlet to the outlet. Initially, the fracture aperture was largest near the inlet with an average aperture of 480 μm and smallest near the outlet with an average aperture of 160 μm. The largest increase in aperture occurred in the one-third of the core near the outlet. This section of the core represents not only the area of largest absolute change in aperture but also the area with the largest average final aperture of 1100 μm. Figures 4(d) and 4(e) show the distribution of fracture apertures before and after flow, respectively. Initially, the median aperture of the fracture was 270 μm. The distribution of fracture apertures changed significantly after flow of the CO_2-acidified brine, resulting in a median aperture of 860 μm.

Along the 6.5 cm length, fracture void volume prior to flow of CO_2-acidified brine was ~0.6 ml and the average cross-sectional area was 0.09 cm^2. After seven days of exposure to the flowing CO_2-acidified brine, the fracture had a void volume of ~1.6 ml and average cross-sectional area of 0.24 cm^2. This represents an increase in flow area of ~2.7 times, resulting in a reduction in average flow velocity from 110 to 42 cm hr^{-1}, and a reduction in flushing from ~17 to ~6 fracture pore volumes hr^{-1}. In the field, a constant pressure gradient is more likely to exist, in which case the increase in flow area would increase the volumetric flow rate.

Close examination of the μCT images shows evidence that the fracture wall was eroding in a nonuniform manner. Figure 5 focuses on the one third of the core near the fluid inlet. Figure 5(a) shows the fracture after the experiment overlain with the initial fracture void shown in white. The μCT images show intermittent regions adjacent to the fracture void space that are slightly blurred. These are partially degraded zones. The zone highlighted by Box 1 in Fig. 5(a) is focused upon in Fig. 5(b), and is on the order of 300–400 μm in thickness. It appears to be of a fairly uniform thickness, suggesting that transport in this degraded zone may have been a limiting factor controlling the continued dissolution of the fracture surface.

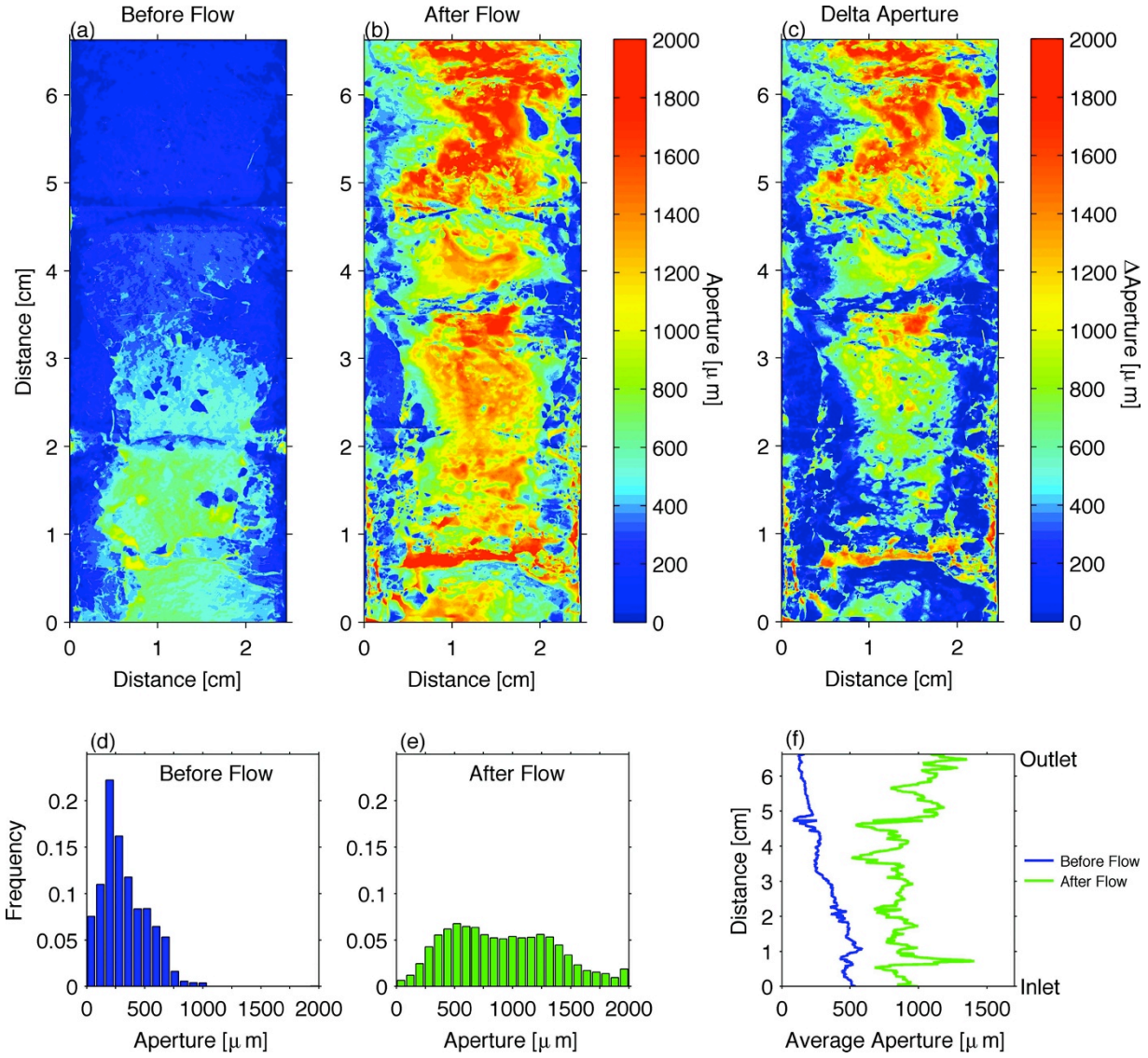

Figure 4. Fracture aperture maps of the fracture before (a) and after brine flow (b). The total change in aperture between the initial and final aperture measurements is shown in (c). Aperture width distributions are shown for the fracture before (d) and after brine flow (e). The average measured aperture along the length of the core is shown in (f).

The BSE and EDS analysis of sectioned segments of the core shed light on the mineralogical content of the fracture boundary and within the degraded zones observed in the μCT images. Along the fracture, calcite dissolved to a much greater extent than the other minerals present in the sample. The non-uniform degradation along the fracture wall is a result of the mineral spatial heterogeneity of the rock. Figures 6(a) and 6(c) show that the largest increases in fracture aperture occurred at points where calcite is in direct contact with the flowing brine. Figure 6(a) is the BSE image corresponding to Box 2 shown in Fig. 5(a). The smallest increases in fracture aperture correspond to areas where there are silicate minerals. In areas where calcite is intermixed with dolomite and other silicate minerals the dissolution of calcite leads to the formation of degraded zones along the fracture boundary as observed in the μCT images. Figure 6(b) provides a good example of preferential calcite dissolution in an area with homogenous mineral distribution. Figure 6(d), which is a close-up of the

clay-rich zone in Fig. 6(c) highlighted within the box, demonstrates how calcite dissolution in an area of higher clay content can leave behind a continuous microporous silicate matrix.

The non-uniform change in average aperture along the length of the core, as shown in Fig. 4(f), is most consistent with an uneven distribution of calcite along the length of the core. Figure 6(c) is from section 2 (Fig. 2), which is the segment of the core that experienced the largest increase in aperture. Large grains of calcite are observed adjacent to the fracture wall.

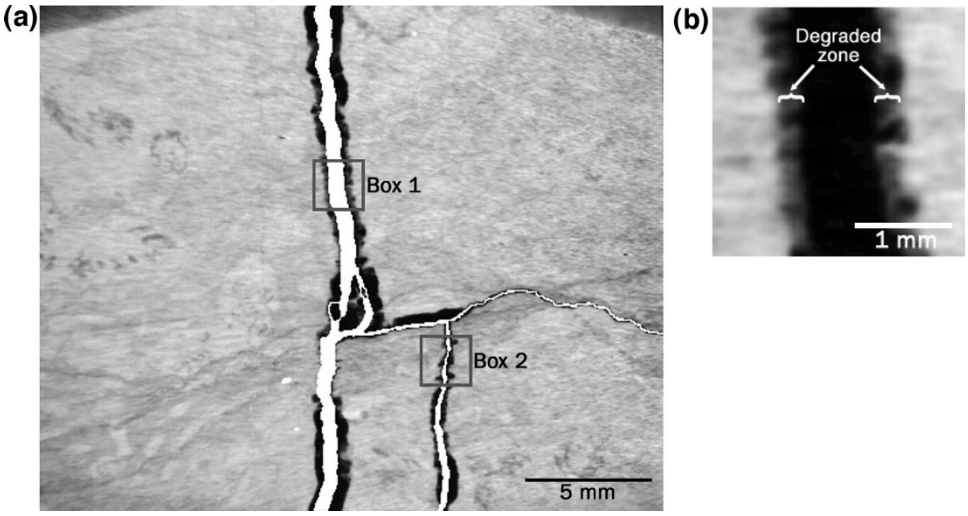

Figure 5. (a) µCT scan of 2-cm section near the core inlet after brine flow. The initial fracture void is shown in white overlying the fracture after dissolution to highlight the changes in fracture aperture. Box 1 in (a) is enlarged and shown in (b) to emphasize the development of a degraded zone along the fracture surface.

Here, there was erosion at a much faster rate than the surrounding rock of mixed calcite, dolomite, and clay mineral composition. There appears to be a distinct dissolution front along these calcite grains, which suggests the large increases in fracture aperture in this section are due to extensive dissolution and not grain plucking.

10.4 Discussion

The results of this experimental study demonstrate that for a carbonate caprock significant fracture erosion is possible when CO_2-acidified brine is able to flow continuously through the fracture. In the context of geologic carbon sequestration, this would increase the likelihood of leakage of CO_2 through the caprock, but predicting the extent and timeframe of this increased risk is complicated by how the fracture geometry evolves. In this discussion section, we put the findings from this experiment in context with comparable studies, and we use the collective findings of these studies to frame a discussion on how flow through caprock fractures may be influenced by geochemical alteration of fracture geometry. We also interpret the finding of the disproportionate dissolution rates of calcite and dolomite.

The rate and extent of geochemically driven evolution of caprock fractures will depend in a coupled way on fluid transport conditions (advective and diffusive mass transport), fluid composition (pH and mineral saturation conditions), caprock mineralogy (carbonates and silicates), and mineral spatial

heterogeneity (mixed or banded). In this experiment, advective flow was dominant over diffusion. If mass transport in the fracture is diffusion-limited, then the erosion of the fracture surface will occur at a significantly reduced rate, as dissolution kinetics would be limited by the rate of diffusion of species away from reactive mineral surfaces. Diffusion of CO_2-acidified brines into the higher pH native fluids within the caprock may produce conditions that favor carbonate mineral precipitation, and thereby enhance the sealing capacity of the caprock.[26] In laboratory experiments involving reactive flow in fractured carbonate rocks, it was found that dissolution was favored in advection-dominated fractures and precipitation (of sulfates) was favored in diffusion-limited fractures.[27] Another relevant scenario is the coupled flow of acidified brine with advection- and buoyancy-driven flow of super-critical CO_2. [28] Andreani *et al*.[17] studied the impact of alternating brine and CO_2 gas flow through a fractured claystone caprock. They observed calcite dissolution during CO_2-acidifed brine flow and an increase in fracture aperture which was attributed to a cyclic process of clay decohesion during CO_2 gas flow followed by clay removal during subsequent brine flow. Upon further investigation of these results, Pèpe *et al*. [29] suggested that during CO_2 gas flow, the interstitial fluids within the microporous clay matrix become highly acidified, leading to clay particle decohesion.

The evolution of caprock fractures will also depend strongly on the mineralogy of the caprock. In this study, there was substantial erosion of the fracture wall where there was calcite, and to a lesser but measurable extent where there was dolomite. The clay minerals, which are less reactive, remained, and possibly inhibited the dissolution of the carbonate minerals by slowing the transport of reaction products to the bulk brine phase. The slower rate of aperture growth in clay-rich regions of the fracture surface is particularly evident in Fig. 6(d). This implies that the presence of clay minerals may reduce the concomitant fracture aperture growth in a carbonate rock. This observation also suggests that weathered fracture surfaces, which can have significant clay mineral deposits, may experience lower aperture growth rates relative to freshly created fracture surfaces. In a similar study, Noiriel *et al*.[13] investigated acidic water flow through an existing fracture in an argillaceous limestone, and reported that the preferential dissolution of calcite led to the development of a microporous clay coating along the fracture wall. Formation of the microporous clay coating was correlated with an increase in surface roughness, and an overall reduction in fracture permeability was primarily attributed to clay particle transport and accumulation within the fracture.

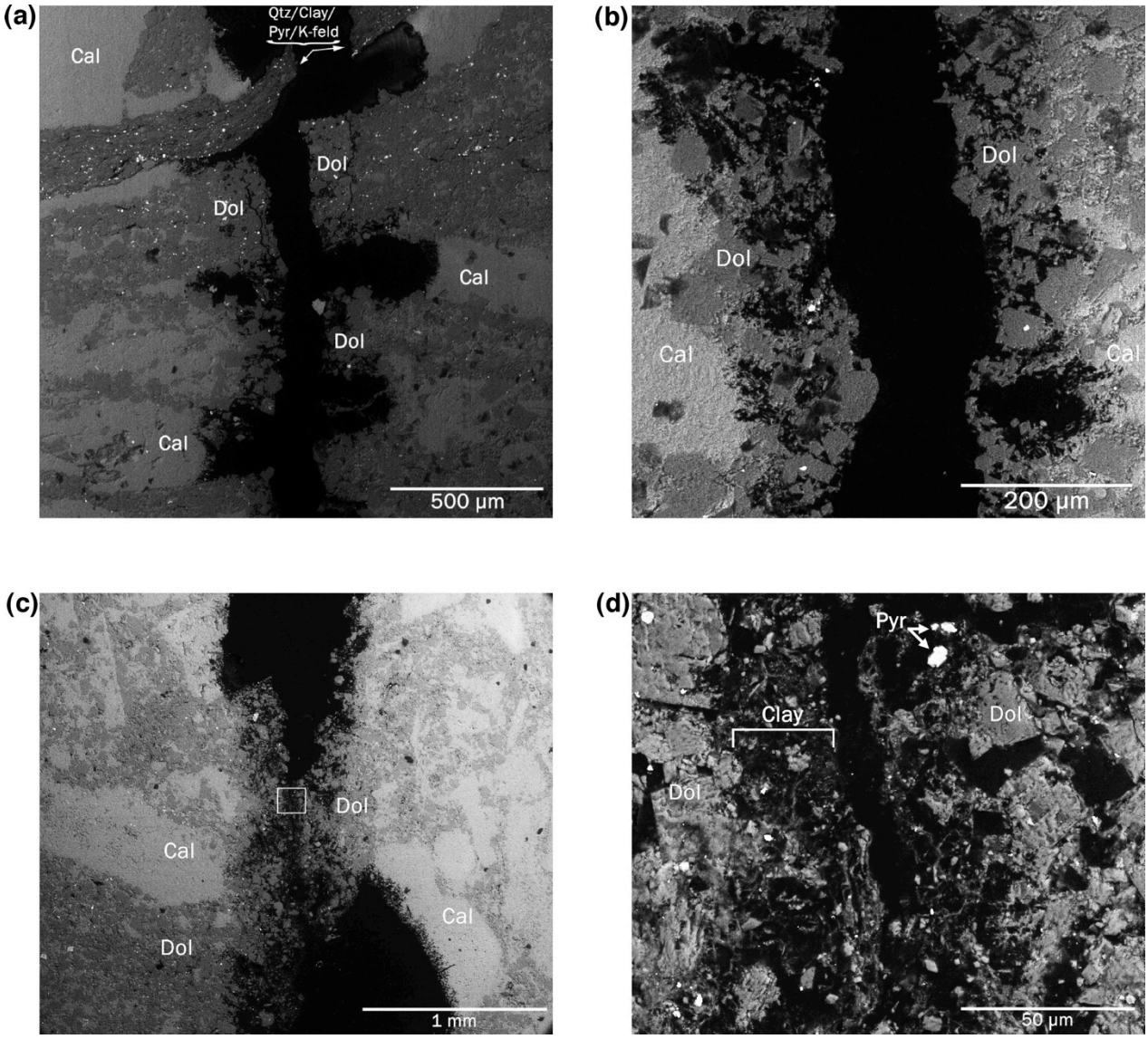

Figure 6. BSE images of (a) area highlighted by box 2 in Fig. 5(a) showing preferential dissolution of calcite leading to non-uniform aperture increases, (b) area of section 2 showing homogenous mineral distribution and development of degraded zone along fracture wall, (c) area of section 2 showing non-uniform aperture increases, and (d) close-up view of clay-rich microporous zone highlighted by box in Fig. 6(c).

The mineralogical composition of the rocks used in the current study differed significantly from the rocks used in the studies by Noiriel *et al.*[13] and Andreani *et al.*[17] All three studies observed preferential dissolution of calcite within fractures of carbonate and carbonate-rich rocks; however, the clay mineral content of the three rock samples varied considerably. Noiriel *et al.*[13] used a limestone containing roughly 25% clay minerals, and Andreani *et al.*[17] used a carbonate-rich shale containing 45% clay minerals. The Amherstburg core used in the current study contained less than 10% non-carbonate minerals with an estimated clay mineral content of 2 to 5% of the bulk rock. The low percentage of clay minerals within the Amherstburg rock core, in addition to the fact that the fracture was fresh and not weathered, meant that the fracture surfaces would provide substantial contact with carbonate minerals.

Finally, the evolution of caprock fracture geometry is strongly dependent on the mineral spatial heterogeneity and configuration, as evidenced in Figs 6(a)– 6(c), particularly as it relates to the fracture surfaces. The preferential dissolution of calcite, coupled with non-uniform mineral distribution along the fracture, led to increases in fracture surface roughness. This uneven fracture erosion is similar to that found by Gouze *et al*.[16] for a fractured limestone containing 15% dolomite. It is well known that fracture roughness can substantially reduce hydraulic flow through a fracture relative to what would be predicted from the average fracture aperture. [30] Additionally, the non-uniform dissolution of the fracture surface may lead to conditions that promote the development of preferential flow paths and possible wormhole formation along the fracture pathway.[31]

In this experiment, it was also observed that fracture aperture growth was negligible where the fracture intersected a silicate-rich band, as shown near the top of Fig. 6(a). The flow resistance through this unaltered silicate band may ultimately dominate the system flow, even though it is only a small portion of the total fracture geometry. According to the principles of critical path analysis in percolation theory, flow rate is largely dominated by the most resistive paths. [32]

In summary, for reactive flow through fractures in mineralogically heterogeneous rocks, the effect of increased fracture aperture may be offset by the effect of increased fracture roughness, and may even be negated if unaltered narrow restrictions remain.

In the remainder of the discussion section, we seek to explain the observed preferential dissolution of calcite over dolomite. Three factors are considered: mineral solubility, thermodynamic driving forces, and dissolution kinetics. The acid-driven mineral dissolution reactions for calcite and dolomite are, respectively,

$$CaCO_3(s) + H^+ \Leftrightarrow Ca^{2+} + HCO_3 \quad (1)$$

$$CaMgCO_3(s) + 2H^+ \Leftrightarrow Ca^{2+} + Mg^{2+} + 2HCO_3 \quad (2)$$

Table 2 contains the temperature- and pressure-adjusted equilibrium constants, K, for these reactions, along with the solubility product (K_{sp}) for the dissolution of one mole of each mineral. Although calcite is slightly more soluble than dolomite, the differences in solubility alone are unlikely to account for the observed preferential dissolution of calcite in this experiment. Values of the saturation index (SI), the logarithm of the ratio of the ion activity product to K, for each of the reactions shown above are given in Table 2. These minerals were at nearly equal saturation states, and in fact dolomite was slightly further from thermodynamic equilibrium. Thus thermodynamic forces were not the determining factor leading to preferential calcite dissolution.

The preferential dissolution of calcite over dolomite in these experiments is therefore attributed primarily to the differences in the reaction rate kinetics. Reaction rate constants for each mineral are also given in Table 2, based on literature-reported values for ambient pressure, 25 °C and pH=4.4.[33] The reaction rate constant for calcite dissolution is nearly one order of magnitude greater than that of dolomite, and therefore, dissolution kinetics was likely the primary driving force of the observed preferential calcite dissolution.

10.5 Conclusion

The experimental results from this study suggest that if hydraulically connected fractures exist in carbonate caprocks, flow of CO_2-acidified brine may lead to rapid dissolution along fracture pathways. The deterioration of the fracture in this experiment was due primarily to calcite dissolution and resulted in an increase in fracture cross-sectional area of ~2.7 times. This finding is not unexpected scientifically, but in the context of geologic sequestration of CO_2 it highlights the vulnerability of carbonate formations as caprocks for securing CO_2 underground, and it underscores the need to carefully evaluate their suitability during site selection. This study also demonstrates the complex manner in which fracture geometry can evolve under reactive flow conditions, making it difficult to predict the actual impact on fracture permeability. The differential dissolution rates of calcite and dolomite led to an uneven erosion of the fracture surface, which caused a substantial increase in surface roughness. The existence of unaltered silicate-rich bands along the fracture flow path and the increase in surface roughness may offset the effect of increases in average fracture aperture. This finding highlights the importance of understanding mineral spatial heterogeneity when trying to predict fracture evolution and ultimately, caprock seal integrity, when in contact with CO_2-acidified brine.

Because of the extreme degree and rate of fracture deterioration in this experiment, it is important to summarize the extent to which the scenario is plausible and representative. Several factors make this a plausible scenario including that the fractured specimen is from a real caprock from an actual CO_2 injection site, one that presumably satisfied numerous site selection criteria. In addition, the brine composition and experimental temperature and pressure conditions are representative of typical subsurface conditions. Finally, fractures in sedimentary rocks can exist, there is uncertainty in their detection, and fracture propagation can result from perturbations in fluid pressures, rapid expansions, and thermal gradients. The co-existence of several unique conditions also contributed to the observed rapid fracture deterioration. First, the carbonate caprock used contained only a small amount of non-carbonate minerals and was therefore quite susceptible to acid-driven dissolution. Second, the mineral surfaces along the fracture wall were not weathered since the fracture was fresh. Third, the brine was under-saturated with respect to calcium. Fourth, the flow rate may be high relative to what might occur in the field (although we have no basis for comparison). Therefore, this finding is representative of what could happen if several plausible events co-occurred.

10.6 References

1. Rutqvist J, Birkholzer JT and Chin-Fu Tsang, Coupled reservoir–geomechanical analysis of the potential for tensile and shear failure associated with CO2 injection in multilayered reservoir–caprock systems. *Int J Rock Mech Min* **45**(2):132– 143 (2008).
2. Shukla R, Ranjith P, Haque A and Choi H, A review of studies on CO2 sequestration and caprock integrity. *Fuel* **89**:2651– 2664 (2010).
3. Smith J, Durucan S, Korre A and Shi J, Carbon dioxide storage risk assessment: Analysis of caprock fracture network connectivity. *Int J Greenh Gas Con* **5**(2):226–240 (2011).
4. Ellis BR, Crandell LE and Peters CA, Limitations for brine acidification due to SO2 co-injection in geologic carbon sequestration. *Int J Greenh Gas Cont* **4**(3):575–582 (2010).
5. Pokrovsky OS, Golubev SV, Schott J and Castillo A, Calcite, dolomite and magnesite dissolution kinetics in aqueous solutions at acid to circumneutral pH, 25 to 150°C and 1 to 55 atm pCO2: New constraints on CO2 sequestration in sedimentary basins. *Chem Geol* **265**:20–32 (2009).
6. Berkowitz B, Characterizing flow and transport in fractured geological media: A review. *Adv Water Resources* **25**(8– 12):861–884 (2002).

7. Dijk PE, Berkowitz B and Yechieli Y, Measurement and analysis of dissolution patterns in rock fractures. *Water Resour Res* **38**(2):1013 (2002).
8. Detwiler RL, Experimental observations of deformation caused by mineral dissolution in variable-aperture fractures. *J Geophys Res* **113**:B08202 (2008).
9. Snow DT, Anisotropic Permeability of Fractured Media. *Water Resour Res* **5**(6):1273–1289 (1969).
10. Brown SR, Caprihan A, Hardy R. Experimental observation of fl uid flow channels in a single fracture. *J Geophys Res* **103**(B3):5125–5132 (1998).
11. Crandall D, Bromhal G and Karpyn ZT, Numerical simulations examing the relationship between wall-roughness and fl uid fl ow in rock fractures. *Int J Rock Mech Min* **47**(5):784–796 (2010).
12. Polak A, Elsworth D, Yasuhara H, Grader AS and Halleck PM, Permeability reduction of a natural fracture under net dissolution by hydrothermal fl uids. *Geophys Res Lett* **30**(20):2020 (2003).
13. Noiriel C, Made B and Gouze P, Impact of coating development on the hydraulic and transport properties in argillaceous limestone fracture. *Water Resour Res* **43**:W09406 (2007).
14. Midwest Regional Carbon Sequestration Partnership (MRCSP). Factsheet for partnership field validation test. NETL Cooperative Agreement DE-FC26-05NT42589. September (2008).
15. Michael K, Golab A, Shulakova V, Ennis-King J, Allinson G, Sharma S and Aiken T, Geological storage of CO2 in saline aquifers – A review of the experience from existing storage operations. *Int J Greenh Gas Con* **4**(4):659–667 (2010).
16. Gouze P, Noiriel C, Bruderer C and Loggia D, X-ray tomography of fracture surfaces during dissolution. *Geophys Res Lett* **30**(5):1267 (2003).
17. Andreani M, Gouze P, Luquot L and Jouanna P, Changes in seal capacity of fractured claystone caprocks induced by dissolved and gaseous CO2 seepage. *Geophys Res Lett* **35**:L14404 (2008).
18. Peters CA, Accessibilities of reactive minerals in consolidated sedimentary rock: An imaging study of three sandstones. *Chem Geol* **265(**1–2):198–208 (2009).
19. Parkhurst DL and Appelo CAJ, *User's guide to PHREEQC (Version 2) – a computer program for speciation, batch-reaction, one-dimensional transport, and inverse geochemical calculations*. USGS Water-Resources Investigations Report. 99–4259, 312pp (1999).
20. Pitzer KS, Thermodynamics of electrolytes 1: Theoretical basis and general equations. J Phys Chem 77:269–277 (1973).
21. Duan Z, Sun R, Zhu C and Chou I, An improved model for the calculation of CO2 solubility in aqueous solutions containing Na^{+}, K^{+}, Ca^{2+}, Mg^{2+}, Cl^{-}, and SO4 . *Marine Chem* **98**:131–139 (2006).
22. Johnson JW, Oelkers EH and Helgeson HC, SUPCRT92 – a software package for calculating the standard molal thermodynamic properties of minerals, gases, aqueous species, and reactions from 1 to 5000 bar and 0 to 1000 °C. *Comput Geosci* **18**:899–947 (1992).
23. Wildenschild D, Hopmans JW, Vaz CMP, Rivers ML, Rikard D and Christensen BSB, Using X-ray computed tomography in hydrology: systems, resolutions, and limitations. *J Hydrol* **267**:285–297 (2002).
24. Cai R, Lindquist BW, Um W and Jones KW, Tomographic analysis of reactive flow induced pore structure changes in column experiments. *Adv Water Resour* **32**:1396–1403 (2009).
25. Feser M, Gelb J, Chang H., Cui H, Duewer F, Lau SH, Tkachuk A and Yun W, Sub-micron resolution CT for failure analysis and process development. *Meas Sci Technol* **19**:094001, 8pp (2008).
26. Gherardi F, Xu T and Pruess K, Numerical modelling of self-limiting and self-enhancing caprock alteration induced by CO2 storage in a depleted gas reservoir. *Chem Geol* **244**:103– 129 (2007).
27. Singurindy O and Berkowitz B, The role of fractures on coupled dissolution and precipitation patterns in carbonate rocks. *Adv Water Resour* **28**(5):507–521 (2005).
28. Bryant SL, Lakshminarasimhan S and Pope GA, Buoyancy-dominated multiphase flow and its effect on geological sequestration of CO2. *SPE J* **13**(4):447–454 (2008).
29. Pèpe G, Dweik J, Jouanna P, Gouze P, Andreani M and Luquot L, Atomic modelling of crystal/complex fl uid/crystal contacts – Part II. Simulating AFM tests via the GenMol code for investigating the impact of CO2 storage on kaolinite/brine/ kaolinte adhesion. *J Crystal Growth* **312**:3308–3315 (2010).
30. Zimmerman RW and Bodvarsson GS, Hydraulic conductivity of rock fractures. *Transport Por Med* **23**(1):1–30 (1996).
31. Szymczak P and Ladd AJC, Wormhole formation in dissolving fractures. *J Geophys Res* **114**:B06203 (2009).
32. Berkowitz B and Balberg I, Percolation theory and its application to groundwater hydrology. *Water Resour Res* **29**(4):775–794 (1993).
33. Chou L, Garrels RM and Wollast R, Comparative study of the kinetics and mechanisms of dissolution of carbonate minerals. *Chem Geol* **78**:269–282 (1989).

Chapter 11. Dissolution-Driven Permeability Reduction of a Fractured Carbonate Caprock

This chapter has been published as:

B.R. Ellis, J.P. Fitts, G.S. Bromhal, D.L. McIntyre, R. Tappero, C.A. Peters. "Dissolution-Driven Permeability Reduction of a Fractured Carbonate Caprock". *Environmental Engineering Science*. 30 (4): 187-193, 2013. DOI: 10.1089/ees.2012.0337

11.1 Abstract:

Geochemical reactions may alter the permeability of leakage pathways in caprocks, which serve a critical role in confining CO_2 in geologic carbon sequestration. A caprock specimen from a carbonate formation in the Michigan sedimentary Basin was fractured and studied in a high-pressure core-flow experiment. In-flowing brine was saturated with CO_2 at 40ºC and 10 MPa, resulting in an initial pH of 4.6, and had a calcite saturation index of -0.8. Fracture permeability decreased during the experiment, but subsequent analyses did not reveal calcite precipitation. Instead, experimental observations indicate that calcite dissolution along the fracture pathway led to mobilization of less soluble mineral particles that clogged the flow path. Analyses of core sections via electron microscopy, synchrotron-based X-ray diffraction imaging, and the first application of microbeam Ca K-edge XANES, provided evidence that these occlusions were fragments from the host rock rather than secondary precipitates. X-ray computed tomography showed a significant loss of rock mass within preferential flow paths, suggesting that dissolution also removed critical asperities and caused mechanical closure of the fracture. The decrease in fracture permeability despite a net removal of material along the fracture pathway demonstrates a non-intuitive, inverse relationship between dissolution and permeability evolution in a fractured carbonate caprock.

11.2 Introduction

The success of geologic carbon sequestration in deep saline formations will rely heavily on our ability to estimate the leakage risks associated with underground storage of large quantities of a buoyant fluid. The existence of potential CO_2 leakage pathways and estimates of CO_2 leakage have been discussed extensively in the literature (Celia and Nordbotten, 2009; Lewicki *et al.*, 2007; Shukla *et al.,* 2010). However, current leakage risk assessment models (e.g. LeNeveu, 2008; Viswanathan *et al.*, 2008) do not account for geochemical alterations of potential leakage pathways in caprock formations, and thus may estimate inaccurate CO_2 or brine leakage rates along a reactive pathway such as that of a fractured carbonate caprock (Ellis *et al.*, 2011).

Geochemical reactions that alter caprock integrity may occur over short time periods, as demonstrated in bench-scale experimental investigations (Andreani *et al.*, 2008; Ellis *et al.*, 2011; Kaszuba *et al.*, 2005; Shao *et al.*, 2010; Smith *et al.*, 2013; Wigand *et al.*, 2009). In particular, CO_2 injection into deep saline aquifers will cause acidification of formation brines (Ellis *et al.*, 2010) and carbonate minerals are susceptible to acid-driven dissolution (Pokrovsky *et al.*, 2009). Therefore, understanding the potential alterations of carbonate caprocks due to reaction with CO_2-acidified brine is a necessary first step toward predicting leakage through these formations. In the context of geologic carbon sequestration, Gherardi *et al.* (2007) simulated enhanced sealing at the caprock-reservoir interface when carbonate precipitation occurs where mass transport of reactive fluids is limited by slow diffusion into the caprock. Similar self-sealing behavior has been observed in wellbore cements (Huerta *et al.*, 2011). Conditions that favor carbonate mineral precipitation within advection-controlled leakage pathways may require mixing of higher pH interstitial waters with calcium- and carbonate-enriched reservoir brines (Nogues *et al.*, 2012; Zhang *et al.*, 2010). Core-flow studies conducted at ambient conditions and low CO_2 partial pressure have demonstrated complex alterations along limestone fracture pathways (Gouze *et al.*, 2003; Noiriel *et al.*, 2007).

This work contributes to the current knowledge, by examining the potential for mineral dissolution and precipitation to alter the permeability of fractured carbonate caprocks under reservoir temperature and pressure conditions relevant to carbon sequestration. This paper presents results from a high-pressure core flow experiment in which CO_2-acidified brine flowed through an artificially-fractured carbonate caprock sample. The core sample used in this study is from the Amherstburg limestone, which serves as the primary caprock for a CO_2 injection demonstration project into the Bass Islands formation in northern Michigan. This experiment builds upon our previous study, Ellis *et al.* (2011), in that both experiments involved a rock specimen from the same formation and were conducted under reservoir temperature and pressure conditions. Both experiments were designed to examine how brine chemistry and mineral heterogeneity determine whether fractures will be widened or may self-seal when exposed to CO_2-saturated brine. The experiments were comparable with regard to pH, but in this experiment the calcite saturation in the brine was more than an order of magnitude closer to equilibrium (calcite saturation index = -0.8). This design allowed for the possibility that calcite saturation might occur within the fracture, thus testing a hypothesis about precipitation-induced caprock sealing in the context of geologic carbon sequestration.

Because of the inherent difficulty in sampling CO_2-saturated fluids at high pressures, we did not rely solely on inferences from effluent solute concentrations. Instead, we relied on pressure gradient

measurements and on a suite of imaging techniques to relate permeability evolution to changes in fracture morphology resulting from mineralogy-specific erosion and deposition processes (see Table 1). 3D micro X-ray computed tomography (μCT) of the core was used to measure net changes in rock mass and morphological alterations of the fracture surface. After the experiment, the fracture was epoxy-stabilized and sectioned, and examined using a combination of electron microscopy and synchrotron-based X-ray spectroscopic and diffraction imaging. This included the development of new procedures for microbeam Ca K-edge X-ray Absorption Near Edge Structure (XANES) spectroscopy at the National Synchrotron Light Source (NSLS).

Small-scale, short-term experiments may not necessarily represent field-scale, long-term behavior of subsurface systems. However, controlled laboratory experiments such as this one provide a unique opportunity to gain insight into the complex physical and chemical processes affecting flow in a reactive rock. And while this single core-flow experiment cannot be interpreted in a statistical sense, the observations are valuable in revealing processes and phenomena that are possible. The aim of this study was to understand processes operative in a reactive carbonate rock exposed to CO_2-saturated brine, and then to re-examine existing paradigms about the performance of these rocks as caprock seals.

Table 1. Imaging Methods and Their Applications in This Study

Imaging method	*Analysis*	*Purpose in this study*
Scanning electron microscopy and energy dispersive X-ray spectroscopy	2D thin sections of core cross-sections	To map Ca and Mg distribution at the fracture boundary and of occlusions within the fracture with surface sensitivity.
Micro X-ray computed tomography	3D scans of the entire core	To quantify rock mass removal from the fracture surface, determine where there was the greatest occlusion of flow, and examine the evolution of fracture roughness.
X-ray fluorescence	2D thin sections of core cross-sections	To map Ca composition.
X-ray diffraction	2D thin sections of core cross-sections	To identify crystalline phases of fracture occlusions.
X-ray adsorption near edge structure	2D thin sections of core cross-sections	To determine Ca-speciation and identify the origin of the occlusions.

11.3 Materials and Methods

11.3.1 Sample characterization.

The Amherstburg is a fossiliferous carbonate formation composed primarily of calcite and dolomite, in roughly equal proportions. Together, these minerals make up >90% of the bulk sample, with the remaining rock containing quartz, K-feldspar, clay minerals, and pyrite. For details on the mineral identification procedure, see Ellis *et al.* (2011). A sub-core, 2.54 cm in diameter and 3.8 cm in length, was taken from a drilling core sampled at 928 m, oriented vertically. A flow path was created by fracturing the dry core using dual knife-edge chisels. Prior to and after fracturing, the core exterior was stabilized in epoxy (which was then machined to a uniform epoxy thickness) in order to ensure no displacement between the two core halves during handling.

11.3.2 Geochemical modelling of initial brine composition.

The experimental brine was designed to represent a CO_2-saturated brine that had already reacted with minerals in the target injection formation, the Bass Islands formation dolostone. A batch of the synthetic brine was prepared by mixing deionized water and salts: NaCl (extra pure, Acros Organics), $CaCl_2$ (>96% pure, Acros Organics), $MgCl_2 \cdot 4H_2O$ (reagent grade ACS, Acros Organics), NaOH (>97% pure, Acros Organics), and Na_2SO_4 (>99% pure, Fisher), which was then contacted with pressurized CO_2. Specifically, the initial brine composition, shown in Table 2, mimicked a CO_2-saturated 1 M NaCl brine reacted with anhydrite, calcite, and dolomite to an initial calcite saturation index of -0.8. PHREEQC was used to estimate initial mineral saturation indices and brine pH using the Pitzer.dat thermodynamic database (Parkhusrt, 1999; Pitzer, 1973). CO_2 solubility was estimated to be 0.98 mol L^{-1} following the work of Duan *et al.* (2006). Activity coefficients of aqueous species were estimated using the Pitzer model (Pitzer, 1973). Brine pH was estimated to be 4.6 at equilibrium with 10 MPa CO_2 pressure.

TABLE 2. INFLOWING BRINE COMPOSITION

Species (total)	*[mol/L]*
Na^+	1.0×10^{0}
Cl^-	1.0×10^{0}
Ca^{2+}	2.9×10^{-2}
Mg^{2+}	2.6×10^{-3}
SO_4^{2-}	1.2×10^{-2}
$CO_{2(aq)}$	9.8×10^{-1}
pH	4.6

11.3.3 Flow-through experiment.

A similar flow-through setup as described in Ellis *et al.* (2011) was used to inject CO_2-saturated brine through the fractured core. A TEMCO triaxial carbon-fiber core holder was used with a confining pressure of 14 MPa. Two separate high-pressure syringe pumps (Teledyne Isco, Inc., Lincoln, NE) delivered CO_2 (99.5% pure, Airgas) and brine to a high-pressure mixing vessel where they equilibrated at 40°C. The measured pH was within ±0.2 of the modeled pH, verifying equilibrium. The pore pressure at core outlet of 10 MPa was maintained via a back-pressure regulator. Measured inlet brine composition is shown in Table 2. Inlet pH was measured at system temperature and pressure with high-pressure pH probes (Corr Instruments, LLC, San Antonio, TX). The pH probes at the flow outlet malfunctioned, thereby preventing measurement of brine effluent pH and subsequent estimation of effluent mineral saturation indices. Brine samples were stabilized with nitric acid and diluted before being analyzed via ICP-OES on a Perkin Elmer Optima 3000 XL.

The experiment was designed to have a constant flow rate of 3 mL hr^{-1}. This constant flow rate was held only for the first 28 hours of the experiment. After this, the flow was controlled by a constant pressure difference of ~2.2 MPa due to a predetermined upper limit of 12.2 MPa for the inlet pore pressure. A temperature of 40°C was successfully maintained in the mixing vessel. Limitations in the maximum allowable surface temperature able to be applied to the carbon-fiber core holder prevented sufficient

heating of the core holder to maintain the desired internal temperature of 40°C. The average temperature measured inside the core was 30°C and is therefore the temperature used to estimate brine viscosity.

11.3.4 Estimation of fracture permeability.

Fracture permeability, k, is calculated by first relating the measured pressure difference, ΔP, to an equivalent hydraulic aperture, b_h, according to the cubic law for flow between two parallel plates (Zimmerman and Bodvarsson, 1996),

$$b_h = \sqrt[3]{\frac{12\,\mu\,L\,Q}{\Delta P\,w}} \qquad (1)$$

where Q is the volumetric flow rate, μ is the viscosity of the fluid, L is the length of the fracture, and w is the fracture width. Although this equation assumes that the fracture walls are both parallel and smooth, which is often not the case for natural fractures, it is useful here in providing a first approximation of fracture hydraulic aperture. A brine viscosity of 0.90 mPa s^{-1} was calculated following Phillips *et al.* (1981). Fracture permeability was then estimated by combining the cubic law with Darcy's law

$$k = \frac{b_h^2}{12} \qquad (2)$$

11.3.5 X-ray computed tomography.

Using a MicroXCT-400 (µCT) scanner (Xradia, Inc., Pleasanton, CA) to distinguish mineral and void space (Ketcham and Carlson, 2001), the fractured core was imaged before and after the experiment, dry and under ambient pressure. The X-ray beam energy was 150 keV and power was 10 W, with scan rotational increments of 0.14°. The 3D reconstructed image had a voxel resolution of 27 µm. The scans yielded good data for 2.4 cm of the total fracture width.

11.3.6 Electron microscopy and spectroscopic imaging.

After the experiment and µCT scan, the core fracture was impregnated with epoxy using methods described by Crandell *et al.* (2012). The core was then sectioned perpendicular to the direction of flow. The samples were examined using a Quanta environmental scanning electron microscope (SEM) at a beam energy of 15 keV. The SEM was used for back-scattered electron (BSE) imaging and energy dispersive spectroscopy (EDS).

At the NSLS (Brookhaven National Lab) X-ray microprobes at beamlines X27A and X26A were used. X-ray fluorescence maps were collected by raster 'fly-scanning' the approximately 7x10 (VxH) micron beam at 17.5 keV over regions of interest. Microbeam Ca K-edge XANES spectra were collected at points of interest. Beam energy was controlled with a Si(111) monochromator. Background subtraction, normalization and Linear Combination Fits (LCF) were performed using Athena software (Ravel and Newville, 2005). X-ray diffraction point spectra were collected at 17.479(2) keV incident beam energy using either a Bruker or Rayonix CCD. The diffraction images were background subtracted and integrated into 1-D intensity versus 2-theta using FIT2D (Hammersley *et al.*, 1996).

11.4 Results

11.4.1 Evolution of fracture permeability.

The experiment lasted three days, and based on observed pressure changes, fracture permeability decreased over this time. There were two distinct periods: the first 28 hours when the flow rate was held constant and the final 51 hours when a constant pressure gradient was maintained. A linear regression of the pressure data for the first 28 hours indicates a rate of change in ΔP of 0.074 MPa hr^{-1}. During the final 51 hours the flow rate was instead used to estimate permeability evolution. The time-averaged flow rate during this period was 0.6 ml hr^{-1}, representing an approximate 80% reduction in flow rate. The observed ΔP is shown in Figure 1 along with the corresponding evolution of fracture permeability. Over the course of the entire experiment, fracture permeability decreased more than an order of magnitude.

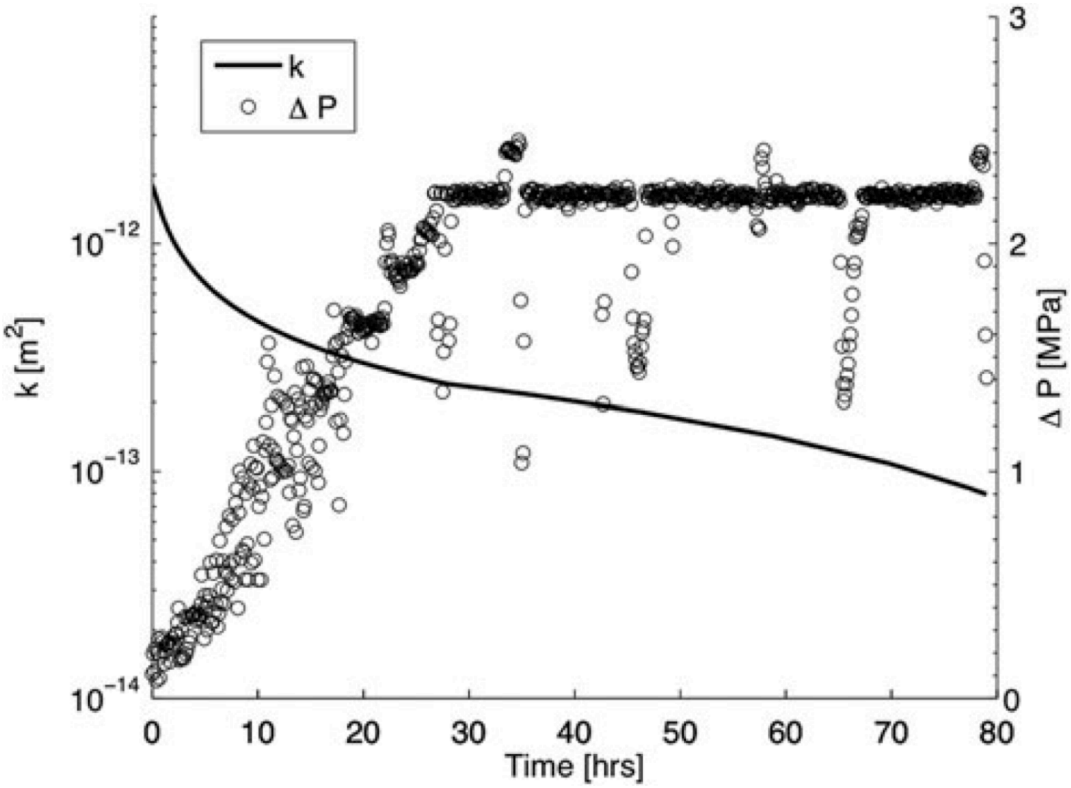

Figure 1: Change in measured pressure difference across the core and corresponding best fit of permeability evolution. As the experimental flow conditions were switched from constant flow rate to constant pressure gradient at 28 hours, two separate linear fits were used to describe permeability evolution over these two distinct flow regimes.

11.4.2 Effluent chemistry.

Analysis of the Ca concentration in the collected brine effluent is given in Figure 2. Figure 2 shows an initial increase in Ca concentration followed by a decrease after cessation of the constant flow rate. The slowed flow rate may have created localized conditions of diffusion-controlled mass transport, and longer fluid residence times that resulted in calcite saturation. While this is an interesting finding, as is discussed later, spectroscopic imaging revealed little evidence of calcite precipitation.

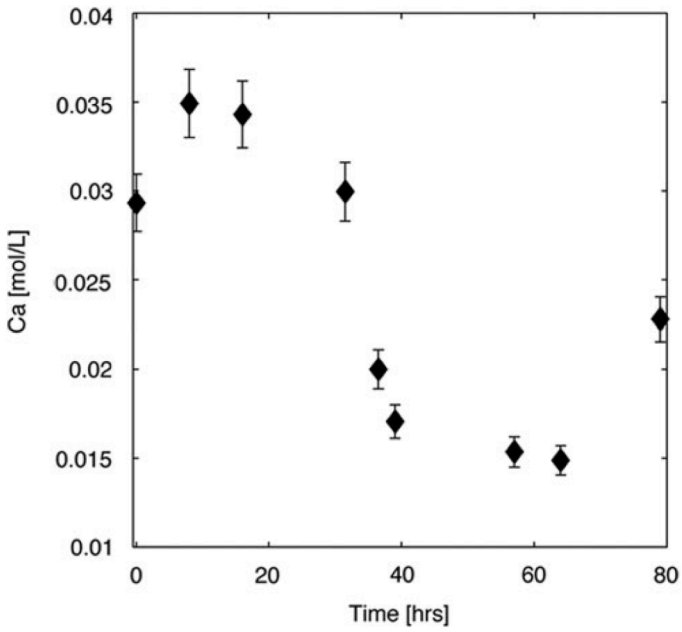

Figure 2: Measured Ca concentration in brine effluent. Initial concentration (see Table 2) is shown at time = 0. The error bars represent the 95% confidence interval of the standard analytical error of 2.8% calculated from duplicate analyses of several brine effluent samples.

11.4.3 X-ray μCT imaging.

The μCT images were processed as described previously (Ellis *et al.,* 2011). The μCT data were used in this study to: (i) quantify and map rock mass removal from the fracture surface, (ii) determine the regions of the fracture where there was the greatest occlusion of flow and (iii) examine the evolution of fracture roughness. Mechanical aperture data derived from the μCT scans do not represent the absolute magnitude of fracture apertures during the flow experiment because of compression under confining pressure. However, the relaxed core measurements do record net changes in mass removal along the fracture. The reproducibility of distances between distinct features in the scans of the two core halves confirmed that the halves returned to their original positions after depressurization. Therefore, the difference in void volume of the before and after scans is a measure of the change in rock mass along the fracture pathway.

Figure 3(a,b) portrays the fracture aperture maps. The increase in aperture variance provides information about the evolution of fracture roughness, which is consistent with previous findings (Ellis *et al*., 2011; Deng *et al*., 2013), and is explained by preferential dissolution of calcite.

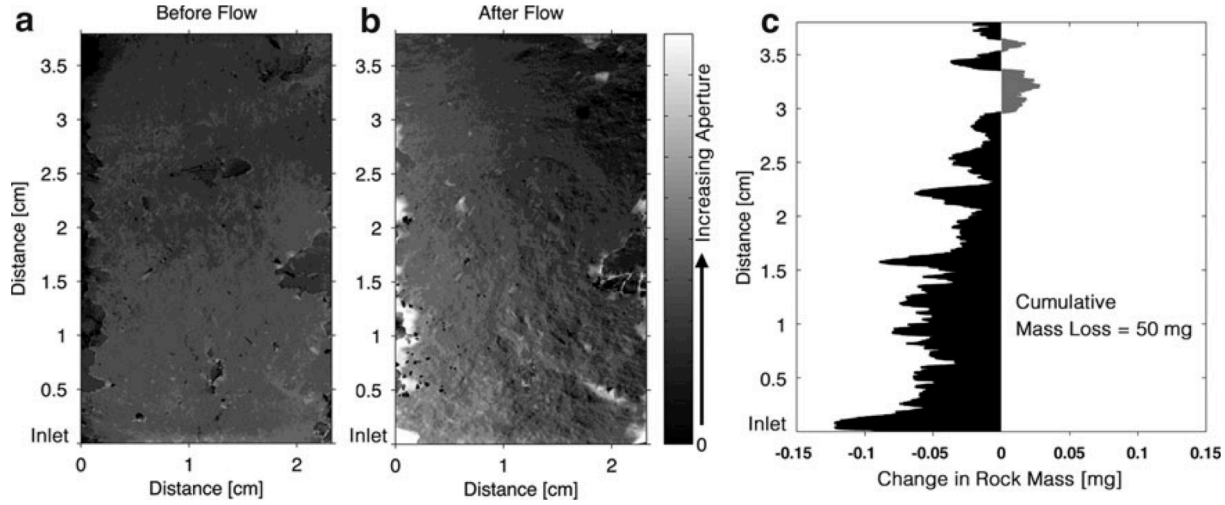

Figure 3: Aperture maps, as estimated from the μCT data, for the fracture before (a) and after (b) flow of the CO_2-acidified brine. The increased aperture variability shown in (b) is demonstrative of the increase in fracture roughness after flow. (c) shows the change in rock mass along the length of the fracture.

The net changes in rock mass along the flow direction are shown in Figure 3(c). Summing the aperture changes over the entire fracture, it was determined that, in total, 50 mg of rock was dissolved. There was greater dissolution at the inlet of the core. There were regions near the outlet where there was a net increase in rock mass within the fracture. Figure 3(b) clearly depicts that this occurred in a region on the right side of the fracture. As is discussed below, in this region evidence of rock fragments within the fracture appears in the μCT scans as voxels with X-ray attenuation values similar to that of the rock matrix (see Figure 4(b)). On the left side, a net increase in fracture aperture is observed, implying that a preferential flow path emerged there.

The principles of critical path analysis in percolation theory dictate that the most resistive paths will control the flow rate along a leakage pathway (Berkowitz and Balberg, 1993). Because we know that the fracture surfaces were not exactly parallel, it is possible that after confining stress was applied, the mechanical aperture near the outlet was restricting flow, while larger apertures emerged upstream.

11.4.4 Electron microscopy and X-ray spectroscopic and diffraction imaging.

Because the μCT analysis revealed regions of increased rock mass near the outlet of the core, a section was taken from that part of the core for subsequent 2D imaging analysis. Results are presented in Figure 4 with the approximate location noted in Figure 4(a). Figure 4(c,d) reveals mineral fragments in the fracture. Because these fragments do not morphologically match the nearby fracture walls, it appears that they did not simply detach from the local surface but rather they have been transported from elsewhere in the flow path. It is likely that these fragments account for the added rock mass observed from the μCT data (see Figure 3(c)).

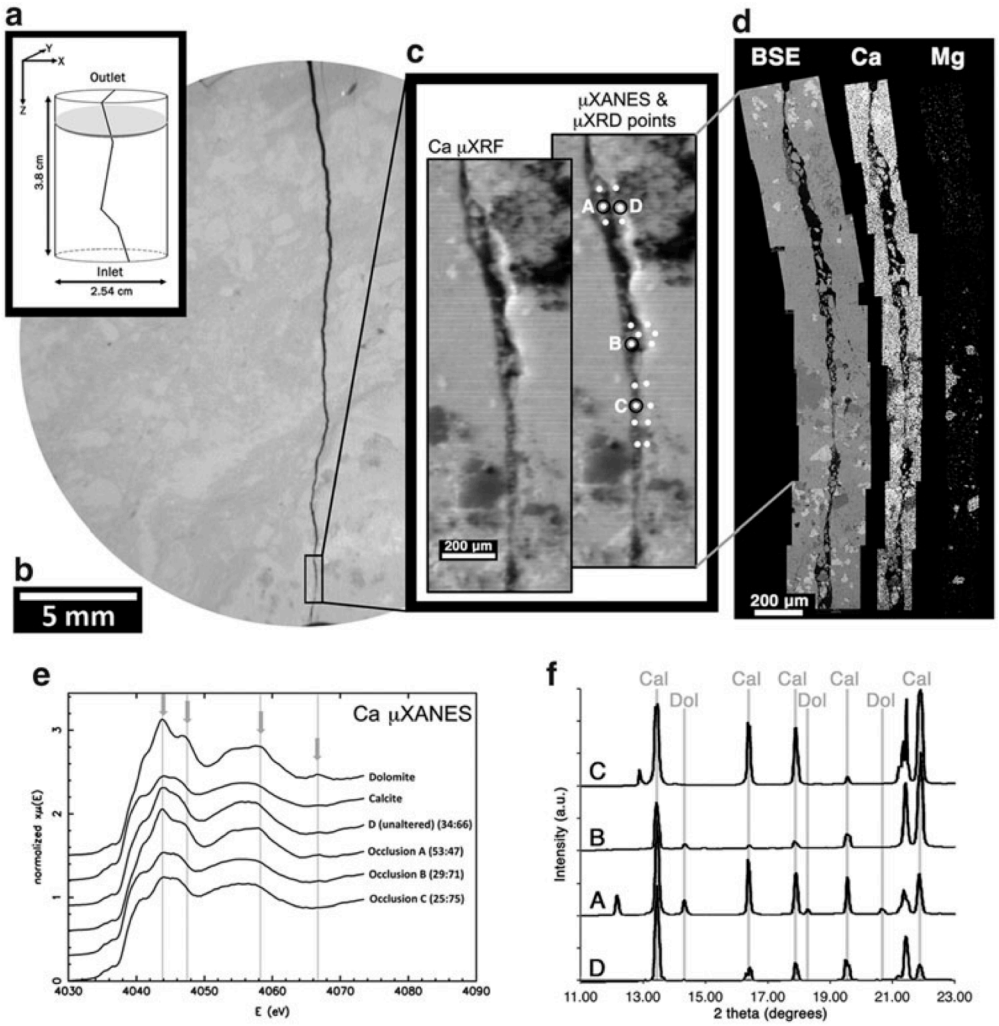

Figure 4: (a) Schematic of fractured core showing core dimensions and location of sub-section analyzed throughout Figure 2; (b) μCT scan showing evidence of fracture closure; (c) μXRF Ca elemental map of box highlighted in 2(b) showing locations of μXRD and μXANES analysis; (d) SEM BSE and EDS maps for Ca and Mg taken at the same location as 2(c); (e) Ca μXANES spectra for points A-D highlighted in 2(c). Calcite and dolomite end-member spectra are also shown along with estimates of dolomite:calcite from linear combination fits; (f) μXRD 1D integrated diffraction data for points A-D with corresponding calcite and dolomite peaks indicated.

Ca μXANES, EDS and μXRD were used to identify the mineralogy of the fragments along the fracture pathway. The Ca μXANES spectra for the subset of points labelled A-D are shown in Figure 4(e) along with the end-member spectra of calcite and dolomite. LCF was used to estimate the relative composition of dolomite and calcite at each point. The smaller fragments (sites B and C) have a signal more similar to calcite, while there is a stronger contribution of dolomite in the larger fragments (site A). The fact that the larger fragments contain dolomite confirms that these particles must have been released from the upstream flow path, as dolomite precipitation is unlikely under the conditions of this experiment. Even though the other spectroscopic techniques (EDS, μXRD) did not confirm it, the Ca μXANES LCF shows the presence of dolomite also in the smaller fragments, so they are also believed to be of upstream origin and not from calcite precipitation. Furthermore, if calcite were to precipitate along the fracture pathway it would be thermodynamically favorable to do so along the calcite-bearing fracture surface (heterogeneous nucleation) rather than within the aqueous phase (homogeneous nucleation) as new particles. Feldspar dissolution and subsequent secondary precipitation of clay minerals is ruled out given the very slow kinetics controlling these reactions and the fact that feldspar minerals were not in abundance (<5%vol).

Figure 5 provides a visual example of how calcite dissolution can lead to release of less reactive mineral particles. Here, calcite dissolution has eroded the rock matrix surrounding a K-feldspar grain. Continued dissolution of the surrounding calcite matrix would have eventually released the grain from the fracture surface. By reasonable conjecture, this is the same way that the dolomite-bearing fragments identified in Figure 4 were generated.

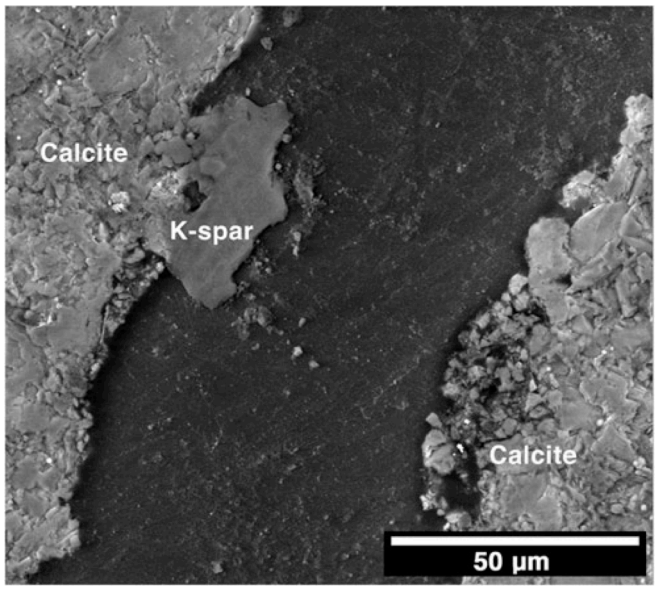

Figure 5: BSE image showing evidence for dissolution of the calcite matrix surrounding a less reactive mineral grain (K-feldspar). Continuation of this process would have resulted in the release of the K-feldspar grain from the fracture surface.

11.5 Discussion

Hypothetically, decreases in fracture permeability due to reactive flows can be attributed to three possible mechanisms: precipitation of secondary minerals in the flow path, occlusion due to particle clogging along the fracture pathway (Noiriel *et al*., 2007; Andreani *et al*., 2008), and dissolution of critical fracture asperities that results in mechanical aperture closure (Polak *et al*., 2003; Yasuhara *et al*., 2006). Although there was a decrease in Ca concentration in the effluent after the flow rate was reduced, calcite precipitation was not identified using any of the imaging methods, so we rule this out as a possible mechanism. Analyses of the particles lodged within the fracture support a scenario where dissolution of calcite led to decohesion and mobilization of less reactive grains that occluded the flow path. Finally, μCT aperture maps suggest that the occluded portion of the fracture produced preferential flow paths along which calcite dissolution removed enough rock mass to eliminate critical asperities and cause mechanical compression of the fracture. Dissolution of critical asperities leading to reduced fracture permeability is consistent with previous studies (Polak *et al.*, 2003). Measurements of mechanical aperture during flow, however, are required to quantify the proportional contribution of these two mechanisms.

These experimental observations of leakage pathway self-sealing shift the focus of efforts to predict permeability evolution from precipitation to coupled geochemical and geomechanical mechanisms. This experiment has shown that calcite dissolution in carbonate rocks may ultimately result in reduced permeability. This is a plausible scenario in formations with compressive stress and in rocks that are mineralogically heterogeneous. This scenario is a counterintuitive result as dissolution is often associated with an increase in porosity, which leads to an increase in permeability. This process would be difficult to predict with existing reactive transport models. Newell and Carey (2012) observed similar fines migration and clogging leading to permeability reductions along a simulated cement-caprock leakage pathway. The observation of dissolution-driven particle migration along a possible CO_2 leakage pathway made by Newell and Carey (2012) supports the findings of our current study, thereby helping to make the case for inclusion of particle transport into future reactive transport simulations assessing CO_2 leakage risk. An excellent example of simulated particle transport and permeability reduction relevant to CO_2 sequestration has been presented by Sbai and Azaroual (2011), albeit for a porous medium rather than for a fractured caprock, and not due to dissolution-induced particle mobilization. Accounting for potential mechanical closure of the fracture following the approach of the thermal-hydrologic-mechanical-chemical modeling employed for the study of geothermal reservoirs (e.g. Taron and Elsworth, 2009) should also lead to more robust CO_2 leakage risk assessments.

In comparing the findings of this study with those of our previous study, Ellis *et al.* (2011), we find that two very similar experiments performed on nearly identical rock cores resulted in opposite outcomes with respect to fracture permeability evolution. This brings into question the reliability of using only a few bench-scale experiments to validate models that estimate fracture permeability evolution, as each experiment may be unique due to spatial variability in mineralogy and different solution chemistries. Experiments conducted at realistic reservoir conditions on actual caprock samples are needed because they may draw our attention to important processes not captured in current models.

11.6 References:

Andreani, M., Gouze, P., Luquot, L., and Jouanna, P. (2008). Changes in seal capacity of fractured claystone caprocks induced by dissolved and gaseous CO_2 seepage. *Geophys. Res. Lett.* 35(14).

Berkowitz, B., and Balberg, I. (1993). Percolation theory and its application to groundwater hydrology. *Water Resour. Res.* 29(4), 775.

Celia, M. A., and Nordbotten, J. M. (2009). Practical modeling approaches for geological storage of carbon dioxide. *Ground Water* 47(5), 627.

Crandell, L. E., Peters, C. A., Um, W., Jones, K. W., and Lindquist, W. B. (2012). Changes in the pore network structure of hanford sediment after reaction with caustic tank wastes. *J. Contam. Hydrol.* 131(1-4), 89.

Deng, H., Ellis, B. R., Peters, C. A., Fitts, J. P., Crandall, D., Bromhal, G.S. (*submitted)*. Modifications of carbonate fracture hydrodynamic properties by CO_2-acidified brine flow. *Energ. Fuel.*

Duan, Z. H., Sun, R., Zhu, C., and Chou, I. M. (2006). An improved model for the calculation of co2 solubility in aqueous solutions containing Na^+, K^+, Ca^{2+}, Mg^{2+}, Cl^-, and SO_4^{2-}. *Mar. Chem.* 98(2-4), 131.

Ellis, B. R., Crandell, L. E., and Peters, C. A. (2010). Limitations for brine acidification due to SO_2 co-injection in geologic carbon sequestration. *Int. J. Greenh. Gas Con.* 4(3), 575.

Ellis, B. R., Peters, C. A., Fitts, J. P., Bromhal, G. S., McIntyre, D. L., Warzinski, R. P., and Rosenbaum, E. J. (2011). Deterioration of a fractured carbonate caprock exposed to CO_2-acidified brine flow. *Greenhouse Gases: Science and Technology* 1(3), 248.

Gherardi, F., Xu, T. F., and Pruess, K. (2007). Numerical modeling of self-limiting and self-enhancing caprock alteration induced by CO_2 storage in a depleted gas reservoir. *Chem. Geol.* 244(1-2), 103.

Gouze, P., Noiriel, C., Bruderer, C., Loggia, D., and Leprovost, R. (2003). X-ray tomography characterization of fracture surfaces during dissolution. *Geophys. Res. Lett.* 30(5).

Hammersley, A. P., Svensson, S. O., Hanfland, M., Fitch, A. N., and Hausermann, D. (1996). Two-dimensional detector software: From real detector to idealised image or two-theta scan. *High Pressure Res.* 14(4-6), 235.

Huerta, N. J., Bryant, S. L., Strazisar, B. R., and Hesse, M. (2011). Dynamic alteration along a fractured cement/cement interface: Implications for long term leakage risk along a well with an annulus defect. *Energy Procedia* 4, 5398.

Kaszuba, J. P., Janecky, D. R., and Snow, M. G. (2005). Experimental evaluation of mixed fluid reactions between supercritical carbon dioxide and NaCl brine: Relevance to the integrity of a geologic carbon repository. *Chem. Geol.* 217(3-4), 277.

Ketcham, R. A., and Carlson, W. D. (2001). Acquisition, optimization and interpretation of X-ray computed tomographic imagery: Applications to the geosciences. *Comput. Geosci.-UK* 27(4), 381.

LeNeveu, D. M. (2008). Cquestra, a risk and performance assessment code for geological sequestration of carbon dioxide. *Energ. Convers. Manage.* 49(1), 32.

Lewicki, J. L., Birkholzer, J., and Tsang, C. F. (2007). Natural and industrial analogues for leakage of co2 from storage reservoirs: Identification of features, events, and processes and lessons learned. *Environ. Geol.* 52(3), 457.

Newell, D. L., and Carey, J. W. (2012). Experimental evaluation of wellbore integrity along the cement-rock boundary. *Environ. Sci. Technol*. doi: 10.1021/es3011404.

Nogues, J. P., Celia, M. A., and Peters, C. A. (2012), Pore network model development to study dissolution and precipitation of carbonates, in *XIX International Conference on Water Resources CMWR 2012*, edited, Urbana, Illinois, USA.

Noiriel, C., Made, B., and Gouze, P. (2007). Impact of coating development on the hydraulic and transport properties in argillaceous limestone fracture. *Water Resour. Res.* 43(9).

Parkhusrt, D. L. A., C.A.J. (1999). User's guide to phreeqc (version 2) - a computer program for speciation, batch-reaction, one-dimensional transport, and inverse geochemical calculations. *USGS Water-Resources Investigations Report*, 99.

Phillips, S. L., Otto, R. J., Ozbek, H., and Tavana, M. (1981). A technical databook for geothermal-energy utilization. *Abstr. Pap. Am. Chem. S.* 181(Mar), 36.

Pitzer, K. S. (1973). Thermodynamics of electrolytes .1. Theoretical basis and general equations. *J. Phys. Chem.-US* 77(2), 268.

Pokrovsky, O. S., Golubev, S. V., Schott, J., and Castillo, A. (2009). Calcite, dolomite and magnesite dissolution kinetics in aqueous solutions at acid to circumneutral pH, 25 to 150 degrees C and 1 to 55 atm pCO_2: New constraints on CO_2 sequestration in sedimentary basins. *Chem. Geol.* 265(1-2), 20.

Polak, A., Elsworth, D., Yasuhara, H., Grader, A. S., and Halleck, P. M. (2003). Permeability reduction of a natural fracture under net dissolution by hydrothermal fluids. *Geophys. Res. Lett.* 30(20).

Ravel, B., and Newville, M. (2005). Athena, artemis, hephaestus: Data analysis for X-ray absorption spectroscopy using ifeffit. *J. Synchrotron Radiat.* 12, 537.

Shao, H. B., Ray, J. R., and Jun, Y. S. (2010). Dissolution and precipitation of clay minerals under geologic CO_2 sequestration conditions: CO_2-brine-phlogopite interactions. *Environ. Sci. Technol.* 44(15), 5999.

Shukla, R., Ranjith, P., Haque, A., and Choi, X. (2010). A review of studies on CO_2 sequestration and caprock integrity. *Fuel* 89(10), 2651.

Smith, M. M., Sholokhova, Y., Hao, Y., and Carroll, S. A. (2013). Evaporite caprock integrity: an experimental study of reactive mineralogy and pore-scale heterogeneity during brine-CO_2 exposure. *Environ. Sci. Technol.* 47(1), 262.

Taron, J., and Elsworth, D. (2009). Thermal-hydrologic-mechanical-chemical processes in the evolution of engineered geothermal reservoirs. *Int. J. Rock Mech. Min.* 46(5), 855.

Viswanathan, H. S., Pawar, R. J., Stauffer, P. H., Kaszuba, J. P., Carey, J. W., Olsen, S. C., Keating, G. N., Kavetski, D., and Guthrie, G. D. (2008). Development of a hybrid process and system model for the assessment of wellbore leakage at a geologic CO_2 sequestration site. *Environ. Sci. Technol.* 42(19), 7280.

Wigand, M., Kaszuba, J. P., Carey, J. W., and Hollis, W. K. (2009). Geochemical effects of CO_2 sequestration on fractured wellbore cement at the cement/caprock interface. *Chem. Geol.* 265(1-2), 122.

Yasuhara, H., Polak, A., Mitani, Y., Grader, A. S., Halleck, P. M., and Elsworth, D. (2006). Evolution of fracture permeability through fluid-rock reaction under hydrothermal conditions. *Earth Planet. Sc. Lett.* 244(1-2), 186.

Zhang, C. Y., Dehoff, K., Hess, N., Oostrom, M., Wietsma, T. W., Valocchi, A. J., Fouke, B. W., and Werth, C. J. (2010). Pore-scale study of transverse mixing induced $CaCO_3$ precipitation and permeability reduction in a model subsurface sedimentary system. *Environ. Sci. Technol.* 44(20), 7833.

Zimmerman, R. W., and Bodvarsson, G. S. (1996). Hydraulic conductivity of rock fractures. *Transport Porous Med.* 23(1), 1.

Chapter 12.Modifications of carbonate fracture hydrodynamic properties by CO_2-acidified brine flow

This chapter has been published as:

Deng, H.; Ellis, B.R.; Peters, C.A.; Fitts, J.P.; Crandall, D.; Bromhal, G.S. "Modifications of carbonate fracture hydrodynamic properties by CO2-acidified brine flow". *Energy and Fuels*. No. 27, pp. 4221 – 4231, 2013. DOI: 10.1021/ef302041s.

12.1 Abstract

Acidic reactive flow in fractures is relevant in subsurface activities such as CO_2 geological storage and hydraulic fracturing. Understanding reaction-induced changes in fracture hydrodynamic properties is essential for predicting subsurface flows such as leakage, injectability, and fluid production. In this study, x-ray computed tomography scans of a fractured carbonate caprock were used to create three dimensional reconstructions of the fracture before and after reaction with CO_2-acidified brine (Ellis et al., 2011, Greenhouse Gases: Sci. Technol., 1:248-260). As expected, mechanical apertures were found to increase substantially, doubling and even tripling in some places. However, the surface geometry evolved in complex ways including 'comb-tooth' structures created from preferential dissolution of calcite in transverse sedimentary bands, and the creation of degraded zones, i.e. porous calcite-depleted areas on reacted fracture surfaces. These geometric alterations resulted in increased fracture roughness, as measured by surface Z_2 parameters and fractal dimensions D_f. Computational fluid dynamics (CFD) simulations were conducted to quantify the changes in hydraulic aperture, fracture transmissivity and permeability. The results show that the effective hydraulic apertures are smaller than the mechanical

apertures, and the changes in hydraulic apertures are nonlinear. Overestimation of flow rate by a factor of two or more would be introduced if fracture hydrodynamic properties were based on mechanical apertures, or if hydraulic aperture is assumed to change proportionally with mechanical aperture. The differences can be attributed, in part, to the increase in roughness after reaction, and is likely affected by contiguous transverse sedimentary features. Hydraulic apertures estimated by the 1D statistical model and 2D local cubic law (LCL) model are consistently larger than those calculated from the CFD simulations. In addition, a novel ternary segmentation method was devised to handle the degraded zones, allowing for a bounding analysis of the effects on hydraulic properties. We found that the degraded zones account for less than 15% of the fracture volume, but cover 70% to 80% of the fracture surface. When the degraded zones are treated as part of the fracture, the fracture transmissivities are two to four times larger because the fracture surfaces after reaction are not as rough as they would be if one considers the degraded zone as part of the rock. Therefore, while degraded zones created during geochemical reactions may not significantly increase mechanical aperture, this type of feature cannot be ignored and should be treated with prudence when predicting fracture hydrodynamic properties.

12.2 Introduction

Understanding changes of fracture hydrodynamic properties due to contact with acidic fluids is essential in numerous subsurface activities, such as geological storage of CO_2, shale gas production, geothermal energy extraction and nuclear waste disposal. Fractures are of special importance due to their prevalence[1], and potential impacts on flow and reactive transport[2]. Both natural and induced fractures are widely documented in subsurface systems[3-5]; including CO_2 storage sites[6,7]. Geomechanical studies have demonstrated that during CO_2 injection, fractures can be created, activated and propagate in caprocks because of shear stresses[8], thermal stresses[9] and crystallization[10]. As fractures serve as conduits for flow, their presence may enhance the risks of CO_2 leakage. Therefore, a comprehensive assessment of caprock integrity requires detailed characterization of fracture hydrodynamic properties and knowledge of their evolution over time. During shale gas and geothermal energy extraction, fractures are often intentionally induced. Their hydrodynamic properties control the production and hence profitability of the fields.

Fractures provide pathways for transport of reactive solutes, resulting in thermodynamic gradients that accelerate water-rock interactions. Geochemical alterations of fracture surfaces and flow-path geometry will ultimately modify hydrodynamic properties of caprocks or production formations. In the context of CO_2 geological storage, both simulation results[11] and experiments[12-14] have shown profound alteration of fracture geometry due to the flow of CO_2-acidified brines. Similarly, acidic fracturing fluids may be used to alter the hydrodynamic properties of fractures created or activated during the exploitation of gas-bearing shale formations. Although shale formations typically have a high content of relatively unreactive clay minerals, they often co-exist with other acid-soluble minerals, e.g. carbonates[15]. Furthermore, if induced fractures are not properly contained within the production formation, but instead propagate into the overlying formations, the hydrodynamic properties of these fractures and their evolution will determine the risks of vertical migration of fracturing fluid and gas, and potentially groundwater pollution.

Reactive transport in fractures and the patterns of dissolution and precipitation are controlled by the flow regime[16-18], initial geometry[2,18], confining stress[17], mineralogy and brine chemistry[13,14]. Numerous simulation studies have investigated the evolution of fracture aperture and hydrodynamic properties that

result from the interactions between fracture surfaces and reactive flow[18-23]. In addition, imaging techniques such as light transmission[24] and 3D micro X-ray computed tomography (xCT)[25-28] provide non-invasive geometric measurement tools, and their applications have enabled observations of acid-driven geometric evolution of fractures[16,17,25,29,30]. Detwiler[17] observed relatively uniform dissolution at low Damkohler number and channelization at high Damkohler number. This same research group also reported that low Peclet number favors formation of channels, while high Peclet number leads to smoothing of small scale roughness without channelization[16]. Furthermore, Szymczak and Ladd[23] found that channelization occurs above a roughness threshold and is favored under the conditions of high reaction rates and intermediate Peclet number. While these studies have greatly advanced our knowledge of some fundamental processes underlying geochemically-driven fracture evolution, they often assumed homogeneous mineralogy and used model fractures.

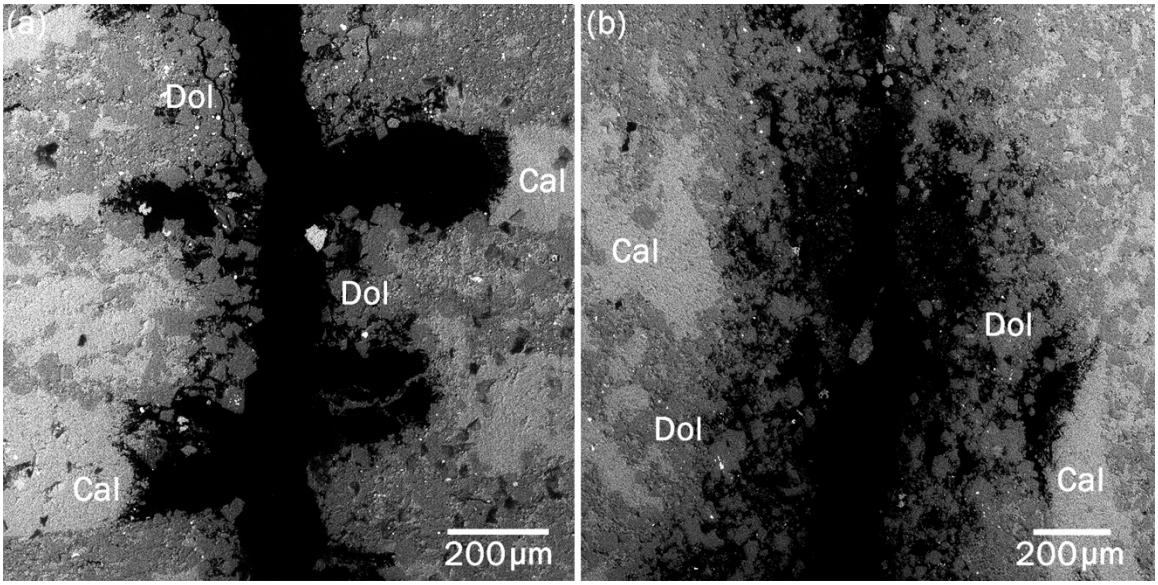

Figure 1. Scanning electron microscopy (SEM) images in back-scattered electron (BSE) mode, showing unique fracture surface geometries that resulted from reaction with CO_2-acidified brine (as a result of the experiment presented in Ellis et al, 2011). (a) comb-tooth wall geometry resulting from receding calcite bands and persistence of less soluble minerals, (b) porous 'degraded zone' along the fracture wall created by preferential dissolution of calcite.

The effects of mineral spatial heterogeneity on fracture evolution are poorly understood, and need consideration as mineral heterogeneity may result in very complex geometric modifications. In a high-pressure experiment, Ellis et al.[13] flowed CO_2–acidified brine through an artificially fractured carbonate core from the Amherstburg formation of the Michigan sedimentary basin. Post-experiment scanning electron microscopy (SEM) imaging revealed extensive dissolution and complex geometric alterations of the fracture created by preferential dissolution patterns, as shown in Figure 1. For example, where the relatively soluble mineral calcite is banded with less soluble dolomite, preferential dissolution of calcite created 'comb-tooth' shaped roughness (Figure 1a). In contrast, where calcite is homogeneously mixed

with dolomite or non-reactive clay minerals and quartz, very porous calcite-depleted areas were formed, which the authors refer to as "degraded zones" (Figure 1b).

It remains an open question as to whether extensive fracture volume increases resulting from dissolution will manifest as substantial alterations to fracture hydrodynamic properties, and thereby compromise caprock sealing capacity. It is possible that geometric alterations such as increased roughness will counteract the impact of fracture volume increase. In an experiment flowing acidic water through a fractured argillaceous limestone rock sample, Noiriel et al.[30] recorded a decrease in permeability that they attributed partly to the increase of fracture roughness.

A large volume of literature exists on fracture roughness and its impacts on flow. One-dimensional models based on the distribution of local apertures have been proposed to incorporate roughness by using a weighted average or standard deviation of apertures[31-33]. Another modeling approach widely adopted is the Local Cubic Law (LCL)[18,19,34-37]. It assumes that the cubic law for smooth parallel wall fractures holds locally, and solves Reynolds equation locally. However, these models do not provide accurate estimations of fracture hydrodynamic properties at relatively high, yet realistic roughness[29,38,39].

Computational fluid dynamics (CFD) simulations have been shown to provide accurate calculations for flow in fractures across a range of plausible fracture roughness[38-40]. By using different meshing tools and applying different degrees of smoothing, Crandall et al.[39] generated six fracture meshes with different degrees of roughness. They found that increase in fracture roughness results in more tortuous flow and lower transmissivity. Yet, roughness in these studies has typically been decoupled from the spatial distributions of minerals and the resulting dissolution patterns.

In this study, our objective was to investigate the relationships between the change in fracture surface geometry and hydrodynamic properties resulting from acid-promoted dissolution. In particular, we investigated the effects of significant fracture volume increase and roughness increase that arises because of mineral spatial heterogeneities. Based on the outcome of the experiment by Ellis et al.[13], xCT scans of the fractured core were used to reconstruct the fracture geometries before and after reaction with flowing CO_2-acidified brines. CFD simulations were performed on 3D finite-element meshes generated from the fracture geometries, allowing a comparison of predicted hydrodynamic aperture with mechanical aperture. To determine if simpler modeling approaches can capture fracture surface geometry effects, hydrodynamic properties were also estimated using a one-dimensional statistical model and a two-dimensional LCL model. The basis for comparison of these model predictions are the fracture hydrodynamic properties calculated from the CFD simulation results. It was not possible to make comparisons with experimental permeabilities, which were not measurable under the flow condition of the experiment, as explained by Ellis et al.[13].

Our study is novel in two aspects. First, the fracture geometries used are the actual results from reaction of a caprock specimen, which is a typical dolomitic limestone that is rich in mineral heterogeneity. Second, we developed a novel segmentation approach to examine the effect of degraded zones, i.e. the calcite-depleted porous rock on reacted fracture surfaces.

12.3 Theoretical Basis

Fracture transmissivity, T, and permeability, k, are both measurements of the ease for fluid to flow through a fracture, as described by the relationship between volumetric flow rate, Q, and the pressure gradient, ∇P, through Darcy's law:

$$Q = -T\frac{(\nabla P)}{\mu} = -\frac{Ak}{\mu}\nabla P \quad (1)$$

where μ is the fluid viscosity and A is the cross-sectional area of the fracture perpendicular to flow. Theory for single phase flow in a smooth parallel fracture[41], frequently referred to as the cubic law, states that T is related to the cube of mechanical aperture, b, the vertical distance between two fracture walls. When the assumption of smooth parallel walls breaks down, the aperture is replaced with its effective value, the hydraulic aperture b_h[33],

$$T = -\frac{Wb_h^3}{12} \quad (2)$$

$$k = \frac{b_h^2}{12} \quad (3)$$

where w is the width of the fracture. Properties T, k and b_h provide three different ways to characterize fracture hydrodynamic properties, and they are related as shown in eqns 1, 2 and 3. The value of the fracture T and fracture intrinsic k is that they can be directly compared with field measurements, lending insights on how the fracture may impact the hydrodynamic properties of the formation. The b_h can be readily compared with b, which can be derived from image analyses or estimated from fracture volume, to investigate whether and how the flow behaves differently from flow in a parallel wall fracture.

12.4 Methods

12.4.1 Segmentation and Meshing

The xCT scans used in this study had voxel resolution of 27 μm. Two separate areas of the fracture were selected to avoid regions that were not amenable to meshing, including a horizontal fracture and the multi-fractured edges. The selected fracture areas have a length of 2.176cm and 3.078cm for Area-1 and Area-2 respectively, and a width of 1.296cm for both areas (Figure 2). xCT images corresponding to the selected fracture areas were processed to isolate the fractures and rock matrix immediately surrounding the fracture boundary on the grayscale xCT images. To segment the grayscale xCT images, we applied Otsu's method[42], which involves searching for thresholds that minimize interclass variance. As an example, Figure 3a and 3c shows the grayscale xCT image for a cross-sectional slice before the reaction. Figure 3b is the histogram for the boxed area of figure 3a showing the threshold generated by Otsu's method. The resulting binary segmentation separating the fracture from the rock is shown in Figure 3d.

The after-reaction xCT images did not show a clean interface, but instead showed fuzzy zones between the rock and the fracture (Figure 3g). These areas have been previously identified using SEM images of core sections (Figure 1b) as 'degraded zones'[13], porous areas created by preferential dissolution of calcite

from regions where it is intermixed with less-reactive minerals. To examine the effect of depleted zones, a ternary segmentation method was devised to classify voxels as either fracture, rock, or degraded zone (Figure 3h). This method did not simply segment voxels based on grayscale intensity, which would have overestimated the degraded zone due to the ubiquitous presence of transitional grayscale intensities at all edges. Instead, an algorithm was developed in which a window with a specific size moves along the rock-fracture interface to identify zones with intermediate grayscale intensities, and only zones with thickness above a cutoff value was segmented as 'degraded zone'. A wide range of window sizes and cutoff thicknesses were tested. Numerous visual inspections were conducted to compare the ternary-segmented images with the original xCT images to ensure that the algorithm was accurately characterizing the degraded zone.

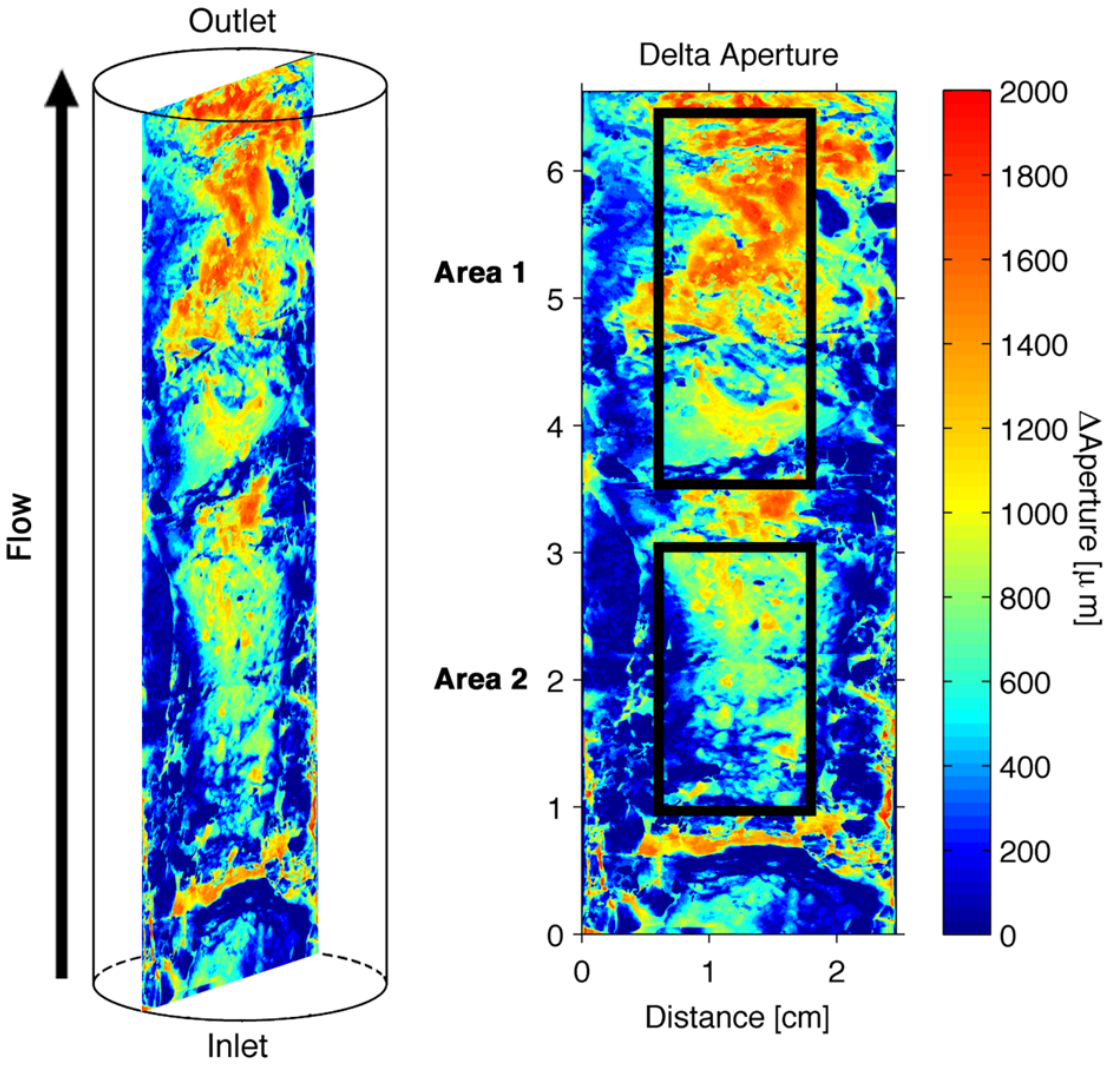

Figure 2. Schematic of the fractured core (left) with a map of fracture aperture change due to reactions with CO_2-acidified brine flow (based on Ellis *et al*., 2011), with black boxes indicating two areas selected for CFD simulation in this study (right). (This map is different from the aperture change maps generated in this work, as a binary segmentation was performed for both before and after reaction xCT images.)

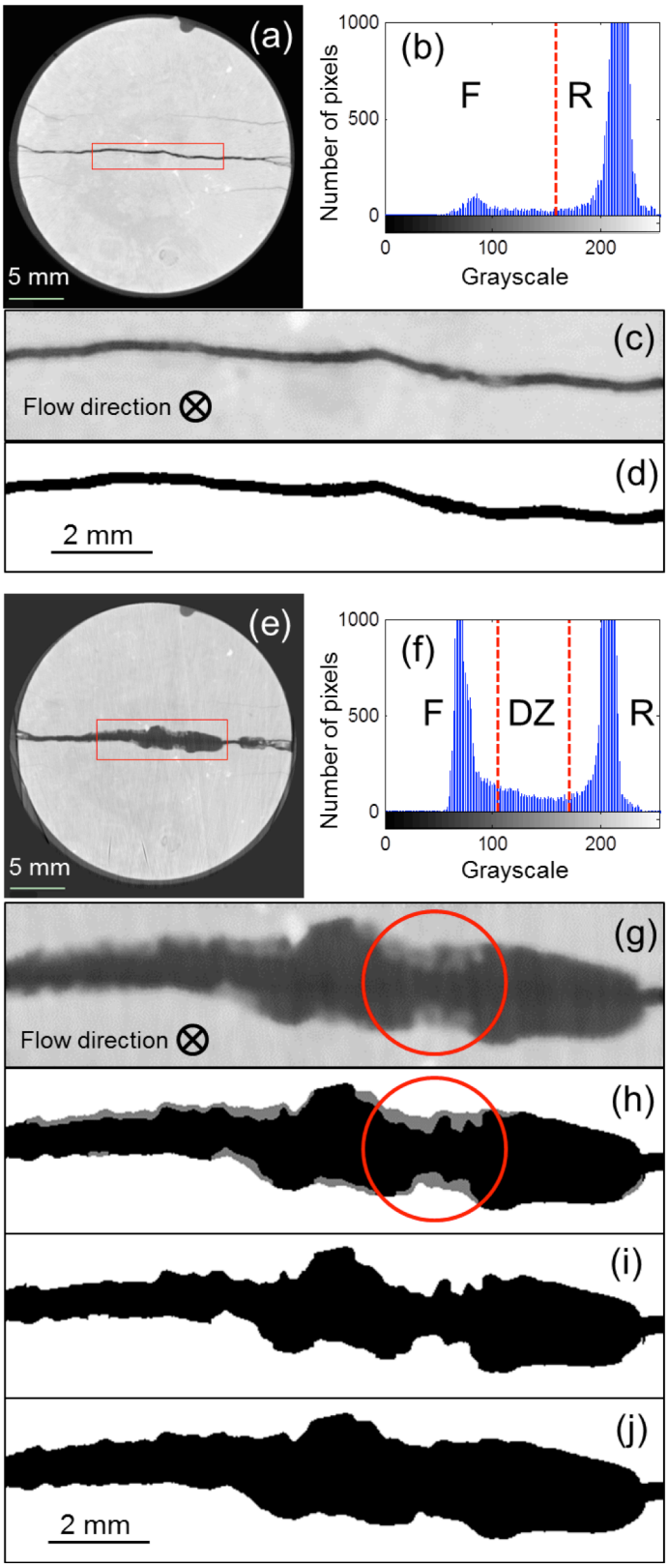

Figure 3. Example images depicting the geometry of the fracture, with a focus on the degraded zone and the ternary segmentation method developed in this work. The location for these images is in Area-2 at y=5.75 cm according to the scale shown in figure 2. (a) xCT image of a cross-section of the fracture taken before the experiment, with the study area identified in the red box, (b) histogram for the grayscale image of the study area in (a), F-fracture, R-rock, (c) close-up of the grayscale xCT image of the study area in (a), and (d) segmented image with black corresponding to the fracture and white corresponding to the rock, (e) xCT image of the same fracture cross-section, taken after the experiment, with the study area indicated in the red box, (f) histogram for the grayscale image of the study area in (e), F-fracture, R-rock, DZ-degraded zones, (g) close-up of the grayscale xCT image, with a circle indicating an area where there is a degraded zone, (h) ternary segmented image with degraded zones shown in gray, (i) binary segmented image showing degraded zone treated as rock, and (j) binary segmented image showing degraded zone treated as fracture.

To examine the impact of the degraded zones on flow, a bounding analysis was conducted to constrain reality between two extremes. In one scenario, the degraded zones were treated as rock (Figure 3i), assuming the degraded zones are impermeable. In the other scenario, the degraded zones were treated as fracture (Figure 3j), assuming no resistance to flow. Reality falls somewhere between these two scenarios. Comparing flow in the two scenarios provide some insights on the impacts of the degraded zone on fracture hydrodynamic properties.

The segmented images were imported into a 3D volumetric mesh generator iso2mesh[43], producing meshes such as that shown in Figure 4. Given the complexity of the fracture geometry, unstructured tetrahedral meshes were generated. Minimal smoothing and simplifications were applied to preserve the complexity of the fracture geometries. Meshing parameters were optimized to ensure good mesh quality (e.g. orthogonality and skewness) and numerical performance (e.g. convergence and computational cost). Six 3D meshes were generated including three meshes each for Area-1 and Area-2: before-reaction binary segmentation, after-reaction with degraded zone treated as rock, and after-reaction with degraded zone treated as fracture. Each mesh contains on the order of 10^6 grids following optimization.

To quantify uncertainties deriving from the choice of mesh density, a smaller area of Area-2 was analyzed using a range of mesh densities. Specifically, the selected Area-2 fracture was the after reaction one with degraded zones treated as rock. This test area was regarded to be the best case for the study of sensitivity to mesh density for two reasons. First, its geometry is the most difficult to mesh, which requires finer grids to capture sharp features. Second, the apertures of the test area cover a wide range of the aperture values of the whole area, ranging from 0 to 1998 μm. Meshes of the test area were generated using a spectrum of meshing parameters, resulting in density increases by a factor of 2 to 20. CFD simulations of these test meshes showed that higher mesh densities result in slightly lower values of hydraulic aperture. An increase of the mesh density by more than 20 times leads to a decrease of 28 μm. Therefore, we can assume that the uncertainty associated with mesh densities is approximately 28 μm.

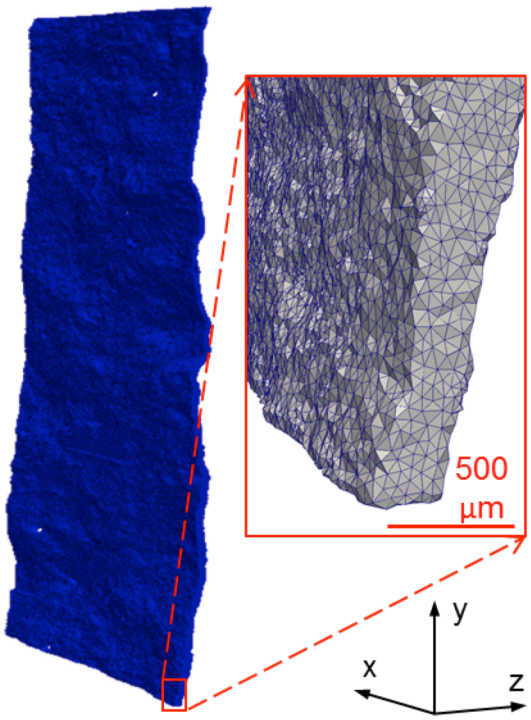

Figure 4. Finite-element tetrahedral mesh of Area-2 before reaction, and a close-up of the mesh in the red box.

12.4.2 Geometric characterizations

To statistically characterize fracture surface geometries, each mesh was converted into a 3D volumetric image with the same voxel resolution of 27 microns as the original xCT images. Fracture aperture was measured as the total number of fracture pixels in each column spanning the two fracture walls in the 3D volumetric image.

Surface roughness was characterized using surface Z_2 parameter and fractal dimension D_f. For a 3D surface with resolution of Δx and Δy on the x- and y- direction respectively, the surface Z_2 parameter is calculated using equation (4)[44],

$$Z_2 = \left\{\frac{1}{(N_x-1)(N_y-1)}\left[\frac{1}{\Delta x^2}\sum_{i=1}^{N_x-1}\sum_{j=1}^{N_y-1}\frac{\left(z_{i+1,j+1}-z_{i,j+1}\right)^2+\left(z_{i+1,j}-z_{i,j}\right)^2}{2}+\right.\right.$$

$$\left.\left.\frac{1}{\Delta y^2}\sum_{j=1}^{N_y-1}\sum_{i=1}^{N_x-1}\frac{\left(z_{i+1,j+1}-z_{i+1,j}\right)^2+\left(z_{i,j+1}-z_{i,j}\right)^2}{2}\right]\right\}^{\frac{1}{2}} \quad (4)$$

where N_x and N_y are the numbers of discrete grids along the x- and y- axis, and z is the height of the surface. A large surface Z_2 parameter corresponds to large variation of the local surface slope and thus corresponds to higher roughness.

Fractal dimensions, D_f, for 2D cross-sections along the flow direction (y) were calculated using the bandwidth method[39,45]. Standard deviation of the vertical displacement, σ_S, was calculated using equation (5) for a range of window size, s.

$$\sigma_S = \sqrt{\frac{1}{N_y-s}\sum_{i=1}^{N_y-s}(z_{i+s}-z_i)^2} \quad (5)$$

The parameter s ranges from Δy, and is cut off at the long wave length, which is approximately one sixteenth of the length of fracture[46]. A linear fitting was applied on the logarithms of σ_S and s to obtain the Hurst exponent, H. Fractal dimension, D_f, is then calculated from H using equation (7).

$$\sigma_S \propto s^H \quad (0 < s < L/16) \quad (6)$$

$$D_f = 2 - H \quad (7)$$

For each fracture surface, calculations of surface Z_2 parameter and D_f used a resolution (Δx and Δy) of 27 μm. The number of grids along flow direction (y) is 806 and 1140 for Area-1 and Area-2, respectively, and the number of grids across the flow direction (x) is 480 for both areas. Therefore there are 480 cross-sections along the flow direction for each surface. D_f was calculated for each cross-section and the average is used for the surface. For each fracture geometry, surface Z_2 parameters and D_f were calculated for both the upper and lower fracture surfaces (which were assigned arbitrarily, as neither surface is up or

down). Since the flow is affected not only by the surface roughness, but also by the degrees of matching between the upper and lower surfaces[47], a midsurface[48] defined as the mean of the two fracture surfaces was used, providing a representation of the fracture undulation. Roughness of the midsurface was also characterized for all the fracture geometries.

12.4.3 CFD Simulations

CFD simulations were conducted by importing the finite-element tetrahedral meshes into OpenFOAM (OpenCFD Ltd, ESI Group) and using its tools to numerically solve the continuity and momentum equations. A steady state solver (simpleFoam) was used. Momentum was solved using the smoothSolver, and pressure was solved with the Geometric-algebraic multi-grid (GAMG) solver. The momentum and continuity equations were coupled using the SIMPLE (Semi-Implicit Method for Pressure-Linked Equations) algorithm. A linear scheme was used to interpolate values from cell center to face center, and a limited non-orthogonal correction with $\psi = 0.7$ was selected to evaluate the surface normal gradient from gradient of values at the cell centers. The convergence criterion for steady state was set as when the normalized residual in the solution falls below 10^{-5}.

Boundary conditions used in the simulations are no-slip wall, fixed pressure at the outlet, and uniform velocity profile at the inlet. The test velocities varies from 10^{-6} m/s to 10^{-3} m/s, ensuring a flow regime of creeping flow, i.e. Re<1. Reynolds number (Re) was calculated for all fracture geometries, using the equation[49]

$$Re = \frac{4\rho Q}{p\mu} \tag{8}$$

where ρ is fluid density and p is the perimeter of the channel. Perimeters were calculated for all the fracture cross-sections perpendicular to flow direction in every fracture. Reynolds number calculated from the velocity range and perimeter range vary between $2\text{x}10^{-4}$ and 0.44. Fluid properties of water were used in all the simulations, with r = 998.2 kg/m^3 and m = 10^{-3} Pa·s. Four different velocities were used for each fracture geometry to capture variability in the calculations, which resulted in negligible variations in the simulation results, and therefore, only averages are reported for each mesh geometry. The CFD simulations resulted in pressure gradient fields, which together with the flow rate were used to calculated fracture T, k, and b_h using equation (1)-(3).

12.4.4 1D empirical model

For comparison, the one-dimensional empirical model proposed by Zimmerman and Bodvarsson[33] was also used. The model (eqn (9)) estimates b_h from b, and accounts for the impacts of roughness by incorporating standard deviation of mechanical aperture, σ, and contact area ratio, c, the ratio of contact area over the fracture surface area.

$$b_h^3 \approx \bar{b}^3\left[1 - \frac{1.5\sigma^2}{\bar{b}^2}\right](1 - 2c) \tag{9}$$

In this study, contact area ratios within Area-1 and Area-2 are negligible.

12.4.5 2D LCL model

Also for comparison, the 2D LCL model[35] was used. In this model, the cubic law is assumed applicable locally. The two-dimensional steady state mass balance equation is given as in (eqn(10)).

$$\frac{\partial}{\partial x}\left[b^3(x,y)\frac{\partial P(x,y)}{\partial x}\right]+\frac{\partial}{\partial y}\left[b^3(x,y)\frac{\partial P(x,y)}{\partial y}\right]=0 \quad (10)$$

Five-point central finite difference numerical approximation was used to solve the equation at each cell, with the harmonic mean of the apertures of the adjacent cells taken as equivalent aperture on the edge. Vertically averaged velocities are then calculated from the pressure fields and Darcy's law (eqn(11) and (12)).

$$\overline{u_x}=\frac{b(x,y)^2}{12\mu}\frac{\Delta P}{\Delta x} \quad (11)$$

$$\overline{u_y}=\frac{b(x,y)^2}{12\mu}\frac{\Delta P}{\Delta y} \quad (12)$$

12.5 Results and Discussion

12.5.1 Fracture Geometric Characterization

Table 1 presents the mesh properties of six fracture geometries. The significant fracture volume increase caused by calcite dissolution is reflected in the higher numbers of cells for the four after-reaction meshes (Table 1). The after-reaction meshes also required finer grids at the geometrically sharp locations to accurately represent surface roughness. As demonstrated in Figure 5a-c, e-g, the distributions of mechanical aperture (*b*) for both Area-1 and Area-2 shift to larger apertures, and span a broader range after reaction. These findings are consistent with the distributions reported in Ellis et al.[13] for the whole fracture. When degraded zones are treated as part of the rock, the histograms shift less (Figure 5c and 5g) relative to when the degraded zones are instead treated as fracture (Figure 5b and 5f).

Table 2 documents all of the major statistics of the mechanical apertures for the six meshes. After reaction, the average aperture of Area-1 doubled. For Area-2, the average aperture tripled. The maximum aperture recorded for the after-reaction meshes increased much more than the average aperture, leading to larger standard deviations.

Degraded zones account for less than fifteen percent of the fracture volumes, and yet cover 70% and 80% of the fracture surfaces in Area-1 and Area-2, respectively. Comparing the aperture distributions of the two different treatments of degraded zones (Table 2), average aperture differences are 141 μm and 271 μm for Area-1 and Area-2, respectively. The differences are due to the relatively small fracture volume occupied by degraded zones, which is also reflected in the thickness histograms for the degraded zones that are shown in Figure 5d and 5h. Larger standard deviations are observed when degraded zones are considered as fracture.

Table 1. Mesh properties of six fracture geometries. DZF - Degraded Zones treated as Fracture, DZR - Degraded Zones treated as Rock.

			Volume (mm^3)	# of grids	Surface Z_2 parameter			D_f		
					Upper wall	Lower wall	Mid-surface	Upper wall	Lower wall	Mid-surface
Area-1	Before Reaction		1.68E+02	3.76E+06	0.85	0.97	0.67	1.33	1.36	1.29
	After Reaction	DZF	3.38E+02	6.41E+06	0.97	0.98	0.69	1.39	1.41	1.33
		DZR	2.98E+02	7.09E+06	1.66	1.92	1.26	1.51	1.56	1.49
Area-2	Before Reaction		1.33E+02	3.48E+06	0.66	0.79	0.55	1.31	1.33	1.28
	After Reaction	DZF	5.28E+02	5.23E+06	1.31	1.28	0.90	1.49	1.49	1.46
		DZR	4.21E+02	9.79E+06	2.17	2.27	1.52	1.57	1.57	1.56

Table 2. Aperture statistics of six fracture geometries. DZF – Degraded Zones treated as Fracture, DZR – Degraded Zones treated as Rock.

			Aperture (b) (μm)					
			min	max	mean	median	std	mode
Area-1	Before Reaction		0	1269	594	594	124	594
	After Reaction	DZF	0	1998	1194	1242	242	1323
		DZR	0	1998	1053	1080	303	1296
Area-2	Before Reaction		0	810	332	324	79	270
	After Reaction	DZF	0	2484	1319	1323	390	1377
		DZR	0	2457	1048	1053	420	1026

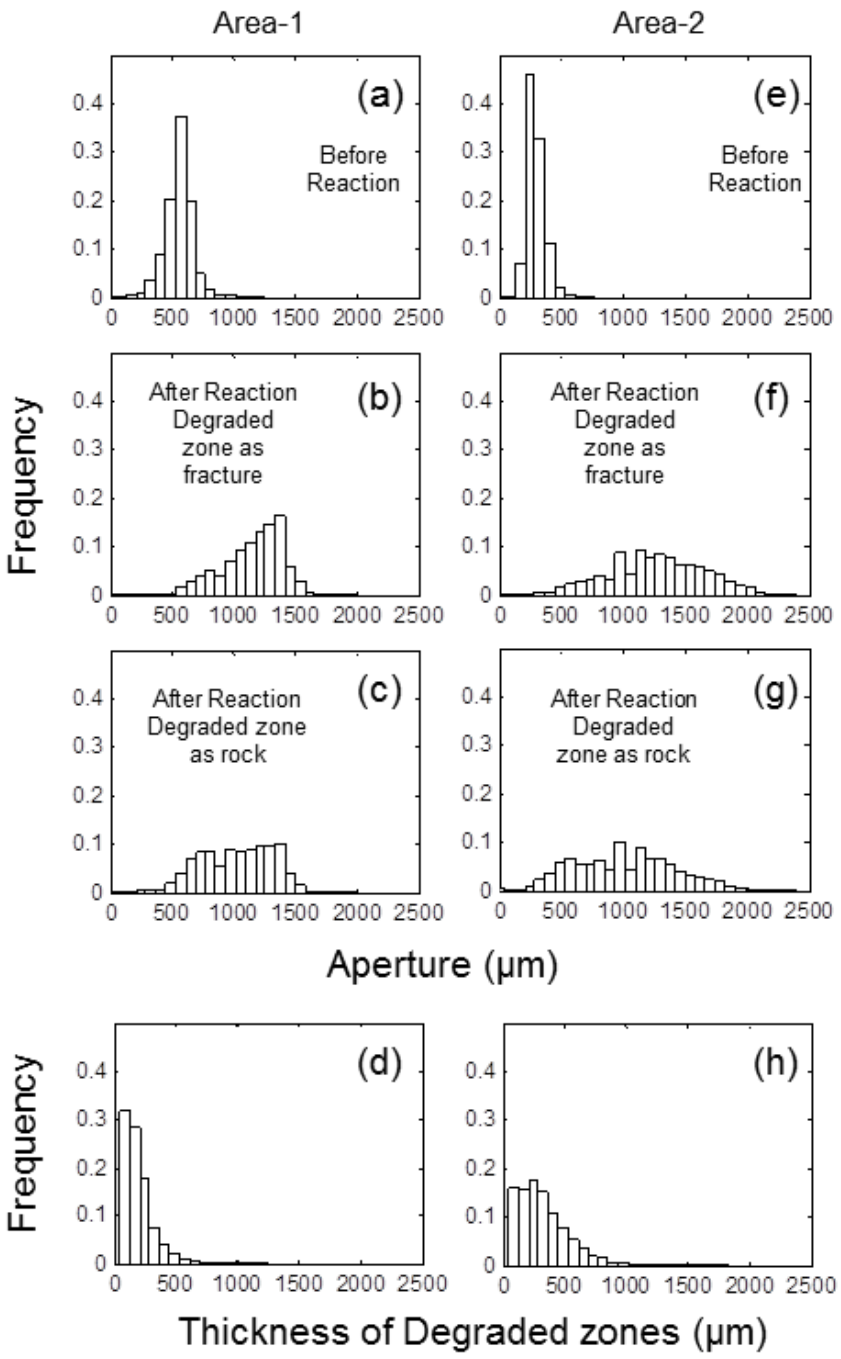

Figure 5. Histograms of the distributions of mechanical apertures for Area-1 (a) before reaction, (b) after reaction with degraded zone treated as fracture, (c) after reaction with degraded zone treated as rock, and Area-2 (e) before reaction, (f) after reaction with degraded zone treated as fracture, (g) after reaction with degraded zone treated as rock. Histograms of the thickness of degraded zones for (d) Area-1, and (h) Area-2.

Table 1 tabulates the roughness parameters. The surface Z_2 parameters are generally larger than the values reported previously[44], which can be attributed to the fine resolution of the meshes. The D_f values calculated for all the fracture meshes fall in the 1 to 2 range of a true fractal, and fluctuate around 1.5, the value for a Brownian fractal profile[50], justifying the adoption of fractal dimension and the method used to calculate D_f in the fracture meshes.

The dissolution reactions significantly enhanced the roughness of the fracture surfaces in both Area-1 and Area-2. Both the surface Z_2 parameters and D_f increase after reactions. This trend is consistent for the upper and lower walls, as well as the midsurface of the fracture meshes, implying that the changes of the two fracture surfaces are not perfectly correlated. However, the lower roughness of the midsurface relative to the fracture walls indicates some degree of symmetry and registry between the two fracture walls. If degraded zones are treated as fracture, the increase in roughness relative to the before-reaction meshes is limited; whereas the roughness increase is more significant when degraded zones are treated as rock. The impacts of degraded zones on surface roughness measured by both surface Z_2 parameters and D_f are consistently observed for both areas.

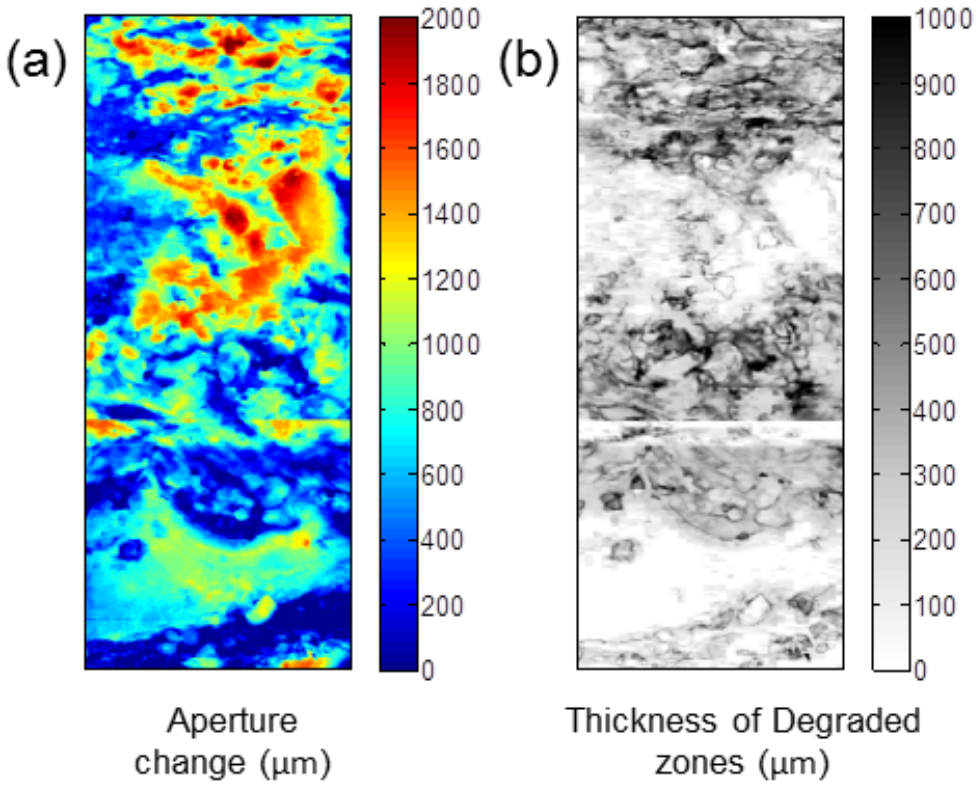

Figure 6. (a) Changes of aperture between after-reaction geometry degraded zones treated as rock and before-reaction geometry of Area-2, and (b) a map of the occurrence and thickness of degraded zones. The linear feature at approximately one third of the area from the bottom is due to the fact that two scans were stitched together.

Figure 6 shows the comparison between the changes in aperture (Figure 6a) and the spatial distribution of degraded zones (Figure 6b). The white regions of Figure 6b, which indicate the absence of degraded zones, are generally correlated with areas of great aperture increase shown in Figure 6a. In contrast, presence of thick degraded zones as shown in darker color in Figure 6b coincide with some of the regions where aperture increase is limited. In regions such as the blue band at the bottom of Figure 6a, aperture increase is small and degraded zones are absent or thin, thus indicating bands of unreactive minerals. The large surface coverage of degraded zones and the variable thickness shown within degraded zones (Figure 6b) are consistent with the observation that treating the degraded zone as rock produces the largest after-reaction increase in fracture roughness.

12.5.2 Fracture hydrodynamic properties

The pressure and velocity fields are shown in Figure 7. Examples of pressure fields are shown only for the before-reaction meshes. The CFD inferred T and k values of the after-reaction meshes are larger than those of the before-reaction meshes (Figure 8), indicating an increase in fracture hydrodynamic properties following exposure of the fracture to CO_2-acidified brine flow. When the degraded zones within Area-1 are treated as fracture, T increased by a factor of 8, from the value before reaction, and k increased by a factor of 4. When the degraded zones in Area-2 are treated as fracture, both T and k increased by more than an order of magnitude. When the degraded zones are treated as rock, however, the margin of the increases in T and k narrowed significantly in both areas. For Area-1, T and k of the mesh for which degraded zones are treated as rocks are approximately half of the values for when degraded zones are treated as fracture. Differences in T and k between the two after-reaction meshes are even larger for Area-2.

The hydraulic aperture inferred from CFD simulations b_{hCFD} are consistently lower than the average b values derived directly from the xCT images (Figure 9). For Area-1, the before-reaction b_{hCFD} is approximately 150 μm less than the b, while the after-reaction differences are twice this more. For Area-2, the initial difference between b_{hCFD} and b is approximately 100 μm, but this difference increased to more than 500 μm after reaction. The discrepancy between b and b_{hCFD} is smaller when degraded zones are treated as fracture. Values of hydraulic aperture estimated using the 1D roughness model developed by Zimmerman and Bodvarsson[33] and the 2D (LCL) model[35] are also smaller than b. These values, however, are consistently larger than the b_{hCFD}. In addition, the differences between hydraulic apertures estimated from the 1D and 2D model and b_{hCFD} and are much larger than the uncertainty in b_{hCFD} associated with increasing mesh density. Finally, although both b_{hCFD} and b increased following reactive flow due to dissolution reactions, the changes in b_{hCFD} are not proportional to the changes in b. The ratios of b_{hCFD} after reaction over b_{hCFD} before reaction are always smaller than the ratios of b, meaning that increase in b_{hCFD} is less than the increase in b.

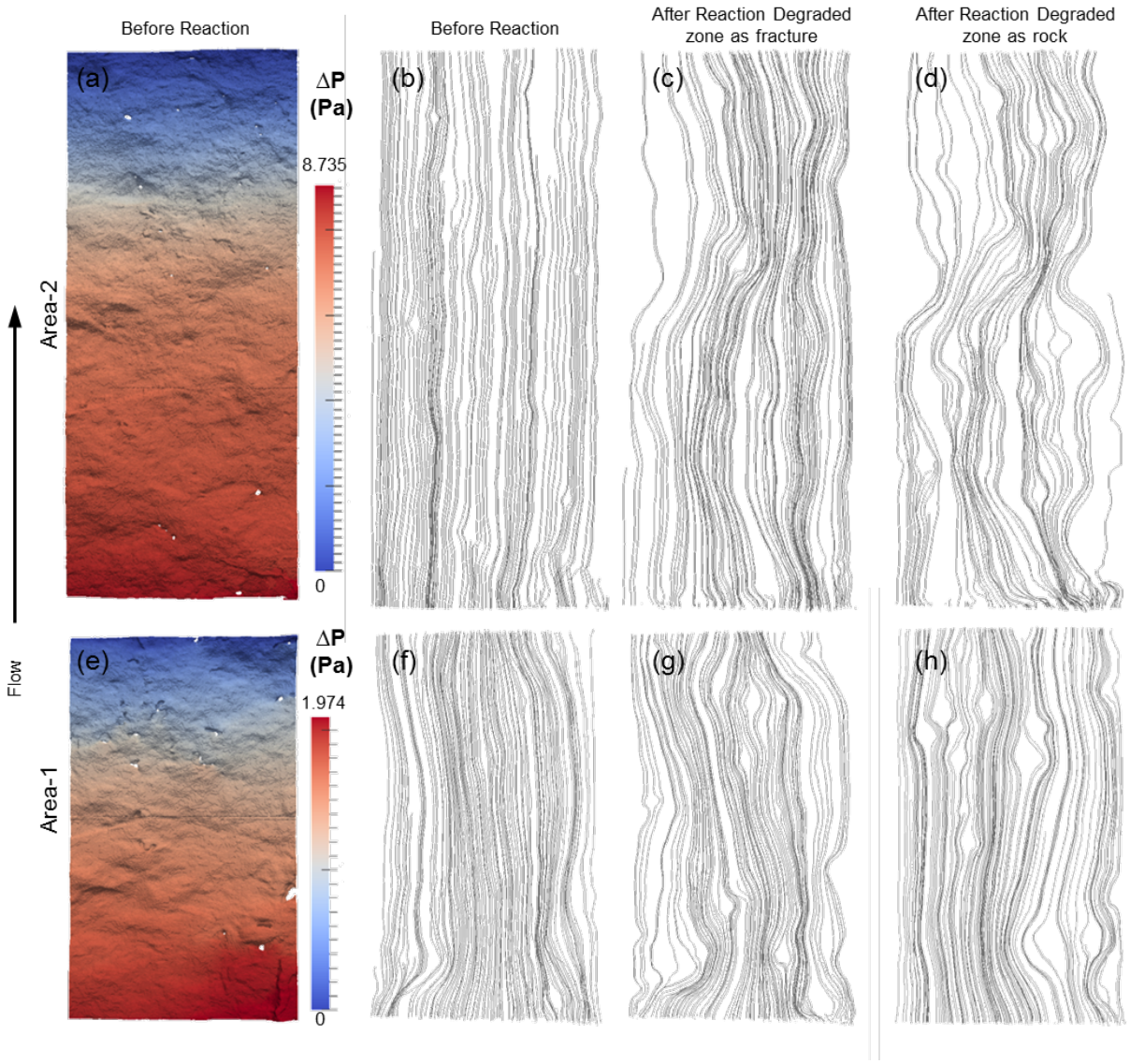

Figure 7. CFD simulation results: (a) Area-2 field of pressure difference (with respect to the outlet) in the before-reaction mesh (b)-(d) Area-2 velocity fields shown as streamlines for before-reaction mesh, after-reaction mesh with degraded zones treated as fracture and after-reaction mesh with degraded zones treated as rock, and (e)-(h) analogous for Area-1. Streamlines were generated by tracking the particles released at the inlet surface (at the bottom). In each geometry, 120 particles were released.

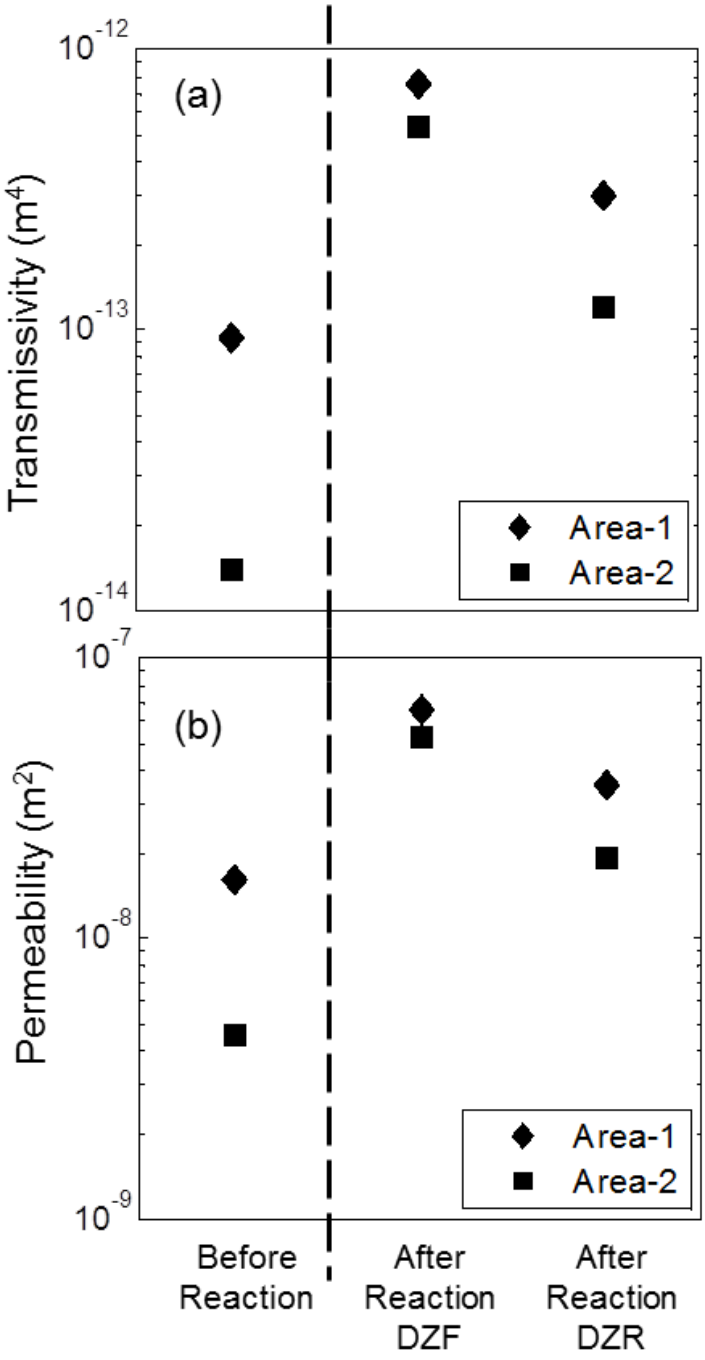

Figure 8. CFD simulation results of (a) transmissivity and (b) permeability of all six fracture geometries. DZF – Degraded Zones treated as Fracture, DZR – Degraded Zones treated as Rock

12.5.3 The Impacts of Fracture Roughness

In a fracture with smooth parallel walls, b and b_h are equivalent, and therefore, b can be used directly to estimate fracture hydrodynamic properties. Monitoring effluent chemistry and using mass balance provide one way to quantify dissolution and infer changes in average b[30]. Alterations in b due to reactions can also be calculated from reactive transport modeling[19,37,51]. In addition, applications of imaging techniques such as μCT scans[25,27] and light transmission[24] allow characterization of fracture morphology and b from images.

For rough-wall fractures, b_h deviates from b (e.g. Figure 9), and the extent of the deviation is primarily controlled by the degree of roughness. It has been pointed out in previous work[16,18,22,30] and confirmed in our study that reactions change both the volume and roughness of fracture. Moving from the before-reaction geometry to the after-reaction geometry where the degraded zones are treated as rock, fracture roughness increases and streamlines in the fractures become more tortuous, deviating more from the parallel streamlines that define b and b_h equivalence (Figure 7). As a result, the deviation of b_h from b, as measured by the ratio between b_h and b grows as roughness increases (Figure 10). This variation in the deviation of b_h from b greatly complicates quantification of the changes in hydrodynamics properties caused by reaction. For example, for the after reaction geometry of Area-2 with degraded zone treated as rock, b has tripled while b_h shows only doubling (Figure 9b). Therefore, if a threefold increase in b_h is assumed based simply on the observed changes in b, k and T are overestimated by more than 100% and 200%, respectively, due to the power law relationships (eqn. (2) - (3)). As k and T are the major inputs for most hydrodynamic models, these overestimations will propagate into the model predictions of key performance parameters such as leakage risks of CO_2 storage and shale gas production.

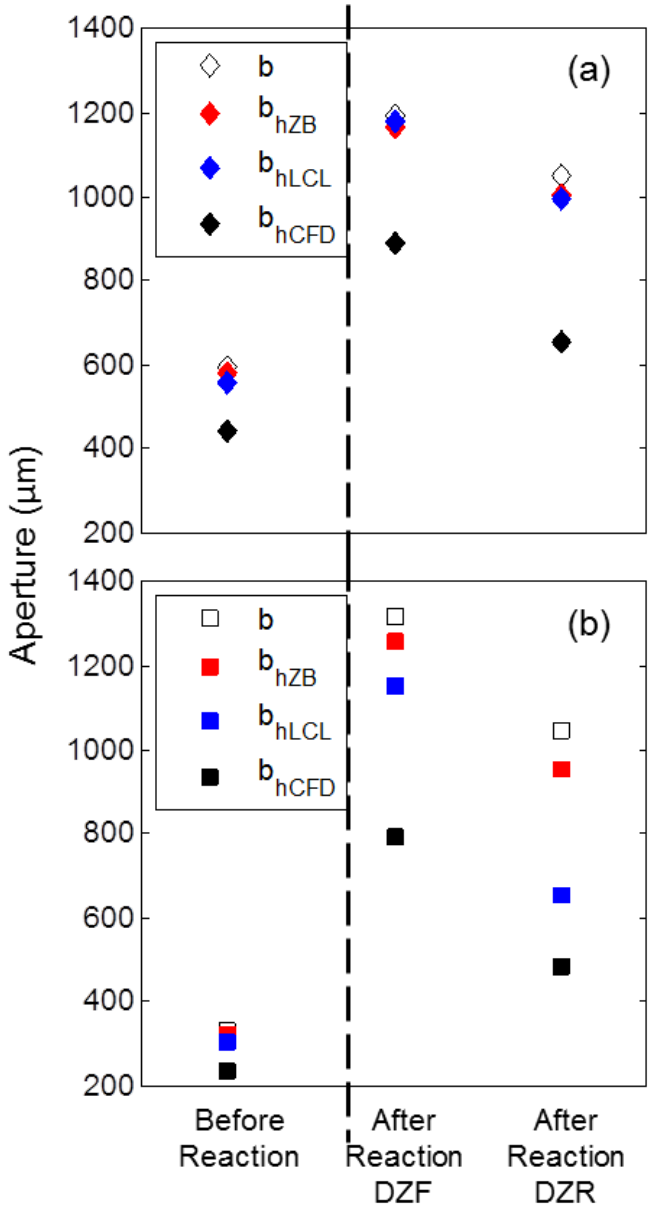

Figure 9. Mechanical aperture (b) and hydraulic apertures inferred from roughness model developed by Zimmerman and Bodvarsson (b_{hZB}), 2D Local Cubic Law (LCL) model (b_{hLCL}) and CFD simulations (b_{hCFD}) for (a) Area-1 and (b) Area-2. DZF – Degraded Zones treated as Fracture, DZR – Degraded Zones treated as Rock.

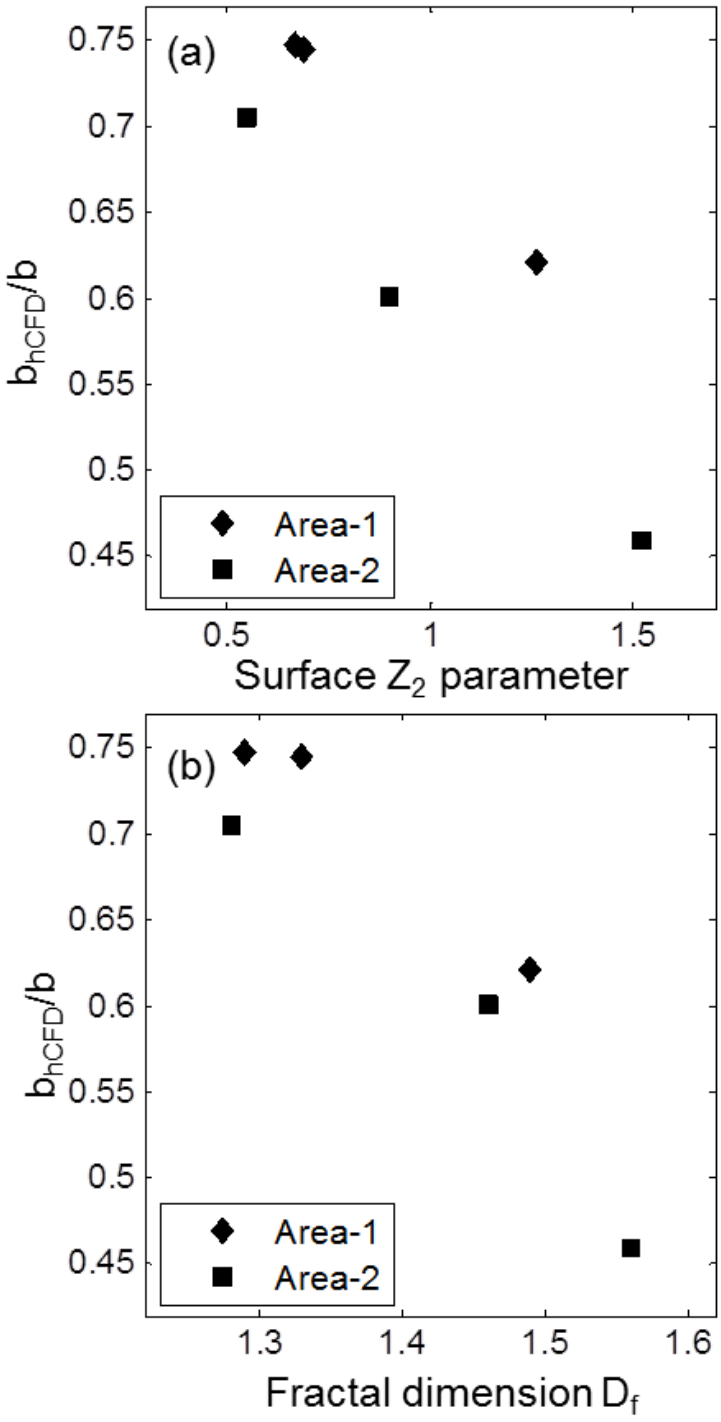

Figure 10. Ratio of hydraulic aperture inferred from CFD simulations over mechanical aperture (b_{hCFD}/b) in comparison with (a) surface Z_2 parameter and (b) fractal dimension D_f of the midsurface.

To account for variations in b along a fracture, Tsang and Witherspoon[31] used a weighted average of b to estimate T. A subsequent study observed that the ratio of b_h and b is related only to the variance of log-aperture, and hence b_h can be estimated from the distribution of fracture b[32]. Based on a comprehensive review, Zimmerman and Bodvarsson[33] proposed a model to account for the impacts of roughness by incorporating standard deviation of b and contact area ratio. In addition to the statistical approach, the 2D LCL model is also widely used. In fractures with low roughness, its capability of capturing fracture hydrodynamic properties was justified and the uncertainties caused by the model were considered negligible compared with other processes[37].

However, for the fracture geometries in this study, both the 1D statistical model developed by Zimmerman and Bodvarsson[33] and 2D LCL model that assumes cubic law applies locally largely over-estimate the flow, and failed to fully capture the impacts the roughness. The poor performance of these modeling approaches is primarily rooted in the severe roughness caused by preferential dissolutions of calcite relative to less soluble silicate and dolomite.

12.5.4 Mineral Heterogeneity and Evolution of Fracture Hydrodynamic Properties

Changes of fracture roughness after exposure to acidic flow are primarily controlled by the spatial distribution of reactive minerals and less soluble minerals. One type of sedimentary feature that results in roughness increase is banding of reactive and unreactive minerals. The cross sections of the fracture along the flow direction at nine x values shown in Figure 11 illustrate that though extensive dissolution has resulted in substantial b enlargement; there are still some regions along the flow pathway where aperture increase is limited due to a contiguous transverse stricture, which exists because of a sedimentary layer of relatively insoluble minerals.

Mineral heterogeneity also affects flow by creation of reaction degraded zones. Two core-flooding studies on different carbonate rocks observed the formation of 'degraded zones' along the fracture boundary following the flow of acidified brines[13,30]. The formation of degraded zones results from the dissolution of calcite from within a matrix of relatively insoluble minerals (e.g., dolomite and silicates). Our study demonstrated that the range of possible transmissivity outcomes is large depending on whether or not there is flow through the degraded zones, even though they account for only a relatively small fraction of the fracture volume. The primary reasons are highlighted by the degraded zone occurrence and thickness map shown for Area-2 in Figure 6b, where degraded zones cover a large fraction of the fracture surface and have a large impact on roughness (Table 1). The large impact of degraded zones on fracture roughness is also consistent with previous findings[52], which documented higher roughness for coated natural fracture surface than uncoated ones.

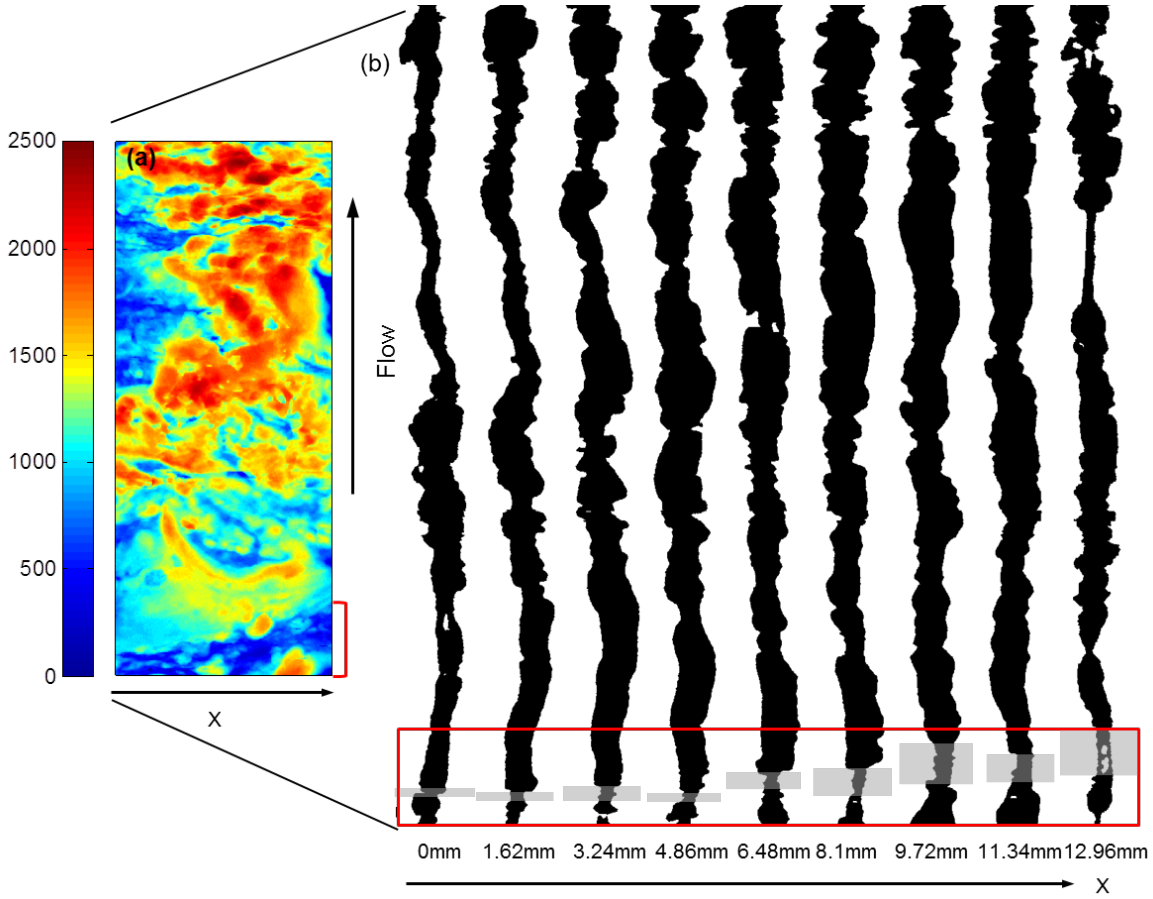

Figure 11. (a) Aperture map (μm) of after-reaction geometry of Area-2 with degraded zones treated as fracture, and (b) Sections of the fracture along the flow direction sampled every 1.62mm. Gray boxes highlight the areas where aperture increase is minimal, corresponding to the blue band near the bottom of the Area-2 fracture.

Our studies on the impacts of geometric alterations on fracture hydrodynamic properties can lend some insights for predicting their evolution as a result of longer exposure to CO_2-acidified brine. For the case of banding of calcite with dolomite, roughness increased dramatically due to preferential dissolution of calcite. However, because the preferential dissolution of calcite is due to differential solubilities of the two minerals, longer-term contact with CO_2-acidified brine will cause dolomite to also dissolve. Consequently, constraints on flow by the dolomite bands will be reduced, and fracture T and k will increase. Since dolomite dissolves slowly compared with calcite, roughness will keep growing, but the effect of this roughness may diminish as the b increases. Therefore, increase of fracture hydrodynamic properties will be disproportional to the fracture volume increase. If instead, calcite is banded with non-reactive minerals such as clay minerals, the non-reactive bands will persist as constraints on the flow and fracture hydrodynamic properties may change only negligibly in response to preferential dissolution of calcite. However, sharp changes in fracture hydrodynamic properties may happen if the geomechanical strength of the non-reactive bands is compromised.

In rocks in which minerals are mixed more homogeneously, i.e. not in bands parallel to sedimentary bedding, preferential dissolution of calcite leads to formation of the degraded zone. If the fluid in the degraded zone is hydraulically isolated, existence of the degraded zone will serve as a protective layer against further erosion, for ions need to diffuse through the degraded zone to reach the reaction front. If the degraded zones are composed of dolomite, dolomite will start to dissolve given longer exposure to CO_2-acidified brine, and the degraded zones will evolve towards the direction of the extreme scenario when degraded zones are considered as fracture. Dissolution of dolomite may be faster compared to the fracture surface due to increase of reactive surface area created by the degraded zones. In contrast, if the degraded zones are composed of aluminosilicates left after preferential dissolution of calcite, they will be preserved even with longer exposure to reactive fluid, and the constraints on flow will remain. Another possibility in this case is decohesion of the aluminosilicates. As inferred from the experimental observations by Ellis et al.[14] and Noiriel et al.[30], the mobilized particles will be transported by the flow and may be carried through the fracture, which leads to b increase and smoothing of fracture walls, or they may be trapped and clog the flow pathway, which results in reduction in fracture hydrodynamic properties.

12.6 Conclusions

The discrepancy between hydraulic aperture, b_h, and mechanical aperture, b, and the incapability of the 1D statistical model and 2D LCL model to capture the differences imply that prudence is required when studying the impacts of reactive transport on fracture hydrodynamic properties. Coupling the detailed fracture geometry reconstructed from xCT images and CFD simulations provides more accurate estimations of fracture hydrodynamic properties. Our study not only has successfully applied this method, but also has extended it to study true geometrical alterations – high roughness and degraded zones, caused by reactive flow. We used xCT images collected before and after a flow-through experiment and CFD simulations to study the changes of fracture hydrodynamic properties due to reactive flow. We found that modifications of hydrodynamic properties are constrained by both the volume dissolved and the development of specific geometric features that can be traced to the underlying mineralogy. In our study, the increase in fracture hydrodynamic properties is mitigated by an increase in roughness caused by zones of banded reactive and non-reactive minerals and the creation of degraded zones. The high degrees of roughness caused by complex mineralogical spatial distributions lead to large discrepancy between b and b_h calculated from CFD simulations. In such cases, the use of b that can be derived from imaging techniques, reactive transport modeling and experimental effluent analyses to estimate fracture hydrodynamic properties and their evolution will result in overestimation of permeability and transmissivity by a factor of two or more. In addition, the 1D statistical model and the 2D LCL model failed to capture flow accurately and overestimate the hydrodynamic properties relative to the CFD simulations. Therefore, if b_h estimated from the 1D and 2D models are used to estimate hydrodynamic properties, the errors will propagate into subsequent modeling, leading to overestimation of leakage risks or production prediction. More experimental studies correlating mineralogical spatial distribution and geometric alterations are needed in the future, as well as the efforts dedicated to incorporating the impacts of the resultant roughness efficiently. Such studies will benefit parameterization of the large-scale models used to predict leakage of CO_2 from geologic storage reservoirs and gas from hydraulically fractured shale formations.

12.7 REFERENCES

1. Bonnet, E.; Bour, O.; Odling, N. E.; Davy, P.; Main, I.; Cowie, P.; Berkowitz, B. Scaling of fracture systems in geological media. *Rev. Geophys.* **2001**, *39,* 347-383.
2. Singurindy, O.; Berkowitz, B. The role of fractures on coupled dissolution and precipitation patterns in carbonate rocks. *Adv. Water Resour.* **2005**, *28*, 507-521.
3. Curtis, J. B. Fractured shale-gas systems. *AAPG Bull.* **2002**, *86,* 1921-1938.
4. Long, J. C. S.; Ewing, R. C. Yucca Mountain: Earth-science issues at a geologic repository for high-level nuclear waste. *Annu. Rev. Earth Planet. Sci.* **2004**, *32,* 363-401.
5. Wood, C. P.; Brathwaite, R. L.; Rosenberg, M. D. Basement structure, lithology and permeability at Kawerau and Ohaaki geothermal fields, New Zealand. *Geothermics* **2001**, *30,* 461-481.
6. Iding, M.; Ringrose, P. Evaluating the impact of fractures on the performance of the In Salah CO_2 storage site. *International Journal of Greenhouse Gas Control* **2010**, *4*, 242-248.
7. Griffith, C. A.; Dzombak, D. A.; Lowry, G. V. Physical and chemical characteristics of potential seal strata in regions considered for demonstrating geological saline CO_2 sequestration. *Environmental Earth Sciences* **2011**, *64,* 925-948.
8. Park, C.; Taron, J.; Gorke, U.; Singh, A. K.; Kolditz, O. In *In The fluidal interface is where the action is in CO2 sequestration and storage: Hydromechanical analysis of mechanical failure;* 10th International Conference on Greenhouse Gas Control Technologies, September 19, 2010 - September 23; Elsevier Ltd: Amsterdam, Netherlands, 2011; Vol. 4, pp 3691-3698.
9. Gor, G. Y.; Elliot, T. R.; Prevost, J. H. Effects of thermal stresses on caprock integrity during CO2 storage. *International Journal of Greenhouse Gas Control* **2013**, *12*, 300-309.
10. Noiriel, C.; Renard, F.; Doan, M.; Gratier, J. Intense fracturing and fracture sealing induced by mineral growth in porous rocks. *Chem. Geol.* **2010**, *269,* 197-209.
11. Gherardi, F.; Xu, T.; Pruess, K. Numerical modeling of self-limiting and self-enhancing caprock alteration induced by CO_2 storage in a depleted gas reservoir. *Chem. Geol.* **2007**, *244*, 103-129.
12. Andreani, M.; Gouze, P.; Luquot, L.; Jouanna, P. Changes in seal capacity of fractured claystone caprocks induced by dissolved and gaseous CO_2 seepage. *Geophys. Res. Lett.* **2008**, *35*; Paper L14404.
13. Ellis, B.; Peters, C.; Fitts, J.; Bromhal, G.; McIntyre, D.; Warzinski, R.; Rosenbaum, E. Deterioration of a fractured carbonate caprock exposed to CO2-acidified brine flow. *Greenhouse Gases: Science and Technology* **2011**, *1*, 248-260.
14. Ellis, B. R.; Fitts, J. P.; Bromhal, G. S.; McIntyre, D. L.; Tappero, R.; Peters, C. A. Dissolution-Driven Permeability Reduction of a Fractured Carbonate Caprock. *Environmental Engineering Science* **2013**, *4;* DOI: 10.1089/ees.2012.0337.
15. Grieser, B.; Wheaton, B.; Magness, B.; Blauch, M.; Loghry, R. In *In Surface reactive fluid's effect on shale;* SPE Production and Operations Symposium 2007, April 1, 2007 - April 3; Society of Petroleum Engineers (SPE): Oklahoma City, OK, United states, 2007; pp 438-444.
16. Detwiler, R.; Glass, R.; Bourcier, W. Experimental observations of fracture dissolution: The role of Peclet number on evolving aperture variability. *Geophys. Res. Lett.* **2003**, *30,* 1648-1651.
17. Detwiler, R. Experimental observations of deformation caused by mineral dissolution in variable-aperture fractures. *Journal of geophysical research* **2008**, *113;* Paper B08202.
18. O'Brien, G. S.; Bean, C. J.; McDermott, F. Numerical investigations of passive and reactive flow through generic single fractures with heterogeneous permeability. *Earth Planet. Sci. Lett.* **2003**, *213,* 271-284.
19. Chaudhuri, A.; Rajaram, H.; Viswanathan, H. Alteration of fractures by precipitation and dissolution in gradient reaction environments: Computational results and stochastic analysis. *Water Resour. Res.* **2008**, *44*; Paper W10410.
20. Detwiler, R.; Rajaram, H. Predicting dissolution patterns in variable aperture fractures: Evaluation of an enhanced depth-averaged computational model. *Water Resour. Res.* **2007**, *43;* Paper W04403.
21. Tartakovsky, D. M.; Dentz, M.; Lichtner, P. C. Probability density functions for advective-reactive transport with uncertain reaction rates. *Water Resour. Res.* **2009**, *45*; Paper W07414.
22. Verberg, R.; Ladd, A. J. C. Simulation of chemical erosion in rough fractures. *Physical Review E - Statistical, Nonlinear, and Soft Matter Physics* **2002**, *65*; Paper 056311.
23. Szymczak, P.; Ladd, A. Wormhole formation in dissolving fractures. *Journal of geophysical research* **2009**, *114;* Paper B06203.

24. Detwiler, R.; Pringle, S.; Glass, R. Measurement of fracture aperture fields using transmitted light: An evaluation of measurement errors and their influence on simulations of flow and transport through a single fracture. *Water Resour. Res.* **1999**, *35*, 2605-2617.
25. Gouze, P.; Noiriel, C.; Bruderer, C.; Loggia, D.; Leprovost, R. X-ray tomography characterization of fracture surfaces during dissolution. *Geophys. Res. Lett.* **2003**, *30*; Paper 1267.
26. Werth, C. J.; Zhang, C.; Brusseau, M. L.; Oostrom, M.; Baumann, T. A review of non-invasive imaging methods and applications in contaminant hydrogeology research. *J. Contam. Hydrol.* **2010**, *113*, 1-24.
27. Karpyn, Z. T.; Grader, A. S.; Halleck, P. M. Visualization of fluid occupancy in a rough fracture using micro-tomography. *J. Colloid Interface Sci.* **2007**, *307,* 181-187.
28. Wildenschild, D.; Sheppard, A. P. X-ray imaging and analysis techniques for quantifying pore-scale structure and processes in subsurface porous medium systems. *Adv. Water Resour.* **2013**, *51*, 217-246.
29. Nicholl, M.; Rajaram, H.; Glass, R.; Detwiler, R. Saturated flow in a single fracture: Evaluation of the Reynolds equation in measured aperture fields. *Water Resour. Res.* **1999**, *35*, 3361-3373.
30. Noiriel, C.; Made, B.; Gouze, P. Impact of coating development on the hydraulic and transport properties in argillaceous limestone fracture. *Water Resour. Res.* **2007**, *43*; Paper W09406.
31. Tsang, Y.; Witherspoon, P. Hydromechanical behavior of a deformable rock fracture subject to normal stress. *Journal of geophysical research* **1981**, *86*, 9287-9298.
32. Renshaw, C. On the relationship between mechanical and hydraulic apertures in rough-walled fractures. *Journal of geophysical research* **1995**, *100*, 24629-24636.
33. Zimmerman, R.; Bodvarsson, G. Hydraulic conductivity of rock fractures. *Transp. Porous Media* **1996**, *23*, 1-30.
34. Cvetkovic, V.; Selroos, J. O.; Cheng, H. Transport of reactive tracers in rock fractures. *J. Fluid Mech.* **1999**, *378,* 335-356.
35. James, S. C.; Chrysikopoulos, C. V. Transport of polydisperse colloids in a saturated fracture with spatially variable aperture. *Water Resour. Res.* **2000**, *36*, 1457-1465.
36. Ghassemi, A.; Kumar, G. S. Changes in fracture aperture and fluid pressure due to thermal stress and silica dissolution/precipitation induced by heat extraction from subsurface rocks. *Geothermics* **2007**, *36,* 115-140.
37. Yasuhara, H.; Elsworth, D. A numerical model simulating reactive transport and evolution of fracture permeability. *Int. J. Numer. Anal. Methods Geomech.* **2006**, *30,* 1039-1062.
38. Petchsingto, T.; Karpyn, Z. T. Deterministic Modeling of Fluid Flow through a CT-scanned Fracture Using Computational Fluid Dynamics. *Energy Sources Part A-Recovery Utilization and Environmental Effects* **2009**, *31*, 897-905.
39. Crandall, D.; Bromhal, G.; Karpyn, Z. T. Numerical simulations examining the relationship between wall-roughness and fluid flow in rock fractures. *Int. J. Rock Mech. Min. Sci.* **2010**, *47*, 784-796.
40. Javadi, M.; Sharifzadeh, M.; Shahriar, K. A new geometrical model for non-linear fluid flow through rough fractures. *Journal of Hydrology* **2010**, *389*, 18-30.
41. Snow, D. Anisotropic permeability of fractured media. *Water Resour. Res.* **1969**, *5*, 1273-1289.
42. Otsu, N. A threshold selection method from gray-level histograms. *IEEE Transactions on Systems, Man and Cybernetics* **1979**, *9*, 62-66.
43. Fang, Q.; Boas, D. A. In *In Tetrahedral mesh generation from volumetric binary and grayscale images;* 2009 IEEE International Symposium on Biomedical Imaging: From Nano to Macro, ISBI 2009, June 28, 2009 - July 1; IEEE Computer Society: Boston, MA, United states, 2009; pp 1142-1145.
44. Belem, T.; Homand-Etienne, F.; Souley, M. Quantitative parameters for rock joint surface roughness. *Rock Mech Rock Eng* **2000**, *33*, 217-242.
45. Dougan, L. T.; Addison, P. S.; McKenzie, W. M. C. Fractal analysis of fracture: a comparison of dimension estimates. *Mech. Res. Commun.* **2000**, *27*, 383-392.
46. Yastrebov, V. A.; Anciaux, G.; Molinari, J. Contact between representative rough surfaces. *Physical Review E - Statistical, Nonlinear, and Soft Matter Physics* **2012**, *86*; Paper 035601.
47. Tsang, Y. W.; Witherspoon, P. A. Dependence of fracture mechanical and fluid flow properties on fracture roughness and sample size. *Journal of Geophysical Research* **1983**, *88*, 2359-2366.
48. Brush, D. J.; Thomson, N. R. Fluid flow in synthetic rough-walled fractures: Navier-Stokes, Stokes, and local cubic law simulations. *Water Resour. Res.* **2003**, *39*; Paper 1085.
49. Konzuk, J. S.; Kueper, B. H. Evaluation of cubic law based models describing single-phase flow through a rough-walled fracture. *Water Resour. Res.* **2004**, *40*; Paper W02402.
50. Edenhofer, O.; Knopf, B.; Barker, T.; Baumstark, L.; Bellevrat, E.; Chateau, B.; Criqui, P.; Isaac, M.; Kitous, A.; Kypreos, S.; Leimbach, M.; Lessmann, K.; Magne, B.; Scrieciu, S.; Turton, H.; van Vuuren, D. P. The

Economics of Low Stabilization: Model Comparison of Mitigation Strategies and Costs. *Energy J.* **2010***, 31*, 11-48.

51. Rawal, C.; Ghassemi, A. In *In Fracture aperture change in response to reactive transport of silica and thermoelastic effects;* -Canada Rock Mechanics Symposium 2008, June 29, 2008 - July 2; Omnipress: San Francisco, CA, United states, 2008; Paper 08-253.
52. Weisbrod, N.; Nativ, R.; Adar, E.; Ronen, D.; Ben-Nun, A. Impact of coating and weathering on the properties of chalk fracture surfaces. *J. Geophys. Res. -Solid Earth* **2000***, 105*, 27853-27864.

Chapter 13. Experimental study of reactive flow in an Eau Claire fracture exposed to CO_2-rich brine

This chapter has been published as:

H. Deng, J.P. Fitts, C.A. Peters, L. Li, D. Crandall, G. Bromhal. "Experimental study of reactive flow in an Eau Claire fracture exposed to CO_2-rich brine" ARMA 13-592. American Rock Mechanics Association, 47th US Rock Mechanics / Geomechanics Symposium, San Francisco, CA June 2013. Vol. 13, p. 592.

13.1 ABSTRACT

Fractures in caprocks represent potential integrity breaches and this integrity may be altered over time if the permeability evolves substantially due to reaction with flowing fluids. This is especially relevant in the context of CO_2 geological storage in which acid-promoted reactions are possible, leading to physical changes of fracture permeability and therefore leakage potential. In this study, we report an experimental study of reactive flow in a core sample from the Eau Claire formation. The core had been collected to characterize the primary sealing unit for the FutureGen 2.0 project, which is injecting CO_2 into the underlying Mt Simon sandstone. Synthetic brine was saturated with CO_2 at 11.0 MPa and flowed through the fracture at a confining pressure of 12.8 MPa for three weeks. Computed tomographic (CT) images from X-ray scanning before and after the experiment showed a small decrease in average aperture. The effective hydraulic aperture calculated from flow and pressure measurements decreased from 6 μm to 4 μm, and is consistent with the CT analyses. Composition maps of Ca abundance based on X-ray fluorescence indicate dissolution of Ca-bearing minerals close to the fracture surface. However, extensive mineralogical analyses from SEM-BSE, EDS and XRD showed low potential of reactivity and no evidence of any secondary precipitation. The decrease of the fracture permeability is consistent with

pressure-enhanced dissolution of critical asperities, but the CT image resolution does not allow direct observation of this mechanism. This experimental study provides one piece of evidence supporting the suitability of the Eau Claire as a reliable caprock.

13.2 Introduction

Mitigating anthropogenic CO_2 emission requires implementation of a portfolio of technologies, including carbon capture and sequestration (CCS) [1]. The Mount Simon Sandstone formation, deposited in the Cambrian period, has been identified as a critically important reservoir for CO_2 sequestration in both the Michigan and Illinois basins [2-4]. Its storage capacity is estimated to be between 11 – 150 billion metric tons in the Illinois basin [5]. However, the suitability of the Mt Simon as a CO_2 geological storage formation also depends on caprock integrity.

The Eau Claire formation overlies the Mt Simon, and will serve as the primary seal. Five lithofacies have been documented in a study based on analyses of 66 core-derived samples of the Eau Claire within Illinois basin from 7 wells [6]. The study has reported porosity varying between less than 5% to more than 20%, and permeability ranging from 10^{-6} mD to 103 mD for the Eau Claire formation.

Porosity and permeability, and therefore caprock integrity, are subject to changes when the caprock is exposed to CO_2-rich brine. The changes in porosity and permeability depend on mineralogy and flow regimes in a complex way. The core flooding experiment through a fractured carbonate caprock by Ellis et al. [7] has demonstrated preferential dissolution of calcite on the fracture walls, creating degraded zones with enhanced porosity. Another similar experiment, however, found fracture closure by particles released from dissolution [8].

Liu et al [9] conducted batch experiments with rock samples from the Eau Claire formation to investigate CO_2-brine-caprock interactions. The experiment was performed at 200 °C and 300 bars for 60 days. Minor dissolution of K-feldspar and anhydrite, and secondary precipitation of pore-filling and pore-bridging clay minerals, primarily illite and smectite were revealed by the SEM and XRD evidence.

For fracture systems, the relevance of findings from batch experiments is limited as fractures provide fast pathways for transport of reactive solutes, creating different reaction rate and mass transfer conditions. It was pointed out that fractures in the Eau Claire are often cemented by calcite which is highly soluble in the presence of CO_2-rich brine [6]. As a result, if fractures are activated or re-opened during injection, their flow conductivity may be altered by calcite dissolution. Here, we report an experimental study of CO_2-brine-rock interactions in fractured Eau Claire samples.

13.3 Experiment

A representative layered Eau Claire sample (Fig. 1) was collected from Meredosia in the county of Morgan, Illinois, the FutureGen 2.0 storage site. The depth of the sample is 1159.6 m, approximately 30 meters above the Mt Simon sandstone. A sub-core with diameter of 2.54 cm and length of 7.3 cm was harvested from the sample, and fractured using the modified Brazilian method for the flow through experiment at the National Energy and Technology Lab (Morgantown, WV USA). The fractured sub-core was placed in a TEMCO triaxial carbon-fiber core holder, on which a confining pressure of 12.8 MPa was applied. The system pore pressure was maintained around 11.0 MPa, which is the hydrostatic pressure at the depth of 1159 m. CO_2 and brine were delivered by two separate high-pressure syringe pumps

(Teledyne Isco, Inc., Lincoln, NE) into a mixing vessel. The brine composition used in the experiment is shown in Table 1. It was modified from that presented by Liu et al [10] by eliminating Fe and adjusting concentration of chloride to satisfy charge balance and achieve the pH of 6.9. The synthetic brine was saturated with pure CO_2 in the mixing vessel at the system pressure, resulting in a pH of 2.7. The experiment was conducted at 20 °C for three weeks at constant flow rates. During the experiment, pressures at the inlet and outlet of the core were recorded every 30 seconds.

Figure 1. A photo of the fractured sub-core of Eau Claire formation.

Table 1. Inlet brine chemistry

Component	Concentration (mol/kgw)
Ca	3.547E-01
Mg	1.033E-01
Na	1.596E+00
K	3.108E-02
C	1.724E-03
S	1.408E-02
Cl	2.513E+00
pH	6.900E+00
Ionic strength	2.565

Before and after the flow-through experiment, the fractured sub-core was scanned in the industrial X-ray computed tomography (CT) scanner at NETL (NorthStar Imaging M-5000). Radiographs were collected at 250 keV and 2.5 mA, and reconstructed to provide information about the fracture geometries and apertures. The core was scanned under effective confining pressure of 1.8 MPa, the same pressure used during the flow-through experiment. The CT images before and after experiment have resolutions of 41.8 μm and 54.8 μm, respectively.

Pieces of rock samples were selected after sub-coring and ground to fine particles for X-ray diffraction (XRD) analyses. Thin-sections were prepared and examined by a Quanta environmental scanning electron microscope (SEM) using back-scattered electron (BSE) microscopy and energy dispersive spectroscopy (EDS) at Princeton University. After the experiment, the core was sectioned along the plane parallel to flow but orthogonal to the fracture face. This was done to analyze potential mineralogical changes near the fracture surface.

An X-ray fluorescence map of Ca was collected at the National Synchrotron Light Source (NSLS) at the Brookhaven National Lab (Upton, NY USA). The map provides an indicator of the presence of the Ca-bearing minerals, including calcite.

13.4 Results

13.4.1 Mineralogy

The BSE image of the rock sample before experiment (Fig. 2a) shows four distinct brightness groups. The brightest group, as shown in the EDS spectrum (Fig. 2b) has strong Ti and O signals, indicating presence of titanium oxide. The dark gray clasts are dominated by Si (Fig. 2c), suggesting quartz. The light gray clasts exhibit presence of Al and K (Fig. 2d), consistent with allogenic feldspar grains. The EDS spectrum indicates presence of organic carbon in the non-clastic material (Fig. 2e), which has been documented by Neufelder et al [6] as well. (Note that these thin sections were not prepared with epoxy, so high organic carbon abundance does not indicate pore space (as in Peters, 2009 [11]) But the black group primarily represents pore space, as indicated by the topographic features on SEM image.

The XRD pattern (Fig. 3a) confirms that the Si-dominant mineral is quartz, and the other predominant mineral with abundant Al and K is potassium feldspar. As illustrated in Fig 1, the rock sample is comprised of sedimentary bedding layers. Pieces of rocks were sampled from the different types of layers and analyzed by XRD to investigate differences in mineralogical composition. The results show that both samples are dominated by quartz and K-feldspar. Carbonate is also abundant in the form of ankerite. The spectrum of the light color sample also displays strong peaks from a magnesium silicate (Fig. 3b).

The representative BSE image and EDS maps of the core section after brine flow are shown in Figure 4, with the fracture boundary located near the bottom of the image. These analyses also indicate dominance of clastic quartz and K-feldspar. Images collected along the fracture boundary region did not show any evidence of secondary mineral precipitation on the fracture surface or in the pores near the fracture surface (Fig. 4).

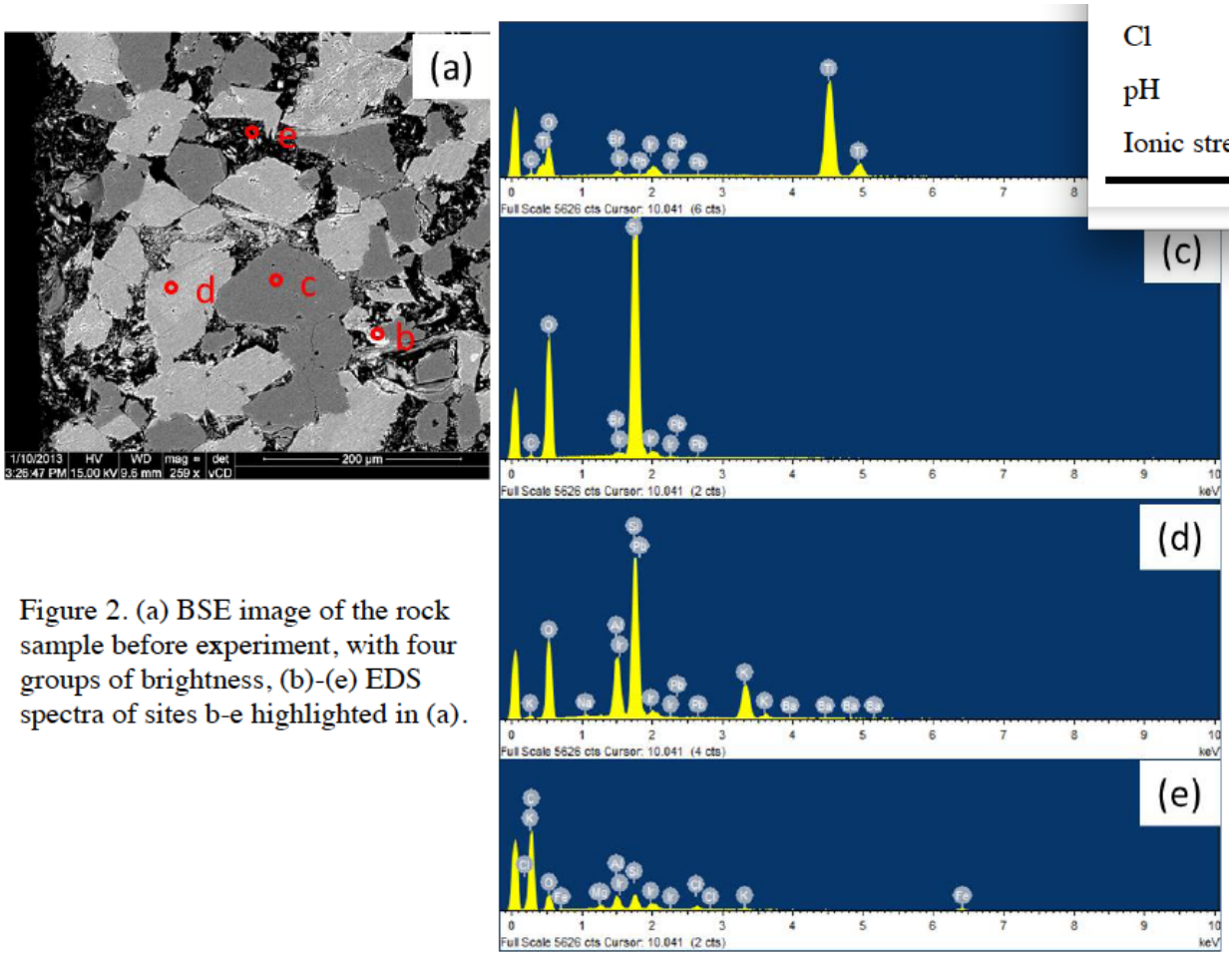

Figure 2. (a) BSE image of the rock sample before experiment, with four groups of brightness, (b)-(e) EDS spectra of sites b-e highlighted in (a).

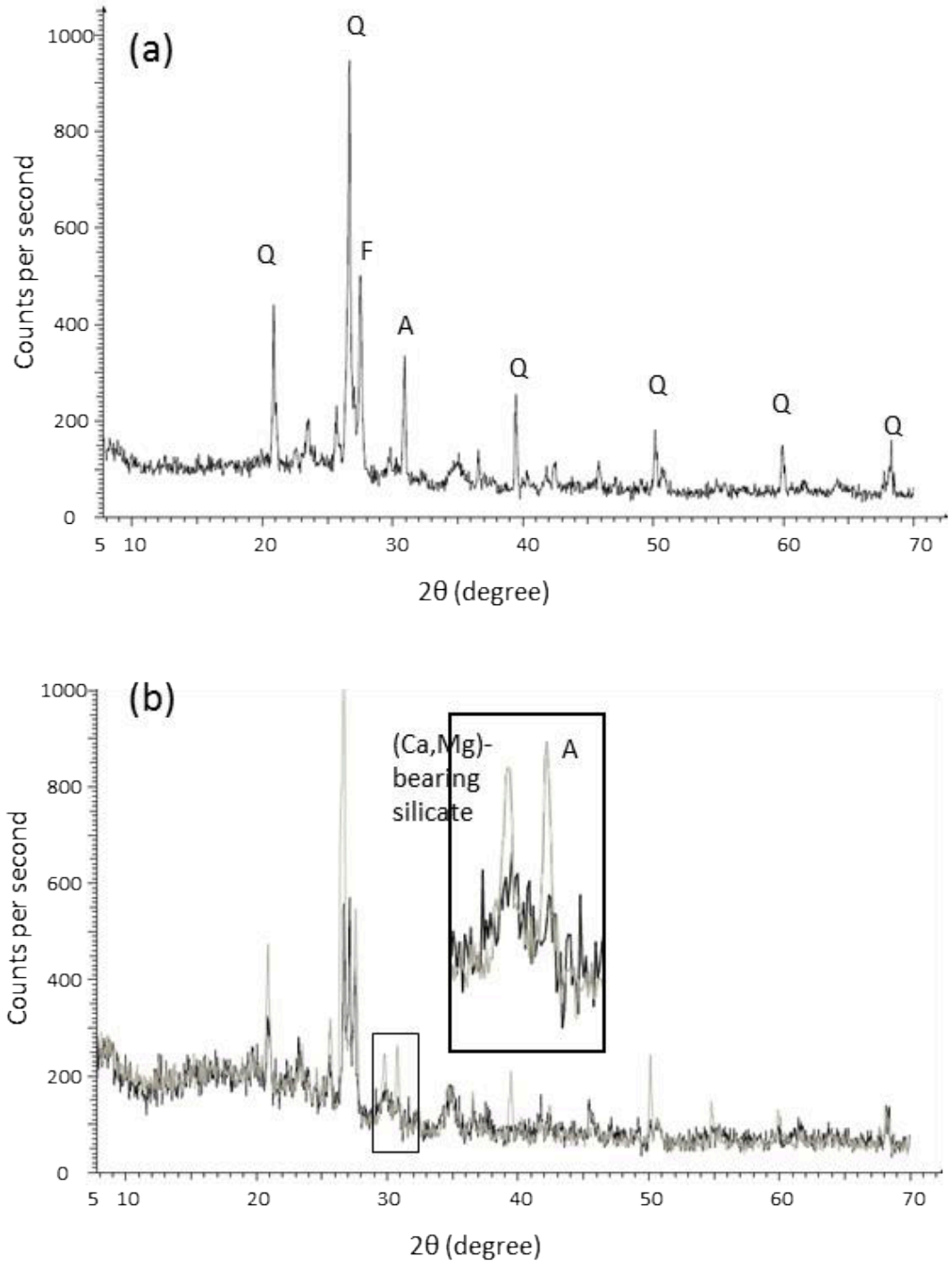

Figure 3. XRD spectra of (a) a mixture of dark-colored and light-colored minerals and (b) samples from the dark-colored band (black line) and light-colored band (gray line). Q is quartz, F is K-feldspar, A is Ankerite

The synchrotron-based X-ray fluorescence map of Ca (Fig. 5) shows the distribution of Ca abundance over a much larger area and with higher sensitivity than would be possible with the SEM-EDS. The results show a lower density of bright spots and the weaker counts per second within those spots close to the fracture surface, suggestion dissolution of Ca-bearing minerals with the fracture boundary region. However, given the limited abundance of Ca-bearing minerals (such as ankerite), the dissolution casts negligible impacts on the rock structure.

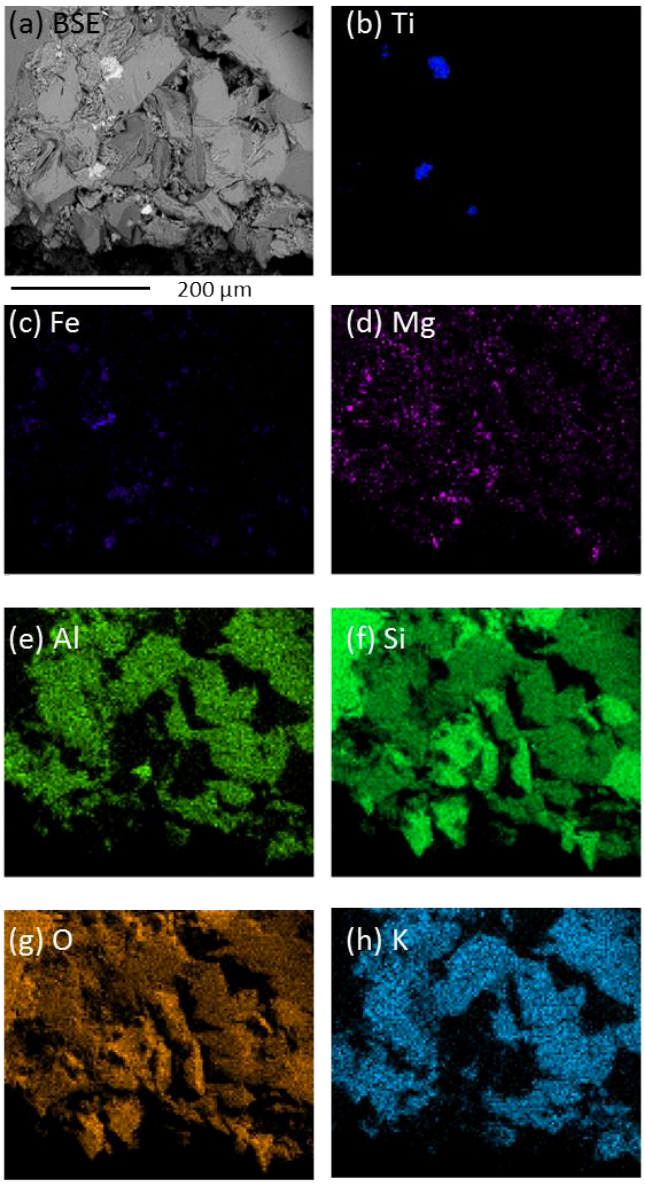

Figure 4. (a) BSE image of the core section after experiment, in which the bottom black area is the fracture boundary, (b) through (h) EDS maps of Ti, Fe, Mg, Al, Si, O and K.

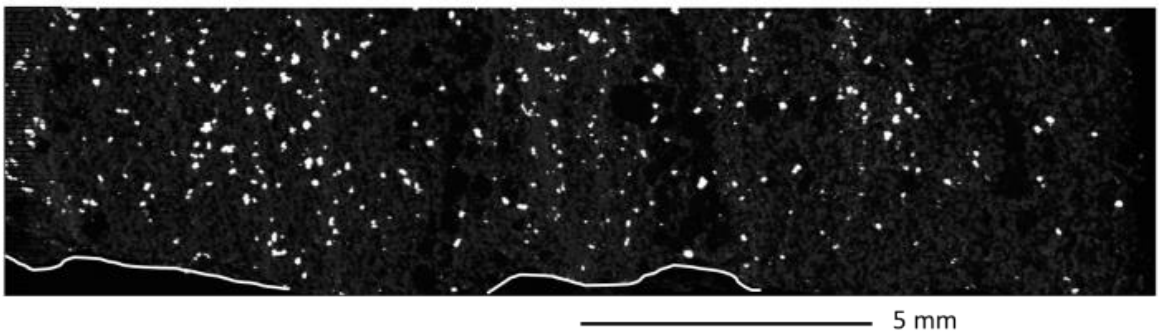

Figure 5. X-ray fluorescence map of calcium in a core section parallel to flow and perpendicular to the fracture boundary, taken after the experiment. The bright spots indicate presence of Ca. The white lines at the bottom indicate the location of the fracture boundary.

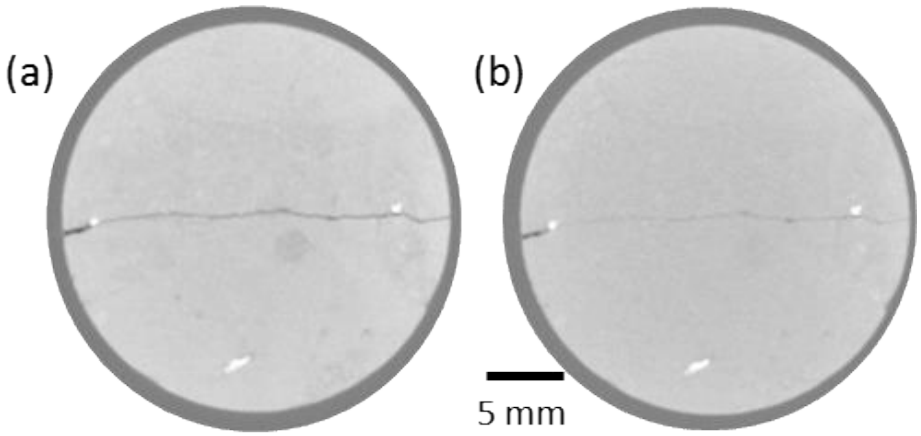

Figure 6. CT images (a) before experiment, and (b) after experiment. The black edges are the carbon-fiber core-holder.

13.4.2 Hydrodynamic properties

Visual inspection of the CT images (Fig. 6) indicates fracture closure. Given the small aperture of the fracture and relatively coarse resolution, digital segmentation of the images was not successful in some areas and therefore quantification of the aperture was performed only for 10 percent of the fraction. The analyzable areas in general have larger apertures, so we know that the quantitative analysis is not representative of the entire fracture. Even with this known bias, the average aperture after the experiment does show a slight decrease compared with the average aperture of the same areas before experiment, reducing from ~260 μm to ~240 μm.

The pressure data represent five minute averages. The pressure difference between the inlet and outlet of the core is plotted in Fig. 7a. It shows variation from $5 \cdot 10^4$ Pa early in the experiment to approximately $3 \cdot 10^5$ Pa near the end of the experiment. The flow rate (Q) of the system was maintained at 0.013 ml/min for the first two days, and increased to 0.026 ml/min afterwards. Analogous to Deng et al. (2013) [12], using the cubic law [13] (eqn (1)), the effective hydraulic aperture (b_h) was calculated from the pressure difference and volumetric flow rate.

$$b_h = \sqrt[3]{\frac{12\mu QL}{W(P_{in}-P_{out})}} \qquad \text{eqn (1)}$$

where L and W are the length and width of the fracture respectively, and μ is the dynamic viscosity of water (at 20 degree C, $1.002 \cdot 10^{-3}$ Pa·s). Fracture permeability then was calculated from the hydraulic aperture (eqn(2)).

$$k = \frac{b_h^2}{12} \qquad \text{eqn (2)}$$

The hydraulic aperture (Fig. 7b) of the fracture over time initially is between 5 to 6 μm, and decreases to between 4 and 5 mm. This reduction is consistent with the evidence that the fracture closed up over the course of the experiment. The resulting fracture permeability (Fig. 7c) decreases from around 2.5 to 1.5 Darcy. This decrease indicates higher resistance to flow.

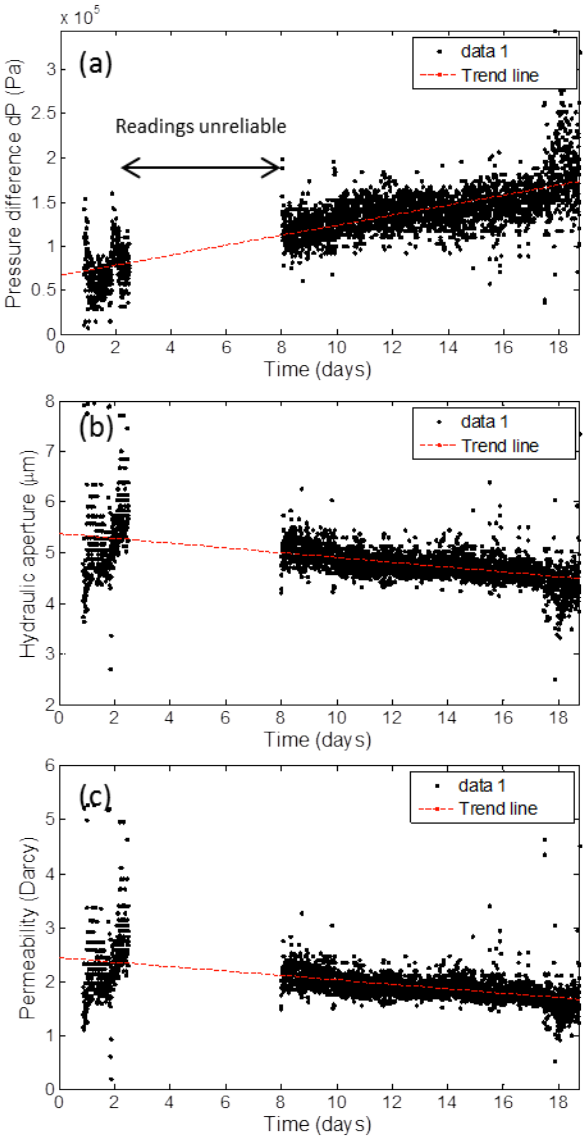

Figure 7 (a) Measured pressure difference, (b) calculated hydraulic aperture and (c) permeability. Red dashed lines showed the linear trends of the data.

13.5 Discussion and Conclusions

During the experiment of flowing carbonic acid-rich brine through a fractured Eau Claire sample, permeability of the fracture was observed to decrease. However, mineralogical analyses of the Eau Claire rock indicate low potential for dissolution reactions that result in significant physical changes to vertical fractures across these types of sedimentary units. Minimum mineralogical alteration was also confirmed by BSE and EDS images of the rock sample before and after the experiment. Although minor dissolution of Ca-bearing minerals was implied by the x-ray fluorescence mapping of Ca abundance, these results do not explain the observed decrease in fracture permeability.

The results of this flow-through experiment are consistent with the possibility of pressure-driven dissolution of critical asperities, a mechanism identified as important in controlling evolution of the fracture permeability under confining pressure [14,15]. It occurs at the contacting points of the two

fracture walls, where local stress is high and dissolution of the asperities is promoted, resulting in fracture closure. The CT image resolution, however, does not allow direct observation of this mechanism.

This experimental study indicates that the integrity of Eau Claire formation as a caprock within this type of sedimentary unit. However, future work is required to reproduce the flow-through experiment under different geochemical conditions. Furthermore, given the known heterogeneity of the formation, it will be prudent to conduct similar experiments on a range of core samples from different lithofacies within the formation.

13.6 References

[1] Pacala S, Socolow R. Stabilization wedges: Solving the climate problem for the next 50 years with current technologies. Science 2004; 305:968-72.
[2] Barnes DA, Bacon DH, Kelley SR. Geological sequestration of carbon dioxide in the Cambrian Mount Simon Sandstone: Regional storage capacity, site characterization, and large-scale injection feasibility, Michigan Basin. Environmental Geosciences 2009; 16:163-83.
[3] Medina C, Rupp J, Barnes D. Effects of reduction in porosity and permeability with depth on storage capacity and injectivity in deep saline aquifers: A case study from the Mount Simon Sandstone aquifer. International journal of greenhouse gas control 2011; 5:146.
[4] Leetaru HE, McBride JH. Reservoir uncertainty, Precambrian topography, and carbon sequestration in the Mt. Simon Sandstone, Illinois Basin. Environmental Geosciences 2009; 16:235-43.
[5] National Energy Technology Laboratory. The 2012 United States Carbon Utilization and Storage Atlas – Fourth Edition (Atlas IV). 2012. http://www.netl.doe.gov/technologies/carbon_seq/refshelf/atlasIV/Atlas-IV-2012.pdf
[6] Neufelder RJ, Bowen BB, Lahann RW, Rupp JA. Lithologic, mineralogical, and petrophysical characteristics of the Eau Claire Formation: Complexities of a carbon storage system seal. Environmental Geosciences 2012; 19:81-104.
[7] Ellis B, Peters C, Fitts J, Bromhal G, McIntyre D, Warzinski R et al. Deterioration of a fractured carbonate caprock exposed to CO2-acidified brine flow. Greenhouse Gases: Science and Technology 2011; 1:248-60.
[8] Ellis BR, Fitts JP, Bromhal GS, McIntyre DL, Tappero R, Peters CA. Dissolution-Driven Permeability Reduction of a Fractured Carbonate Caprock. Environmental Engineering Science 2013; In Press.
[9] Liu F, Lu P, Griffith C, Hedges SW, Soong Y, Hellevang H et al. CO2-brine-caprock interaction: Reactivity experiments on Eau Claire shale and a review of relevant literature. International Journal of Greenhouse Gas Control 2012; 7:153-67.
[10] Liu F, Lu P, Zhu C, Xiao Y. Coupled reactive flow and transport modeling of CO2 sequestration in the Mt. Simon sandstone formation, Midwest U.S.A. International Journal of Greenhouse Gas Control 2011; 5:294-307.
[11] Peters C. Accessibilities of reactive minerals in consolidated sedimentary rock: An imaging study of three sandstones. Chem Geol 2009; 265:198-208.
[12] Deng H, Ellis BR, Peters CA, Fitts JP, Crandall D, Bromhal GS. Modifications of Carbonate Fracture Hydrodynamic Properties by CO_2-Acidified Brine Flow. Energy Fuels 2013.
[13] Snow d. Anisotropic permeability of fractured media. Water Resour Res 1969; 5:1273.
[14] Yasuhara H, Elsworth D, Polak A. Evolution of permeability in a natural fracture: significant role of pressure solution. Journal of Geophysical Research 2004; 109:11 pp.
[15] McGuire TP, Elsworth D, Karcz ZK. The effects of coupled chemical-mechanical processes on the evolution of permeability in a carbonate fracture. 2010:American Rock Mechanics Association.

Chapter 14. Permeability evolution due to dissolution and precipitation of carbonates using reactive transport modeling in pore networks

This chapter has been published as:

J.P. Nogues, J.P. Fitts, M.A. Celia, C.A. Peters. "Permeability evolution due to dissolution and precipitation of carbonates using reactive transport modeling in pore networks", *Water Resources Research*, Vol 49: 6006-6021, doi:10.1002/wrcr.20486, 2013.

14.1 Abstract

A reactive transport model was developed to simulate reaction of carbonates within a pore network for the high-pressure CO_2-acidified conditions relevant to geological carbon sequestration. The pore network was based on a synthetic oolithic dolostone. Simulation results produced insights that can inform continuum-scale models regarding reaction-induced changes in permeability and porosity. As expected, permeability increased extensively with dissolution caused by high concentrations of carbonic acid, but neither pH nor calcite saturation state alone was a good predictor of the effects, as may sometimes be the case. Complex temporal evolutions of interstitial brine chemistry and network structure led to the counterintuitive finding that a far-from-equilibrium solution produced less permeability change than a nearer-to-equilibrium solution at the same pH. This was explained by the pH buffering that increased carbonate ion concentration and inhibited further reaction. Simulations of different flow conditions produced a non-unique set of permeability-porosity relationships. Diffusive-dominated systems caused dissolution to be localized near the inlet, leading to substantial porosity change but relatively small permeability change. For the same extent of porosity change caused from advective transport, the domain

changed uniformly, leading to a large permeability change. Regarding precipitation, permeability changes happen much slower compared to dissolution-induced changes and small amounts of precipitation, even if located only near the inlet, can lead to large changes in permeability. Exponent values for a power law that relates changes in permeability and porosity ranged from 2 to 10, but a value of 6 held constant when conditions led to uniform changes throughout the domain.

14.2 Introduction

Over the last decade numerous studies have been undertaken to understand the physics that govern the transport of supercritical CO_2 in the subsurface and its subsequent trapping or leakage in the context of geological carbon sequestration [*Bachu and Adams*, 2003; *Birkholzer et al.*, 2009; *Brosse et al.*, 2010; *Burton et al.*, 2008; *Celia et al.*, 2011; *Doughty and Pruess*, 2004; *Grimstad et al.*, 2009; *Nogues et al.*, 2012; *Pawar et al.*, 2009; *Pruess et al.*, 2003]. All of these studies have considered static material properties, such as permeability and porosity, for geologic formations and leakage pathways. The evolution of permeability and porosity due to geochemical reactions has yet to be considered in models that consider leakage risks. To do so, transport models must incorporate methods for predicting dynamic material properties either by numerically upscaling constitutive relationships, developing simplified empirical rules or by using multi-scale/multi-physics methods (as the one developed by Flemisch et al. [2011]). All of these methods would require an understanding of the reactions that can substantially alter the rock matrix, and the different ways the rock matrix evolves under different conditions.

The relevant geochemical reactions that can substantially alter the rock matrix are those between CO_2-acidified brines and carbonate minerals because these reactions are sufficiently fast and potentially lead to changes in the permeability and porosity in short time scales [*Assayag et al.*, 2009; *Ellis et al.*, 2013; *Ellis et al.*, 2011; *Luquot and Gouze*, 2009; *Noiriel et al.*, 2004; *Noiriel et al.*, 2005; *Smith et al.*, 2012]. In a geological sequestration operation, carbon dioxide dissolves into the resident brine forming carbonic acid. The resulting thermodynamic state of disequilibrium drives dissolution of the mineral matrix. This then has the effect of releasing cations, such as Ca^{2+}, Mg^{2+} or Fe^{3+} from the mineral matrix, which may buffer the acid to some extent. When these reactions occur in caprock sealing formations that overlay CO_2 injection formations, permeability and porosity changes may jeopardize the trapping mechanisms considered for reliable CO_2 storage. Conversely, there are scenarios in which mixing of fluids creates thermodynamic disequilibrium that drives precipitation of carbonate minerals, thereby reducing porosity [*Emmanuel and Berkowitz*, 2005; *Xu et al.*, 2005; *Zhang et al.*, 2010].

Several modeling studies have examined the role of geochemical reactions and their effects on permeability and porosity within the context of geological carbon sequestration. For instance, Gherardi et al. [2007] simulated changes in porosity in carbonate-rich shales due to the geochemical reactions between calcium-rich waters and resident brine, using the TOUGH-REACT simulator [*Xu et al.*, 2006]. Through numerical experiments, they found conditions that caused the porosity at the boundary between formation rock and caprock to decrease from 15 % to 0 % porosity due to precipitation of calcite. Andre et al. [2007] used the TOUGH-REACT simulator as well, to study CO_2 storage in the carbonate-rich Dogger aquifer in the Paris Basin, France. They saw that when CO_2-saturated water was injected, the porosity near the injection well increased significantly due to dissolution of the porous material. Finally, Liu et al. [2011] used TOUGH-REACT to model CO_2 injection in the Mt. Simon sandstone formation, USA. Like Andre et al. [2007], they saw a dissolution front caused by the acidified brine. In general,

most of these studies have shown that the geochemical reactions between CO_2-rich brines and carbonate rocks have effects on the permeability and porosity due to the dissolution or precipitation of carbonate minerals.

All of the reactive transport models used in the previous studies described the interplay of geochemical reactions and transport at the continuum or Darcy scale. Permeability is a continuum-scale property that manifests from the collective conductivities of flow between many pores, and thus is sensitive to reaction-induced alterations at the pore-scale. Furthermore, it can be argued that geochemical reactions are best described at the pore scale because they are driven by small-scale chemical gradients and because heterogeneities in porous rocks create variability in local chemical conditions [*Kim et al.*, 2011; *L Li et al.*, 2006; *Steefel et al.*, 2005]. Reactive-transport modeling in pore networks is an approach in which geochemical reactions and transport of species is modeled at the pore-scale enabling simulation of the effects of the small-scale heterogeneities, and simulation of permeability and porosity for the entire domain.

At the pore scale, relevant studies have found that, (i) dissolution and precipitation of carbonate minerals can occur simultaneously [*Kang et al.*, 2010]; (ii) at the scale of a single pore the reduction in flow area is proportional to the reactive and convective processes [*X Li et al.*, 2010]; and (iii) mixing of disparate waters can lead to precipitation and reduction in porosity [*Tartakovsky et al.*, 2007]. Szymczak and Ladd [2009] performed pore-scale simulations in 2D and showed that the creation and evolution of wormholes had a close dependence on the relationships between reaction and flow rates. None of these pore-scale studies linked the changes in mineral volume fraction (or porosity) to changes in permeability. Moreover, their results mainly focused on regular or periodic networks in one or two dimensions or systems where pore-to-pore heterogeneity was not taken into consideration. Algive et al. [2012] developed a methodology to use a reactive pore network model to extract upscaling factors to tie the pore-scale effects of reactive transport to the core-scale values of permeability and porosity. Their work simplified the geochemistry and transport by incorporating most geochemical dynamics and transport into dimensionless variables, and in doing so prevented a full description of the different physical and chemical parameters. Mehmani et al. [2012] developed a novel approach that coupled several pore-scale models using mortar coupling domain decomposition to study the evolution of precipitation-induced cementation of calcite. They were able to study large changes in permeability and porosity by coupling of 64 pore scale models (1 mm x 1 mm x 1 mm each) but with a limited description of the chemistry represented by two main parameters, the Damkohler number (Da) and an “alpha” parameter which described the deviation from equilibrium of the precipitation reaction. Mehmani et al. [2012] showed that a low Da and “alpha” number created precipitation at the inlet of the network, and that a high Da and “alpha” combination created more uniform precipitation. More recently the work by Yoon et al. [2013] was able to simulate $CaCO_3$ precipitation due to transverse mixing in a 2-D microfluidic pore network. They captured the essential physiochemical dynamics of precipitation that was characterized by a fast initial precipitation rate that leveled off as the mixing was hindered.

In this study, we present a new reactive transport model that simulates carbonic acid-driven reactions in a 3-D network of pores in order to predict the changes in permeability and porosity at the continuum scale. Through a series of simulations, the main questions that are addressed are: 1.) How do the degree of acidity and the calcite saturation state, controlled by the amount of CO_2 and calcium in inflowing waters, affect the changes in permeability and porosity? 2.) What are the effects, on the network permeability and

porosity, of different flow conditions (i.e. pressure gradients)? 3.) How do different patterns of mixing reactive boundary waters promote precipitation and reduction in permeability and porosity? and 4.) How do single parameter power law equations perform when predicting the evolution of permeability due to porosity changes? Ultimately these four questions help tackle the more general question of what are the most plausible changes that can occur in a CO_2 sequestration operation.

The pore network used in this study was developed with the aid of the algorithm proposed by Raoof and Hassanizadeh [2010]. The pore network structure was based on a statistical characterization of a synthetic micro-computed-tomography (μ-CT) image of an oolithic dolostone from Biswal et al. [2009]. To focus on the effects of physical heterogeneity, i.e. pore volumes and pore throats, the network was spatially uniform with respect to mineralology. The reactive transport model developed for this work accounts for reactions of acidic fluids with both carbonates and aluminosilicates. The model predicts evolution of pore sizes and pore-to-pore conductivities. In this paper, we present numerous simulation results focused on the permeability-altering effects of different chemical, flow and mixing conditions. The findings are examined in the context of sub-continuum-scale variations in geochemical conditions and reaction rates.

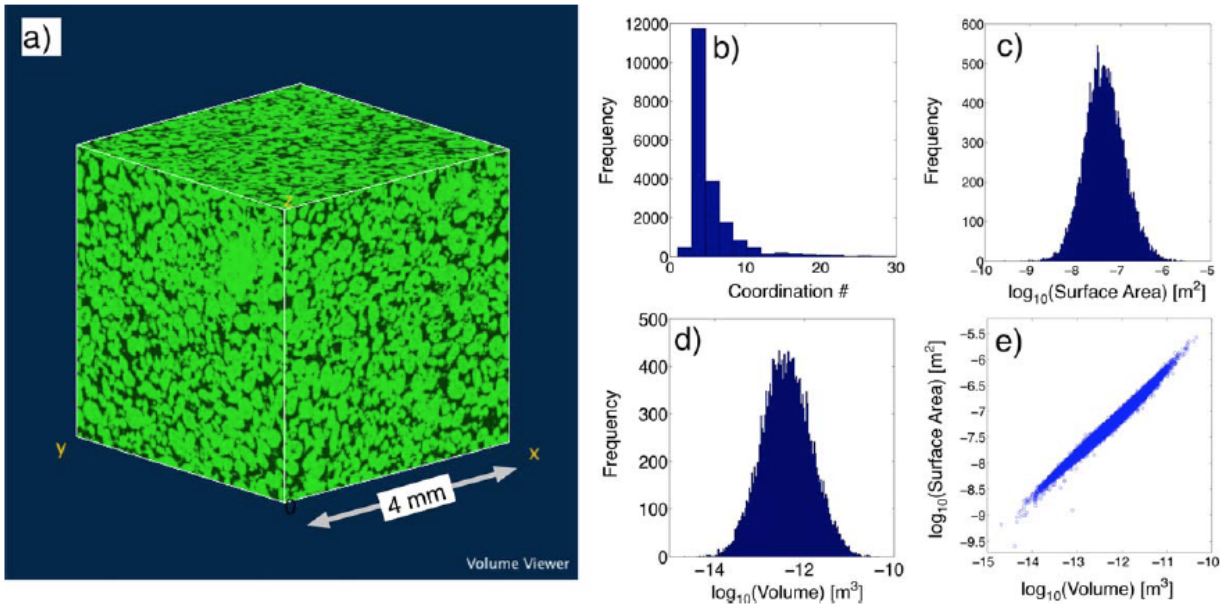

Figure 1. Synthetic dolomitized oolithic grainstone from *Biswal et al.* [2009] and the corresponding statistics derived using 3DMA-Rock: (a) Three-dimensional μ-CT image, (b) histogram of pore coordination numbers, (c) histogram of pore body surface areas, (d) histogram of pore body volumes, and (e) pore surface area versus pore volume.

14.3 Pore Network Creation

The random pore network used in this study relies on the algorithm presented by Raoof and Hassanizadeh [2010] where each pore body can have a maximum of 26 connections along 13 different directions within

a regular cubic lattice. To accurately represent a carbonate rock we used statistics derived from a synthetic 3D μ-CT image of a dolomitized oolithic grainstone (Figure 1a) developed by Biswal et al. [2009], which follows a stochastic geometry model known as a germ-grain model (see Biswal et al. [2007]). The statistics were extracted using the 3DMA-Rock software package [*Lindquist et al.*, 1996; *Shin et al.*, 2005]. The statistical distributions of pore volumes, pore-to-pore connections, pore surface areas, and pore center coordinates are shown in Figure 1. The extracted network consisted of 20,128 pores with an average coordination number of 5, and an average pore volume size of 4.0e-13 m^3. The coordination number refers to the number of connection a pore has: for instance, a coordination number of 4 means that a pore is connected to 4 other pores.

For this study, a smaller network was created in order to have a faster computational model. The network is a cube that is 1.87 mm in length on each axis and is composed of 1,728 pores. The porosity (ϕ) is defined as,

$$\phi = \frac{\sum_i V_i}{V_T} \qquad (1)$$

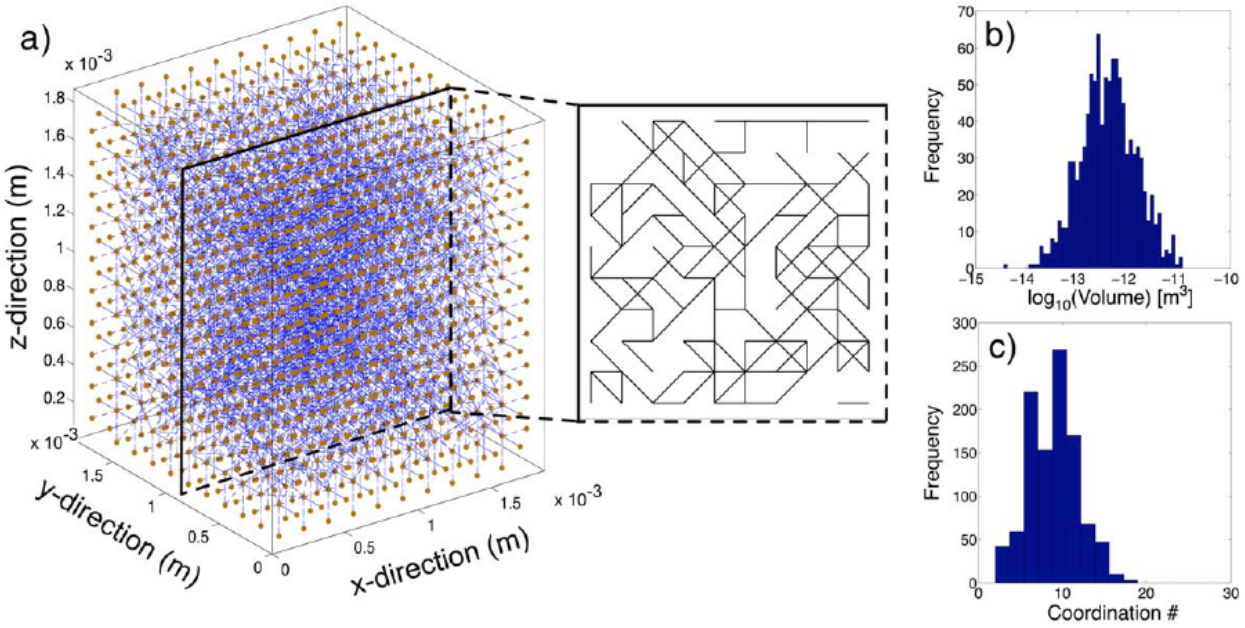

Figure 2. (a) Ball and stick representation of the network with a cross-sectional slice of the pore-to-pore connectivity, (b) histogram of network pore volumes, and (c) histogram of network coordination numbers.

where V_i [L^3] corresponds to the volume of pore *i* and V_T [L^3] is the constant network volume. Table 1 outlines the properties of the network. A representation of the network in a stick-and-ball format is shown in Figure 2, along with histograms of pore volumes and coordination numbers. The pore volume histogram in Figure 2b matches with the original pore volume histogram from the 3D synthetic μ-CT

image (Figure 1d). For our model we chose to have more tortuosity in the network, therefore the coordination number distribution does not match exactly the ones from the 3D synthetic μ-CT image – though the values come from the same population.

For the model in this study we have assumed that all pore throats are cylindrical in shape and have a characteristic diameter, which is used to calculate the conductivity across the pores. Moreover, these connecting throats are used only in the calculation of the conductivity value that feed into the pressure equation; they do not hold any volume within the system. The conductivity, C_{ij} [L^4TM^{-1}] between pores *i* and *j* is defined by the Hagen-Poisueille equation [*Sutera*, 1993] for an incompressible fluid,

$$C_{ij} = \frac{d_{ij}^4 \pi}{128 v l_{ij}} \qquad (2)$$

where d_{ij} is the diameter [L] of the "effective" cylinder connecting pores ***i*** and ***j***; l_{ij} is the distance [L] between the centroids of adjacent pores; and v is the viscosity [$MT^{-1}L^{-1}$] of the flowing fluid. The initial pore-to-pore conductivities of the network were assigned using the methods developed by Li et al. [2006]. Conductivities were sampled from a lognormal distribution in which there is correlation with the total volume of adjacent pores. In this work, the geometric mean of C_{ij} was chosen such that the intrinsic permeability of the system would be around 10^{-14} m^2 (10 mD). The geometric standard deviation of C_{ij} was equal to unity.

Table 1. System properties of the pore network along with the mineral abundances within the network.

System Properties		Mineral	% by Volume
Initial porosity [-]	0.133	Albite	5
Initial permeability [m^2]	8.16E-15	Anorthite	5
Side of network cube [mm]	1.87	Calcite	10
System volume [m^3]	6.53E-09	Dolomite	60
Total number of pores	1,728	Kaolinite	5
		Quartz	15

The solid matrix comprises of five reactive minerals plus quartz in the relative amounts shown in Table 1. The carbonate minerals that dominate carbonate formations are calcite and dolomite [*Al-Jaroudi et al.*, 2007; *Mukherji and Young*, 1973; *Stehli and Hower*, 1961]. A dolostone is in its majority dolomite (50 to 90 %), with 3 to 10% clays [*Usenmez et al.*, 1988]. For this study, the mineralogy assigned to the entire network was distributed uniformly. Each pore in the system was allotted mineral volumes according to the relative amounts in Table 1.

In the work of Peters [2009] it was shown that the surface area coverage by authigenic clay minerals in consolidated grainstones can be substantially larger than the relative abundance of these clay minerals on a volume basis. For this work, we selected surface area allocations that are consistent with those trends. We allotted 50% of the surface area to kaolinite, while dolomite received 10% and both anorthite and

albite received 5% of the surface area each. Since calcite is considered to be at equilibrium, surface area was not needed to calculate reaction rate.

14.4 Reactive Transport Modeling

The reactive transport model developed for this work has as its main purpose the modeling of permeability and porosity evolution due to carbonic acid-driven precipitation and dissolutions in a pore network system. The model development follows methods previously presented (*L. Li et al.* [2006] and *Kim et al.* [2011]); this work is distinct in the focus on carbonates, which are present in large amounts and which are relatively highly reactive, and with the added capability to account for changes to the pore volumes induced by precipitation and dissolution of mineral phases. The reactive transport architecture follows that of the STOMP ECKEChem model [*White and McGrail*, 2005] and proposed by *Fang et al.* [2003]. The two processes of transport and geochemical reaction/speciation are separated and solved sequentially in a non-iterative manner, a method presented by Steefel and MacQuarrie [1996] under the name of Sequential Non-Iterative Approach (SNIA). A sensitivity analysis was done to choose the adequate time step of the model and justify the sequential approach – the time step was fixed at a value at which the system porosity and permeability evolution did not change significantly from previous time steps. The model first solves the pressure equation, which provides the pore-to-pore fluid flow velocities, under the assumption of an incompressible and constant-density fluid. Then, the solute transport equations are solved for the selected basis components. After the new component concentrations are determined, a geochemical batch reactor module is applied to each pore element. Finally, the model accounts for the changes in volume and pore-to-pore conductivity due to precipitation or dissolution of minerals. The model processes involved are outlined below, with details given in Nogues [2012].

14.4.1 Reactive species

The model considers a total of 18 aqueous species and 5 mineral species. Through the Tableau method the basis components were determined to be the total Carbonate-bearing species, CT, the total Calcium-bearing species, CaT, the total Magnesium-bearing species, MgT, the total Silica-bearing species, SiT, the total Aluminum-bearing species, AlT, the total Chloride-bearing species, ClT, and the total Sodium-bearing species, NaT. In our model we replace the total aqueous protons concentration, HT, by the charge balance equation in order to reduce the number of equations we solve when considering transport. In addition to the eight mole and charge balance equations, there were fourteen independent reaction equations, corresponding to the reactions listed in Table 2.

Calcite was considered to be at equilibrium, based on its fast reaction rate [*Plummer et al.*, 1978] and based on preliminary batch reaction simulations we did which showed that the reaction rates of this mineral were much higher than the others. We saw that the time for calcite to reach equilibrium, after being perturbed, was much faster (in the order of tenths of seconds) in comparison to the other minerals (hundreds to thousands of seconds). Treating the reaction of calcite as an equilibrium reaction thereby avoided numerical issues of stiffness.

The complete system (equilibrium and kinetic) of non-linear geochemical equations is solved iteratively, on a pore-by-pore basis, using a Newton method.

Table 2. Chemical reactions and equilibrium constants at 50 °C. The equilibrium values are from the EQ3/6 database [Wolery et. al, 1990].

	Reactions	$\log K_{eq}$
Equilibrium	$H_2O \leftrightharpoons OH^- + H^+$	-13.3
	$H_2CO_3^* \leftrightharpoons HCO_3^- + H^+$	-6.15
	$HCO_3^- \leftrightharpoons CO_3^{2-} + H^+$	-10.3
	$H_4SiO_4 \leftrightharpoons H_3SiO_4^- + H^+$	-9.83
	$H_3SiO_4^- \leftrightharpoons H_2SiO_4^{2-} + H^+$	-12.6
	$Al^{3+} + OH^- \leftrightharpoons Al(OH)^{2+}$	8.76
	$Al(OH)^{2+} + OH^- \leftrightharpoons Al(OH)_2^+$	18.9
	$Al(OH)_2^+ + OH^- \leftrightharpoons Al(OH)_3$	27.3
	$Al(OH)_3 + OH^- \leftrightharpoons Al(OH)_4^-$	33.2
	$CaCO_{3(s)} \leftrightharpoons Ca^{2+} + CO_3^{2-}$	-8.66
Kinetic	$CaAl_2Si_2O_{8(s)} + 8H^+ \leftrightharpoons Ca^{2+} + 2Al^{3+} + 2H_4SiO_4$	21.7
	$Al_2Si_2O_5(OH)_{4(s)} + 6H^+ \leftrightharpoons 2Al^{3+} + 2H_4SiO_4 + H_2O$	3.80
	$NaAlSi_3O_{8(s)} + 8H_2O \leftrightharpoons Na^+ + Al(OH)_4^- + 3H_4SiO_4$	-1.67
	$CaMg(CO_3)_{2(s)} + 2H^+ \leftrightharpoons Ca^{2+} + 2HCO_3^- + Mg^{2+}$	1.63

14.4.2 Transport and pressure equations

In the model the pressure field is determined by solving a system of flow equations in which the net flow into and out of each pore is balanced:

$$\sum_{j=1}^{nc} Q_{ij} = 0 = \sum_{j=1}^{nc} C_{ij}\left(P_i - P_j\right) \quad (3)$$

where Q_{ij} is the flow rate [L^3T^{-1}] from pore i to pore j, nc is the number of pores connected to pore i and P_i and P_j are the fluid pressures [$ML^{-1}T^{-2}$] in pore i and j respectively. The permeability of the network, k [m^2], is defined from the Darcy equation as

$$k = \frac{-Q\mu L}{A\Delta P} \quad (4)$$

where Q is the total flow out of the network [L^3T^{-1}], μ is the dynamic viscosity [MTL^{-1}], L is the length across the network [L], A is the outflow area [L^2] and ΔP is the pressure difference across the system [MT^2L^{-1}].

The basis components are transported from pore-to-pore by advection and diffusion. The transport equations are modeled at the pore scale as follows,

$$V_i \frac{d[\cdot]_i}{dt} = \sum_{Q_{ij}>0} Q_{ij}[\cdot]_j + \sum_{Q_{ij}<0} Q_{ij}[\cdot]_i + \sum_{j=1}^{nc} D_{ij}^* a_{ij} \frac{[\cdot]_j - [\cdot]_i}{l_{ij}} + V_i S_{r,i} \quad (5)$$

where $[\cdot]_i$ represents the concentration [ML^{-3}] of a specific component in pore i, D_{ij}^* is the effective molecular diffusion coefficient [L^2T^{-1}] for that component, a_{ij} is the cross-sectional area [L^2] between pores i and j and is equal to $0.25\pi d_{ij}^2$, and $S_{r,i}$ is the mass rate [$MT^{-1}L^{-3}$] of change due to kinetic or equilibrium reactions with mineral phases. Through operator splitting, the last term is not solved in conjunction with the transport of the solutes.

14.4.3 Equilibrium reactions

The equilibrium reactions are represented by the mass action equations [*Steefel and MacQuarrie*, 1996],

$$[*]_s = K_s^{-1}\gamma_s^{-1} \prod_{s=1}^{N_c} (\gamma_p [*]_p)^{\upsilon_{ij}} \quad (6)$$

where, $[*]_s$ and $[*]_p$ are the molar concentrations [ML^{-3}] of the secondary and primary component species respectively, and γ_s and γ_p are their respective activity coefficients. The equilibrium constant is K_s, the number of components is N_c, and υ_{ij} is the stoichiometric reaction coefficient for a specific component species. The ionic strength was modeled as a constant because variations in the concentrations of reactive species would negligibly affect it. The activities were calculated using the Davies equation presented by Butler [1982] , with a constant ionic strength of 0.45 M, which represents the limit of applicability of the Davies equation. Use of this ionic strength rather than the actual value of 1.2 M contributes negligible error.

14.4.4 Kinetic rate laws

The four kinetically-controlled minerals in this study are albite, anorthite, dolomite and kaolinite. The rate of mass change due to reaction for each is written as,

$$S_{r,i} = \frac{dM_g}{dt} = r_g A_{r,g} \quad (7)$$

where, M_g is the mass of mineral g, normalized by the pore volume [ML^{-3}]. The kinetic rate is expressed by r_g [$ML^{-2}T^{-1}$] and $A_{r,g}$ is the specific reactive area [L^2L^{-3}] of mineral g, which is used for both dissolution and precipitation. The kinetic rate r_g captures the rate of both dissolution and precipitation and it is given by transition state theory as shown by Lasaga [1998] and takes the following non-linear form,

$$r_g = (k_{OH}\{OH^-\}^{n_{OH}} + k_{H2O}\{H_2O\}^{n_{H2O}} + k_H\{H^+\}^{n_H})(1 - \Omega^m) \quad (8)$$

where k_{OH}, k_{H2O} and k_H are the temperature-dependent reaction rate constants [$ML^{-2}T^{-1}$], $\{OH^-\}$, $\{H_2O\}$ and $\{H^+\}$ are the activities of the chemical species that have a catalytic or prohibitory effect, which are raised by constant exponents n_{OH}, n_{H2O} and n_H. Ω is the ionic activity product (IAP) over the equilibrium constant K_{eq}, which gets modified by empirical parameter *m*. The reaction rate constants and the empirical parameters are shown in Table 3.

Table 3. Reaction kinetic parameters at 50 °C.[1]

	$\log_{10}k$ (mol $m^{-2}s^{-1}$)						
	H_2O	OH^-	H^+	n_{H_2O}	n_{OH^-}	n_{H^+}	m
Albite	-10.5	-13.5	-8.23	1	-0.57	0.46	1
Anorthite[2]	-11.7	-13.5	-3.32	1	0.33	1.5	1
Dolomite[3]	-6.82	0	-2.7	1	-	0.5	1
Kaolinite[2]	0	-15.7	-10.8	-	0.3	0.4	0.9

1. All parameters altered to 50 °C using Arrhenius Law from the STP values shown in the EQ3/6 database.
2. Same as the values used in the models of Li et al. [2006] and Kim et al. [2011]
3. Data from [*Xu et al.*, 2007]

14.4.5 Network evolution

In order to capture the changes caused by mineral precipitation or dissolution, we developed a mathematical construct to modify the pore-to-pore conductivities by relating these changes to changes in pore volumes. The mathematical construct was chosen following the conceptual understanding that pore throat diameters are likely related to the volumes of the connected pores. For a given pore, as its pore volume is reduced or increased, each pore throat diameter associated with that pore body is updated using the following equation,

$$d_{ij}^{new} = d_{ij}^{prior} + d_{ij}^{prior}\left[\frac{V_i^{new} - V_i^{prior}}{V_i^{prior}} + \frac{V_j^{new} - V_j^{prior}}{V_j^{prior}}\right] \quad (9)$$

where d_{ij}^{new} and d_{ij}^{prior} are the new and prior throat diameter [L] connecting pore *i* and *j*, respectively. Equation (9) is consistent with the original method of assigning conductivities, which was based on the assumption that there is a correlation between the pore body volumes and the size of the throats connecting them. Limit constraints are in place to prevent precipitated mineral to occupy more space than the original pore volume, and flow in the pore is prevented once 99 % of the pore volume has been filled.

The fraction of the pore surface area assigned to each mineral is scaled down or up as minerals dissolve or precipitate. If a mineral does not exist but it is thermodynamically favored to precipitate, the model assigns a minimal fraction of the surface area to it. The evolution of the fraction of surface area follows an

equation similar to Equation (9) in which the fraction is scaled by the relative mineral volume in that specific pore.

It is important to note that the while the surface area fractions assigned to different minerals do change, the model does not change the total surface area. The choice to model the total surface area as unchanged is one of convenience. This modeling choice has negligible impact on the simulation results because the reaction rate of the most important reactive mineral, calcite, is independent of surface area because it is modeled as being at equilibrium.

14.5 Simulation Methods

In all the simulations, flow was driven in the x-direction (Figure 2a) by imposing pressure boundary conditions at the boundaries, with no-flow conditions on the other four boundaries. In order to prevent boundary effects to affect the evolution of the pore network, diffusion of ions from the outlet boundary into the domain was prohibited. In order to have comparable systems each simulation was run for 10,000 injected pore volumes through the entire network – effectively removing the dependency of time in the analysis. In all the simulations, the initial condition chosen for the chemical composition of the resident brine was close to equilibrium with respect to calcite and dolomite (Table 4).

Table 4. Initial and boundary conditions used in the first analysis of this study.

	Resident brine initial concentrations	Inflowing water concentrations
CT [mol/L]	1.80e-3	4.2e-4 to 1.5
CaT [mol/L]	7.53e-4	1.0e-4 to 3.34e-2
MgT [mol/L]	2.26e-4	3.33e-5 to 1.11e-2
SiT [mol/L]	5.2e-5	5.2e-5
AlT [mol/L]	9.06e-5	9.06e-5
NaT [mol/L]	1.2	1.2
ClT [mol/L]	1.2	1.2
pH	8.2	3 to 6
SI Calcite	0.067	-6.1 to 0.04
SI Dolomite	-0.043	-12 to -0.09

14.5.1 Changes in Permeability and Porosity due to different CaT and CT concentrations

The first question investigated in this study pertains to the effects that different inflowing brines have on the network's porosity and intrinsic permeability. Flow-through simulations were run with different combinations of CaT and CT concentrations for the inflowing water, with the amount of magnesium (MgT) kept constant at one third of CaT, thereby limiting the degrees of freedom to two independent variables. The different boundary conditions were chosen from the ranges shown in Table 4. The maximum allowable CT value of 1.5 mol/L corresponds to the upper limit of CO_2 solubility in brines as reported by Duan et al. [2006]. Figure 3a shows the pH values that correspond to the different combinations of CT and CaT. Figures 3b and 3c show the saturation index (SI) values of calcite and dolomite for the same conditions as in Figure 3a. Note that conditions with low CaT and high CT concentrations correspond to negative values of SI which indicates that the water is undersaturated with respect to the mineral and thermodynamically favors dissolution. The selected boundary condition values were bounded by an upper limit of pH 6 and by the SI equilibrium line for calcite. That is, all the inflowing fluids were either under-saturated or at equilibrium with respect to dolomite and calcite.

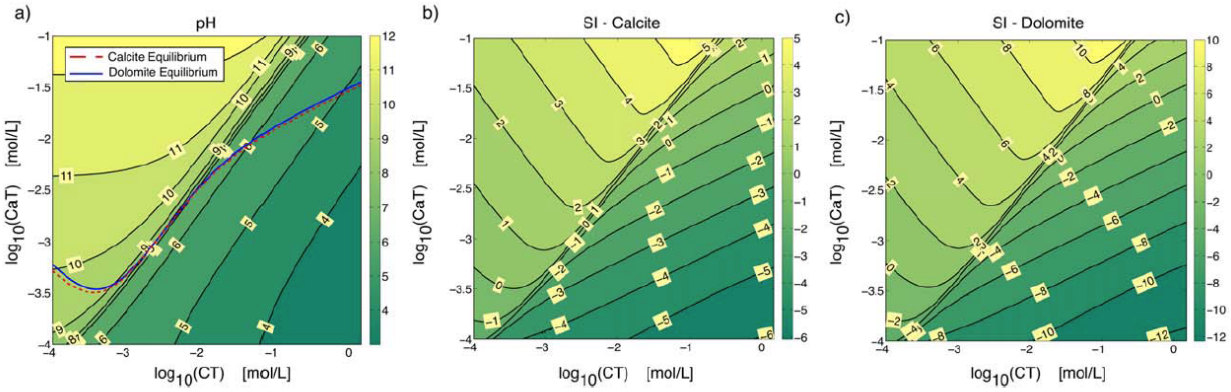

Figure 3. The concentrations and conditions of the inflowing boundary waters in the first analysis of this study: (a) pH contours with the equilibrium lines of calcite and dolomite superposed and (b and c) saturation index contours of calcite and dolomite, respectively, over the CT and CaT variable space.

14.5.2 Evolution of Permeability and Porosity due to Flow rate variation

The second analysis was performed to understand how the network's permeability and porosity evolve as a result of variation in the flowrate. We ran comparative simulations by imposing different pressure gradients across the network. The pressure gradients were imposed such that the pore-scale transport spanned the range of diffusive- and advective-dominated regimes. This analysis was conducted with two different pH boundary conditions, 3 and 5. These concentrations are shown in Table 5 along with the range of pressure gradients imposed.

Table 5. Initial and boundary conditions for the second analysis, as well as the range of pressure gradients and the SI values.

	Resident brine initial concentrations	pH 3 boundary water concentrations	pH 5 boundary concentrations
CT [mol/L]	1.80e-3	1.5	3.16e-1
CaT [mol/L]	7.53e-4	1.0e-4	1.15e-2
MgT [mol/L]	2.26e-4	3.33e-5	3.46e-3
SiT [mol/L]	5.2e-5	5.2e-5	5.2e-5
AlT [mol/L]	9.06e-5	9.06e-5	9.06e-5
NaT [mol/L]	1.2	1.2	1.2
ClT [mol/L]	1.2	1.2	1.2
$\Delta P/\Delta X$ [kPa/m]		0.26 to 13.4	
SI Calcite	0.067	-6.1	-0.686
SI Dolomite	-0.043	-12	-1.54

14.5.3 Evolution of Permeability and Porosity due to Mixing Scenarios

The third analysis explored the effects of pore-scale mixing on the evolution of the permeability and porosity of the network. We created three inflow boundary scenarios, which involved injection of two inflowing waters that when mixed would be reactive. The conditions that we were trying to replicate in these scenarios were similar to the ones presented in Tartakovsky et al. [2008] and Zhang et al. [2010] where two waters that were oversaturated with either Ca^{2+} or CO_3^{2-} flowed into the porous medium in order to create precipitation as they mixed.

Figure 4 shows the three different inflowing boundary patterns that were simulated. Two fluids flowed through the network at the same time and the initial brine was the same as the one used in the previous simulations with a pH of 8.2 (see Tables 4 or 5). As can be seen from Figure 4 there are a total of 100 boundary nodes separated in two sets of 50. The three different inflowing boundaries are referred as 'Half', 'Cross' and 'Check' as suggested by their geometrical shape.

The compositions of the two brines were chosen by trial and error to find pairs for which only the mixing could create conditions of dissolution and precipitation. In other words, if each sample of water were to flow alone through the network there would be no significant dissolution or precipitation. The selected pairs of brines are presented in Table 6. The brines chosen for the dissolution case were close to equilibrium with respect to calcite and dolomite. The brines chosen for the precipitation case were oversaturated with respect to calcite and dolomite.

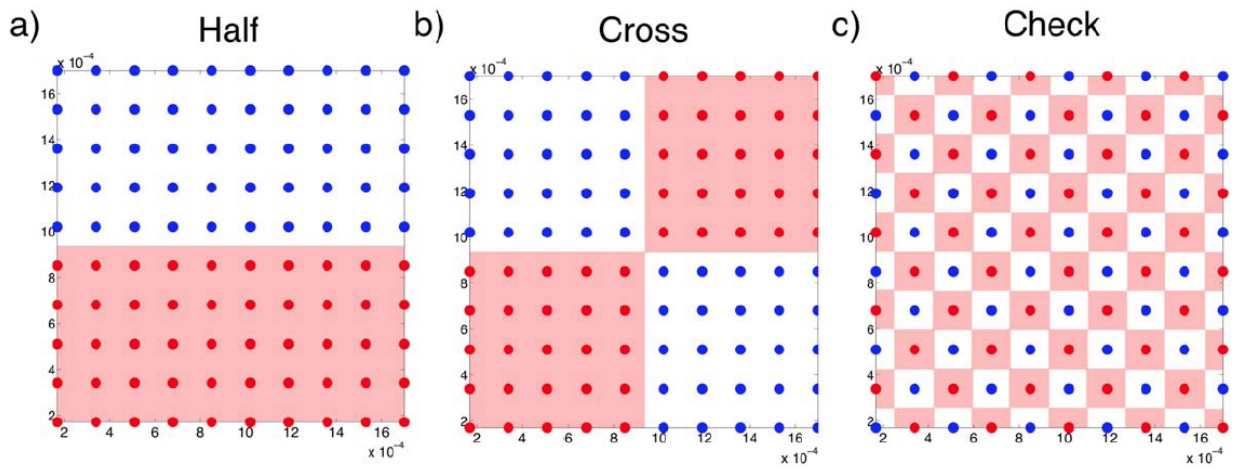

Figure 4. Flow patterns for inflowing waters over the y-z space at the network boundary.

The pressure boundary condition was the same for each of the three different mixing simulations. In the dissolution case the pressure gradient imposed across the system was of 0.26 kPa/m. For the precipitation case two pressure gradients were tested, one set of simulations with a 0.26 kPa/m gradient and another with a 13.4 kPa/m. Both sets of simulations were run until 10,000 pore volumes flowed through the network or a simulation time of 300 days had passed (whichever was reached first).

Table 6. Boundary conditions of the inflowing brines for the analysis of mixing patterns.

	Dissolution Case		Precipitation Case	
	Conc. I	Conc. II	Conc. I	Conc. II
CT [mol/L]	1.10	1.5e-2	0.97	7.35e-4
CaT [mol/L]	0.1	1.6e-2	4.18e-5	7.65e-2
MgT [mol/L]	3.01e-2	3.86e-3	1.17-5	2.93e-2
SiT [mol/L]	1.95e-7	3.65e-7	2.63e-7	4.94e-7
AlT [mol/L]	3.82e-7	1.97e-7	7.67e-7	7.83e-7
NaT [mol/L]	1.41	0.61	1.49	0.19
ClT [mol/L]	1.62	0.64	0.47	0.39
pH	4.6	6.2	8.5	8.7
SI Calcite	0.074	0.14	1.81	2.15
SI Dolomite	-0.027	-0.0001	3.41	4.22

14.6 Results and Discussion

While the modeling of pore-scale transport and geochemical reactions allows for detailed views of how each individual pore evolves regarding its chemistry, flow rates, volume and surface area, we focus our results on the integrated, upscaled values of permeability and porosity.

14.6.1 Changes in Permeability and Porosity due to different CaT and CT concentrations

The first analysis looked at how changes in the network permeability and porosity depended on the chemistry and thermodynamic potentials of the inflowing waters, while keeping pressure differences across the network constant. Figure 5 shows the resulting changes in porosity ($\Delta\phi$) and relative changes in permeability (k/k_o) after 10,000 injected pore volumes over the variable space of CaT and CT in the inflowing water. The highest changes seen for both permeability and porosity correspond to the smallest concentration of CaT and the highest concentrations of CT, where the pH equals 3, with a difference in porosity of 0.37 and a change in permeability of 2000 times the initial value. Conversely, the smallest changes in permeability and porosity are seen for conditions nearest calcite saturation, as expected. For example, when the CaT concentration is $10^{-2.9}$ mol/L, CT is $10^{-1.4}$ mol/L, and pH is 6, the difference in porosity is 0.03 with a corresponding change in permeability of 2 times the initial value.

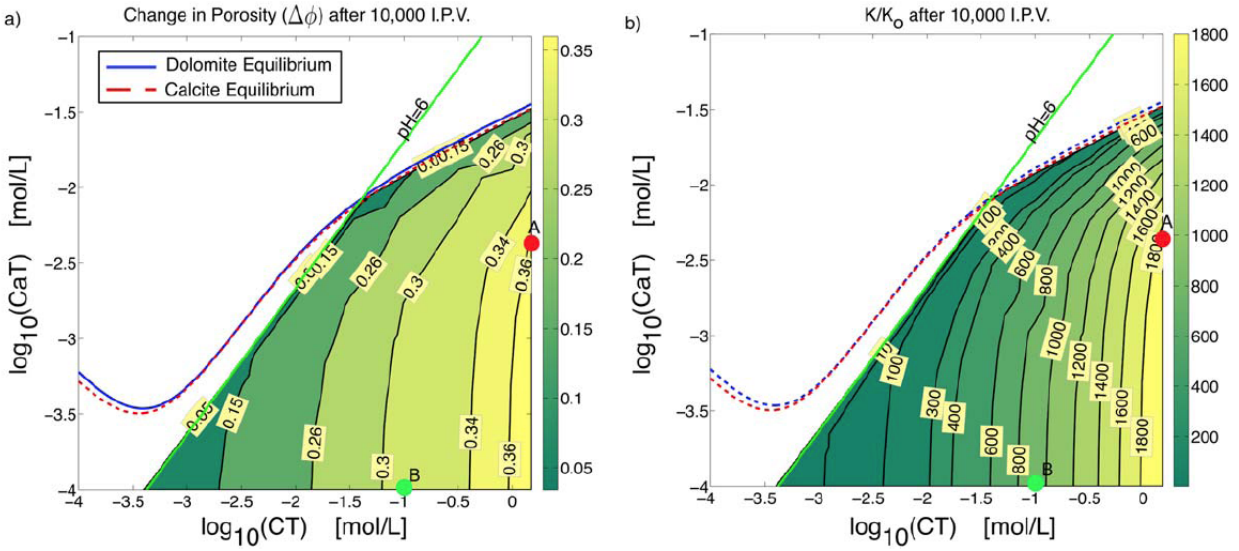

Figure 5. Contours showing (a) the changes from initial porosity and (b) the relative change in permeability with respect to the initial permeability (k_o) over the CT and CaT variable space, after 10,000 injected pore volumes. The two dots labeled "A" and "B" show a case where boundary condition with a higher SI value produces a larger change in the permeability and porosity.

Final values of permeability and porosity are dependent in a complex way on the amounts of CT and CaT in the inflowing waters. First, we can see that no single geochemical variable (CT, CaT, pH, saturation index, nor alkalinity, which is essentially proportional to CaT) alone is a good indicator of evolution of porosity and permeability. That is, the contours in figure 5 do not mimic the contours of any of the possible independent variables. It is a minimum of two independent geochemical variables that are needed for predictive purposes. While this is not surprising from a scientific point of view, it bears practical relevance because it means there is not a simple relationship that can defensibly be developed

for reduced-order models, for the range of conditions examined here. The only simplification that can be made is that for values of CaT less than 10^{-3} mol/L, the changes in permeability and porosity are dependent only on CT. Only at CaT concentrations greater than $10^{-2.5}$ mol/L does dissolved calcium begin to hinder changes in porosity and permeability.

Furthermore, the amounts of CT and CaT dictate the paths of evolution of the permeability, porosity, pH and SI values, and may lead to counter-intuitive results. For instance, in Figure 5 two dots are marked 'A' and 'B' for two different inflowing boundary conditions with the same pH value but case A has a calcite SI = -3 and case B has calcite SI = -5.5. Their resulting changes in permeability and porosity are interesting. For the case that is closer to equilibrium (case A) there is a larger change in permeability and porosity than for the smaller SI value (case B). This at first might seem counter-intuitive but the fact is that the boundary condition with a higher SI value has a higher concentration of CT, and therefore requires the addition of more calcium out of the mineral matrix in order to reach an SI value of '0'. These results indicate that it is both the relative and absolute amounts of CT and CaT that determines the ultimate evolution of the system.

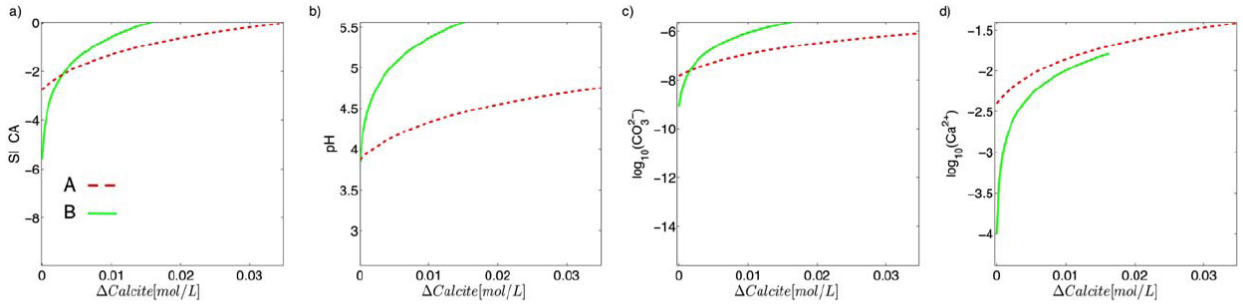

Figure 6. Evolution of geochemical parameters inside a single pore in two different systems with the same boundary pH and different SI values: (a) Saturation index of calcite, (b) pH of the pore water, (c) concentration of carbonate ions, and (d) concentration of calcium ions.

To better understand this, we conducted a simple numerical simulation of calcite dissolution in a single pore with an initial condition corresponding to the boundary water condition of interest. For initial conditions corresponding to cases A and B, Figure 6a shows the evolution of calcite dissolution (on the x axis) as the pore reaches calcite saturation. Also shown in Figure 6 are the evolution paths of pH, carbonate ion and calcium ion. As the equilibration of calcite is done instantaneously in our model, this numerical simulation is solely for illustrative purposes. In case A, the amount of calcite dissolution is greater than in case B. In case A, there is only a slight pH increase, from 3.8 to 4.6, compared to case B in which the pH is buffered from 3.8 to 5.6 because of the significant buffering that comes from even the small amount of calcite dissolution. This large pH shift means that the speciation of system 'B' results in a higher concentration of CO_3^{2-}, which brings the system close to calcite saturation faster. The Saturation Index of Calcite is given by,

$$SI\ Calcite = log_{10}\left(\frac{\{CO_3^{2-}\}\{Ca^{2+}\}}{K_{sp}}\right) \quad (10)$$

where $\{CO_3^{2-}\}$ and $\{Ca^{2+}\}$, represent the activities of carbonate and calcium ions, respectively; and K_{sp} is the solubility product of Calcite in solution. This comparative evolution of the two cases with the same pH but different SI conditions is seen regardless of the flow regime, diffusion or advective dominated. In conclusion, it is the evolutionary path that matters, and a system that is far from calcite saturation because of a low CT concentration can move quickly toward calcite saturation thus slowing ongoing reaction and inhibiting further change in porosity and permeability.

It should also be noted that for the simulations that produced smaller increases in permeability and porosity, it took a longer time to reach 10,000 pore volumes because the conductivities throughout the network did not increase as fast as those near the inlet. For the system as a whole, this did not result in an increase in flow rate. The differences in how these systems respond as functions of pore volumes injected can be seen in Figure 7, which shows a set of curves corresponding to different boundary CaT and CT values. Figure 7a shows the evolution of the porosity with respect to the injected pore volumes and Figure 7b shows the evolution of the network permeability with respect to injected pore volumes. In these figures, we can see two distinct regions of evolution: a linear increase in permeability and porosity at early times followed by a semi-logarithmic increase at later times. The linear increase is mainly due to the dissolution of calcite, which is an instantaneous reaction in our model. As calcite is depleted, dolomite dissolution, which is kinetically controlled, determines the change in pore volumes and therefore governs the long-term permeability evolution of the network.

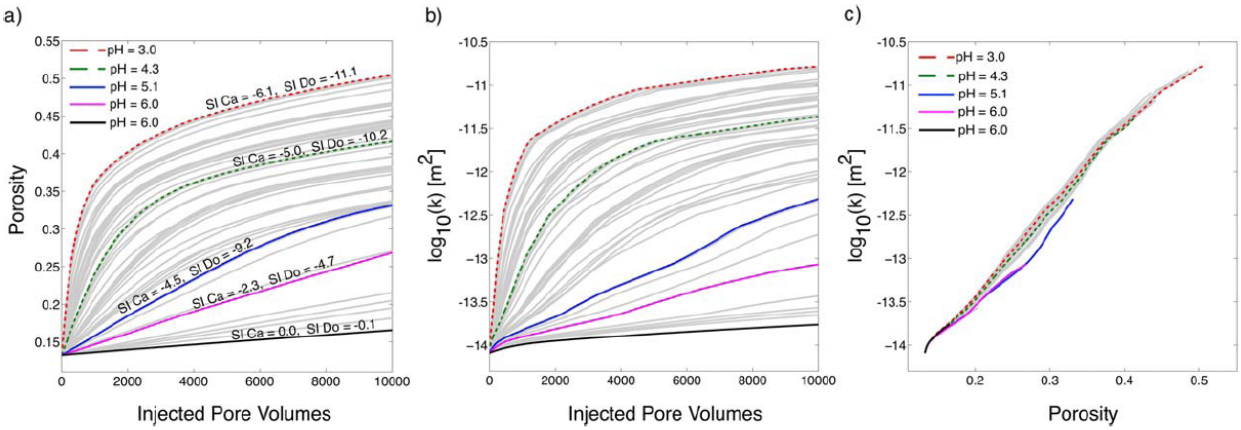

Figure 7. Evolution curves of the (a) porosity and (b) permeability (in log base 10) of the system with respect to injected pore volumes for 50 different inflowing combinations of CaT and CT values. The labels "SI Ca" and "Si Do" stand for the Saturation Index values with respect to calcite and dolomite, respectively. (c) Permeability (in log base 10) versus porosity curves for 50 different inflowing combinations of CaT and CT values.

In Figure 7c, which shows the permeability (in log space) of the network with respect to porosity. This figure shows that a rather singular relationship exists for the variation of permeability with porosity despite the wide range of pH and SI conditions tested. Thus, while there is complexity in how the extent of the change depends on boundary chemistry, there is a tight, unique relationship between permeability and porosity.

The variation that does exist in Figure 7c can be explained by the slight effect of kaolinite precipitation. For example for the case of pH 6.0 (line labeled 'Si Ca=0.0, Si Do=-0.1' in Figure 7a) kaolinite's original

volume increased by 20 % while dolomite and calcite decreased its original volume by 8 % and 0 %, respectively. The overall effect is dissolution due to the large amount of dolomite to start with (60% by volume) compared to the small amount of kaolinite (5% by volume). In this example, of all the volume added by precipitation and subtracted by dissolution, dolomite dissolution contributed 83% of it. In systems with less calcite and dolomite, the effect of anorthite dissolution and kaolinite precipitation would be more substantial.

It can be argued that the permeability vs. porosity curve, regardless of the pH, SI values and alkalinity of the inflowing waters, is for practical purposes unique – given a homogenous mineral distribution with constant flow conditions. We can also see that if any simplification were to be made to the geochemical modeling it would be appropriate to not include kaolinite, anorthite and albite in cases where carbonate minerals are abundant.

14.6.2 Changes in Permeability and Porosity due to Flow Conditions

Carbonate reactions are transport-limited [*Bernabé et al.,* 2003] and the reaction extent is sensitive to how quickly reactive water is distributed throughout the network. Singurindy and Berkowitz [2003] found in column experiments of calcareous sandstone that because dissolution of calcium carbonate is mass transfer limited, higher flow rates cause a more rapid dissolution of the porous medium. In Figure 8 we show the evolution of porosity and permeability for three different pressure gradients (which serves to illustrate the effect of flow rate) and two different pH conditions as functions of injected pore volumes. Here we see that in a high-pressure gradient system (i.e. ΔP =13.4 kPa/m), in which water flows faster through the network, there is less permeability and porosity change for the same number of pore volumes compared with a slow flowing system (i.e. ΔP =0.26 kPa/m). This is because the residence time of the slow moving reactive fluid is longer than that of the fast flowing system so there is more time for reaction and a greater extent of change in the slow-flowing system for a given number of pore volumes. If the abscissa were represented as time the curves in these graphs would be switched and faster flowing waters would reach higher permeability and porosity changes in a smaller amount of time compared to a slow flowing system.

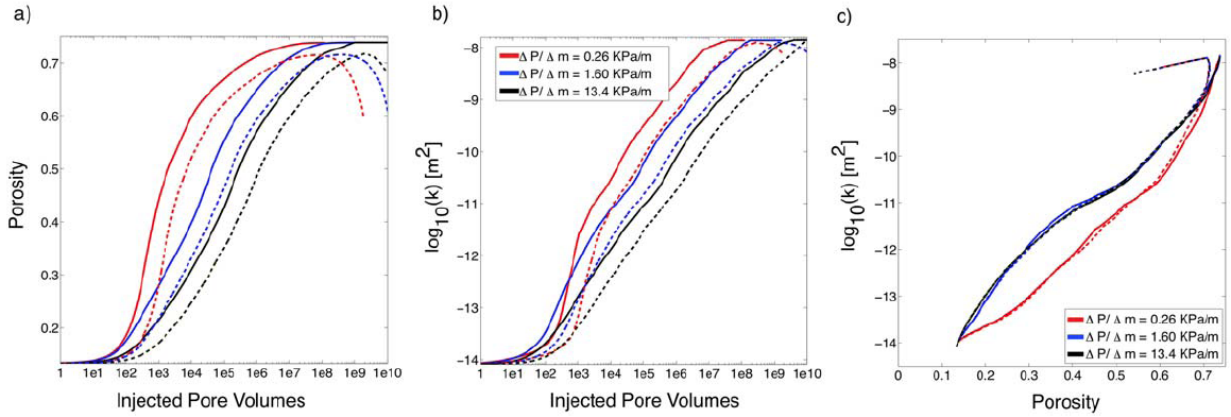

Figure 8. Evolution of the (a) porosity and (b) permeability with respect to injected pore volumes for three different flow regimes. Solid lines correspond to an inflowing pH of 3 and dashed lines correspond to an inflowing pH of 5. (c) The $\log_{10}(k)$ versus porosity relationship for three different flow regimes.

The resulting sub-domain structure changes are explored in Figure 9 where the average volume changes along the x-direction (i.e. the flow direction) are shown when the overall network porosities reach 0.2, 0.4 and 0.6. In a low-pressure gradient regimes the reaction is first concentrated at the inlet boundary which dissolves first since the inflowing water does not advance that easily through the network, making the dissolution front progress slowly with time. The changes for the smallest pressure gradient are concentrated close to the inflow boundary while for the largest pressure gradient the changes are uniformly distributed across the network. This figure is characteristic of how transport-limited reactions change the permeability and porosity of the network as a function of pressure gradients.

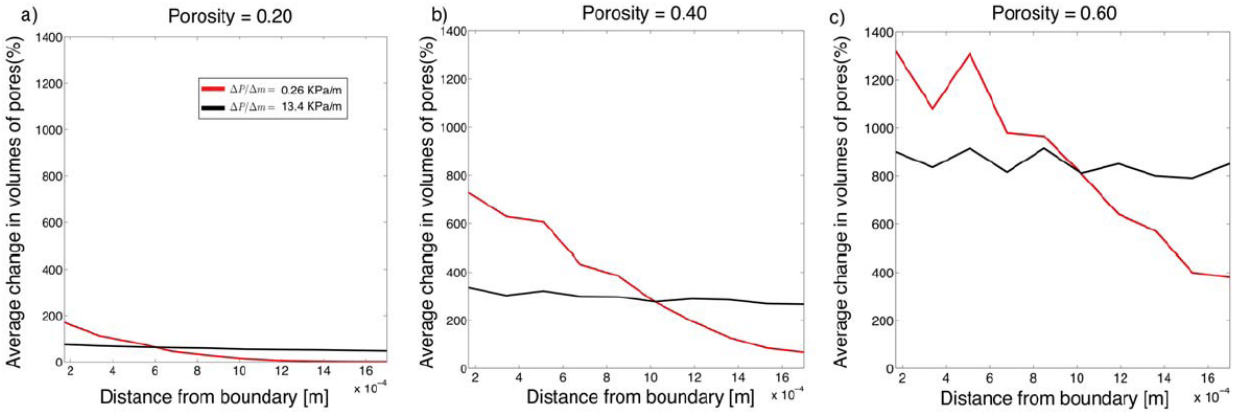

Figure 9. Average change of volumes of pores across the network for three different final porosities: (a) 0.2, (b) 0.4, and (c) 0.6.

As shown in Figure 8c, there is a distinct difference in the evolution of the permeability and porosity between the two different pH waters flowing through the network. For a pH of 3, the system dissolves all the calcite and dolomite and does not precipitate any kaolinite. For a pH of 5 however kaolinite precipitates continuously. The highest values of permeability and porosity reached with a pH of 3 are not reached with a pH of 5. After all the dolomite and calcite have dissolved away in the pH 5 scenario, kaolinite keeps precipitating and takes over the evolution of the network. This continual precipitation of kaolinite makes the permeability and porosity relationship take a turn at the end.

In Figure 8c we see that the simulations with pressure gradients of 1.6 and 13.4 kPa/m follow the same path regardless of their pH, while the simulation with a pressure gradient of 0.26 kPa/m takes a different path. Therefore, slow flow conditions create sub-domain-scale structure in porosity evolution, which leads to non-uniqueness in how permeability evolves with porosity. Much like the work presented by Luquot and Gouze [2009] here we see that the dissolution regime – and the subsequent non-uniqueness – can be related back to reactivity and flow rate.

14.6.3 Changes in Permeability and Porosity due to Mixing

The changes seen for the different mixing scenarios for the dissolution case are shown in Figure 10. Each pattern of mixing produces a different evolution of the permeability and porosity curve. When each boundary brine flows through the network by itself (curves labeled pH 4.5 and 6.2), the changes in permeability and porosity are minimal. Conversely, the scenario with the 'Check' pattern produces the highest amount of change in porosity, while the mixing pattern that separates the boundary in two halves

produces the least amount of change. This indicates that more mixing near the boundary leads to more rapid changes in porosity. However this change does not correspond to a proportional change in permeability as can be asserted by Figures 10a and 10b. The 'Cross' and 'Half' patterns reach the same permeability values but with much less change in porosity. This indicates, that as before the diffusion dominated regime concentrates dissolution at the inlet and therefore the outlet sees minimal change in porosity. In Figure 10c we also see the comparative results, which produce a non-unique evolution of the network's permeability and porosity. We can see that the mixing alone produces very different permeability evolutions. From Figure 10c we see that for the 'Half' mixing pattern there is a larger change in permeability for the same change in porosity, compared to the 'Check' pattern. This shows the importance of localized dissolution and its effect on the overall conductivity of the system. The simulation of the 'Half'-pattern mixing caused dissolution in particular areas of the network where the changes in the pore-to-pore conductivities lead to a change in continuum scale permeability that was larger than the 'Check'-pattern produced for the same amount of volume change. These results indicated the importance of localized dissolution, which creates pathways across the network that increases the continuum scale conductivity.

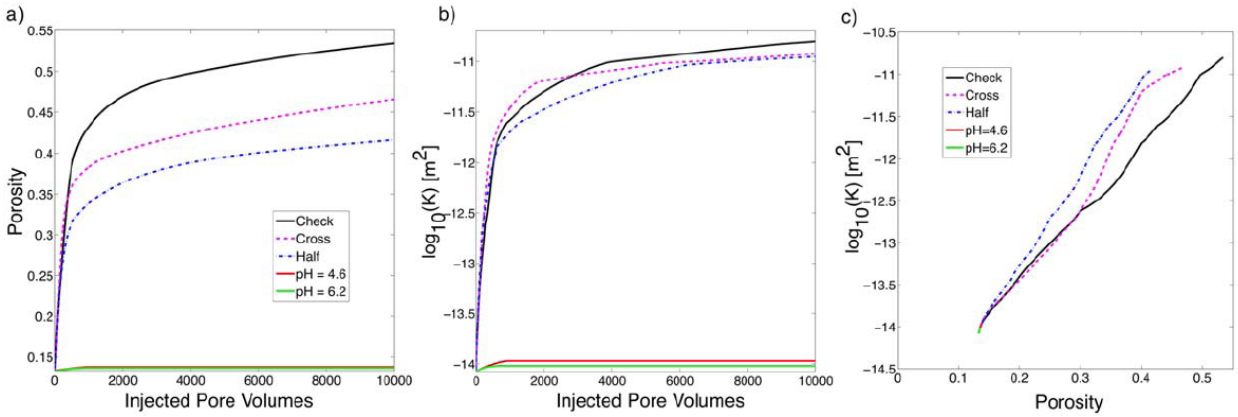

Figure 10. Evolution of the (a) porosity and (b) permeability of the system with respect to injected pore volumes for the analysis of dissolution for different mixing patterns at the boundary. (c) The $\log_{10}(k)$ versus porosity relationship for these simulations.

The fact that the increase in permeability and porosity was significant for all three scenarios indicates that the mixing was not only limited to the pores next to the boundary but that the entire network had enough mixing of reactive fluids to create dissolution along the whole length of the network. Figure 11 shows the average pore volume change across the network corresponding to an initial porosity of 0.3 for all three mixing scenarios. No clear pattern of dissolution is evident; it seems the entire network saw some form of dissolution. However, due to the low-pressure gradient imposed for these simulations, most of the dissolution happened near the inlet. The 'Check' pattern produces somewhat of a uniform dissolution front at the boundary because it is the one that promotes the most amount of mixing across the faces of the pore network. This observation indicates that mixing lengths are very small compared to the overall size of the volume. That is, enough mixing is promoted in the first pores of the network to create uniform dissolution.

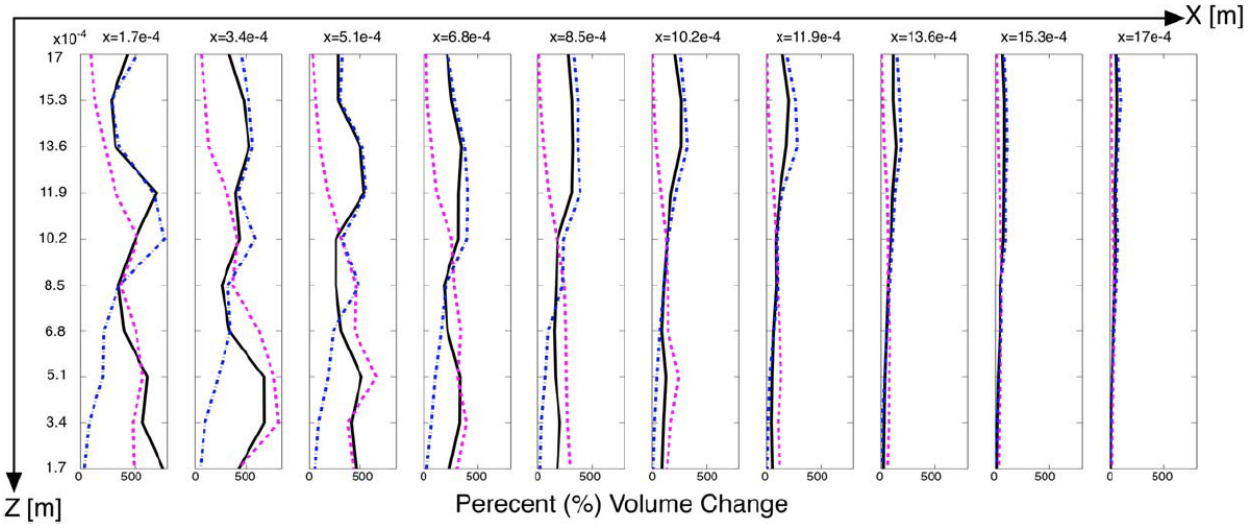

Figure 11. Set of plots showing the average volume change (averaged in the *y* direction, transverse to flow) along the *x* direction and *z* direction for different mixing scenarios. Black lines correspond to the "Check" pattern, dashed magenta lines correspond to the "Cross" pattern, and the dash and dotted blue lines correspond to the "Half" pattern.

The results of porosity and permeability evolution for the precipitation-induced simulations, in which we used two solutions that when mixed are over saturated, are shown in Figure 12. As expected, the introduction of only one fluid at a time (i.e. pH 8.48 or 8.69) produces minimal change. However, when mixtures of these fluids are injected, the changes are more substantial. The decrease in permeability and porosity is largest when three fluids are mixing; that is when the resident brine (pH 8.2) and the two inflowing waters are mixed. Once the initial resident brine is completely flushed from the system there is a more gradual decrease in the permeability and porosity due to the smaller amounts of calcium and carbonate ions in the two inflowing waters. This shows that the mixing of the three waters creates a more effective scenario for reducing the permeability than when only the two boundary waters mix. Emmanuel and Berkowitz [2005] found similar results when they modeled a continuum scale 2D-channel with increase precipitation and porosity reduction in regions where significant mixing occurred.

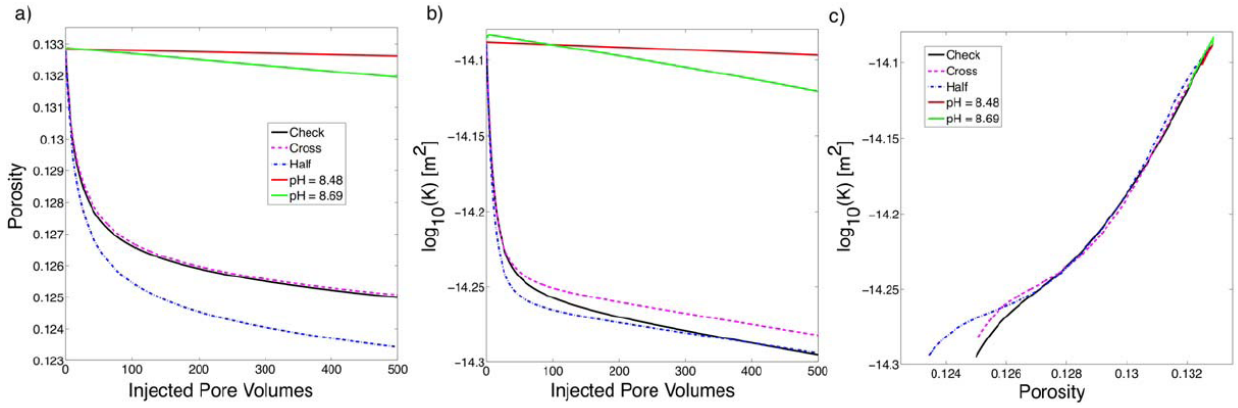

Figure 12. Evolution of the (a) porosity and (b) permeability with respect to injected pore volumes for three different mixing patterns at the boundary for the case of over-saturated mixtures. (c) The $\log_{10}(k)$ versus Porosity relationship for three mixing scenarios.

The main mineral precipitated throughout the evolution of the network was calcite. In Figure 12c we see that, just as in the dissolution case, there is a difference in the relationships between permeability and porosity depending on how the waters mix, implying non-uniqueness in the evolution of the network. The 'Half' mixing scenario sees a larger decrease in porosity but the same change in permeability compared to the 'Check' pattern, indicating the presence of localized precipitation, which does not reduce the boundary-to-boundary conductance. More importantly, decrease in permeability due to precipitation is a much slower mechanism than an increase in permeability due to dissolution. While dissolution opens up the network creating more space for unreacted water to flow in, precipitation hinders the movement of the unreactive water and therefore for the same amount of time the increase in permeability and porosity is greater in the dissolution scenario.

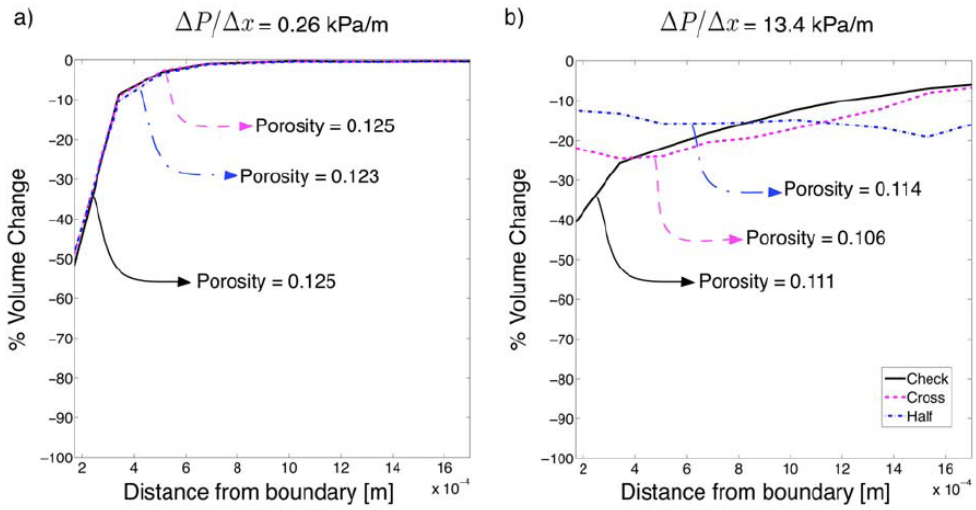

Figure 13. For the analysis of precipitation due to over-saturated mixtures, percent volume change averaged over the *y-z* space for imposed pressure gradients of (a) 0.26 kPa/m and (b) 13.4 kPa/m after 400 injected pore volumes.

Much like in the dissolution case, due to the low-pressure gradient imposed on the network, most of the reaction was concentrated near the inflow boundary. There is however a fundamental difference in the precipitation scenario because the precipitation front does not move across the network with time. Once calcite precipitates, the extra ions are depleted from solution reducing the thermodynamic drive for further precipitation, and downstream transport is inhibited due to reduction in pore-to-pore conductivity. This has a direct effect on the permeability of the system, which decreases a significant amount without much change in porosity. In general it can be said that in a diffusive dominated scenario small changes in porosity would lead to large change in permeability. The only way to get a significant reduction in permeability and porosity due to precipitation is by changing to an advective dominated system, where transport of ions across the network are on a time scale that is faster relative to the reaction time scale. In Figure 13, we show this occurrence by plotting the average volume changes across the network for two flow scenarios, the original 0.26 kPa/m (Figure 13a) scenario and a highly advective scenario with an imposed pressure gradient of 13.4 kPa/m (Figure 13b). We plot the average percent volume change as a function of distance away from the boundary after 400 injected pore volumes. The resulting porosity changes in each flow scenario, regardless of the mixing condition, are about the same. However, the higher advection scenario produces more precipitation throughout the network due to its ability to

transport ions farther from the inflow boundary. Also, in the highly advective scenario the mixing patterns create different evolutions across the network. The 'Check' pattern has precipitated mostly near the inflow boundary because it is quickly mixed while the 'Half' and 'Cross' scenarios take longer to mix and therefore spread the precipitation across the network. These simulation scenarios show that precipitation of carbonate minerals would happen in a very small region unless there is a high advective drive that distributes the precipitation.

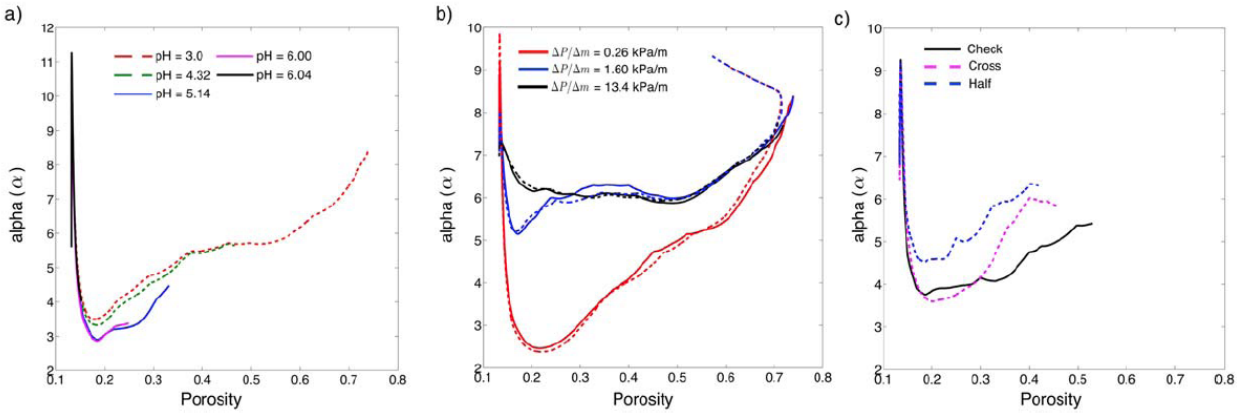

Figure 14. Values of power law parameter α as a function of network porosities, for (a) different inflowing chemistries; for (b) different pressure gradient conditions, where solid lines correspond to an inflowing pH = 3 and dashed lines for an inflowing pH = 5; and for (c) different mixing scenario for the dissolution simulations with pressure gradient of 0.26 kPa/m.

14.6.4 Implications for Power Law Approximations

Usually, continuum scale models of permeability use a simple constitutive relationship that relates porosity to permeability such as:

$$k = k_o \left(\frac{\phi}{\phi_o}\right)^{\alpha} \tag{11}$$

where, k_o and ϕ_o, refer to the initial permeability and porosity of the system, respectively, and α is the power law parameter. These relationships are derived theoretically or by fitting parameters to laboratory experiments and usually take a cubic law form. Other relationships include changes in reactive surface area, hydraulic radius and effective and critical porosity [*Bernabé et al.*, 2003; *Gouze and Luquot*, 2011; *Martys et al.*, 1994]. In this work it has been shown that there is not a unique relationship even when considering the same porous material. The evolution of the network in time and in space dictates the relationship between permeability and porosity. Figure 14 explores the relationship between α as shown in Equation (11) and the porosity evolution for some of the simulations in this work. The three different sets of α vs. porosity relationships in Figure 14 relate to three analyses in this work. For at least the first two scenarios (Figures 14a and 14b), there is a region where the cubic law (α~3) applies: between the porosity values of 0.15 and 0.25, which coincidentally is within the range of reported porosities in laboratory experiments [*Bernabé et al.*, 1982; *Bourbie and Zinszner*, 1985; *Pape et al.*, 1999]. However, as porosity increases, higher values of α are needed to relate porosity to permeability. This is important because usually laboratory experiments do not report permeability and porosity relationships for large

values of porosity (i.e. greater than 30 % porosity). The implication of these results is that a cubic law might be applicable only for a small region of porosity values and as the porosity increases the alpha value should also increase.

In Figure 14b it can also be seen that in high-pressure gradient conditions (1.6 and 13.4 kPa/m) the α value holds constant at 6 between porosities of 0.25 to 0.5 (compared to the other curves). This fairly constant value of α could be explained by realizing that all the pores across the network are dissolving uniformly. The increase in porosity can be thought of being constant and therefore a constant power relationship holds for a longer span of porosity values. This finding was also presented by Martys et al. [1994] in a different form: They showed using a random packing of spheres model that as they decreased the porosity of the system (by increasing sphere size) a single value of α was able to capture the evolution of the permeability with respect to porosity. On the other hand, the evolution of α for the curves for low pressure gradient simulations (i.e. curves on Figure 14a) reflects the slower movement of the dissolution front across the system, making changes in porosity occur in different section of the network with time, starting from the pores near the boundary and eventually dissolving the nodes at the outlet of the network.

In all the cases, as porosities reach their final value the power law parameter increases almost in a linear fashion as a function of porosity. This increase can be explained by the fact that porosity might change by a factor between 2 and 6 in relation to its original value throughout the evolution of the network, but the permeability might change between 10^2 and 10^4, in relation to its original value, and therefore it follows from Equation (13) that α should increase as porosity increases. The initial large values of α were explained by Bernabe et al. [2003] by stating that selective enlargement of the well-conducting pores create conditions for a large change in permeability with little change in porosity.

In the third analysis (Figure 14c), the evolution of α at early times is controlled by dissolution near the inlet, and the resulting localized increases in pore-to-pore conductivity. However, as porosity increase becomes more uniform across the network, the evolution paths of α in these mixing scenarios resemble those of the other analyses presented in Figures 14a and 14b.

These results show the wide range of α values that can be expected, even for a relatively simple system, and that in order to accurately capture the evolution of permeability at the continuum scale a single value of α cannot be used, and the use of a value of 3 would seriously underestimate the change in permeability. For this specific study we see that the value of α can take values from as low 2.5 up to values of 10. In general the values of α start high then quickly drop down to its lowest value (~ 2 or 3) and the slowly move up to a maximum value (~ 5 to 9). The approach taken to represent the evolution of permeability at the continuum scale can be achieved either by carrying more information from the pore-scale in order to know a priori the right alpha values to choose (i.e. pH/SI regime, mixing scenario, boundary conditions, etc.), or making scaling arguments that would eliminate the least likely scenarios. In the examples here, the high-pressure gradient vs. the low-pressure gradient curves can be used as bounding curves of the possible α values. The results shown coincide with the laboratory experiments by Gouze and Luqout [2011], which found a range of values to fit a power law relationship that linked porosity to permeability. They found much like we have that this parameter was dependent on the type of rock, the flow conditions and the reactivity of the system.

14.7 Conclusions

This study investigated the evolution of continuum-scale parameters, permeability and porosity, induced by transport and reactions at the pore-scale. The methodology developed for this study consists of modeling the transport of CO_2-rich waters in a pore network model, the subsequent chemical reactions that occur with primary or secondary minerals and the change in pore volumes that affect continuum-scale parameters. This study showed how the permeability and porosity of a pore network evolves depending on the chemical reactivity of the inflowing water, the transport processes that dominate the system (i.e. advective vs. diffusive) and the mixing patterns that might occur within a network.

Overall there are 6 major conclusions that can be made from this study: 1.) In general the higher the solution concentration of carbonic acid in the inflowing water the faster the system dissolves, with the caveat that the more calcium ions in solution, the less dissolution occurs. Neither the calcite saturation index nor any other single geochemical variable, alone, is sufficient to predict the extent of porosity change. 2). Despite the complexity in the effect of solution chemistry on the extent of change in porosity and permeability, the relationship of the permeability to the porosity of the network can be said to be unique, for a given flow condition and a similar porous structure as the one modeled in this work with homogenous mineral distribution. 3.) In a CO_2 sequestration operation, it is more likely for dissolution to occur than precipitation due to the anticipated high concentration of CT and the low values of SI and pH that occur. 4.) Slow flow conditions create non-unique porosity-permeability relationships whereas fast flow conditions produce a unique porosity-permeability relationship because these conditions produce uniform changes across the domain. 5.) Mixing waters that are by themselves unreactive can create conditions of precipitation or dissolution. The larger the spatial extent of mixing of these waters within the network, the larger the change in permeability and porosity. 6.) Using a power law relationship with a single exponent parameter (e.g. cubic law) to equate a porosity change to a permeability change may not capture the correct evolution of the network permeability. The constant values that this parameter takes are between 2 and 10 and depend on the flow rate and geochemistry of the system, but a value of 6 may be representative of high flow rate conditions.

These insights illuminate the complex phenomena involved in the modification of material properties of a porous medium when CO_2-rich waters react with carbonate rocks. The insights offered are to be considered when, in the future, continuum-scale models try to account for dynamic material properties that might affect the trapping capabilities of carbonate formations within a geological sequestration of CO_2 framework.

14.8 References

Al-Jaroudi, S. S., A. Ul-Hamid, A.-R. I. Mohammed, and S. Saner (2007), Use of X-ray powder diffraction for quantitative analysis of carbonate rock reservoir samples, *Powder Technol.*, *175*(3), 115-121.

Algive, L., S. Bekri, F. H. Nader, O. Lerat, and O. Vizika (2012), Impact of Diagenetic Alterations of the Petrphysical and Multiphase Flow Properties of Carbonate Rocks Using a Reactive Pore Network Modeling Approach, *Oil & Gas Science and Technology - Rev. IPF Energies nouvelles*, *67*(1), 147-160.

Andre, L., P. Audigane, M. Azaroual, and A. Menjoz (2007), Numerical modeling of fluid-rock chemical interactions at the supercritical CO2-liquid interface during CO2 injection into a carbonate reservoir, the Dogger aquifer (Paris Basin, France), *Energy Convers. Manage.*, *48*(6), 1782-1797.

Assayag, N., J. Matter, M. Ader, D. Goldberg, and P. Agrinier (2009), Water-rock interactions during a CO2 injection field-test: Implications on host rock dissolution and alteration effects, *Chem. Geol.*, *265*(1-2), 227-235.

Bachu, S., and J. J. Adams (2003), Sequestration of CO2 in geological media in response to climate change: capacity of deep saline aquifers to sequester CO2 in solution, *Energy Convers. Manage.*, *44*(20), 3151-3175.
Bernabé, Y., W. F. Brace, and B. Evans (1982), Permeability, porosity and pore geometry of hot-pressed calcite, *Mechanics of Materials*, *1*(3), 173-183.
Bernabé, Y., U. Mok, and B. Evans (2003), Permeability-porosity Relationships in Rocks Subjected to Various Evolution Processes, *Pure Appl. Geophys.*, *160*(5), 937-960.
Birkholzer, J. T., Q. Zhou, and C.-F. Tsang (2009), Large-scale impact of CO2 storage in deep saline aquifers: A sensitivity study on pressure response in stratified systems, *Int. J. Greenhouse Gas Control*, *3*(2), 181-194.
Biswal, B., P. E. Oren, R. Held, S. Bakke, and R. Hilfer (2007), Stochastic multiscale model for carbonate rocks, *Phys. Rev. E*, *75*(6).
Biswal, B., R. J. Held, V. Khanna, J. Wang, and R. Hilfer (2009), Towards precise prediction of transport properties from synthetic computer tomography of reconstructed porous media, *Phys. Rev. E*, *80*(4).
Bourbie, T., and B. Zinszner (1985), Hydrualic and Acoustic Properties as a Function of Porosity in Fontainebleau Sandstone, *J. Geophys. Res.*, *90*(B13), 11524-11532.
Brosse, E., et al. (2010), Selection and Characterization of Geological Sites able to Host a Pilot-Scale CO 2Storage in the Paris Basin (GeoCarbone-PICOREF), *Oil & Gas Science and Technology - Revue d'IFP*, *65*(3), 375-403.
Burton, M., N. Kumar, and S. L. Bryant (2008), Time-Dependent Injectivity During CO2 Storage in Aquifers. SPE Paper 113937, in *SPE/DOE Symposium on Improved Oil Recovery*, edited, pp. 1-15, Tulsa, Oklahoma, USA.
Butler, J. N. (1982), *Carbon dioxide equilibria and their applications*, Addison-Wesley, Reading, MA.
Celia, M. A., J. M. Nordbotten, B. Court, M. Dobossy, and S. Bachu (2011), Field-scale application of a semi-analytical model for estimation of CO2 and brine leakage along old wells, *Int. J. Greenhouse Gas Control*, *5*(2), 257-269.
Doughty, C., and K. Pruess (2004), Modeling Supercritical CO2 injection in heterogeneous porous media, *Vadose Zone J.*, *3*, 837-847.
Duan, Z. H., R. Sun, C. Zhu, and I. M. Chou (2006), An improved model for the calculation of CO2 solubility in aqueous solutions containing Na+, K+, Ca2+, Mg2+, Cl-, and SO42-, *Mar. Chem.*, *98*(2-4), 131-139.
Ellis, B. R., J. P. Fitts, G. S. Bromhal, D. L. McIntyre, R. Tappero, and C. A. Peters (2013), Dissolution-Driven Permeability Reduction of a Fractured Carbonate Caprock, *Environ. Eng. Science*, *30(4), 187-193*.
Ellis, B. R., C. A. Peters, J. P. Fitts, G. S. Bromhal, D. L. McIntyre, R. P. Warzinski, and R. E.J. (2011), Deterioration of a fractured carbonate caprock exposed to CO2-acidified brine flow, *Greenhouse Gases: Sci. Technol.*, *1*, 248–260.
Emmanuel, S., and B. Berkowitz (2005), Mixing-induced precipitation and porosity evolution in porous media, *Adv. Water Res.*, *28*(4), 337-344.
Fang, Y. L., G. T. Yeh, and W. D. Burgos (2003), A general paradigm to model reaction-based biogeochemical processes in batch systems, *Water Resour. Res.*, *39*(4).
Flemisch, B., et al. (2011), DuMux: DUNE for multi-{phase,component,scale,physics, …} flow and transport in porous media, *Adv. Water Res.*, *34*(9), 1102-1112.
Gherardi, F., T. F. Xu, and K. Pruess (2007), Numerical modeling of self-limiting and self-enhancing caprock alteration induced by CO2 storage in a depleted gas reservoir, *Chem. Geol.*, *244*(1-2), 103-129.
Gouze, P., and L. Luquot (2011), X-ray microtomography characterization of porosity, permeability and reactive surface changes during dissolution, *J. Contam. Hydrol.*, *120-121*(0), 45-55.
Grimstad, A.-A., S. Georgescu, E. Lindeberg, and J.-F. Vuillaume (2009), Modelling and Simulation of Mechanisms for Leakage of CO2 from Geological Storage, *Energy Procedia*, *1*(1), 2511-2518.
Kang, Q., P. Lichtner, H. Viswanathan, and A. Abdel-Fattah (2010), Pore Scale Modeling of Reactive Transport Involved in Geologic CO2 Sequestration, *Transp. Porous Media*, *82*(1), 197-213.
Kim, D., C. A. Peters, and W. B. Lindquist (2011), Upscaling geochemical reaction rates accompanying acidic CO2-saturated brine flow in sandstone aquifers, *Water Resour. Res.*, *47*(1), W01505.
Lasaga, A. C. (1998), *Kinetic theory in the earth sciences*, Princeton University Press, Princeton, NJ.
Li, L., C. A. Peters, and M. A. Celia (2006), Upscaling geochemical reaction rates using pore-scale network modeling, *Adv. Water Res.*, *29*(9), 1351-1370.
Li, X., H. Huang, and P. Meakin (2010), A three-dimensional level set simulation of coupled reactive transport and precipitation/dissolution, *International Journal of Heat and Mass Transfer*, *53*(13-14), 2908-2923.
Lindquist, W. B., S. M. Lee, D. A. Coker, K. W. Jones, and P. Spanne (1996), Medial axis analysis of void structure in three-dimensional tomo- graphic images of porous media, *J. Geophys. Res.*, *101*, 8297 – 8310.

Liu, F., P. Lu, C. Zhu, and Y. Xiao (2011), Coupled reactive flow and transport modeling of CO2 sequestration in the Mt. Simon sandstone formation, Midwest U.S.A, *International Journal of Greenhouse Gas Control*, *5*(2), 294-307.

Luquot, L., and P. Gouze (2009), Experimental determination of porosity and permeability changes induced by injection of CO2 into carbonate rocks, *Chem. Geol.*, *265*(1-2), 148-159.

Martys, N. S., S. Torquato, and D. P. Bentz (1994), Universal scaling of fluid permeability for sphere packings, *Phys. Rev. E*, *50*(1), 403-408.

Mehmani, Y., T. Sun, M. T. Balhoff, P. Eichhubl, and S. Bryant (2012), Multiblock Pore-Scale Modeling and Upscaling of Reactive Transport: Application to Carbon Sequestration, *Transp. Porous Media*, *95*(2), 305-326.

Mukherji, K. K., and G. M. Young (1973), Diagenesis of the black river (middle ordovician) limestones in southern ontario, canada, *Sediment. Geol.*, *9*, 21-51.

Nogues, J. P. (2012), Investigations in Upscaling Transport and Geochemistry in Porous Media: Modeling CO2 Sequestration at the Pore, Continuum and Reservoir Scales, Princeton University, Princeton.

Nogues, J. P., B. Court, M. Dobossy, J. M. Nordbotten, and M. A. Celia (2012), A methodology to estimate maximum probable leakage along old wells in a geological sequestration operation, *Int. J. Greenhouse Gas Control*, *7*, 39-47.

Noiriel, C., P. Gouze, and D. Bernard (2004), Investigation of porosity and permeability effects from microstructure changes during limestone dissolution, *Geophys. Res. Lett.*, *31*(24), L24603.

Noiriel, C., D. Bernard, P. Gouze, and X. Thibault (2005), Hydraulic Properties and Microgeometry Evolution Accompanying Limestone Dissolution by Acidic Water, *Oil & Gas Science and Technology - Rev. IFP*, *60*(1), 177-192.

Pape, H., C. Clauser, and J. Iffland (1999), Permeability prediction based on fractal pore-space geometry, *Geophysics*, *64*(5), 1447-1460.

Pawar, R. J., T. L. Watson, and C. W. Gable (2009), Numerical Simulation of CO2 Leakage through Abandoned Wells: Model for an Abandoned Site with Observed Gas Migration in Alberta, Canada, *Energy Procedia*, *1*(1), 3625-3632.

Peters, C. A. (2009), Accessibilities of reactive minerals in consolidated sedimentary rock: An imaging study of three sandstones, *Chem. Geol.*, *265*(1-2), 198-208.

Plummer, L. N., T. M. L. Wigley, and D. L. Parkhurst (1978), The Kinetics of Calcite Dissolution in CO2-Water Systems at 5oC to 60oC and 0.0 to 1.0 ATM CO2, *Am. J. Sci.*, *278*, 179-216.

Pruess, K., T. Xu, J. Apps, and J. Garcia (2003), Numerical Modeling of Aquifer Disposal of CO2, *SPE Journal*, *8*(1), 49-60.

Raoof, A., and S. Hassanizadeh (2010), A New Method for Generating Pore-Network Models of Porous Media, *Transp. Porous Media*, *81*(3), 391-407.

Shin, H., W. B. Lindquist, D. L. Sahagian, and S. R. Song (2005), Analysis of the vesicular structure of basalts, *Comput. Geosci.*, *31*(4), 473-487.

Singurindy, O., and B. Berkowitz (2003), Evolution of hydraulic conductivity by precipitation and dissolution in carbonate rock, *Water Resour. Res.*, *39*(1), 1016.

Smith, M. M., Y. Sholokhova, Y. Hao, and S. A. Carroll (2012), Evaporite Caprock Integrity: An Experimental Study of Reactive Mineralogy and Pore-Scale Heterogeneity during Brine-CO2 Exposure, *Environ. Sci. Technol.*, *47*(1), 262-268.

Steefel, C., and K. T. B. MacQuarrie (1996), Approaches to Modeling of Reactive Transport in Porous Media, in *Reactive Transport in Porous Media*, edited by P. C. Lichtner, C. Steefel and E. H. Oelkers, Mineralogical Society of America, Washington D.C.

Steefel, C., D. J. De Paolo, and P. C. Lichtner (2005), Reactive Transport Modeling: An essential tool and a new research approach for the Earth Sciences, *Earth Planet. Sci. Lett.*, *240*, 539-558.

Stehli, F. G., and J. Hower (1961), Mineralogy and Early Diagenesis of Carbonate Sediments, *J. Sediment. Petrol.*, *31*(3), 358-371.

Sutera, S. P. (1993), The History of Poiseuille's Law, *Annual Review of Fluid Mechanics*, *25*, 1-20.

Szymczak, P., and A. J. C. Ladd (2009), Wormhole formation in dissolving fractures, *J. Geophys. Res., [Solid Earth]*, *114*.

Tartakovsky, A. M., P. Meakin, T. D. Scheibe, and B. D. Wood (2007), A smoothed particle hydrodynamics model for reactive transport and mineral precipitation in porous and fractured porous media, *Water Resour. Res.*, *43*(5), W05437.

Tartakovsky, A. M., G. Redden, P. C. Lichtner, T. D. Scheibe, and P. Meakin (2008), Mixing-induced precipitation: Experimental study and multiscale numerical analysis, *Water Resour. Res.*, *44*(6).

Usenmez, S., G. M. Friedman, and D. C. Kopaska-Merkel (1988), Fabric and Composition of Dolostones and Dedolomites from near Karapinar (Adana, Southern Turkey), *Carbonates Evaporites*, *2*(2).

White, M. D., and B. P. McGrail (2005), STOMP Subsurface Transport Over Multiple Phases. Version 1.0. Addendum: ECKEChem Equilibrium-Conservation-Kinetic Equation Chemistry Transport*Rep.*, Pacific Northwest National Laboratory, Richland, WA.

Wolery, T., J., K. Jackson, J., W. Bourcier, L., C. Bruton, J., B. Viani, E., K. Knauss, G., and J. Delany, M. (1990), Current Status of the EQ3/6 Software Package for Geochemical Modeling, in *Chemical Modeling of Aqueous Systems II*, edited, pp. 104-116, American Chemical Society.

Xu, T., J. A. Apps, and K. Pruess (2005), Mineral sequestration of carbon dioxide in a sandstone-Shale system, *Chem. Geol.*, *217*(3-4), 295-318.

Xu, T., E. Sonnenthal, N. Spycher, and K. Pruess (2006), TOUGHREACT-A simulation program for non-isothermal multiphase reactive geochemical transport in variably saturated geologic media: Applications to geothermal injectivity and CO2 geological sequestration, *Comput. Geosci.*, *32*(2), 145-165.

Xu, T., J. A. Apps, K. Pruess, and H. Yamamoto (2007), Numerical modeling of injection and mineral trapping Of CO2 with H2S and SO2 in a sandstone formation, *Chem. Geol.*, *242*(3-4), 319-346.

Yoon, H., A. J. Valocchi, C. J. Werth, and T. A. Dewers (2013), Pore-scale simulation of mixing-induced calcium carbonate precipitation and dissolution in a microfluidic pore network, *Water Resour. Res.*, *48 W02524*.

Zhang, C. Y., K. Dehoff, N. Hess, M. Oostrom, T. W. Wietsma, A. J. Valocchi, B. W. Fouke, and C. J. Werth (2010), Pore-Scale Study of Transverse Mixing Induced CaCO(3) Precipitation and Permeability Reduction in a Model Subsurface Sedimentary System, *Environ. Sci. Technol.*, *44*(20), 7833-7838.

Chapter 15. The impacts of microfracture geometry on effective permeability

15.1 Background

Natural and induced microfractures are widely documented, and their presence largely increases permeability of the fractured rock (Gutierrez *et al.*, 2000; Takahashi *et al.*, 2003; Ameen and Hailwood, 2008; Iding and Ringrose, 2010). The enhanced permeability is favorable in some cases, for it improves oil and geothermal production. As a matter of fact, hydraulic fracturing is a common practice in the fields of petroleum and geothermal energy. In other cases the enhanced permeability is unfavorable, as it may compromise the performance of storage site for CO_2 and nuclear wastes, and raise public concerns. Either way, investigations on permeabilities induced by microfractures is a critical component for the evaluation of fractured reservoirs and caprocks.

In view of the complexity of microfracture networks, the method of effective permeability tensor is preferred and widely applied (Lee *et al.*, 2001; Terimoori *et al.*, 2005; Iding and Ringrose, 2010), providing an efficient tool to capture the hydraulic property of a fractured system. The effective permeability tensor is controlled by the geometry of the microfracture networks, and its estimation requires extensive knowledge on geometrical parameters such as fracture length, aperture, orientation and density. However, full characterization of the geometry of a microfracture network is difficult, if not impossible (Nelson, 1985; Ameen and Hailwood, 2008), because measurements of these geometrical parameters can only be achieved by microscopy or tomography study of core samples. Instead, probabilistic distributions of these parameters derived from field data using geostatistical models are generally used (Wang *et al.*, 2008).

This application of geostatistics poses a need to understand the impacts of the distributions of these geometrical parameters, so that (i) we thoroughly understand the extent and sources of uncertainty and variability in permeability, and (ii) efficiency can be improved in the process of collecting geostatistical data. Hence, it is one of the objectives of this study to examine the sensitivity of effective permeability of

a microfracture network to the distribution types and parameterization of the distributions of fracture length and aperture, and identify the most influential parameters. Variations of orientation distribution were not considered so that the study is better concentrated on the impacts on the magnitude of effective permeability. In addition, the current work aims to examine how changes in fracture porosity will affect the effective permeability. For one reason, compared with the conventional density parameters, such as linear frequency (number of fractures along the sampling line) and volumetric density (areas of fracture surfaces over the volume studied), fracture porosity provides a less time-consuming and more intuitive way to describe fracture density. For another, empirical relations between porosity, which is easily measured, and corresponding maximum fracture porosity have been developed in the field of petroleum. Insights on the responses of effective permeability to changes of fracture porosity will allow us to estimate the possible ceiling for microfracture-induced permeability with given (fracture) porosity.

15.2 Methods

In the fundamental paper in 1969, Snow developed a mathematical model to calculate effective permeability tensor for fracture networks. Each fracture was assumed to be isotropic, uniform and infinite, and modeled as a planar void confined by two smooth parallel walls (figure A1(a)), filled with single phase incompressible Newtonian fluid. For a single fracture, the Navier-Stokes equation was solved, giving the fluid velocity in direction i (v_i) as

$$v_i = -\frac{a^2}{12}\frac{g}{\nu}J_i \qquad \text{eqn (1)}$$

where a is the aperture size, g is the gravitational acceleration, ν is the kinematic viscosity, and J_i is the projection of hydraulic gradient on the corresponding direction. Coupling with Darcy's law, the intrinsic permeability (k) of a single fracture was given as the Cubic Law

$$k = \frac{a^3}{12L} \qquad \text{eqn (2)}$$

where L is the dimension of the cube studied. The Cubic Law was validated by Witherspoon *et al.* (1980) with experimental measurements for both open and closed fractures, with fracture apertures ranging from 250 μm to 4 μm, regardless of the rock type.

It was assumed that fluids are independent at the intersections of fractures. Hence, contributions to permeability tensor from different fractures can be summed up. For a fracture network, the effective permeability tensor is

$$k_{ij} = \frac{1}{12}\sum\frac{a^3}{|n_i D_i|}(\delta_{ij} - n_i n_j) \qquad \text{eqn (3)}$$

where δ_{ij} is the Kronecker delta, n_i is the projection of the unit vector ($\boldsymbol{n}$) normal to the fracture surface on reference axis i, and D is the sampling line. The effective permeability tensor is symmetric. Its magnitude highly depends on the size of fracture aperture, as it is related to a^3, while the anisotropy is attributable to the variation in fracture orientations.

The existence of such symmetric effective permeability was verified later by Long *et al.* (1980). If a fractured rock behaves similarly to a homogeneous porous medium, the plot of $1/\sqrt{K_g}$ (where K_g is the measurement of permeability in the direction of gradient) and α (angle of gradient to the reference axis) should be an ellipse in polar coordinates, and the hydraulic property of the fracture network can be described by a symmetric permeability tensor (Long *et al.*, 1980). Using this tool, the authors found that dense fractures, non-uniform orientation, constant aperture and large REV favor the existence of a symmetric effective permeability tensor.

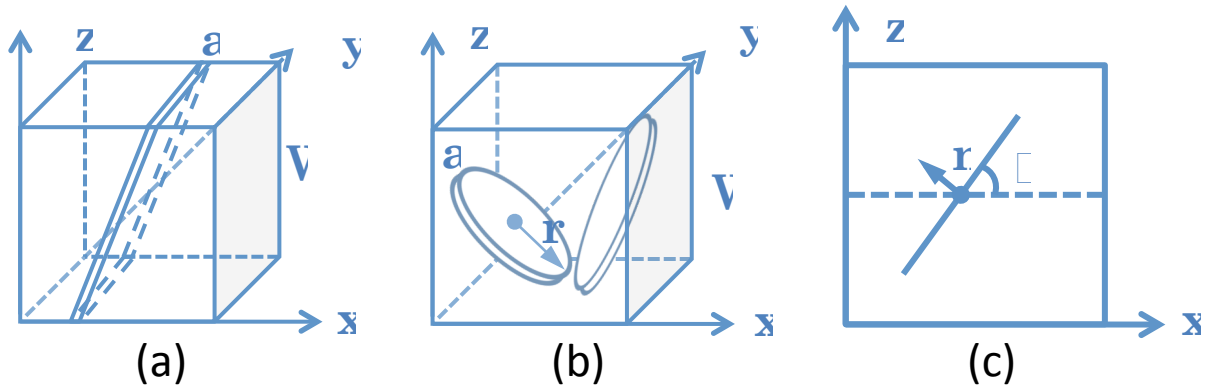

Figure A1. Schematics of microfractures (a) as planes; (b) as disks; and (c) as line segments in 2D. (a-aperture, W-dimension of the study domain, r-radius, n-normal, θ-orientation).

Oda (1985) introduced a crack tensor (P_{ij}), determined by the fracture network geometry only, to calculate effective permeability. In this model, each fracture was deemed as a disk with radius *r*, aperture *a*, and randomly distributed center (figure A1(b)), relaxing the assumption of infinity. The geometry of the fracture network was characterized by a density function ($E(\boldsymbol{n}, r, a)$) and fracture density (ρ).

$$k_{ij} = \lambda(P_{kk}\delta_{ij} - P_{ij}) \qquad \text{eqn (4)}$$

$$P_{kk} = P_{11} + P_{22} + P_{33} \qquad \text{eqn (5)}$$

$$P_{ij} = \frac{\pi}{4}\rho \int_0^\infty \int_0^\infty \int_\Omega r^2 a^3 \boldsymbol{n_i n_j} E(\boldsymbol{n}, r, a) d\Omega dr dt \qquad \text{eqn (6)}$$

where λ is a constant on the interval (0, 1/12], equal to 1/12 if the fractures are infinite, Ω is the space for all solid angles of a unit sphere, and ρ is the ratio of the number of fractures over the volume of the cube studied.

Oda's method provides an efficient tool to calculate effective permeability tensor from fracture network geometry, and was adopted in the current study. Out of consideration of computational cost, 2D fracture networks were studied here.

For each simulation, a 2D fracture network was generated according to the given distributions of the length, aperture and orientation, the domain size (W) and fracture porosity (φ_f). Each fracture was denoted by a line segment (figure A1(c)), whose center was randomly distributed in the domain (Lee *et al.*, 2001). Fracture roughness was neglected. Each fracture was assigned a single value from lognormal distribution (Long *et al.*, 1980; Nelson, 1985; Wang *et al.*, 2008). Fracture length (L) was lognormally distributed (Long *et al.*, 1980; Iding and Ringrose, 2010) as well, while the orientation (θ) was uniformally distributed. Monte Carlo sampling was then conducted to pair these parameters. The number of fractures (m) was not given explicitly. Instead, it was jointly determined by fracture porosity, domain size, length and aperture (eqn (7)). Since fractures that extend outside of the domain were truncated, the number of fractures (m) was allowed to fluctuate to compensate for the truncated fracture porosity. Fracture porosity of the generated fracture network should not deviate from the given fracture porosity by 1%. Equations (8)-(10) were used to calculate the effective permeability tensor.

$$m = \frac{W^2 \varphi_f}{E[L]E[a]} \qquad \text{eqn (7)}$$

$$P_{ij} = \frac{1}{W^2} \sum_{k=1}^{m} L^{(k)} a^{(k)^3} n_i^{(k)} n_j^{(k)} \qquad \text{eqn (8)}$$

$$P_{kk} = P_{11} + P_{22} \qquad \text{eqn (9)}$$

$$k_{ij} = \lambda (P_{kk} \delta_{ij} - P_{ij}) \qquad \text{eqn (10)}$$

In this study, $\lambda = 1/12$ was used, as the numerical experiments of Oda (1985) demonstrated that when the density of the fractures is large or the orientation of the fractures are distributed rather than fixed, λ is close to 1/12.

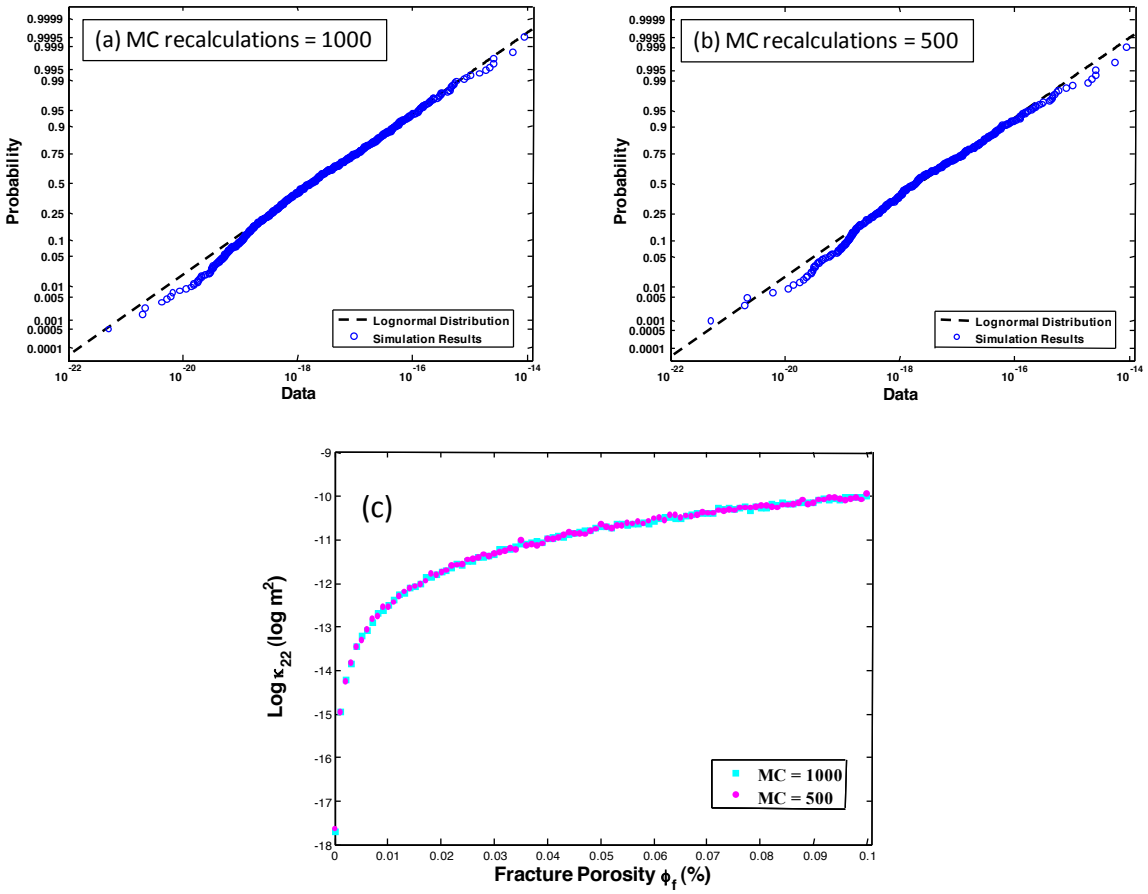

Figure A2. Probability plots for one Monte Carlo simulation with (a) 1000 recalculations, and (b) 500 recalculations. (c) Comparison of results from Monte Carlo simulations with 500 and 1000 recalculations.

As is described in the results section, for a Monte Carlo simulation, the resulting permeabilities follow a lognormal distribution (figure A2(a)). Hence, the average of the logarithms of all values from one Monte Carlo simulation was used and then analyzed. Since 500 recalculations are able to capture the lognormal distribution (figure A2(b)), with means very close to those of 1000 recalculations (figure A2(c)), and save considerable computational cost, each Monte Carlo simulation includes 500 recalculations in this study.

15.3 Results

Start with the finding that the resulting permeability is lognormal, and point to figure A2.

Following increasing domain size, permeability increases as well. This trend slows down after the domain size reaches 10 m (figure A3). Hence, a domain size of 10m was used to provide representative sampling.

Fracture length is related to effective permeability of the microfracture network through fracture density (eqn (7)) and intrinsic permeability for each fracture (eqn (8)-(10)). Increasing average length leads to decreasing fracture density and increasing intrinsic permeability. The results show that the power of the former dominates the latter, and causes effective permeability to decrease (figure A4(a)). However, as average length approaches to domain size, its impact vanishes. On the contrary, enlarged aperture corresponds to higher effective permeability (figure A4(b)). Though enhancing aperture results in reduction in fracture density (eqn (7)), its influence on intrinsic permeability (eqn (8)-(10)) dominates. Compared to average length, effective permeability is less sensitive to changes in average aperture with given fracture porosity.

The variance of length has little effect on effective permeability. The variation in effective permeabilities of fracture networks with different variances of length has a narrow range, and there is no clear trend (figure A5(a)). However, raising the variance of aperture leads to marked increase in effective permeability (figure A5(b)), mostly likely due to occurrence of fractures with wide apertures. Compared with average aperture, the effect of the variance of aperture is even stronger.

Exponential distributions for length (Long *et al.*, 1980) and aperture (Wang *et al.*, 2008) were also documented in literatures. In the present study, it is found that for length, effective permeabilities associated with exponential distribution are close to lognormal distribution (figure A6(a)), while for aperture, outcome values of exponential distribution deviate considerably from those of lognormal distribution (figure A6(b)). In addition, it was suggested that length and aperture are sometimes correlated (Oda, 1985), which means the joint distribution of length and aperture cannot be simply replaced by two independent distributions. Although it is demonstrated in the results that systems with high correlation between length and aperture have slightly higher effective permeability, it is not significant (figure A7).

Elevation of fracture porosity resulted in increasing effective permeability as expected (figure A8). One order of magnitude increase in the fracture porosity corresponds to about three orders of magnitude enhancement in effective permeability (eqn (11)), surpassing the impacts of the distributions of both length and aperture.

$$\kappa_{22} = 0.0059\varphi_f^{2.3353}, R^2 = 0.9991 \qquad \text{eqn (11)}$$

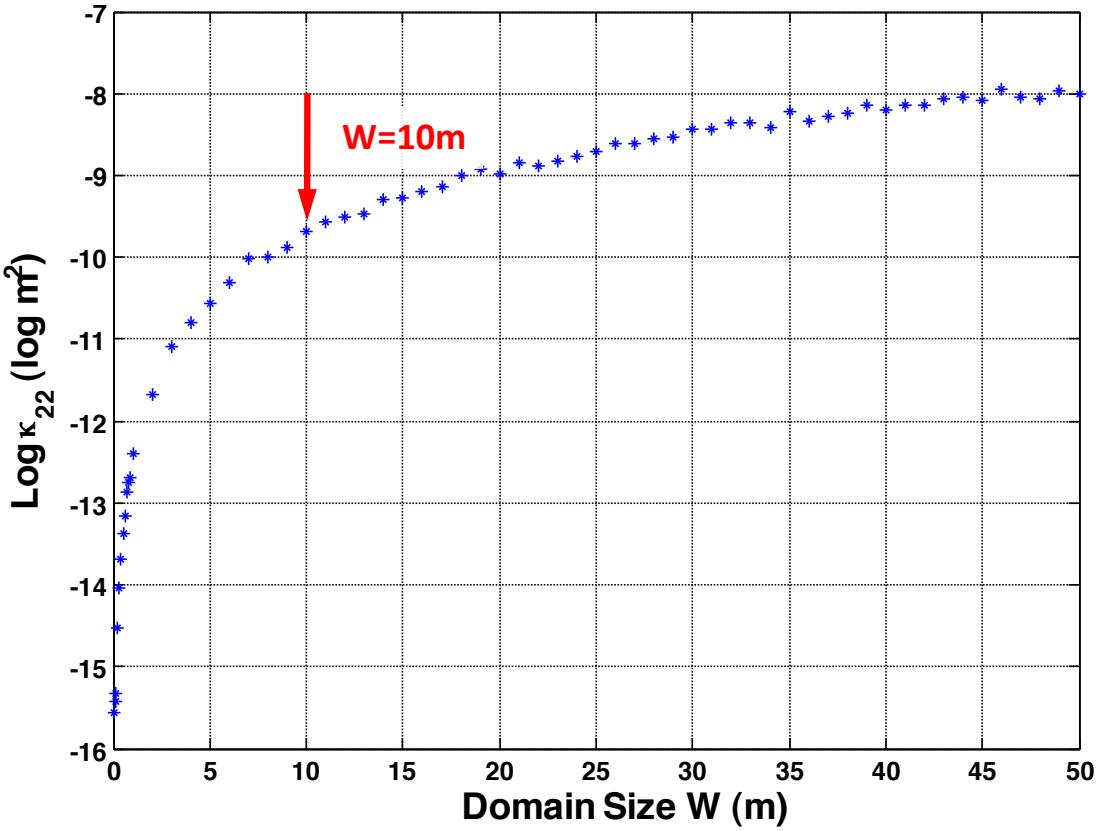

Figure A3. Impacts of the domain size on effective permeability

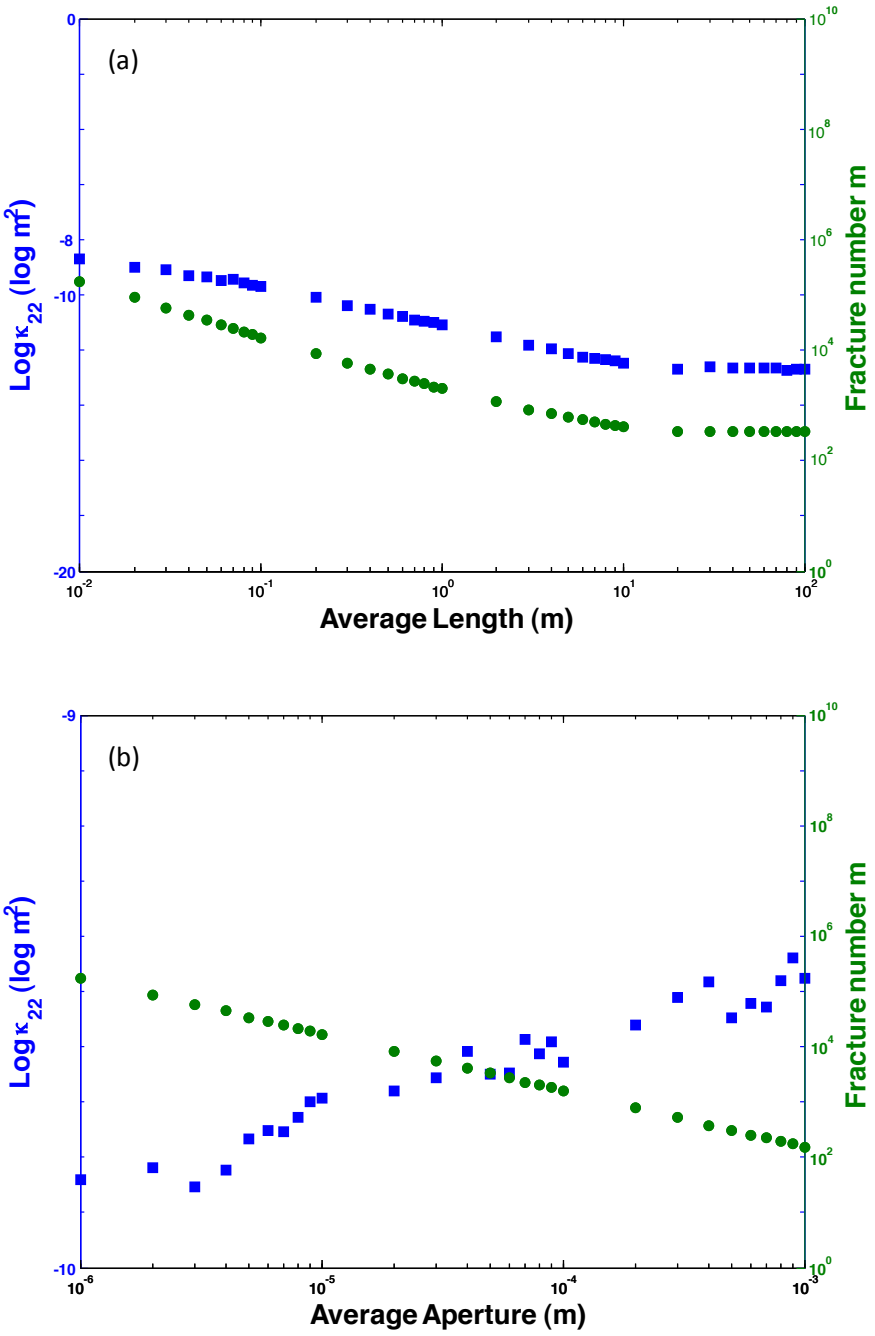

Figure A4. Responses of effective permeability and number of fractures to changes in (a) average length, (b) average aperture. (Both fracture length and aperture are lognormally distributed.)

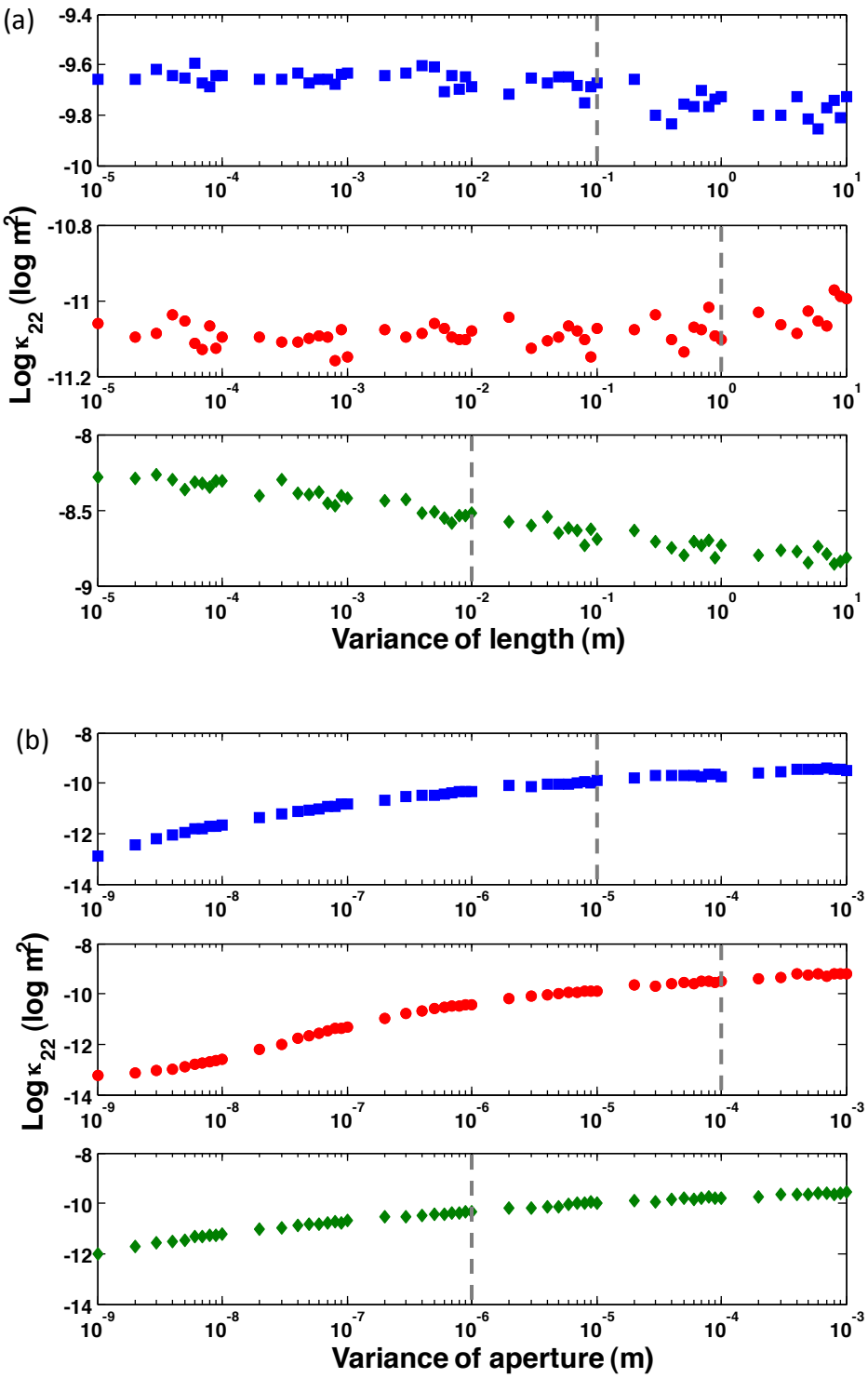

Figure A5. Sensitivity of effective permeability to changes in the variance of (a) length, and (b) aperture. (The grey dashed lines are the average in each case.)

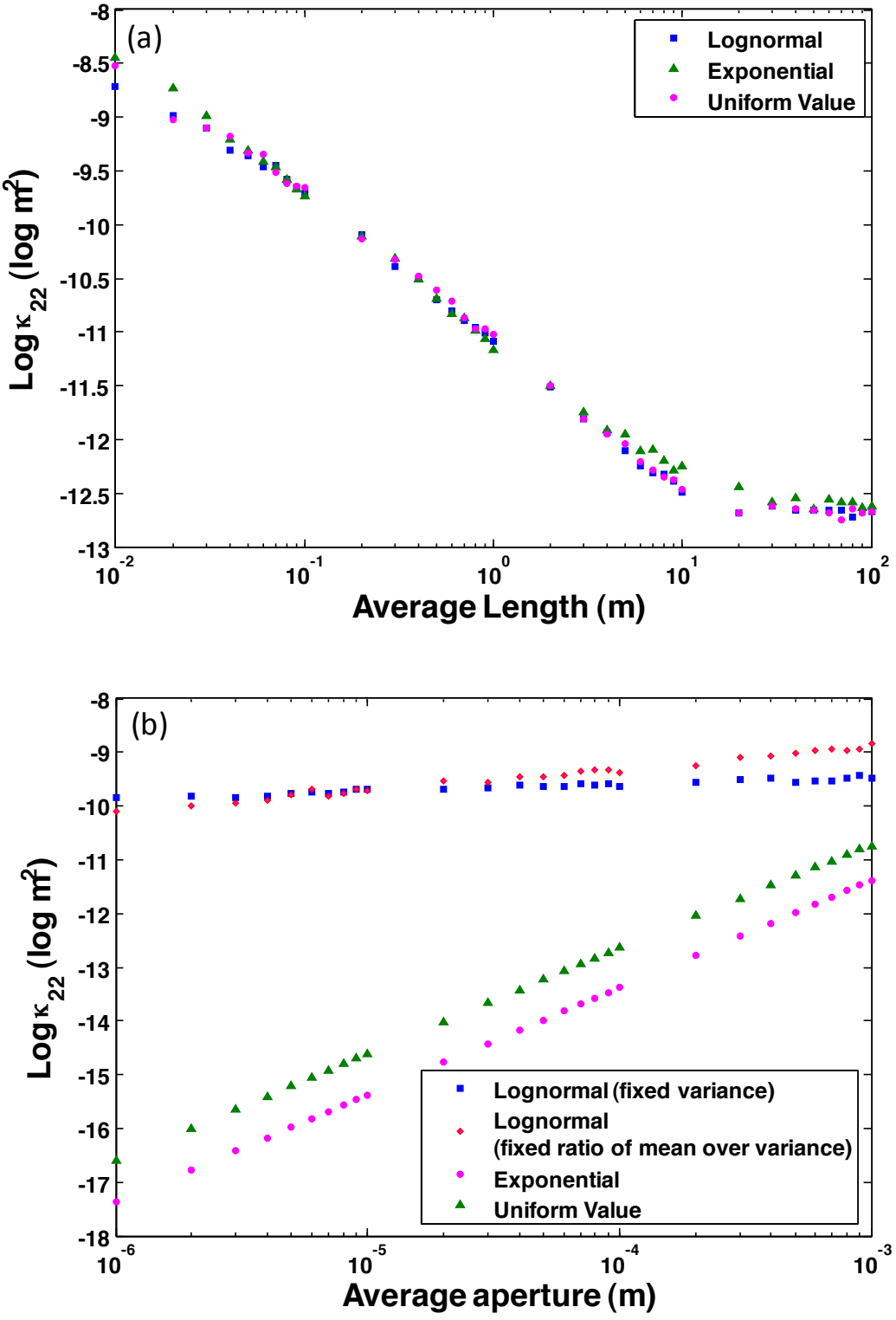

Figure A6. Comparison of the impacts on effective permeability of different distribution types of (a) length, and (b) aperture.

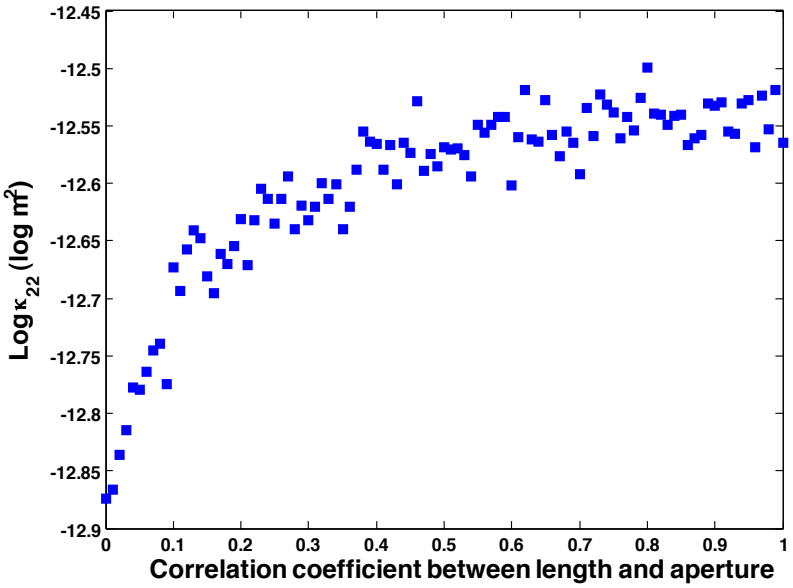

Figure A7. Impacts of correlation between fracture length and aperture on effective permeability.

To evaluate the impacts of connectivity on effective permeability, unconnected fractures or fractures only intersect with other fractures once were removed (figure A9(a), (b)), and the resultant effective permeabilities were compared with values estimated from all fractures. The results show that consideration of connectivity leads to reduction in effective permeability (figure A10). With low fracture density, effective permeabilities of connected fractures can be 6 orders of magnitude smaller than those without considering connectivity. As fracture density increases, the discrepancy between effective permeabilities with and without elimination of unconnected fractures narrows to less than one order of magnitude.

15.4 Conclusions

Based on the results above, the following conclusions can be drawn:

In general, fracture porosity (fracture density) is the most influential parameter for the determination of effective permeability of a microfracture network. When fracture porosity is small, indicating low fracture density, connectivity becomes the dominant factor.

With fixed fracture porosity, determination of average length must be made with caution, as it has a strong impact on effective permeability. The impacts of average aperture and the variance of aperture are considerably smaller, but the distribution of aperture must be carefully selected, as exponential and lognormal distributions gave very different outcomes. The less influential factors are the variance of length and the correlation between length and aperture.

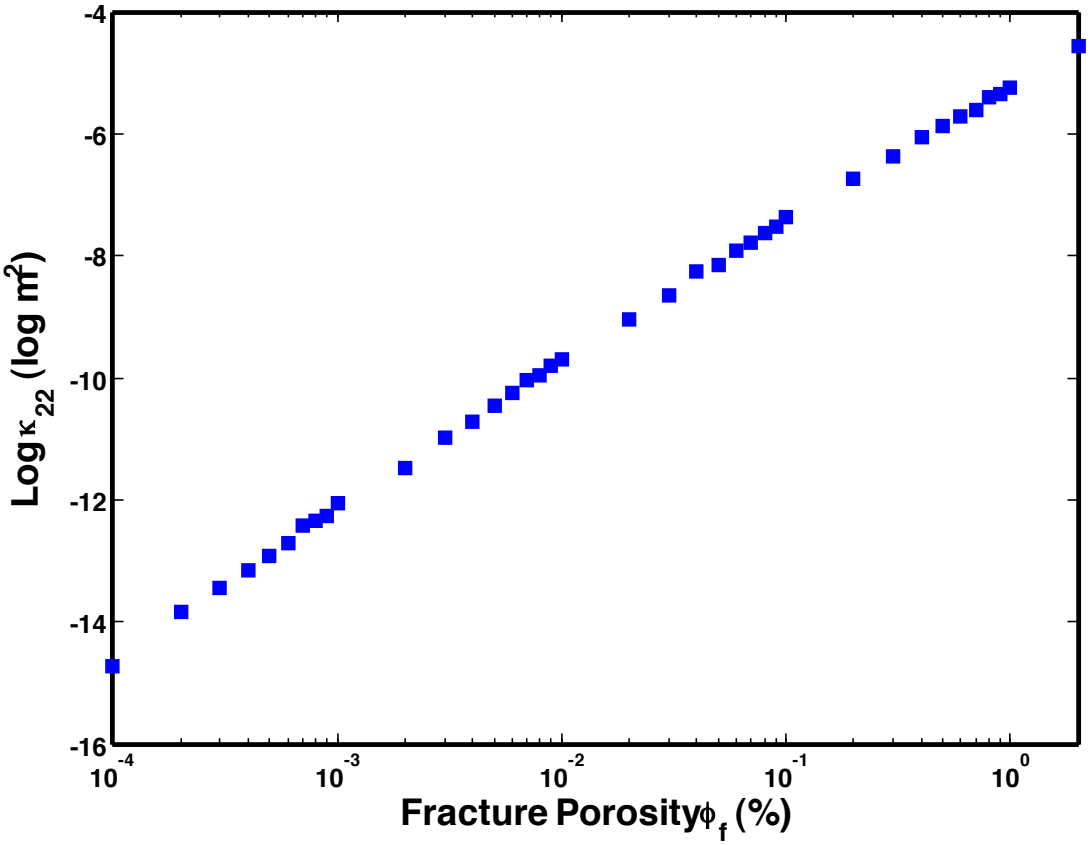

Figure A8. Sensitivity of effective permeability to changes in fracture porosity.

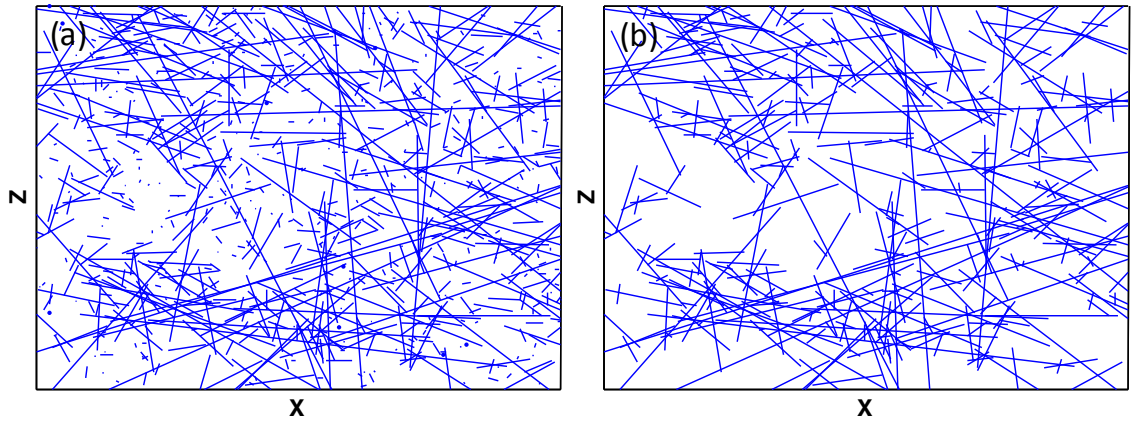

Figure A8. Examples of the (a) generated fracture work, and (b) the backbones of the generated fracture network.

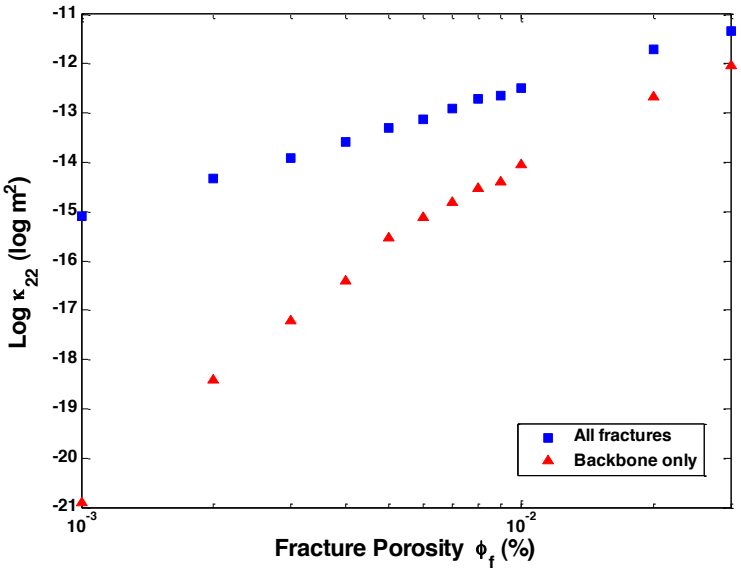

Figure A9. Comparison of effective permeabilities of the generated microfracture network and its backbones.

15.5 Reference

Ameen, M. S. and E. A. Hailwood (2008). "A new technology for the characterization of microfractured reservoirs (test case: Unayzah reservoir, Wudayhi field Saudi Arabia)." Aapg Bulletin 92(1): 31-52.

Gutierrez, M., L. E. Oino, et al. (2000). "Stress-dependent permeability of a de-mineralised fracture in shale." Marine and Petroleum Geology 17(8): 895-907.

Iding, M. and P. Ringrose "Evaluating the impact of fractures on the performance of the In Salah CO2 storage site." International Journal of Greenhouse Gas Control 4(2): 242-248.

Lee, S. H., M. F. Lough, et al. (2001). "Hierarchical modeling of flow in naturally fractured formations with multiple length scales." Water Resources Research 37(3): 443-455.

Long, J. C. S., J. S. Remer, et al. (1982). "Porous-media equivalents for networks of discontinuous fractures." Water Resources Research 18(3): 645-658.

Nelson, R.A., 1985, Geologic analysis of naturally fracture reservoirs, in Petroleum Geology Engineering, v. 1, Gulf Publishing Company.

Oda, M. (1985). "Permeability tensor for discontinuous rock masses." Geotechnique 35(4): 483-495.

Snow, D. T. (1969). "anisotropic permeability of fractured media." Water Resources Research 5(6): 1273-&.

Takahashi, T., K. Tanifuji, et al. (2003). "Permeability enhancement by microfracturing in granite under supercritical water conditions." Jsme International Journal Series a-Solid Mechanics and Material Engineering 46(1): 24-29.

Teimoori, A., Z. X. Chen, et al. (2005). "Effective permeability calculation using boundary element method in naturally fractured reservoirs." Petroleum Science and Technology 23(5-6): 693-709.

Wang, Q., Y. Li, et al. (2008). Calculation of permeability tensor of fractured rock mass based on statistics and its application in the fissured water around the tunnel. Boundaries of Rock Mechanics, Taylor & Francis: 707-710.

Witherspoon, P. A., J. S. Y. Wang, et al. (1980). "Validity of cubic law for fluid-flow in a deformable rock fracture." Water Resources Research 16(6): 1016-1024.

Chapter 16. A summary of papers and conference presentations from this project

16.1 Table 1. All publications, manuscripts, and conference presentations deriving from this project.

Y1Q1	--		
Y1Q2	--		
Y1Q3	Ellis, B.R.; Hui, W.C.E.; Peters, C.A. Fitts, J.P.; Bhatt, V. 2010. "Potential benefits of retrofitting power plants with combined CO_2-SO_2 emission control for co-injection in geologic carbon sequestration". 9th Annual Conference on Carbon Capture & Sequestration, Pittsburgh, PA May 10-13, 2010.	conference presentation	ELink product number DOE/FE0000749-1
Y1Q4	Ellis, B.R.; Bromhal, G.S.; McIntyre, D.L.; Peters, C.A. 2010. "Changes in caprock integrity due to vertical migration of CO2-enriched brine". *10th International Conf. on Greenhouse Gas Control Technologies*, 19th-23rd Sept 2010, Amsterdam, Netherlands.	conference presentation	Elink product number DOE/FE0000749-2
Y2Q1	H. Deng, C. A. Peters, J. P. Fitts, M. Pollak, E. Wilson, 2010. "Hydrogeological characterization of a potential CO2 injection site in Ottawa County, Michigan". Abstract H53E-1080 2010 Fall Meeting, AGU, San Francisco, Calif., 13-17 Dec.	conference presentation	Elink product number DOE/FE0000749-3
	B.R. Ellis, J.P. Fitts, G. Brohmal, D. McIntyre, R. Warzinski, E. Rosenbaum, C. A. Peters. 2010. "Computed Tomography Analysis of Alterations in Fractured Caprock Resulting from CO_2-acidified Brine", 2010 GSA Annual Meeting. *GSA Abstracts with Programs* 42(5).	conference presentation	Elink product number DOE/FE0000749-4
Y2Q2	Ellis, B.R.; Bromhal, G.S.; McIntyre, D.L.; Peters, C.A. 2011. "Changes in caprock integrity due to vertical migration of CO_2-enriched brine", *Energy Procedia*, 4: 5327-5334.	conference paper	Elink product number DOE/FE0000749-5
Y2Q3	B.R. Ellis, C.A. Peters, J.P. Fitts, G. Bromhal, D. McIntyre, B. Warzinski. "Investigation of caprock fracture evolution after CO2-brine flow", Tenth Annual Conference on Carbon Capture & Sequestration, May 2011, Pittsburgh, PA.	conference presentation	Elink product number DOE/FE0000749-6
	M.F. Pollak; J.M. Bielicki; D.S. Bael; J.A. Dammel; M. Rahimi, E.J. Wilson, "Leakage Risk, Interference, and CO_2 Storage Capacity". Tenth Annual Conference on Carbon Capture & Sequestration, Pittsburgh, PA, May 2-5, 2011.	conference presentation	Elink product number DOE/FE0000749-7

	E. Wilson; M. Pollak; J. Belicki; C. Peters; M. Celia; J. Fitts; V. Bhatt. "Integrating Geologic Storage of Carbon Dioxide with Other Subsurface Activities", Tenth Annual Conference on Carbon Capture & Sequestration, Pittsburgh, PA, May 2-5, 2011.	conference presentation	Elink product number DOE/FE0000749-8
	J.M. Bielicki; D.L. Bael; J.A. Dammel; M.F. Pollak; M.S. Rahimi; E.J. Wilson. "RISCS: A model of Risk Interference of Subsurface CO_2 Storage." The 6th Trondheim Conference on Carbon Dioxide Capture, Transport, and Storage, Trondheim Norway, June 12-15, 2011.	conference presentation	Elink product number DOE/FE0000749-9
	Dammel, J., Bielicki, J., Pollak, M., and Wilson, E. (2011). "A Tale of Two Technologies: Hydraulic Fracturing and Geologic Carbon Sequestration." *Environmental Science & Technology, 45(12) pp 5075-5076.*	journal paper	Elink product number DOE/FE0000749-10
Y2Q4	Ellis, B.R.; Peters, C.A.; Fitts, J.P.; Bromhal, G.S.; McIntyre, D.L.; Warzinski, R.P.; Rosenbaum, E.J. 2011. "Deterioration of a fractured carbonate caprock exposed to CO2-acidifed brine flow". *Greenhouse Gases: Science and Technology*. 1(3): 248	journal paper	Elink product number DOE/FE0000749-11
	C. A. Peters, A. F. Clarens, J. P. Fitts, C. M. Oldenburg, P. F. Dobson, J. S.Y.Wang, Y. Guglielmi, B. R. Ellis, S. Wang."Safe and effective geologic sequestration of CO_2: Partnerships for multi-scale experimental studies", Oral presentation at *Global Sustainability and Environmental Engineering: AEESP 2011 Conference.* Univ. of South FL, July 2011, Tampa, FL	conference presentation	Elink product number DOE/FE0000749-12
	B.R. Ellis; C.A. Peters; J.P. Fitts; G. Bromhal; D. McIntyre; B. Warzinski. "Investigation of caprock fracture evolution after CO2-brine flow". Global Sustainability and Environmental Engineering: AEESP 2011 Conference. Univ. of South FL, July 2011, Tampa, FL.	conference presentation	Elink product number DOE/FE0000749-13
	Ellis, B.R., Peters, C.A., Fitts, J.P., Bromhal, G.S., McIntyre, D.L., Warzinski, R.P. (2011), "Geochemical alteration of fracture geometry during leakage of CO2". Oral presentation at the 2011 Goldschmidt Conference, Prague, Czech Republic. Mineralogical Magazine, Vol. 75 (3), pg. 806	conference presentation	Elink product number DOE/FE0000749-14
Y3Q1	Brian R. Ellis; Catherine A. Peters; Jeffrey P. Fitts; Juan P. Nogues; Michael A. Celia; Mark Dobossy; Adam Janzen (2011), Alteration of Caprock Fracture Geometries During Flow of CO2-acidified Brine: Informing Basin-scale Leakage Models From Pore-scale modeling and Core-scale Experiments, Abstract GC42A-08 presented at 2011 Fall Meeting, AGU, San Francisco, Calif., 5-9 Dec.	conference presentation	Elink product number DOE/FE0000749-15
	Jeffrey M. Bielicki; Melisa Pollak; Elizabeth Wilson; Thomas R. Elliot; Bin Guo; Juan P. Nogues; Catherine A. Peters (2011), Your View or Mine: Spatially Quantifying CO2 Storage Risk from Various Stakeholder Perspectives, Abstract H42C-08 presented at 2011 Fall Meeting, AGU, San Francisco, Calif., 5-9 Dec.	conference presentation	Elink product number DOE/FE0000749-16
	Hang Deng; Dustin Crandall; Seth King; Brian R. Ellis; Grant S. Bromhal; Jeffrey P. Fitts; Catherine A. Peters (2011), Change in fracture permeability after the flow-through of CO2-acidified brine, Abstract GC51A-0935 presented at 2011 Fall Meeting, AGU, San Francisco, Calif., 5-9 Dec.	conference presentation	Elink product number DOE/FE0000749-17

	Juan P. Nogues; Catherine A. Peters; Jeffrey P. Fitts; Michael A. Celia (2011), Investigation of dissolution and precipitation of carbonate rocks using reactive transport modeling in pore networks, Abstract GC51A-0940 presented at 2011 Fall Meeting, AGU, San Francisco, Calif., 5-9 Dec.	conference presentation	Elink product number DOE/FE0000749-18
	Bin Guo; Edward N. Matteo; Thomas R. Elliot; Juan P. Nogues; Hang Deng; Jeffrey P. Fitts; Melisa Pollak; Jeff Bielicki; Elizabeth Wilson; Michael A. Celia; Catherine A. Peters (2011), Semi-analytical estimation of wellbore leakage risk during CO2 sequestration in Ottawa County, Michigan, Abstract GC51A-0948 presented at 2011 Fall Meeting, AGU, San Francisco, Calif., 5-9 Dec.	conference presentation	Elink product number DOE/FE0000749-19
Y3Q2	--		
Y3Q3	Bielicki, J.M.; Pollak, M.; Wilson, E.J.; Peters C.A.; Fitts J.P. (2012). "Spatially Integrated Assessment of Leakage Risk from CO_2 Storage Reservoirs from Multiple Stakeholder Perspectives" *11th Annual Conference on Carbon Capture Utilization & Sequestration*, April 30 - May 3, 2012, Pittsburgh, PA. Poster Presentation.	conference presentation	Elink product number DOE/FE0000749-20
	Pollak, M.F., Bielicki, J.M., Dammel J.A., Fitts J.P., Peters C.A., Wilson, E.J. (2012). Estimating Financial Consequences of Leakage from Geologic Sequestration. *11th Annual Conference on Carbon Capture Utilization & Sequestration*, April 30 - May 3, 2012, Pittsburgh, PA. Oral Presentation.	conference presentation	Elink product number DOE/FE0000749-21
	V. Bhatt , D. Mahapatra, H. Li. (2012) "Evaluating Opportunities for Long-term Deployment of CCS in U.S. Energy Market". *11th Annual Conference on Carbon Capture Utilization& Sequestration*, April 30 - May 3, 2012, Pittsburgh, PA. Oral Presentation.	conference presentation	Elink product number DOE/FE0000749-22
	J. P. Nogues, M. A. Celia, C. A. Peters. "PORE NETWORK MODEL DEVELOPMENT TO STUDY DISSOLUTION AND PRECIPITATION OF CARBONATES", XIX International Conference on Water Resources CMWR 2012, June 17-22, 2012. Archived online at http://cmwr2012.cee.illinois.edu/SubsurfaceBiogeochemReactiveTrans%28Proceedings%29.html	conference paper	Elink product number DOE/FE0000749-23
Y3Q4	Peters, C.A.; Fitts, J.P.; Celia, M.A., Kalb, P.D.; Bhatt, V.; Wilson, E.J.; Bielicki, J.M.; Pollak, M. "Basin-Scale Leakage Risks from Geologic Carbon Sequestration: Impact on CCS Energy Market Competitiveness" U.S. DOE NETL, Developing the Technologies and Building the Infrastructure for CO_2 Storage. Pittsburgh August 21-23, 2012.	Conference presentation	Elink product number DOE/FE0000749-24
Y4Q1	M.F. Pollak, J.M. Bielicki, J.A. Dammel, E.J. Wilson, J.P. Fitts, C.A. Peters. "The Leakage Impact Valuation (LIV) Method for Leakage from Geologic CO_2 Storage Reservoirs" International Conference on Greenhouse Gas Technologies (GHGT-11), 18th-22nd November 2012, Kyoto International Conference Center, Japan. *Energy Procedia*, 37 (2013) 2819-2827.	conference paper	Elink product number DOE/FE0000749-25
	J.M. Bielicki, M.F. Pollak, E.J. Wilson, J.P. Fitts, C.A. Peters, "A Methodology for Monetizing Basin-Scale Leakage Risk and Stakeholder Impacts." International Conference on Greenhouse Gas Technologies (GHGT-11), 18th-22nd November 2012, Kyoto International Conference Center, Japan. *Energy Procedia*, 37 (2013) 4665-4672.	conference paper	Elink product number DOE/FE0000749-26
	J.M. Bielicki, M. F. Pollak, C. A. Peters, E. J. Wilson. "CCS in a hot, crowded world: Integrating subsurface	Conference	Elink product number

	management", 2012 APPAM Fall Research Conference: Policy Analysis & Public Management in an Age of Scarcity: The Challenges of Assessing Effectiveness & Efficiency, November 8-19, 2012. Archived at http://appam.confex.com/appam/2012/.	presentation	DOE/FE0000749-27
	BR Ellis, JP Fitts, CA Peters "Mineral Spatial Heterogeneity Constrains Permeability Evolution in a Limestone Fracture" Abstract H11A-1139 presented at 2012 Fall Meeting, AGU, 3-7 Dec. 2012.	Conference presentation	Elink product number DOE/FE0000749-28
	B Guo, JP Fitts, M Dobossy, JM Bielicki, CA Peters, "Accounting for geochemical alterations of caprock fracture permeability in basin-scale models of leakage from geologic CO2 reservoirs", Abstract H23A-1344, presented at 2012 Fall Meeting, AGU, San Francisco, Calif., 3-7 Dec. 2012.	Conference presentation	Elink product number DOE/FE0000749-29
	Deng, H., Ellis, BR., Peters, C.A., "Modification of Fracture Hydraulic Properties by CO_2-Acidified Brine Flow" American Institute of Chemical Engineering: 2012 AICHE Annual Meeting, Pittsburgh, PA. Nov. 2012.	Conference presentation	Elink product number DOE/FE0000749-30
	Bielicki, J., Middleton, R., Wilson E., Fitts, J., and Peters, C. (2012). "Carbon Dioxide Pipeline Infrastructure Dependence on Reservoir Risk" American Institute of Chemical Engineering: AICHE Annual Meeting. Pittsburgh, PA. Nov. 2012.	Conference presentation	DOE/FE0000749-31
Y4Q2	B.R. Ellis, J.P. Fitts, G.S. Bromhal, D.L. McIntyre, R. Tappero, C.A. Peters. "Dissolution-Driven Permeability Reduction of a Fractured Carbonate Caprock". *Environmental Engineering Science*. 30 (4): 187-193, 2013. DOI: 10.1089/ees.2012.0337	Journal paper	Elink product number DOE/FE0000749-32
	Deng, H.; Ellis, B.R.; Peters, C.A.; Fitts, J.P.; Crandall, D.; Bromhal, G.S. "Modifications of carbonate fracture hydrodynamic properties by CO2-acidified brine flow". *Energy and Fuels*. No. 27, pp. 4221 – 4231, 2013. DOI: 10.1021/ef302041s.	Journal paper	Elink product number DOE/FE0000749-33
	J.P. Nogues, J.P. Fitts, M.A. Celia, C.A. Peters. "Permeability evolution due to dissolution and precipitation of carbonates using reactive transport modeling in pore networks", *Water Resources Research*, Vol 49: 6006-6021, doi:10.1002/wrcr.20486, 2013	Journal paper	Elink product number DOE/FE0000749-34
	H. Deng, J.P. Fitts, C.A. Peters, L. Li, D. Crandall, G. Bromhal. "Experimental study of reactive flow in an Eau Claire fracture exposed to CO_2-rich brine" ARMA 13-592. American Rock Mechanics Association, 47th US Rock Mechanics / Geomechanics Symposium, San Francisco, CA June 2013. Vol. 13, p. 592.	conference paper	Elink product number DOE/FE0000749-35
	C.A. Peters, J.P. Fitts, D. Mahapatra, E. Matteo, M.F. Pollak, J.M. Bielicki, V. Bhatt, E.J. Wilson. "Economics and Policy Drivers Module (EPDM) Cost Calculator for Geologic Carbon Sequestration and Leakage Assessment". Princeton University, Princeton, NJ 08540. Excel Spreadsheet available at http://www.subsurfacerisk.umn.edu/publications.html. June 2013.	software	ESTSC software DOE/FE0000749-36
post end-date	J. Bielicki, J. Fitts, C. Peters, E. Wilson. 2013 "Monetizing Leakage Risk of Geologic CO_2 Storage using Wellbore Permeability Frequency Distributions". *Geophysical Research Abstracts*. Vol. 15 EGU2013-10924. EGU General Assembly 2013.	Conference presentation	Elink product number DOE/FE0000749-37
	J.P. Fitts and C.A. Peters, "Caprock Fracture Dissolution and CO_2 Leakage", In: *MSA Reviews in Mineralogy & Geochemistry* "Geochemistry of Geological CO_2 Sequestration." Eds. D. DePaolo, D. Cole, I. Bourg, A. Navrotsky. 2013. Vol 77 pp. 459 – 479 (2013).	peer reviewed book chapter	Elink product number DOE/FE0000749-38

	H. Deng, J. Fitts, R. Tappero, C. Peters, S. Wirick, W. Rao. "X-ray imaging studies of water-rock interactions at fracture surfaces during fluid flow", 2013 National Synchrotron Light Source/Center for Functional Nanomaterials (NSLS/CFN) Joint Users' Meeting, Brookhaven National Lab, Upton, NY, May 20-22, 2013.	Conference presentation	DOE/FE0000749-39
	J.M. Bielicki; M.F. Pollak; J.P. Fitts; C.A. Peters; E.J. Wilson. "Causes and Financial Consequences of Geologic CO_2 Storage Reservoir Leakage and Interference with other Subsurface Resources". *International Journal of Greenhouse Gas Control*. 2014. Vol. 20: 272-284.	Journal paper	Elink product number DOE/FE0000749-40
	C.A. Peters, J.P. Fitts, E.J. Wilson, M.F. Pollak, J.M. Bielicki, V. Bhatt (2014) "Basin-Scale Leakage Risks from Geologic Carbon Sequestration: Impact on Carbon Capture and Storage Energy Market Competitiveness", Princeton University, Princeton, NJ. DOE Project Final Report DOE/FE0000749-41, February 2014.	Technical report	Elink product number DOE/FE0000749-41
In prep.	J.M. Bielicki, J.P. Fitts, C.A. Peters, E.J. Wilson. "The Potential for Leakage from Geologic CO_2 Storage in the Michigan Basin". 2014. In preparation for *Environmental Science & Policy*.	Journal paper – in preparation	DOE/FE0000749-42
	Bin Guo, Jeffrey P. Fitts, Mark E. Dobossy, Catherine A. Peters. "Simulation of permeability evolution of leakage pathways in carbonate-rich caprocks with carbonic and sulphurous acid". Manuscript in preparation for *Water Resources Research.*	Journal paper – in preparation.	DOE/FE0000749-43
	J.M. Bielicki, M.F. Pollak, E.J. Wilson, J.P. Fitts, C.A. Peters "RISCS: A Model for Monetizing Risk Interference of Subsurface CO_2 Storage". 2014. In preparation for *Environmental Science & Policy*.	Journal paper – in preparation.	DOE/FE0000749-44